Thermal durability of novel thermoelectric materials for waste heat recovery

Gunstein Skomedal

Thermal durability of novel thermoelectric materials for waste heat recovery

Doctoral dissertation for the degree Philosophiae Doctor (PhD) at the Faculty of Engineering and Science with specialization in Renewable Energy

University of Agder
Faculty of Engineering Sciences
2016

Doctoral Dissertations at the University of Agder 130

ISSN: 1504-9272
ISBN: 978-82-7117-823-9

Printed by the Printing Office, University of Agder
Kristiansand

Preface

In the autumn of 2012, Marianne Engvoll from TEGma AS contacted me and asked if I was interested in doing a PhD on thermoelectric materials. Uneducated as I was, I immediately googled “thermoelectricity” and the subject hit me straight away as something I would love to work more with. As a material scientist, the prospect of exploring novel materials was of course very interesting. In addition, the possible application of thermoelectric materials to recover wasted energy was a great motivator. I was soon adopted into two ongoing projects on thermoelectricity; ThermoMag, a EU FP7 project on magnesium silicide, and ThermoMat, a NFR project on skutterudites - both novel, promising, thermoelectric materials. In both projects, the common interest was up scaling of the production of both materials and modules, and assessment of the thermal durability of these. The topic of the thesis therefore quickly crystallized around exploring the thermal durability of mainly these two novel material types – skutterudites and silicides.

During the three years I have now studied these classes of materials and their potential, I’ve met a lot of people from around the world of whom I’ve received support and help from. First and foremost I would like to thank my two supervisors Hugh Middleton (UiA) and Marianne Engvoll (TEGma AS) for inviting me to work with them and with great support during the work on the thesis. I hope that we can continue our great collaboration.

A big thanks to Lennart Holmgren (TermoGen AB) for letting me work together with him in his fabulous lab at the island Gotland in Sweden. Also thanks to other ThermoMag partners with collaboration and steady supply of thermoelectric materials which I could study further.

I was very lucky to stay 10 weeks at the Institute of Materials Research, Thermoelectric Functional Materials, DLR, Cologne. This was absolutely the most fruitful period of my PhD in terms of scientific experiments and results. A big thanks to Andreas Sesselmann, Reinhard Sottong, Echart Müller and all the other very good colleagues there, I really appreciate the possibility to work with you.

Thank you to all my colleagues at the University of Agder, especially those who had to share office, frustration and joy with me. A special thanks to Nils R. Kristiansen for many interesting discussion and collaboration on a couple of the papers. Also colleagues at Center for Materials Science and Nanotechnology at University of Oslo deserves recognition, in particular Reidar Haugsrud for helpful discussions and collaboration. I would also like to thank Anders Hope Amundsen (Elkem AS) for help with SEM imaging.

Last but not least, a huge thanks to my wife Ragnhild, who not only supported me throughout this period, but also gave birth to our beautiful daughter Solveig, at the end of these three years. Such an event sets things in perspective. Hopefully, she will grow up in a world where thermoelectricity not only is a phenomena left to stubborn scientist to explore, but are implemented on a large scale to do away with some of the enormous energy waste we see worldwide today.

Being one of the first to work with thermoelectricity at the University of Agder, I have chosen to include a rather comprehensive introductory part for the benefit of future students of the field. I hope that this work can inspire young researchers to deepen their understanding and further explore the conversion of heat into electricity through thermoelectric materials.

An extra motivator for me during the work on the thesis have been the fact that my mother grew up only a few kilometers away from the cobalt mines in Skuterudåsen, where skutterudites were first found and characterized, and that I used to visit these regularly during my childhood. I would recommend to the reader a visit to Blåfarveværket in Buskerud county in Norway, to explore how the cobalt-rich mineral skutterudite, not only can be used to convert heat into electricity, but also create some of the most beautiful color of “Blå” (blue).

Gunstein Skomedal
Kristiansand, Norway
March 2016

Abstract

Thermoelectric Generators (TEG) are a potential technology for waste heat recovery. At their hearts, thermoelectric materials convert a heat flux into electric current. By placing TEGs on the surface of a waste heat source, some of the heat can be converted into valuable electric energy. However, todays state-of-the art materials have low efficiencies, are limited to low temperature operation, contains toxic and rare elements and are in general not cost-effective for such applications. New thermoelectric materials are needed that can overcome these barriers.

In this thesis, two classes of materials have been investigated; skutterudites and silicides. Both have relatively high efficiencies, can be used at high temperatures (400-500°C) and contain cheaper and less toxic compounds than state-of-the-art materials. To move these materials from lab-scale testing into real-life applications, the focus is shifted from optimizing for thermoelectric efficiency to long-term stability. As these materials will be used at higher temperatures, different temperature activated processes leading to degradation of the materials needs to be accounted for and controlled, such as oxidation and interdiffusion. Adoption into industrial mass production requires simple and cheap synthesis methods that produces homogenous materials. Homogenous materials are very important for achieving stable thermoelectric and mechanical properties over time.

Secondary phases can easily form during synthesis of skutterudites, and knowledge about the formation and annihilation of such phases during synthesis was therefore studied thoroughly as these can have unbeneficial effect on both thermoelectric properties and thermal durability. Understanding the mechanisms and kinetics governing skutterudite formation is of great importance for optimizing synthesis parameters leading to faster and more homogenous production of skutterudites. P-type skutterudites with composition $Fi_{0.6}Co_2Fe_2Sb_{12}$ (Fi = In, Ca, Ce and Yb) were synthesized to look at the effect of filler element and microstructure. Ce-filled sample was furthermore synthesized using four different methods to assess the effect of synthesis method on secondary phase formation and thermoelectric properties. A precursor method was found to not only be the fastest method, but also produce the most homogenous material with highest zT of 0.7. An important contribution of this thesis is the results and discussion around peritectic formation and transformation in the skutterudite system. In addition to grain size, the diffusivity of the filler element in

skutterudite was found to be the main factor governing transformation time into phase pure skutterudite.

High temperature oxidation of skutterudites as a function of filler atoms and iron content were furthermore investigated. Residual secondary phases resulting from incomplete transformation into the phase pure skutterudite, such as $FeSb_2$ and $CeSb_2$, were found to have severe effects on the oxidation rate. High iron content was also found to lower the onset temperature of oxidation in accordance with previous studies. In addition, the effect of In as a filler element was found to form an intermediate InSb layer that actually caused a reduction in oxidation rate.

Also the high temperature oxidation of Mg_2(Si-Sn) was studied as a function of the Sn content. All these materials formed a passivating outer layer of MgO. Above a certain ignition temperature, the MgO layer broke down and the oxidation proceeded exponentially. An increasing Sn content was found to significantly lower the ignition temperature due to formation of liquid Sn below the MgO layer. Similarly, the Pilling-Bedworth ratio (ratio of volume of oxide to volume of underlying alloy) was found to affect the ignition temperature.

In both these oxidation studies, the common theme is that variations in elemental composition affect the resistance towards oxidation significantly. Clearly, these materials need to be optimized not only in terms of thermoelectric performance, but also stability towards oxidation. First of all, oxidizing resistant materials can be employed in application without the need of protective environments such as coatings or encapsulations. Secondly, control of the oxidation mechanisms is import in a mass production process both to ease the production process and to avoid accumulation of oxides in the final material.

An alternative to oxidation resistant materials is the application of coatings on the outer surfaces. Several commercially available coatings were tested on both skutterudite and silicide. An aluminum-based coating was found most promising and could protect both material classes from oxidation during thermal cycling up to temperatures of 500-550°C. It is believed that further optimization of this type of coating has a good future for use in protection of thermoelectric materials at high temperatures.

To assess how different thermally activated degradation process affect the performance of thermoelectric materials and modules, long term testing of both single functionalized legs and prototype modules were conducted.

A new test method was developed, where several single legs were electrically characterized separately throughout thermal cycling. This made it possible to compare different types of coatings with uncoated material, thereby identify the effect of the degradation processes upon performance. Both diffusion of metal contact into thermoelectric leg, oxidation in from sides, and crack formation, were found to significantly affect the performance of the legs over time, by reducing open circuit voltage and increasing inner resistance.

Finally, several silicide based modules were assembled and tested. The n-type and p-type material was Mg_2(Si-Sn) and $MnSi_{1.75}$ respectively. The highest power of 3 W was measured for one of these modules at hot side temperatures of 700°C and an estimated efficiency of 5.3% – the highest efficiency recorded to date for modules made purely of silicides. However, long term testing of one of these modules revealed gradual reduction in performance. Post-characterization showed how particularly oxidation and interdiffusion between thermoelectric leg and metal contact played a major role in the decline in power output.

CONTENT

1 Introduction

The title *“Thermal durability of novel thermoelectric materials for waste heat recovery”* consists of several concepts that will each be defined accordingly. What is understood by thermal durability? What new materials are the most promising alternatives for future exploitation in thermoelectric devices? What is the role of thermoelectric material in waste heat recovery? The first section 1.1 will show the potential for waste heat recovery and how this becomes more and more important in the coming time. In section 1.2, a general introduction to waste heat recovery is found. Shortcomings of the state-of-the-art technology choices in this field are discussed, and thus form a motivation for looking into thermoelectric material as a new and alternative way to utilize waste heat sources. Then in section 1.3, the current limitation in the field of thermoelectricity is briefly discussed with emphasis on new challenges that arise when going from lab-scale research to large-scale development, production and end-use applications. The objectives and scope presented in section 1.4 are based on this discussion. Finally, the outline of the thesis is found in section 1.5, which gives a brief summary of each chapter.

1.1 Background

Our world hungers for energy. As global population is growing and more and more people want to increase their quality of life, this will also yield higher energy consumption. According to recent reports, the energy demand will continue to increase by 30–40% the next 20 years [1, 2]. Today most of the energy, around 80%, comes from fossil fuels and will continue to do so in the near future. Because of the greenhouse gases these energy conversion technologies emit, along with their inherently non-sustainable usage of limited resources, others sources of energy will eventually need to take over a much higher portion of energy production. Renewables, even though they account for very small portions of the energy production today, are anticipated to take care of much of the growth in energy production in the coming decades. But producing more clean and renewable energy is not the only solution. We also need to utilize the energy we already produce in a much more efficient way. In the EU, there are clear targets on improving energy efficiency by at least 20% by 2020 (from 2010 levels), and 27% by 2030 [3]. Also many other nations have targets on energy efficiency as one of the most important means to reduce their greenhouse gas emissions.

A detailed study of the total energy use in the US has been conducted every year by the Lawrence Livermore National Laboratory [4]. The last results from 2014 can be found in Figure 1.1. It shows how an estimate of 60% (59.4 Quads[1]) of the energy use in the US ends up as rejected heat, where most of this is waste heat.

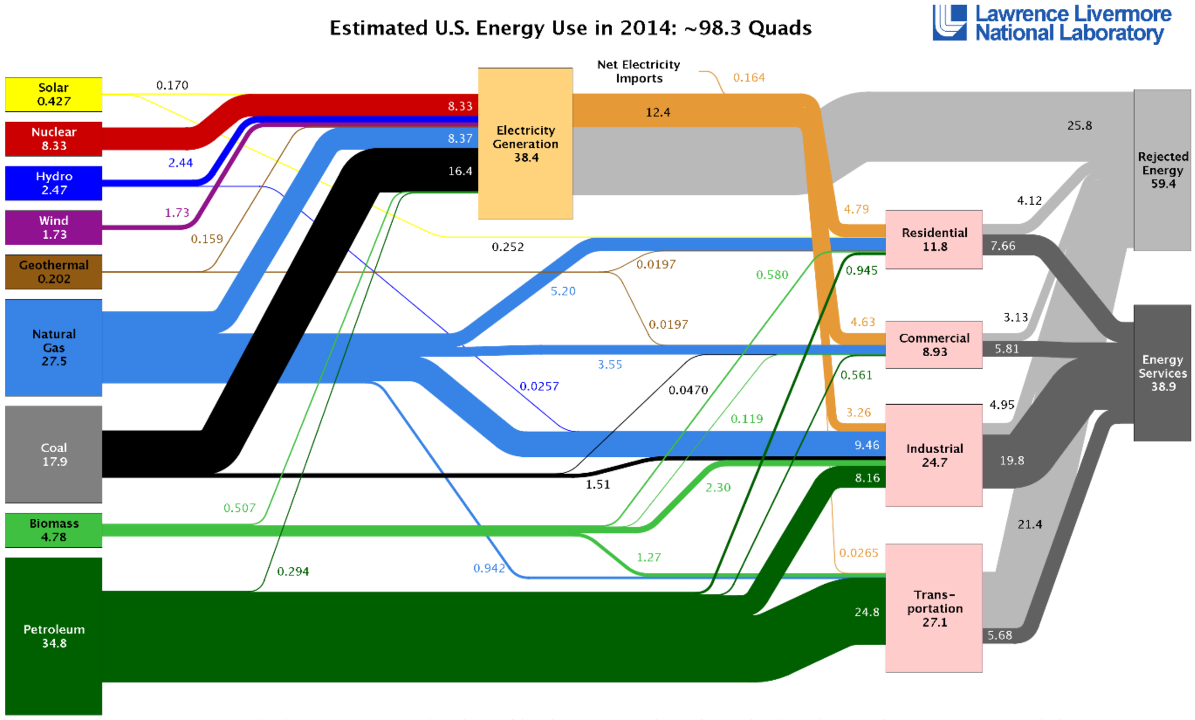

Source: LLNL 2015. Data is based on DOE/EIA-0035(2015-03), March, 2014. If this information or a reproduction of it is used, credit must be given to the Lawrence Livermore National Laboratory and the Department of Energy, under whose auspices the work was performed. Distributed electricity represents only retail electricity sales and does not include self-generation. EIA reports consumption of renewable resources (i.e., hydro, wind, geothermal and solar) for electricity in BTU-equivalent values by assuming a typical fossil fuel plant "heat rate." The efficiency of electricity production is calculated as the total retail electricity delivered divided by the primary energy input into electricity generation. End use efficiency is estimated as 65% for the residential and commercial sectors 80% for the industrial sector, and 21% for the transportation sector. Totals may not equal sum of components due to independent rounding. LLNL-MI-410527

Figure 1.1 US energy production and consumption in 2014. Approximately 60% of the energy ends up as rejected energy, which is not directly utilized [4].

1.2 The basics of waste heat recovery

Waste heat can be defined as “heat energy in the shape of hot air, steam or fluid which is not utilized in the energy production process and is therefore lost to the environment” [2]. The major part of the rejected energy seen in Figure 1.1 is waste heat resulting from the burning of fossil fuels in electric power production and high temperature industrial processes. The transport sector also accounts for a very large part of the rejected energy (27.1 Quads). In a normal gasoline engine for cars, only about 25% of the energy is converted into useful energy while the rest is rejected through coolant and exhaust gases as waste heat [5]. It is obvious that the potential for utilizing this energy better is enormous.

---

[1] 1 Quads = BTU = 1.055×10^{18} J

[2] The Norwegian encyclopedia, *Store Norske Leksikon*, available online on snl.no/spillvarme (30.10.13)

In a report on waste heat in Norway from Enova in 2009, it was concluded that around 25% of waste heat in Norwegian industry could be exploited for waste heat recovery [6]. However, here only existing technologies like steam-turbine, steam-engine, Stirling-engine and ORC (organic rankine cycle) were discussed. The recent decision to install a new energy recovery system at Elkem Salten,[3] which will recover 30% of the electricity consumption, is just one example of how more and more effort is put into exploiting this potential [7].

A similar report on waste heat recovery technologies and opportunities in the US industry concluded that most of the potential of waste heat recovery on large-scale industrial plants with clean gaseous exhaust streams was already exploited to a large extent [8]. But for dirtier exhaust gases, smaller scale applications, and lower temperature waste heat streams, energy recovery is seldom installed and should therefore be further developed. Heat sources that are many in numbers but relative small in size, such as cells in an aluminum plant, vehicles and ships, represent a significant potential.

Heat recovery has its theoretical foundation in thermodynamics. Waste heat has a lower energy value (a higher entropy, a lower exergy) than other forms of energy, such as electricity. The carnot efficiency is the highest theoretical efficiency a heat recovery system can obtain and is given by

$$\eta_{carnot} = (T_H - T_C)/T_H \tag{1.1}$$

where T_H is the temperature of the waste heat, T_C the temperature of the cold side heat exchanger and η the ratio between the work done by the system (for example electricity generated) and the heat energy supplied. This equation shows how the higher the temperature of the waste heat is, the more efficiently this energy can be exploited further. It is therefore obvious that the waste heat recovery programs, such as the ones supported by Enova, aim at picking the lowest hanging apples first, where either the waste heat can be directly used as district heating (energy loss only during transport) or the higher temperature and volume waste heat sources where the conversion efficiency is the highest.

The higher-hanging apples, where the temperature is too low or the energy volume too small, are seldom considered usable with existing technology to encompass investment in energy recovery systems. Steam turbines, which are the most used technology for

---

[3] Elkem Salten is a silicon plant north in Norway.

converting heat into electricity, take up a lot of extra space, need extra maintenance and complicate the total process further, while also having a much higher cost per watt produced at lower temperatures. The same factors limit most of the existing waste heat recovery technologies.

Thermoelectric Generator (TEG) is one technology that has a huge potential when it comes to utilizing parts of this waste heat energy source [9]. A TEG is a solid-state device that converts a heat flow directly into electric energy without any moving parts (see Chapter 2 for a more detailed description). It is also easily scalable to any size, and can be utilized as well for lower temperature waste heat recovery purposes. On the negative side, TEG technology is still not fully developed and today's solutions have quite low efficiency and are nevertheless very expensive. But this is about to change.

The thermoelectric market as a whole is expected to be a multibillion USD industry within 2023 [10], where three main areas of applications are seen; waste heat recovery systems in cars, wireless sensor applications and other consumer applications. The main challenge now is up-scaling the production processes of known thermoelectric materials to lower the price. It is believed that this growth will also open up other areas convenient for thermoelectric energy harvesting, especially for waste heat recovery purposes.

1.3 Current limitation to thermoelectric technology

So far the main obstacles for using TEG's in commercial application are mostly stated as material related [11]:

a. Low efficiency
b. Too expensive material and systems
c. Low durability at elevated temperatures
d. Toxic compounds
e. Low abundance of raw materials

Furthermore, other challenges arise on the system level, as infrastructure of the generator vastly increases the cost of the system as a whole. Especially cost and complexity in relation with transporting heat to and from the generator through heat exchangers are important [12, 13]. For now most attention has been given point (a). Still, the hunt for a material with high efficiency is on-going, mostly through optimization of thermoelectric material properties leading to higher *figure of merit,* $z = \alpha^2\sigma/\kappa$, where α is the Seebeck coefficient, σ the electric conductivity and κ the thermal conductivity (more details in chapter 2). Several breakthroughs have been made in the last decades [14, 15] which have spurred a lot of research activity in the field. Multiplied with temperature, the dimensionless figure of merit, zT is used to compare thermoelectric materials over a temperature range. **Figure 1.2** shows the zT as function of temperature of some of today's state-of-the-art thermoelectric materials. At low temperatures, telluride-based compounds (Bi_2Te_3 and Sb_2Te_3) are today's industry standard, with fairly high efficiency and good durability. But the temperature range is too low for use in transport and industrial waste heat recovery, and the cost efficiency-ratio is still too high to enter the market for other applications than niche products.

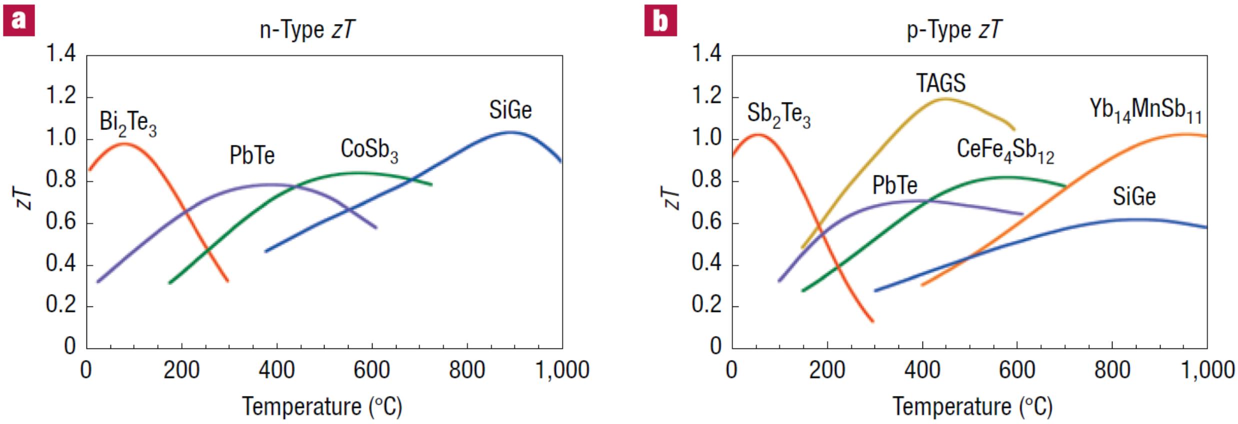

Figure 1.2 zT values of different state-of-the-art thermoelectric material plotted against temperature. The zT value is directly related to the overall efficiency of the material converting heat to electricity. Graphs from [14].

On the medium to high-end side of the temperature scale, many promising materials are coming up as good alternatives for waste heat recovery applications. One of these materials is skutterudite-based compounds [16], which are one of the materials that will be looked at more at in this thesis. The basic chemical formula is $CoSb_3$ and zT values of 1.7 [17] have been achieved. This material can be used in temperatures up to 500–600°C, but at this time no mass-production exists.

Another promising material is magnesium silicide and its solid solution with magnesium stannide, Mg_2Si-Mg_2Sn [18]. This class of material has shown zT values in the order of 1.3 [19], but still challenges remain to produce this material on a larger scale. It was chosen for a EU-framework program project, ThermoMag [20, 21] due to the high abundance of raw materials in Europe (and globally), the very low density (as weight is an important factor in many applications), and non-toxicity which is an issue becoming more and more important.

One of the best achieved zT value for a medium to high temperature thermoelectric material so far reported is 2.2 for PbTe [22]. But as already mentioned the problem with these types of material is the use of toxic raw material compounds which are not in compliance with current and future EU regulation (REACH, RoHS). Also other material types have shown promising potential, such as half heuslers and oxides. However, the work carried out in this thesis is limited to study of skutterudites and silicides. A more details discussion on different thermoelectric materials and their pros and cons are found in Chapter 2.

Even though little thermoelectric material for medium to high temperatures is produced today, different types of material are maturing for industrialization as shown above. The transport sector is demanding good solutions to keep up with the demand for ever higher efficiencies and lower CO_2 emissions. This is accelerating many activities towards mass production of thermoelectric materials. The learning rates of silicon solar PV-technology [23] are believed to also hold for thermoelectric materials and modules, as the production processes are in many aspects very similar (ingot-wafer-dies-modules). Thus, the hope is that the price of this material will decrease enough to make it competitive for waste heat recovery purposes. In the end it all boils down to cost per kWh, and the specific material type used is of little interest to the end-user.

When going from lab-scale to pilot-scale and eventually industrial scale a lot of new challenges will eventually turn up. To assure homogeneity of the produced material in all steps of the process is one aspect of this, and good methods to test materials and modules as they are produced need to be evolved to be able to control the process. This is key to achieve thermoelectric systems that will be stable over time. Automatic production processes will help ensure homogeneity, increase reliability and lower the cost.

The cost of the final system is not only dependent on mass production. Also the lifetime needs to be high. If waste heat is the energy source, the marginal price of energy is zero. Thus for a thermoelectric system, the price per kWh is defined by the installation cost, since very little maintenance is needed. The final price of the energy will therefore depend to a large degree on the predicted lifetime of the system. An example is the cost estimates carried out by Rowe and Min shown in Figure 1.3, where the energy price is plotted against the lifetime of the thermoelectric system [24]. As they conclude, *"Evidently, the reliability of commercially available modules needs to* *be improved for 'high' temperature operation".* In other words, any degradation process that can lead to reduced lifetimes of the system needs to be controlled and limited. The main topic of this thesis is to explore these degradation processes for some of the new thermoelectric materials that show the highest potential for mass production.

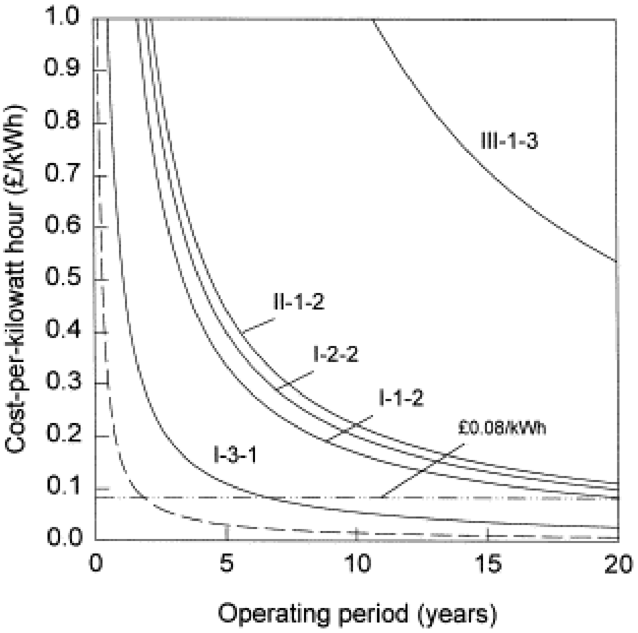

Figure 1.3 Cost per kWh as a function of lifetime of different thermoelectric systems found in the work by Rowe and Min [24].

1.4 Objectives and scope

When discussing a component's or material's long term performance, two words often come up; durability and reliability. Durability is defined as the duration of the object with respect to its usage, while reliability represents likelihood of interruptions in usage during the object's lifetime. For a thermoelectric material in a module, we expect slow or abrupt irreversible changes, either chemically or mechanically, that will define the product's lifetime. In other words, how durable it is. The reliability of a TEG is more relevant for other parts of the system and the term is therefore not used in the title of this thesis.

The thermal durability of a thermoelectric material is understood as the resistance towards degradation due to temperature-activated processes.

The focus will not be on increasing the efficiency of the thermoelectric material any further, but to investigate and improve other properties that are more important for application purposes. Some of the most important topics that will be investigated in this thesis are:

- Cheap and fast synthesis routes resulting in a homogenous and stable material that is easily reproduced.
- Understanding and control of thermally activated degradation processes:
    - on surfaces, such as oxidation, sublimation and interlayer diffusion
    - in bulk, such as phase changes, ionic diffusion, grain growth and other defect relation phenomena
    - thermo-mechanical, such as crack formation and propagation at the hot side of the elements and at interfaces.
- Investigate how different degradation mechanisms affect the performance of a thermoelectric material and device over time.

1.5 Thesis outline

Chapter 1 (the present chapter) gives an overview over the importance of waste heat recovery and the role of thermoelectricity in the coming time. Current limitations and possibilities of thermoelectric technology are discussed and form the background for the work carried out in this thesis.

Chapter 2 gives an overview of the fundamental principles underlying thermoelectricity, and the evolution of good thermoelectric materials is described in an historical context. Also the basic properties determining the performance of a thermoelectric module are covered. Together with the discussion on thermally activated degradation processes given in chapter 3, this chapter will form an important basis of the work on thermal durability of thermoelectric materials and systems and how physical degradation processes affect the thermal and electrical performance of the system under consideration. In addition, this chapter gives a brief overview of several different novel thermoelectric materials, including the materials that are investigated in this thesis.

Chapter 3 covers degradation processes relevant to thermoelectric materials operating at high temperatures. Most focus is given solid state diffusion processes such as interdiffusion, phase changes and sublimation, but also the effect of thermo-mechanical stresses on the system will be discussed. High temperature oxidation will additionally be covered in more detail, since this is an important issue for thermoelectric applications in oxidizing environments.

Chapter 4 is dedicated to experimental work and results carried out as part of this thesis with references to journal articles written on the same topics. It is divided into several subsections, each covering degradation processes at different levels in a thermoelectric module, from phase changes found during synthesizing material up to failure of metallization and bonding in prototype modules. In particular, the effect of these degradation processes upon the performance of a thermoelectric device over time is discussed.

1.6 List of publications

Paper 1 Gunstein Skomedal, Nils R. Kristiansen,Marianne Engvoll, Hugh Middleton, *Methods for Enhancing the Thermal Durability of High-Temperature Thermoelectric Materials,* Journal of Electronic Materials (2013), 42(12).

Paper 2 A. Sesselmann, G. Skomedal, H. Middleton, E. Müller, *The influence of synthesis procedure on the microstructure and thermoelectric properties of p-type skutterudite* $Ce_{0.6}Fe_2Co_2Sb_{12}$, Journal of Electronic Materials (2015), 44(11).

Paper 3 Gunstein Skomedal, Alexander Burkhov, Alexander Samunin, Reidar Haugsrud, Hugh Middleton, *High temperature oxidation of* $Mg_2(Si\text{-}Sn)$, Corrosion Science, submitted 15th december 2015.

Paper 4 Gunstein Skomedal, Lennart Holmgren, Hugh Middleton, I.S. Eremin, G.N. Isachenko, Martin Jaegle, Karina Tarantik, Nikolas Vlachos, Maria Manoli, Theodora Kyratsi, David Berthebaud, Nhi Y. Dao Truong, Franck Gascoin, *Design, assembly and characterization of silicide-based thermoelectric modules*, Energy Conversion and Management (2016) 110.

Paper 5 Gunstein Skomedal, Nils R. Kristiansen, Reinhard Sottong, Hugh Middleton, *Novel method for evaluating thermoelectric performance and durability of functionalized skutterudite legs.* To be submitted.

All papers are found in full version in Appendix I.

2 Thermoelectricity

The word *Thermoelectricity* is a combination of the Greek word for heat – *therme* – and electricity. It forms a very fundamental relation between the two forms of energy that are by far the most important to our society today, namely heat and electricity. These two forms of energy are at the same time on very different ends of the scale when as concerns usability. Heat is, apart from keeping us warm, a low-valued energy source, as the laws of thermodynamics limits the amount of useful work we can get out of it, as was discussed in section 1.2. Electricity, on the other hand, is one of the most valuable forms of energy that exists and forms the foundation of modern society, powering almost all new technologies that we use. The ability to convert heat into electricity directly is therefore an extremely useful property. So how did we discover thermoelectricity? And how do we describe it?

2.1 Basic principles

In 1821 Thomas Johann Seebeck discovered something interesting: when connecting two dissimilar metals on both ends and heating one of these connections, he was able to measure a magnetic field at the other end. It was later proven that this was indeed an electric potential he had measured. For a material, the Seebeck coefficient is denoted by $\alpha = \mathrm{dV}/\mathrm{dT}$ where dV is the electric potential corresponding to the electromotive force (emf) induced by the temperature difference, dT. Thirteen years later, Jean Charles Athanase Peltier discovered the opposite effect: when applying an electrical current over the connection of two dissimilar metals, heat was generated at the junction. The Peltier coefficient is defined as $\Pi = \dot{\mathrm{Q}}/\mathrm{I}$ where $\dot{\mathrm{Q}}$ is the heat flow and I the electric current. A continuous version of the Peltier effect was described by Lord Kelvin in 1851, where the Thomson coefficient is introduced. The Thomson coefficient is defined as $\mathrm{K}_T = \dot{\mathrm{q}} / \mathrm{J}\,\mathrm{dT}$, where $\dot{\mathrm{q}}$ is the heat generated per unit volume and J is the current density. Lord Kelvin also found the relationship between the Seebeck and Peltier coefficient to be $\Pi = \alpha\mathrm{T}$. Together these three effects constitute what we call the *thermoelectric effect*: a heat difference over a material generates a corresponding voltage which under an external load will produce an electric current. The *thermoelectric conversion efficiency* of a material is thus the ratio of electric energy produced over the heat energy supplied [25].

In the early twentieth century, Altenkirch expanded the theory of thermoelectricity when defining the figure of merit of a material

$$z = \frac{(\alpha^2 \, \sigma)}{\kappa} \tag{2.1}$$

where σ is the electrical conductivity and κ the thermal conductivity. z has the unit K^{-1} so often z is multiplied by temperature to give the *dimensionless figure of merit zT*. Mostly metals with the highest α were assessed in the beginning. But these seldom reached zT values of more than 0.1–0.2 as the Seebeck coefficient was still relatively low and heat quickly dissipated through the metals with high electrical and thus thermal conductivity (Wiedemann-Franz law; see section 2.2.1). It wasn't until the advances in quantum mechanics gave way for a completely new understanding of the electric and thermal properties of materials in the middle of the twentieth century that new semiconducting materials were studied on a large scale, especially by the Ioffe institute in the former Soviet Union and the RCA laboratory in the US. In a semiconductor both the Seebeck coefficient and electrical conductivity can be manipulated with doping of elements with a different valens than the host material and zT values of up to 1.5 were reported.

The first thermoelectric coolers and generators (modules) were also designed around these times. In principle, a thermoelectric module is made of small dice of alternately n and p type semiconductors connected electrically in series as seen in Figure 2.1. When one end of the module is heated and the other is cooled, charge carriers in the material (electrons in n-type and holes in p-type) will diffuse from the hot to the cold side and thus give rise to an electric potential which upon connection to an external load will produce electric power.

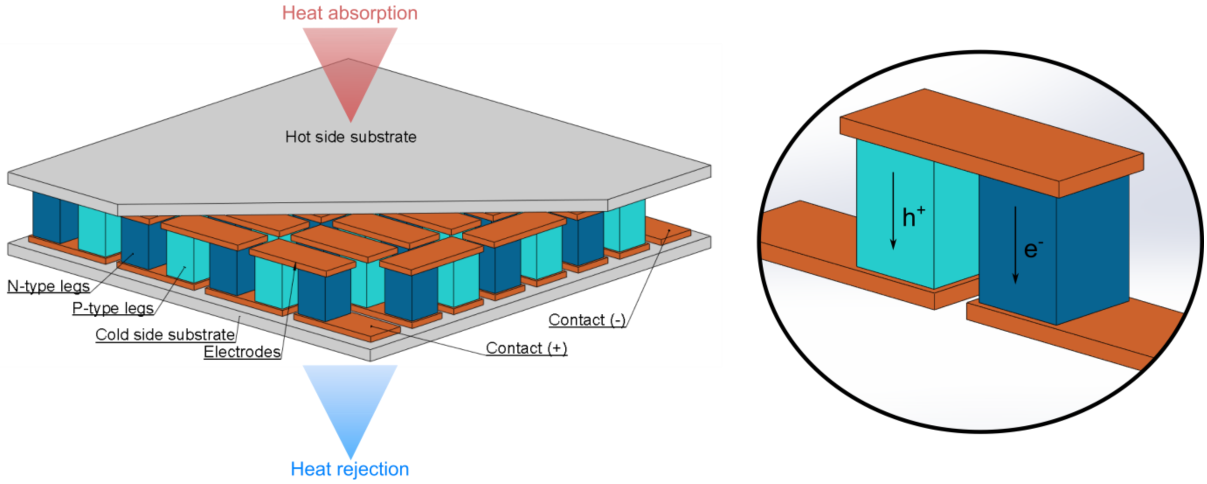

Figure 2.1 Typical thermoelectric module with alternating n- and p-type legs connected electrically in series. Heat is absorbed on one side and rejected on the opposite side producing a current through the TE-legs.

The efficiency of these modules can be expressed directly as a function of the temperature on hot side (T_H) and cold side (T_C) as

$$\eta_{\max} = \frac{T_H - T_C}{T_H} \frac{\sqrt{1 + Z\overline{T}} - 1}{\sqrt{1 + Z\overline{T}} + \frac{T_C}{T_H}} \tag{2.2}$$

where $\overline{T} = (T_H + T_C)/2$. Z is the *figure of merit of the module*, $Z = \alpha_{np}^2/R_i K$, where α_{np} is the combined Seebeck coefficient of the n and p materials, R is the electric series resistance of the legs and K is the total thermal conductance of the module (the parallel thermal transport through n and p legs). Where zT encompasses the temperature-dependent material properties, ZT is defined assuming constant material properties in the given temperature range. If the n and p-type material has similar thermoelectric properties, the ZT will not deviate more than 10% from the true zT [26]. In Figure 2.2, the theoretical conversion efficiency is plotted as a function of the temperature for different ZT values.

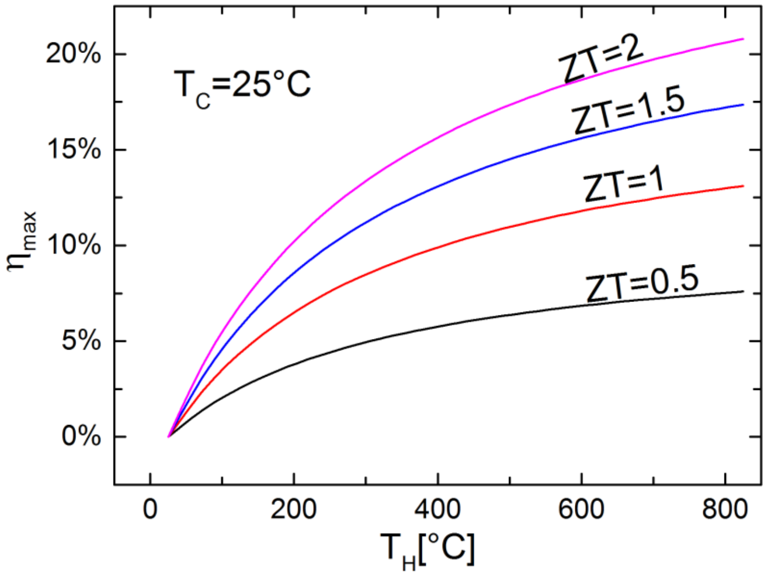

Figure 2.2 Theoretical maximum conversion efficiency of a thermoelectric module as a function of temperature and ZT values (see equation (2.2)).

During the Cold War, research on thermoelectricity was mostly spurred by the search for new ways to produce power for military use and space exploration. The first Radioisotopic Thermoelectric Generators (RTG) were taken in use in 1961 in the Transit 4A spacecraft [27]. Voyager 1 and 2 have been travelling since 1977, powered by RTG, and Mars Curiosity is another example of recent usage. The efficiency of these generators is typically not more than 5–7%, they are very expensive and they depend on radioactive material as a heat source and are thus not convenient for normal electricity generation.

In 1993 two important papers were published by Hicks and Dresselhaus theorizing that the zT of materials could be vastly improved by introducing 0D and 1D quantum effects [28, 29]. This combined with the introduction of new methods to produce advanced nanostructured materials have open up a completely new world for the research on and production of thermoelectric materials [15].

2.2 Thermoelectric materials

There exist a wide variety of different thermoelectric (TE) materials today. Some of them have been known and used for decades, while others are a result of more recent developments of both understanding of the physics and more advanced production processes. TE materials can be categorized on many different levels, such as crystal structure, conversion efficiency, cost and temperature range. The temperature regime for most typical waste heat energy sources is between 300–700°C (mainly transportation and process industry) [8], so the focus will be on materials that can handle temperatures in this range.

2.2.1 Important material properties

When discussing the material properties, it is important to not only look at one factor alone, but the combination of several of the factors depending on usage. For example, thermoelectric materials used in cars should be a trade-off between the conversion efficiency and other factors that will influence price and durability, such as raw material price or production process. At the other end of the scale, high efficiency materials that are more expensive could be utilized in applications where the total cost of the system is mainly governed by other things than the thermoelectric module itself.

Thermoelectric properties

The thermoelectric properties yield the conversion efficiency of the material and are thus the most important properties when evaluating thermoelectric materials. As already mentioned in section 2.1, these can be summarized in the zT value of the material, which is related to the Seebeck coefficient (α), the electrical conductivity (σ) and the thermal conductivity (κ) according to equation (2.1). All these values are dependent on the charge carrier density of the material, as seen in Figure 2.3. This is mainly because diffusion of charge carriers is the main transport mechanism to consider in metals and semiconductors [30].

The Seebeck coefficient is a measure of the entropy transported by moving charge carriers divided by the carrier's charge, and can be described by the equation

$$\alpha \sim \frac{1}{eT}\langle E - E_F \rangle \tag{2.3}$$

where e is the electrical charge, E_F the Fermi energy and $\langle E - E_F \rangle$ the average energy per carrier, excess of the Fermi energy. The diffusive movement of charge carriers will always be from the hot to the cold end. If electrons are the majority carrier, the Seebeck coefficient will become negative. This is called an n-type material. If holes are the majority carrier it will be positive, thus a p-type material. The Seebeck coefficient is inversely proportional with the number of charge carriers. This is illustrated in Figure 2.3. The electrical conductivity, on the other hand, increases with the number of charge carriers, n, and is given by the well-known relation derived from the Drude model of electrical conductivity

$$\sigma = n\mu e \tag{2.4}$$

where μ is the mobility of the charge carrier and e the elementary charge. Here we see that the Seebeck coefficient and electrical conductivity need to be optimized with respect to charge carriers to have the highest efficiency of the material. The product $\alpha^2\sigma$ is termed *power factor* and should be optimized to find good thermoelectric materials.

The heat transport in a material is a function of the lattice vibration (phonons) and electron movement given by the Wiedemann–Franz law:

$$\kappa = \kappa_{el} + \kappa_{ph} \tag{2.5}$$

$$\kappa_{el} = L\sigma T \tag{2.6}$$

Here κ_{el} and κ_{ph} are the electronic and phonon contribution to the thermal conductivity respectively and L is the Lorenz factor.[4] From these equations, it can be seen how the electronic contribution of the thermal conductivity is linearly dependent on the electric conductivity. Since the ratio σ/κ should be maximized to increase the zT value, κ_{ph} must be reduced. This has led to the optimal thermoelectric material

---

[4] $L = \frac{\pi^2}{3}\left(\frac{k_B}{e}\right) = 2.4 \times 10^{-8}\ J^2K^{-2}$ for free electrons. The Wiedmann-Franz law is only strictly true for metals but can be used as an approximation also for semiconductors, where other values of L should be found experimentally

being called a “Phonon-glass, electron-crystal” where the phonons are disrupted as in a glass (amorphous material), while the electrons can move more freely, as in a crystalline material (see section 2.2.3).

As the charge carrier concentration increases as a function of temperature, so do the thermoelectric properties change as well. The thermoelectric properties are therefore normally mapped over a large temperature range as seen in Figure 2.3.

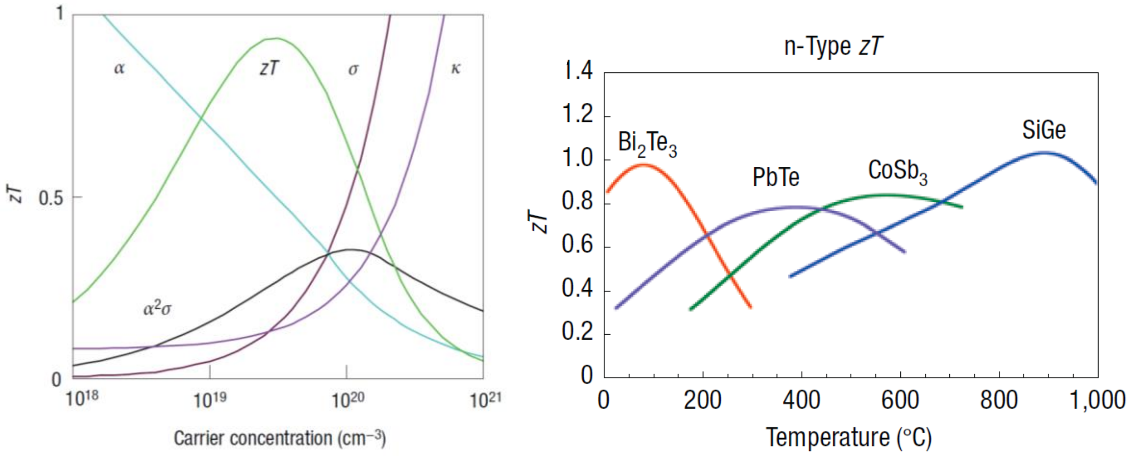

Figure 2.3 The left figure shows the ZT value and the Seebeck coefficient (α), electrical conductivity (s) and thermal conductivity (κ) as a function of carrier concentration. In the right figure typical ZT values as a function of temperature for different materials are shown [14].

Mechanical properties

In a TE-module, the TE-material will experience large compressive forces between the hot and cold sides to ensure good electrical and thermal contact. This demands fairly high compression strength of the material so it will not break into pieces when put under pressure. An even more important property to consider is the material’s coefficient of thermal expansion (CTE). The thermoelectric material used in waste heat recovery in vehicles will undergo large temperature changes during its lifetime. The hot side will go from ambient temperature when the motor is off, up to 600–700°C when the car is running at high load [31]. Since a thermoelectric generator needs both good n- and p-type materials, it is important that both of these can be constructed from similar material systems to minimize any thermal stress mismatch which can lead to failure of the TE-module. If the CTE of the contact materials (typical metals with CTE in the range 10–20 [32]) is different from the thermoelectric materials, this can cause large stresses to build up in junction and eventually lead to breakages of the bonding or the TE-material itself. Similarly, other components in the system with different CTE such as the substrate where the electrodes and TE-materials are mounted, will add to the total stress-build up. Consequently, also matching elastic modulus is important, so that stresses are uniformly distributed throughout the material layers. Especially during design of application, where the material will experience rapid heating and cooling in cycles over longer periods, this is important to have in mind when choosing matching n- and p-type materials and the right contact materials. An overview of other important mechanical properties and typical values for thermoelectric materials can be found in [33].

Chemical properties

As the TE-material has to withstand large temperature variations over time, it is vulnerable to instability and degradation. This is particularly a concern for medium to high temperature thermoelectric materials (see definition in section 2.2.2). Chemical stability is also one of the limiting cases of the temperature region the material can operate under and will be covered in more detail in Chapter 3.

The stability of the structure itself can be important. Effects such as grain growth and diffusion and accumulation of dopants forming secondary phases could affect the thermoelectric and mechanical properties. As the temperature is raised close to or above the melting point of some of the constituents of the TE-material, these can sublimate. One example of this is Sb in $CoSb_3$ which will start to sublimate significantly above 550°C in inert atmospheres [34].

Most of the TE-materials are based on metals or semimetals, of which none is especially noble. This means that they will all be attacked by oxygen when exposed to air. At lower temperatures, normally the oxide layer is just a few nanometers thick, which can be enough to hinder continuous oxidation. But as the material is heated up, the oxidation process can speed up and cause unstable oxidation layers to grow [35]. This will over time destroy the TE-material completely. Some materials will also at higher temperature form a passivizing layer (e.g. silicon) while other can exhibit self-propagating oxidation reactions (e.g. magnesium). It is important to know these processes when adapting the TE-material into different applications.

Synthesis

The synthesis of thermoelectric materials can be very different depending on the material type, and this will of course be one of the main cost drivers of the final product [36]. Still, some general process concepts can be found. Here only the process from raw materials until functionalized legs is briefly described.

Since most of the thermoelectric materials used today are a mixture of several elements, the first step is to mix these together following the stoichiometric of the final product. This could, for example, be done by mixing pure powders of each of the components together and heating this up to a temperature above that of the component with the highest melting point. After mixing the material together, the mixture is then cooled down to room temperature. Depending on the demand of the shape and size of the final product, this solidification can follow many different routes, such as czochralski method, gas-atomizing or just simple solidification. Solid-state synthesis with mechanical alloying such as ball milling is also a possible route for creating powder [37].

Most modern TE-materials are made with nanostructuring methods to enhance the TE-properties further. The final product should have as many and as small grains as possible, as this will decrease the thermal conductivity and thus increase the overall efficiency [38]. A subsequent step after solidification is then often powder production (crushing and sieving). If gas-atomizer or ball milling is used, this is already accomplished. The powder is then pressed and sintered at high pressures and temperatures (for example hot-pressing and spark plasma sintering, SPS), yielding discs or ingots in typical size of 50–150mm diameter and 3–50mm thick. The discs or ingots are then cut into dice with typical dimension between 2 and 10mm in each direction. An alternative approach is to press and sinter the dice directly, but this is only applicable for lab-scale processes, as the production speed is reduced significantly. See Figure 2.4 for a schematic overview over the different process steps.

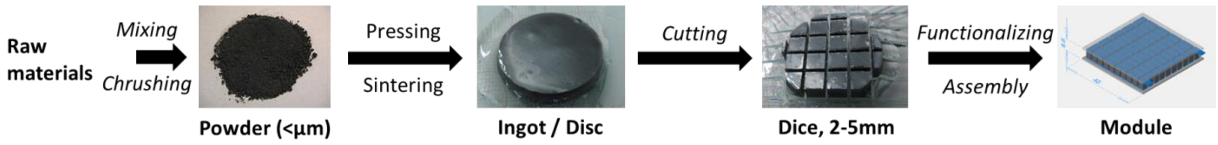

Figure 2.4 Typical synthesis route of thermoelectric materials. The pictures are from production of Mg_2Si material at Fraunhofer IPM as part of the ThermoMag project [21].

After the dice are cut into wanted geometry, they are functionalized to lower contact resistances, provide a surface suitable for further contacting and increase durability. This includes depositing thin layers of metal on both the hot and cold sides of the dice. Some technologies widely used are sputtering and electroplating [39, 40]. Additionally, the remaining four sides of the legs that are exposed to the surrounding atmosphere will in some cases need protection in the form of coatings. These functionalized legs can then be directly assembled into a module. The assembly of a full module is described in more detail in section 2.3.3.

Abundance

The raw materials used in thermoelectric materials can be taken from nearly the whole periodic system of elements, and must be taken into consideration when evaluating the scalability of the thermoelectric material, especially for mass production processes. The abundance of an element in earth's crusts (as seen in Figure 2.5) does highly influence the price. It can also have environmental impacts, such as resource mining of rare earth minerals where the ore contains only very small portions and needs a lot of energy and water to extract the wanted substance. For example some of the most used thermoelectric materials consist of more than 50 at% tellurium (Te) which is one of the least abundant elements. This will of course affect the price.

The purity demand of the raw materials can also vastly influence the total price. Since the transport mechanism of charge carrier is only influenced by certain types of foreign elements, the purity demand can vary significantly and depend on the type of impurity. However, it will generally be lower than what used in for example photovoltaics (5N), typically around 99.99% [13, 41]. The trade-off between efficiency and price is also here the main factor to consider.

The location of the ore is also a question of geopolitics just as with oil. An example of this is how China during the last two decades has built up a near monopoly on rare earth elements [42]. This will disrupt the normal market mechanisms and thereby the price of the material.

Health and environmental impact

The materials employed in a thermoelectric device can leave trace elements of its constituents both during production, in use and in the end as waste. It is thus important to consider the toxicity of these trace elements. More and more countries are employing strict regulation on the use of such toxic elements in consumer products such as the REACH and RoHS directives in EU.

Since many of the elements used in thermoelectrics have quite low abundance, the environmental impact on extracting and processing these can be huge. The local, regional and global environment can be highly affected through the emission of greenhouse gases and pollution of air, water and soil and should therefore be an important part of the scalability assessment of TE-materials [43].

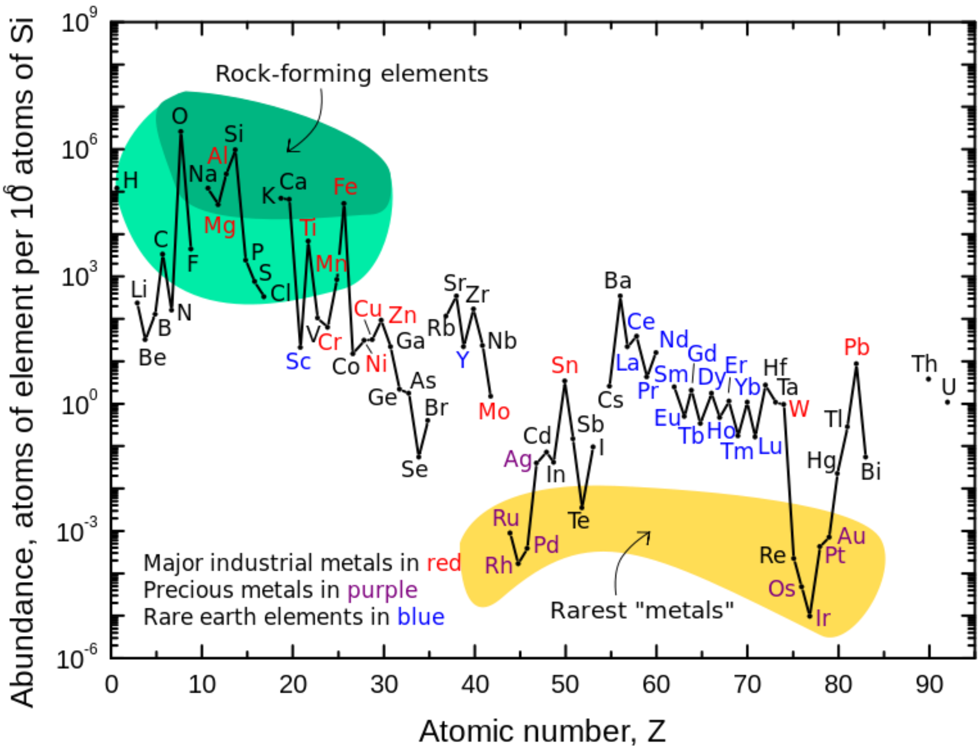

Figure 2.5 Abundance of the elements in the earth's crust, courtesy of the U.S. Geological Survey

2.2.2 State-of-the-art materials

The most used materials today are still based on formulas developed in the 1950s and '60s. These materials were basically found when alloying semiconducting materials with isomorphous elements or compounds. To increase the electrical conductivity and reduce the lattice thermal conductivity, they were also heavily doped. Since all the thermoelectric properties of the material are dependent on temperature they are usually divided into three different groups:[5] low temperature below 200°C, medium temperature between 200°C and 600°C and high temperature above 600°C [14]. Typical zT values as a function of temperature are found in Figure 2.3 and Figure 2.11.

Low temperature, < 200°C

The most common materials found in this temperature range are Bi_2Te_3 and Sb_2Te_3 solid solutions [44]. The mixing of these two compounds will introduce some variations in the mass on the anionic lattice position in the crystal, leading to phonon scattering and thus decreased thermal conductivity. The best bismuth telluride-based materials used today have zT values up to 1.5 [45].

---

[5] There is no clear definition of the temperature regimes, thus the temperature values can vary considerably depending on the source.

Bismuth telluride will vaporize above 400°C according to the reaction $Bi_2Te_3 \rightarrow 2BiTe(g) + 1/2Te_2(g)$, which limits the use up to approximately 300°C.

Medium temperature, 200 – 600°C

The group IV-tellurides, PbTe, GeTe and SeTe, are the most common materials in this temperature range. Both n and p type materials can be made. The most used p-type is also called TAGS, short for $(GeTe)_{0.85}(AgSbTe_2)_{0.15}$, with a zT of up to 1.2. For n-type materials, the typical zT is a bit below 1, but high zT values of 2.2 at 915K have been reached by using nanostructuring methods. Both addition of SrTe nanoparticles dispersed in the crystal and mesostructuring of the crystal grains using powder processing techniques were used to achieve these high zT values [22].

High temperature, > 600°C

At high temperatures the most frequently used TE-materials are Silicon-germanium alloys. These have successfully been used for several long-term space missions such as Voyager 1 and 2. Still, they have very high thermal conductivity because of the diamond structure, which imposes a limitation on the maximum zT value. So far, there has been no success in getting zT values more than 1. Because of this limitation on efficiency (especially on the lower side of the temperature range), in addition to complicated production processes and the relatively expensive raw materials, these material are not adequate for terrestrial applications such as waste heat recovery.

2.2.3 Novel materials

The search for new TE-materials can be roughly divided into two groups: increasing the power factor, $\alpha^2\sigma$, or decreasing the lattice thermal conductivity, κ_{ph}. The first approach was the most frequently used in the early age of semiconductors, while the second has gotten more and more attention the last decades. Some general rules to follow when looking for new thermoelectric materials were formulated by Slack [46] and focus on the increase of the zT value:

- Reduction of the lattice thermal conductivity, κ_{ph}
- High carrier mobility, μ
- The density of state effective mass m* should be equal to the free electron mass m^0
- The bandgap energy, E_g, should be equal or higher than 0.25 eV
- μ, κ_{ph} amd m* are independent of the charge carrier concentration n, and κ_{ph} and m* are independent of temperature

The characteristic these rules imply is often summarized as a *Phonon Glass, Electron Crystal* (PGEC) material. These are materials with very low lattice thermal conductivity, similar to amorphous materials, but still have electric properties like a crystalline material. Examples of these types of materials are skutterudites and clathrates, and will be further treated below.

Another way to decouple the thermal and electrical conductivity is to use nanostructuring techniques in the production of the material, as mentioned in section 2.2.1. Several reviews on novel nano-engineered thermoelectric materials have been published the last couple of years, and also form the base of the selection of materials below [15, 22, 38, 47].

Skutterudites

The name skutterudite stems from Skuterudåsen in Modum, Norway. It was there in the middle of the eighteenth century that the cobalt-rich mineral was first discovered. This discovery led to the construction of, at that time, one of Norway's largest industrial sites where the ore was extracted to produce distinct cobalt-blue color pigments for the porcelain industry [48]. However, the thermoelectric properties of skutterudite were not recognized until relatively recent times. In 1996, filled skutterudites were proposed as a new thermoelectric material which could reach zT values up to 1.4 [49]. Later there has been demonstrated even higher zT values, up to 1.7 at 850K [17]. The general formula of skutterudites is MX_3 where M is a group IX transition metal (Co, Ni or Fe) and X a nonmetallic atom (such as Sb, As and Sn). The most promising of these, which has received most attention is $CoSb_3$ [50].

A look at the unit cell of skutterudite seen in Figure 2.6 offers some explanation for its good thermoelectric properties. The inherent void in the structure between the octahedron formed by the nonmetallic atoms can be filled with large foreign elements which will act as rattler atoms decreasing the group velocity of the phonons and thus the lattice thermal conductivity. The filler atoms are typically either lanthanides, actinides, alkali earth or even some elements from the boron and carbon groups. The optimum filler atoms will also act as a dopant increasing both the Seebeck coefficient and the electrical conductivity. The filler amount is typically 0.5-2 at%. Filled $CoSb_3$ is an n-type material. P-type skutterudites are normally achieved by substituting Co with Fe, resulting in holes in the valence band. A general formula for a filled P-type skutterudite is

$$Fi_y Co_{4-x} Fe_x Sb_{12} \tag{2.7}$$

where Fi denotes the filler element and y is the fill-fraction, limited to 1 (fully filled). Typically, the fill-fraction y, will strongly depend on the amount of Fe in the system. For example, the fill fraction limit of Ce ranges from $Ce_{0.08}Co_4Sb_{12}$ to $Ce_1Fe_4Sb_{12}$ [51]. Both y and x are then optimized for each type of filler atoms to reach the highest possible zT.

The oxidation of skutterudite above 380°C and the sublimation of Sb above 550°C limit the use of skutterudite to enclosed environments [52] . As Skutterudite is one of the two main materials that is treated in this thesis, a more detailed description of the degradation processes such as oxidation will be further discussed in Chapters 3 and 4.

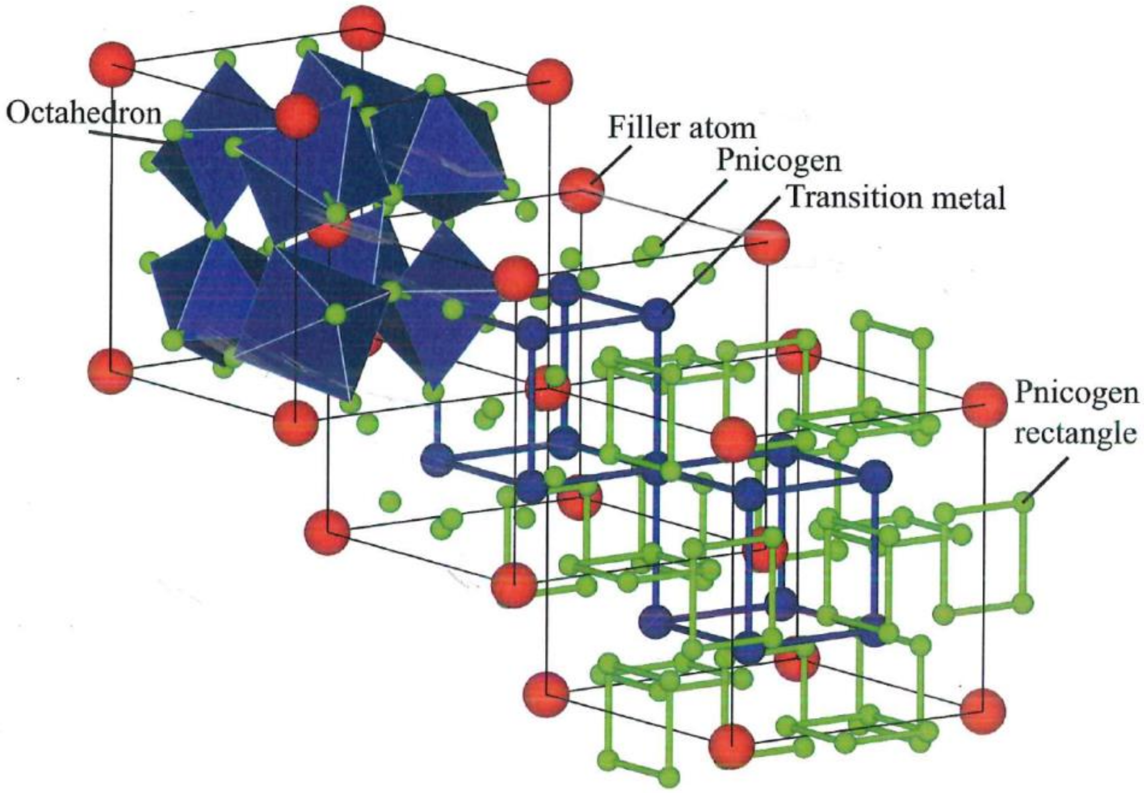

Figure 2.6 Schematic drawing of a filled skutterudite crystal structure. The pnicogen lattice position is where the non-metallic element is positioned, forming an octahedron around the transition metal atom. In the voids between the octahedron, filler atoms can be inserted to enhance thermoelectric properties. Drawing taken from [50].

Mg_2B^{IV} solid solutions

These materials were tested already in the early ’60s but were largely left undeveloped for many decades [53]. They have gotten renewed attention lately as it has a good potential as a cheap and environmental friendly TE-material [54]. The density is also very low (around 3 g/cm^3) which is important in applications where weight should be minimized, such as the transport sector. The general chemical formula is Mg_2B^{IV} where B^{IV} represents the group IV elements Si, Sn, and Ge, and the crystal structure is that of CaF_2 as seen in Figure 2.7(a). When these compounds are mixed as solid solutions, as seen in the phase diagram in Figure 2.7(b), it can increase the TE-properties dramatically. The difference in mass between the B^{IV} components introduces effective phonon scattering centers, reducing the lattice thermal conductivity as seen in Figure 2.8. The best zT value of 1.3 has been reached for $Mg_2Si_{0.6}Sn_{0.4}$ doped with Sb [19] and 1.4 for $Mg_2Si_{0.53}Sn_{0.4}Ge_{0.05}Bi_{002}$ [55]. The zT values of $Mg_2(Si_{0.4}Sn_{0.6})_{0.99}Sb_{0.01}$ tested as part of this thesis can be found in Figure 2.12. To achieve beneficial thermoelectric properties, dopants are introduced in the lattice to increase charge carrier density and consequently the power factor. Most dopants, such as Sb or Bi, results in n-type behavior. Unfortunately, few good p-type alternatives for this material group have been found. However, it is possible to combine other p-type materials from other material groups and with similar thermoelectric properties. So far, limited work is found on testing this material group in actual application, one reason being the lack of a good p-type alternative. The long term stability of Mg_2B^{IV} at higher temperatures is also uncertain. Above 400-500°C, Mg_2Si will completely decompose after short exposure to an oxidizing environment and some kind of protective coating is needed [56]. In this thesis, the performance of these materials in modules is presented (Paper 4), along with investigations on the high temperature oxidation behavior (Paper 3). Both these aspects are important for further consideration of this material group as a potential future material for waste heat recovery applications.

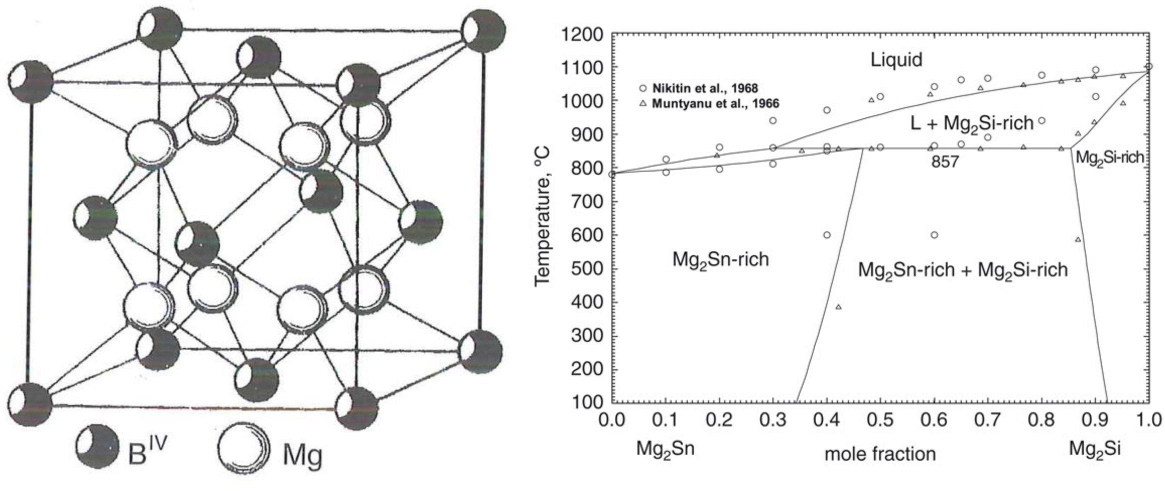

Figure 2.7 Left: Crystal structure of Mg_2B^{IV} compounds, where B = Si, Sn or Ge [18]. Right: Phase diagram of Mg_2Si and Mg_2Sn and its solid solutions [57].

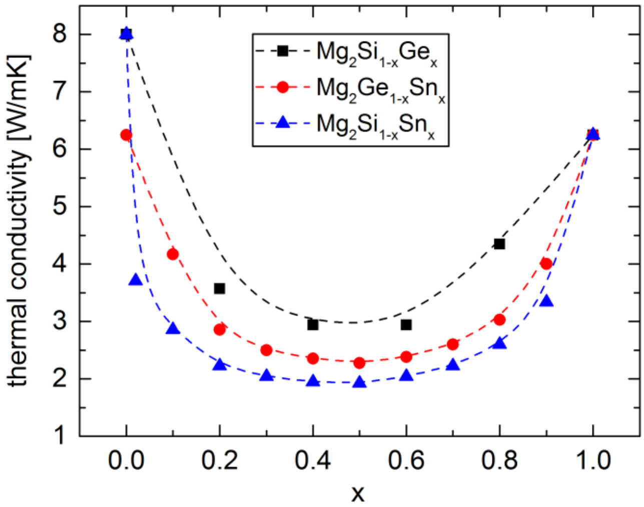

Figure 2.8 Thermal conductivity of different Mg_2B^{IV} solid solutions. Values from [18].

Silicides

The silicides are an interesting material group for thermoelectric power generation, as they not only show good thermoelectric properties, but also make use of cheaper raw materials, and offer very good mechanical and chemical stability [58, 59].

Higher manganese silicide (HMS, $MnSi_x$, x=1.70-1.77) is the most promising TE-material of the silicide group (with exception of Mg_2Si treated above). It is an example of a material with a complex and large crystal structure. This often leads to an amorphous behavior of the lattice part of the thermal conductivity, as the phonons are scattered effectively by the large distance between atoms. The c-axis of the crystal structure is more than three times the length of the perpendicular axes, leading to a strong anisotropy of the crystal and thus also of the thermoelectric and mechanical properties. The zT curve of a HMS material is found in Figure 2.12.

Chromium disilicide, $CrSi_2$, is another interesting silicide material. It has a hexagonal crystal structure similar to HMS, but has still not been made with higher ZT values than approximately 0.3. Other types of silicide are $FeSi_2$, Ru_2Si_3 and CoSi.

Clathrates

Clathrate comes from the Latin word *clatratus* which means *encaged*, and are an example of PGEC material. The general formula is $A_xB_yC_{46-y}$ where B and C are tetrahedrally bonded, forming a rigid framework of cages which encloses guest metal atoms, A, as seen in Figure 2.9. The metal atoms in the voids will act as barriers to phonon transport through the materials thus yielding a very low thermal conductivity.

There exists a wide variety of clathrate structures and these are divided into nine different groups (I-IX), depending on the cage structure, space group and intermetallic representatives [60].

The guest atoms will cause disturbances in the lattice, disrupting phonon movement and suppressing the thermal conductivity. To increase the thermoelectric efficiency further, dopants are introduced such as Ga on the framework sites. The amount of compounds used to make clathrates can be large and the demand for purity of raw materials is high, to ensure formation of correct phases during synthesis. The complexity of the production process will of course be an obstacle when considering mass production of the material [61].

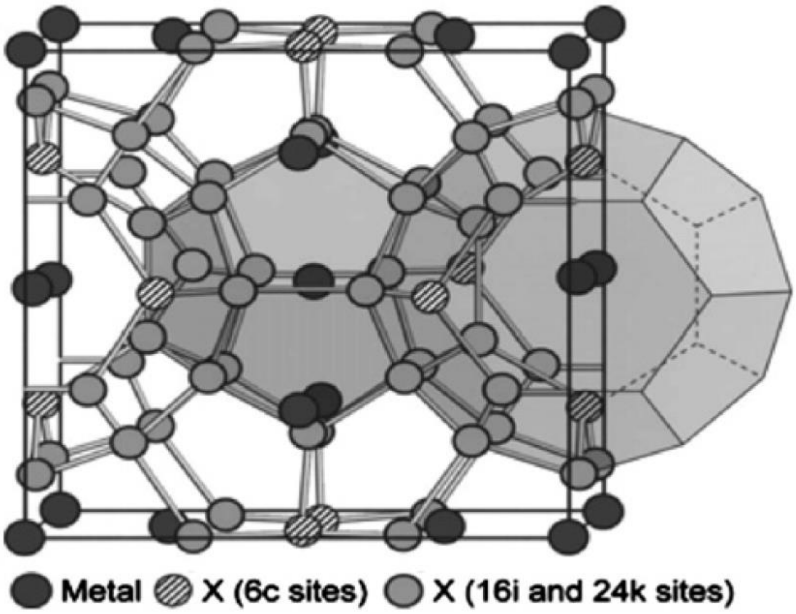

Figure 2.9 Crystal structure of type-I clathrate compounds with general formula $A_xB_yC_{46-y}$ [47]. The metal atom, A, is enclosed in cages formed by the tetrahedrally bonded B and C atoms in the X sites.

Half-heussler compounds

Half-heussler compounds are the more environmentally friendly version of PbTe. The general chemical formula is ABX; a simple rock salt crystal formed by A and X and filled with B. Example of these are MgAgAs and ZrNiSn. They have a high Seebeck coefficient and electrical conductivity, but also quite high thermal conductivity. This has somewhat been overcome by introducing nano-scale composites in the structure and increasing the phonon scattering on the boundaries. zT values of up to 1.5 have been reported [62]. Another benefit of these materials is their relatively good mechanical properties and thermo-mechanical stability over time.

Oxides

The most obvious benefit of an oxide TE-material is its thermal stability and oxidation resistance at high temperatures, along with very low thermal conductivity. On the other hand, it has also inherently very low electrical conductivity and was thus ignored as a candidate for TE for long time. This was changed when $NaCo_2O_4$-like oxides were discovered that showed very promising TE-properties. This has spurred the research on further oxide materials in the last decades. The good TE properties of $NaCo_2O_4$ have their roots in its nanoblock crystal structure, as seen in Figure 2.10, with alternating layers of CoO_2 and disordered Na atoms. The CoO_2 layers act effectively as good electron conductors, while the sodium layer disturbs phonon transport through the matrix. zT values of up to 0.8 have been reported. Another interesting oxide group is that based on Ca-Co-O. These materials have a similarly layered crystal structure as for $NaCo_2O_4$. Other types of oxides which are under investigation are $STiO_3$ and ZnO.

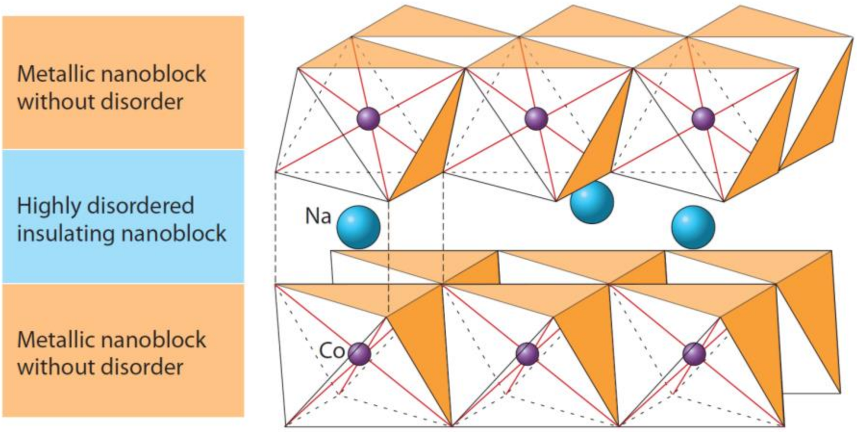

Figure 2.10 Crystal structure of $NaCo_2O_4$. The inherent nanoblock structure of the crystal lattice enhances the electrical conductivity considerably compared to other oxide materials [38].

Zn_4Sb_3

Another very good thermoelectric material is Zn_4Sb_3. This is a p-type material with reported zT values up to 1.3, because of its very low thermal conductivity similar to that of glass. The material is on the other hand limited by its instability at higher temperatures. Already at 250°C, it starts to decompose both in oxidizing and inert atmospheres [63, 64]. If good coating and encapsulation techniques can be developed, it is believed that this material can be used for commercial applications up to at least 400°C.

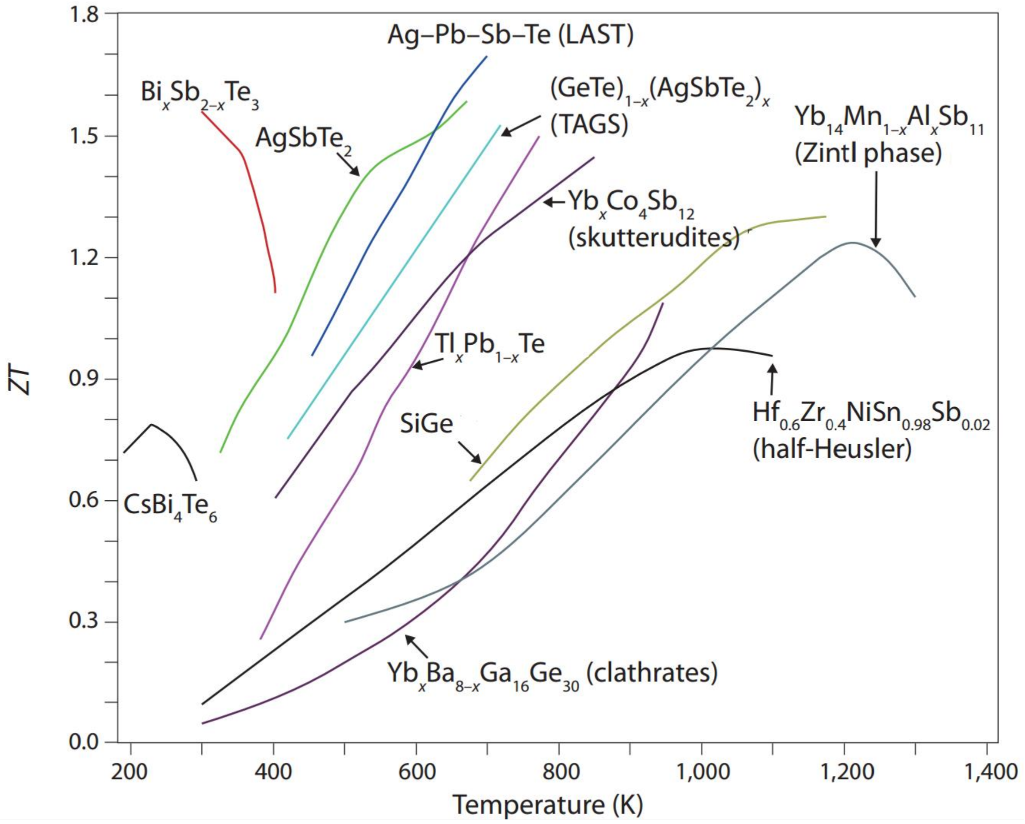

Figure 2.11 Overview over the zT of different materials as a function of temperature [38].

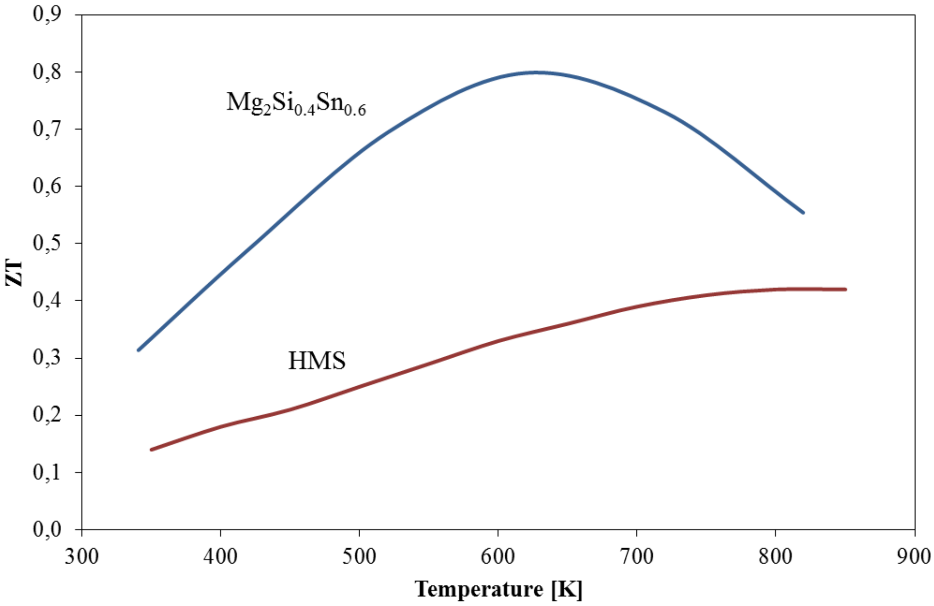

Figure 2.12 zT values of $Mg_2Si_{0.4}Sn_{0.6}Sb_{0.01}$ solid solution and HMS as a function of temperature. These materials have been used as n- and p-type materials for a demonstration module as part of the ThermoMag project [21].

Table 2.1 Thermoelectric materials with different properties. CTE = Coefficient of Thermal Expansion [$10^{-6}K^{-1}$], MCE = Mechanical Compression Strength [MPa], ZT = Dimensionless Figure of Merit. Values from references mentioned in text if not otherwise indicated. A relative color scale is introduced for comparison of materials for waste heat recovery purposes (when possible); green is good, yellow is acceptable and orange is not sustainable.

Material type	Chemical composition	Temp-range	Thermoelectric properties (ZT)	Mechanical properties	Stability and durability	Synthesis	Material cost[6] [$/kg]	Health and environmental impact[7]
Bismuthtelluride	Bi_2Te_3, Sb_2Te_3, Bi_2Se_3	-100 – 250°C	S: 100 - 250 µV/K σ: 100 - 1000 S/m ρ: 1 - 2 W/m·K zT: ~1	CTE = 12 -16 [65] Brittle for coarse grained structures. Improved with nanostructuring	Stable in air up to 300°C	Crystal growth; monocrystalline for high efficiency and multicrystalline for low price	Te = 100 (99,99%) Bi = 20 (99,99%)	Te highly toxic
Groyp 4 tellurides	PbTe, GeTe, SiTe	200-600°C	zT: ~ 1 - 1.2	MCS: ~120 MPa	n-type stable p-type very unstable at higher T		Pb = 2 (>99%)	Pb and Te highly toxic
Silicon-Germanium alloys	SiGe	600C – 1000°C	zT: 0.8 - 1.2		Very high stability	High purity materials, mono and multi crystal growth	Si = 15 (99,99999%) Ge = 1800 (99,99%)	Ge low abundance
Skutterudites	MX_3 M = **Co**, Fe, Ni X = **Sb**, As Fillers: **In, Ce**, ..	300-700°C	n-type: 1 - 1.8 p-type: 0.8 - 1.2	CTE: 9-13 [66]	Oxidation above 380°C, sublimation of Sb above 550°C	Hot pressing and sintering	Co: 30 (99,3%) Sb: 10 (99,65%)	Sb/As medium toxic and impact on environment.
Mg_2B^{IV} solid solutions	$\mathbf{Mg_2}$(**Si-Sn**-Ge)	200-500°C	S: 100 - 250 µV/K σ: 1000 - 3000 S/cm ρ: 1 - 2.5 W/m·K zT: ~1	Relatively brittle CTE: 9-11	Decomposes and oxidizes easily above 400-500°C, needs protection	Direct comelting + crystallization.	Mg = 3 (99,9%) Sn = 23 (>99%)	Non-toxic without Ge
Silicides	$\mathbf{MnSi_{1,72}}$ (HMS), $FeSi_2$, $CrSi_2$, CoSi, Ru_2Si_3	300-700°C	zT_{HMS}: ~0.8 zT_{CrSi2}: ~0.3 zT_{FeSi2}: ~0.4	Strongly anisotropic CTE_{HMS}: 7-13 CTE_{CrSi2}: 8-9 CTE_{FeSi2}: 8-12	Generally very stable in whole temperature range, little to no oxidation	Czochralski method, floating zone, Bridgman method	Mn = 2.5 (99,7%) Cr = 8.6 (99%) Fe = ~1 (99%)	Non-toxic and abundant raw materials
Clathrates	$A_xB_yC_{46-y}$ A=Na, K, Rb B=Al, Ga, In C=Si, Ge, Sn	300-700°C	zT >1 ,high potential	CTE = 6-14 [67]		Powder metallurgical, Crystal growth	Depends a lot on the final elemental structure. High purity of elements	
Half-Heussler compounds	ABX A=Mg, Zr, Ti, Hf B=Ag, Ni X=As, Sn	300-700°C	zT: 1 - 1.5	High hardness and thoughness [68] CTE: 10-12 [69]	Oxidation above 300-400°C [70]	Arc melting, spark plasma sintering (SPS)	Cheap without Hf	Best materials with Hf content
Oxides	$\mathbf{Na_xCoO_2}$, Ca-Co-O, $SrTiO_3$, ZnO	400-1000°C	zT: ~0.3	Weak mechanical strength	Very stable at high temperature. No oxidation.	Crystal growth. Metallization difficult	Relatively cheap raw materials, Na, Ca in oxide form	Non-toxic and environmental friendly materials

---

[6] Prices of materials from http://www.metal-pages.com/ and http://www.infomine.com/investment/ (30.10.2013).

[7] The health and environmental impact is roughly evaluated based on the toxicity of the constituents for humans, and the impact of extraction and production on the environment.

2.3 Thermoelectric modules

The Seebeck coefficient of typical good thermoelectric materials lies in the order of 100-200 µV/K. At a temperature difference of 100K, this yields 10-20 mV, which is by far not enough to power most electrical devices. This is solved by connecting the thermoelectric material in series, with alternating n- and p-type legs forming a thermoelectric module as seen in Figure 2.1. The *open circuit voltage* over the device is expressed as

$$V_{OC} = N_p \int_{T_C}^{T_H} \alpha_p dT - N_n \int_{T_C}^{T_H} \alpha_n dT \tag{2.8}$$

where N_p and N_n are the number of p- and n-type legs (usually an equal amount) and α_p and α_n are the temperature-dependent Seebeck coefficients of p- and n-type respectively. The minus sign before n-type material in this equation reflects the negative sign of the Seebeck coefficient. The internal resistance of the module with leg height l, is then

$$R_i = N_p \int_0^l \frac{dx}{\sigma_p(T)A_p} + N_n \int_0^l \frac{dx}{\sigma_n(T)A_n} + N_p\left(R_{chp} + R_{ccp}\right) + N_n(R_{chn} + R_{ccn}) \tag{2.9}$$

where $\sigma_{p,n}(T)$ is the temperature-dependent electrical conductivity, $A_{p,n}$ and l is the cross sectional area and length of the thermoelectric legs, and R_{chp}, R_{ccp}, R_{chn} and R_{ccp} are the contact resistance on the hot (h) and cold (c) sides of p- and n-type legs respectively. A simplified version of equation (2.9) will be used later in the thesis where $R_i = R_{TE} + R_{contact}$ (the resistance of the thermoelectric material and contact resistance respectively). The resistance of the electrodes, R_{el}, connecting the TE legs is normally several orders of magnitude lower in a regular module (pure metals) and is therefore left out of these equations.

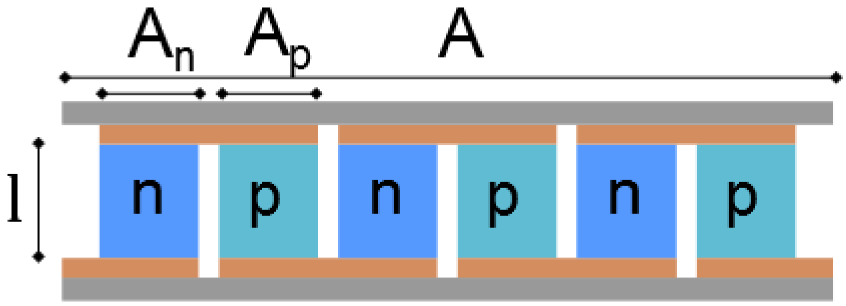

Figure 2.13 Sketch of a thermoelectric module with alternating n and p-type materials connected electrically in series and thermally in parallel.

From equation (2.8) it is seen that all the legs should experience the same temperature gradient. This implies that heat is transported over all the legs connected *thermally in parallel*. The heat flow through a thermoelectric material or module under load is given by

$$\dot{Q} = K\Delta T + \alpha I T_H - \frac{1}{2} I^2 R_i \tag{2.10}$$

where the first term is conductive heat with K as the thermal conductance of the material/module; the second term is the Peltier effect and the last term represents Joule heating (1/2 since it goes in both directions). In parallel configuration, K can be approximated by the sum of thermal conductivity of the thermoelectric materials in addition to the total thermal conductance at the hot (K_{ch}) and cold (K_{cc}) sides of the module

$$\frac{1}{K} \approx \frac{l}{\kappa_p N_p A_p} + \frac{l}{\kappa_p N_p A_p} + \frac{1}{K_{ch}} + \frac{1}{K_{cc}} \tag{2.11}$$

The thermal conductance at the hot and cold sides is furthermore comprised of the thermal resistivity of contact materials and substrate in addition to the thermal contact resistance between each thermal interface. Consequently, the temperature profile over the module has a form similar to that shown schematically in Figure 2.14. To optimize the efficiency of the module, most of the temperature difference should occur over the thermoelectric material, thus a minimization of the thermal conductance, not only of the thermoelectric material, but the whole module is important. In addition, the heat transfer to the module from external heat sources needs to be optimized to match the thermal impedance of the module to reach maximum system efficiencies [71]. When modeling a real system, also parasitic heat losses through the side of the material or module must be considered.

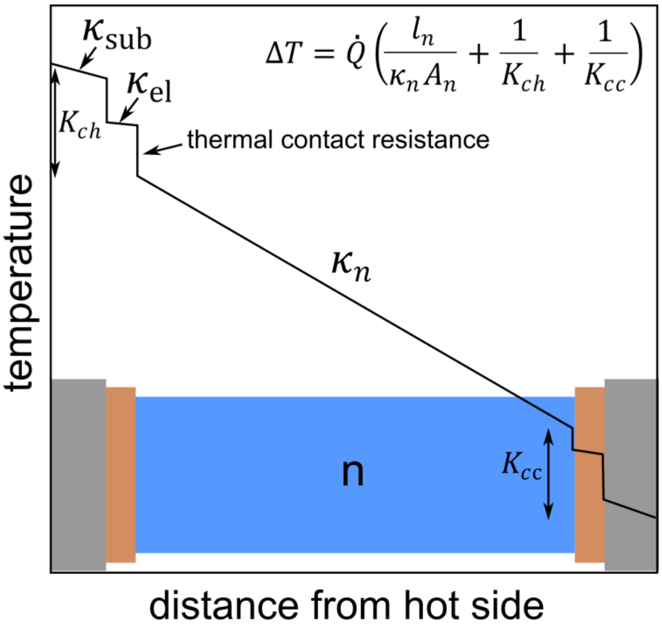

Figure 2.14 Typical temperature profile over a thermoelectric module.

In combination, these two principles of TE legs connected electrically in series and thermally in parallel, have formed the basis of all thermoelectric modules and are reflected in the design seen in Figure 2.1. Still, there exist several ways of connecting the legs within the module, and varying the geometry to reach the highest efficiencies. This will be further discussed in section 2.3.2.

The following sections will cover basic considerations around designing, assembling and testing thermoelectric modules. For a spesific example of a silicide-based module the reader is referred to Paper 4 of this thesis.

2.3.1 Current-Voltage charateristics

When an external load, R_L, is applied to the module under a temperature gradient, the voltage will be reduced accordingly and given by

$$V = R_L I = V_{OC} - R_i I \tag{2.12}$$

Using this simple relation, the I-V curve can be plotted by varying an external load and finding the values at zero load (open circuit) or at any other load. At constant temperature (unchanging V_{OC}), the I-V curve is linear and R_i can be calculated from the slope of the curve. An example is given in Figure 2.15.

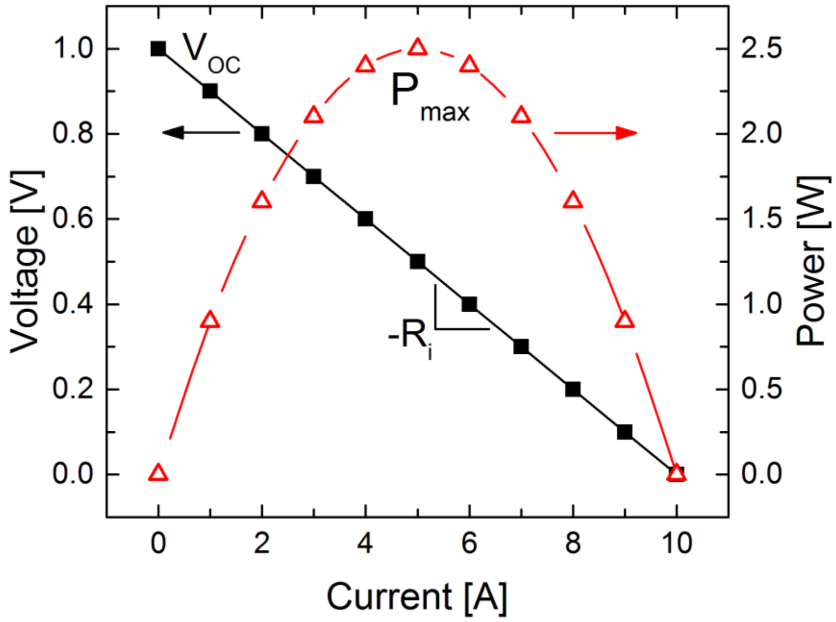

Figure 2.15 Example of I-V curve of a thermoelectric module at constant temperature difference with V_{OC} = 1V and R_i = 0.1Ω.

From equation (2.12) the current under an external load can be expressed as

$$I = \frac{V_{OC}}{R_i + R_L} \tag{2.13}$$

which gives us the following expression for the power output of the module at the external load R_L as a function of the two main characteristics of the module, V_{OC} and R_i:

$$P = VI = R_L I^2 = \frac{V_{OC}^2 R_L}{(R_i + R_L)^2} \tag{2.14}$$

Derivation of equation (2.14) with respect to R_L and setting equal to 0, the maximum power is found when we have load matching conditions, that is $R_L = R_i$:

$$P_{max} = \frac{V_{OC}^2}{4R_i} \tag{2.15}$$

Here it must be said that the maximum power of the module does not equal the power at maximum efficiency for utilizing the heat available. Maximum efficiency (equation (2.2)) is reached when $R_L = R_i\sqrt{1 + Z\bar{T}}$ [72, 73]. The maximum power principle is normally used when trying to optimize power for a given module/system design (geometry fixed), while maximum efficiency principle should be used when optimizing a module/system for a given application to utilize most of the heat available.

2.3.2 Design considerations

Optimization of module design is a field of its own with a lot of models covering thermal transport, heat exchange coefficients of hot and cold sides, geometry of legs and difference between n and p-type materials, and many other parameters. Extensive work exists describing strategies when designing modules with conventional design [72, 74, 75], and will therefore not be treated further here. Regardless of design choice, some basic building blocks of the module are found for almost any system, of which the most common are illustrated in Figure 2.16 and listed in Table 2.2. Many of these parts are essential when evaluating lifetime performance of a thermoelectric device. For example, the metallization layers that ensure good bonding between electrode and thermoelectric material are crucial to achieve low thermal and electric contact resistance. Any degradation of the metallization will directly increase the Ohmic losses, leading to a reduced power output of the device. Therefore, it is not only a good match of n- and p-type thermoelectric materials that must be found when designing a module, but also all the materials that are needed for a functional and durable module.

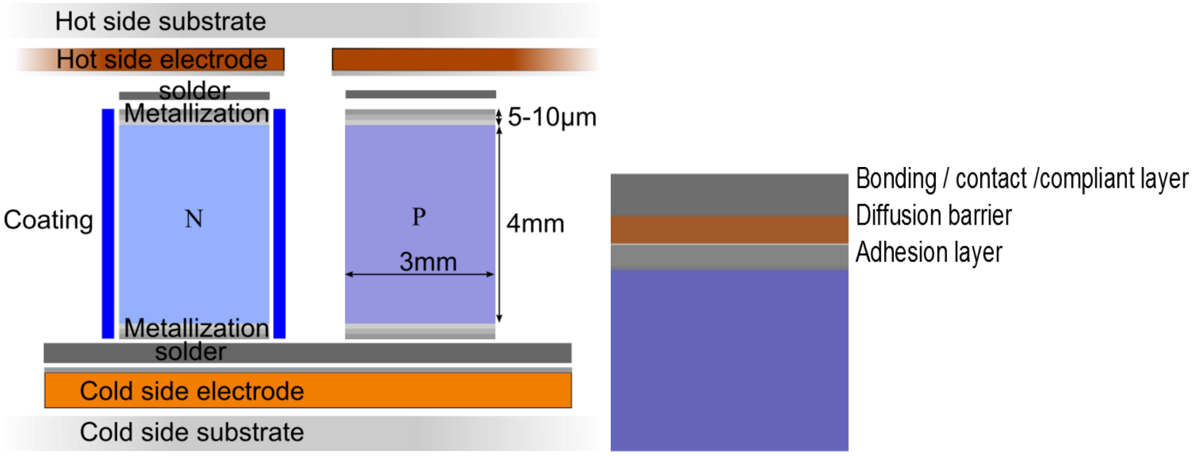

Figure 2.16 Left: Schematic view of a unicouple within a thermoelectric module with typical parts indicated. Right: typical metallization layers on top of a TE leg.

Table 2.2 Typical parts of a thermoelectric module in addition to the thermoelectric material.

Part	Function	Favorable properties	Typical materials
Substrate	Fixture for mounting electrodes and TE legs	High thermal cond. Electric isolator. Mechanically strong.	Al_2O_3, Si_3N_4, anodized Al
Electrodes	Electrical transport between TE legs. Thermal transport from substrate.	High thermal and electrical conductivity. Chemically inert. Hot side matching CTE with TE material.	Cu, Ag, Ni, Stainless Steel
Solder	Bonding between electrode and TE material (including metallization).	Bonds at low temperatures. Good electric and thermal conductivities. High reliability at high temp.	Cold side: Pb-Sn Hot side: Ag-based.
Metallization	Thin metallic layer, forming bond between TE material and electrode.	High thermal and electrical conductivity. Hot side matching CTE with TE material. Diffusion barrier.	Different metals and intermetallics
Coating	Protect side of legs from sublimation and oxidation.	Dense, chemically inert. Thermal and electric insulator. Matching CTE.	Enamel, glass-ceramic, thin metal layers
Thermal insulation	Reduce parasitic heat losses from sides of TE-material.	Very low thermal conductivity. Matching CTE.	Silicone (<300°C), Aerogel
Encapsulation	Protect TE-material and electrodes from sublimation and oxidation.	Ductile, low thermal conductivity.	Stainless steel casing

Metallization

The metallization is one of the most important parts of a TE module and therefore deserves some extra comments. Metallization is a term borrowed from the electronic packaging industry, where one or more thin layers of metal are deposited on the surface of the semiconductor, mostly to form contacts between the device and external circuit [76]. For thermoelectric materials, the metallization should ensure good thermal and electrical contact, as well as be reliable. It should hinder diffusion out of and into the TE material (diffusion barrier), have low thermal and electrical contact resistance (adhesion layer), bond well with the electrode (bonding layer) and finally take up stresses between electrode and TE material (compliant layer) [77]. One material seldom achieves these properties alone and several layers are therefore needed. The total of these layers comprises the metallization.

Possibly the most important property of the metallization is the Coefficient of Thermal Expansion (CTE). It should be nearly equal to that of the TE material to reduce accumulation of strains between them. A CTE mismatch could lead to cracking and spallation of the metallization during usage, especially when exposed to rapid thermal cycling.

Coating and encapsulation

Protection from the environment is of utmost importance for a thermoelectric device working in corrosive conditions. If the device is meant to work in air, oxidation can be a severe problem both for the thermoelectric material and the metal parts. One solution is to cover both the side of the TE legs along with the hot side electrodes and connections with a coating. This could either be in the form of thin metal layers deposited on the side similar to the metallization [78], or slurry solution which is painted on and dried, such as composite glass [79], enamel coatings [80] or even metal-based paints, which have shown promise in experiments carried out in this thesis (Paper 1).

In a thermoelectric system working in inert atmospheres, one of the main challenges with device durability is linked to sublimation of the surface [81]. A solution to this is to encapsulate the module and fill it in with inert gas such as He or Ar. This will significantly reduce sublimation rates, as shown by NASA. The use of encapsulation is also an alternative to coating for avoiding oxidation and an example is seen in Figure 2.17.

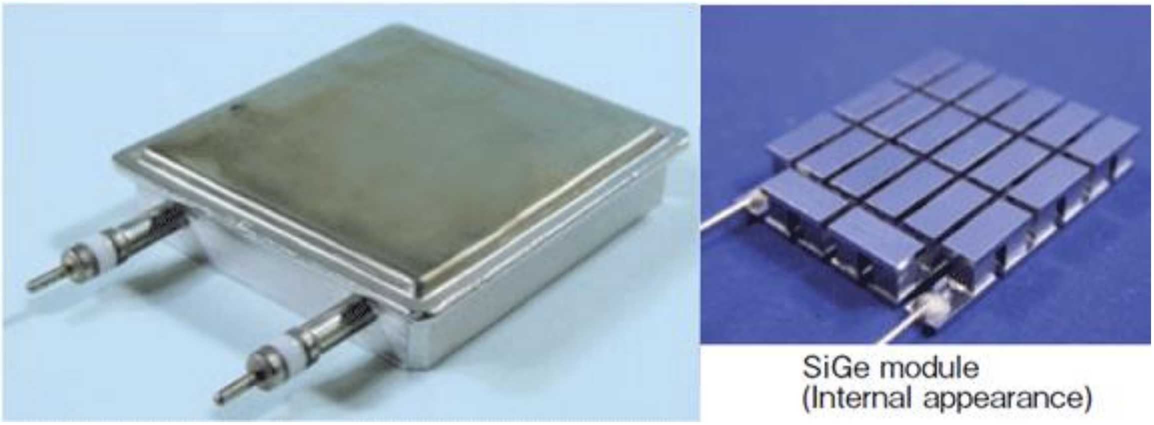

Figure 2.17 SiGe thermoelectric module with encapsulation (left) and without (right). Courtesy Hitachi Chemicals, Japan [82].

2.3.3 Module assembly

When the material system surrounding the TE material is chosen, the parts are assembled. There exists no definite order of which process should precede which. Still, some general ideas are found in literature on how things are usually done on the lab-scale.

Metallization on TE material can be achieved by several methods. Direct bonding of metallic powder or films during sintering of TE material is frequently used for several material systems [39, 83]. This is a simple method that minimizes extra handling steps and ensures good bonding. A challenge with this method is that it is hard to control the thickness of the layer. It is also difficult to apply several different layers if this is needed.

The second option is to apply metallization directly on the TE-material after sintering. As mentioned in section 2.2.1, TE material is typically made in the form of ingots that can further be cut into discs and dice (legs). Metallization can then either be applied to the surface of the discs themselves, or on the individual legs after dicing. Two of the most common methods of metallization are electroplating or deposition (chemical or physical vapor deposition) [84]. One or more thin layers (typically from hundreds of nanometers up to a few micrometers) are deposited on both the hot and cold sides of the TE legs. Different metallization schemes could be used for hot and cold sides.

The metallized thermoelectric legs (often termed *functionalized* legs) are then placed on electrodes and soldered/brazed. The electrodes can be either loose or pre-mounted on substrates. Another option is to use metal spray techniques or Ag-based paints [85]. Sometimes the metallization step is not done at all and TE legs are directly bonded on electrodes [86]. This is however not a good option for high temperature devices as the diffusion of electrode material into thermoelectric material and vice versa is very hard to avoid without a proper diffusion barrier. Also other methods such as SLID bonding shows great potential [87].

The cold side electrodes are often bonded first as these often should only withstand low temperatures (<100–200°C). Simple solders can be used in these cases. The hot side electrodes and substrates are then subsequently bonded on. Alternatively, when no good solder option exists at the wanted hot side temperatures, diffusion bonding can be used, where the electrodes and metallized TE material are pressed together in the module and diffusion between them during usage forms bonds which also reduce contact resistance. Wires are soldered on at each side of the series-connected TE legs and form the plus(+) and minus(–) connection to the module where the external load is applied.

Finally, the module needs some protection from the environment, either through coating or encapsulation. Coatings and thermal insulation are applied in between all the legs of the module. Additionally sealant or encapsulation is used to protect the module from a corrosive environment. For low temperature modules, high temperature sealants can used that can withstand temperatures up to 300–350°C (for example Permatex® Clear RTV Silicone Adhesive Sealant). For higher temperatures aerogel can be used [88].

2.3.4 Performance testing

A thermoelectric module should go through thorough and detailed testing to assess different parts of the design parameters. Especially parameters affected by interface properties cannot be known exactly until after assembly. How good is the bonding between electrode and the thermoelectric material? What is the thermal and electrical resistance between the different interconnects?

The most important outcome of these tests is to be able to determine the *total efficiency of the module*, η_{module}, that is the amount of electrical power drawn from the module compared to the heat supplied as discussed earlier in this chapter.

In addition, the durability is a critical aspect that governs the resistance towards degradation over time, in other words avoiding reduction in efficiency. Any change in electrical or thermal properties that leads to a reduction in efficiency must be discovered and measured. From the rate of change, the lifetime performance of the module could in principle be calculated. The longest “tests” known to date are those of the RTGs in NASA unmanned missions [27, 81]. Here, the generators have outperformed the estimates on several occasions, showing potential for long-term stable performance of thermoelectric systems.

The simplest way to evaluate the performance is to assemble prototype unicouples or small modules and test them directly under a temperature gradient over a prolonged time, measuring thermal and electrical properties. This is indeed the most common way to test thermoelectric modules and generators, and there exists extensive literature on different ways to do this [24, 89, 90]. I-V curves are measured to find V_{OC} and R_i (Figure 2.15), while one or more thermo-elements positioned as close to the module hot and cold sides as possible is used to measure hot and cold side temperatures that are experienced by the module. If the thermoelectric properties are known, the measured V_{OC} can be compared to calculated values using equation (2.8). A deviation between these two values then represents a temperature difference between the measured value and the actual value felt by the thermoelectric leg. This can be interpreted as a thermal impedance between the module cold side and the thermoelectric leg and is an important factor in a thermoelectric module.

Similarly the electrical contact resistance between electrodes and TE legs can be estimated from comparing the measured R_i with that calculated from equation (2.9). Alternatively, the contact resistance can be measured by specially made test-rigs such as the 3 point methods described by Mengali et al., Thimont et al. and Kim et al. [91-93].

To get the exact value of the module efficiency, more advanced set-ups are needed, where also the heat flow though the module can be estimated. Typical methods are using metal blocks with known thermal conductivity with several thermo-elements positioned at regular intervals throughout the block [94, 95]. Then the heat flow can be calculated by applying Fouriers Law in one dimension

$$\frac{\dot{Q}}{A} = -\kappa * \frac{dT}{dx} \tag{2.16}$$

As can be seen, many of these tests are cumbersome and have long lead times. Both in a research phase and in an industrial scale process there is a huge value in getting feedback on the performance of a module design. For example, if a module is measured and there is a gradual increase in the inner resistance, it is not easy to know what causes this increase. It could be a result of changes in the electrical resistivity of the thermoelectric material or mechanical failures of the bond of just one of the TE-legs in series, which will completely overshadow any secondary effects. This is the topic of discussion in section 4.5.

2.3.5 System design and cost

The thermoelectric module is only a part of the system when making a thermoelectric generator (TEG). In a TEG, other aspects are equally important. In particular, the role of heat exchangers has been pointed out as key in archiving high performing TEG [12, 96]. To utilize the available heat, the heat exchangers need to be able to transport enough heat to the thermoelectric module which requires a high temperature gradient. A rule of thumb is that half of the temperature drop should be over the heat exchangers to achieve the highest system efficiencies [97].

The most important parameter at system level is in many cases not efficiency, but specific cost, that is cost per Watt installed ($/W). When assessing the total cost of the system, the cost of the thermoelectric material is often found to be insignificant compared to other material cost that is involved in the construction of TEG [98] . The design and optimization of TEG will not be covered here and readers are advised to check out [24] and [99] for a good overview over what controls the performance and cost of TEG in different applications. It is interesting to note that system costs below 1$/W are estimated for systems based on several novel thermoelectric materials [13]. If the energy cost is free (as for example in the case of waste heat), the cost of power over the lifetime (20 years, assuming constant heat source) will be very low and competitive with market prices down to 1 c$/kWh. However, this requires long life times and shows how important the durability of the thermoelectric device is for cost competitive use in real life applications.

3 Thermally activated degradation processes.

This thesis discusses *thermal durability*, i.e. *resistance towards degradation due to temperature-activated processes*, or changes in the material due to heating. But why is temperature so important? In general, heat is understood as atomic vibration and temperature is a relative measure thereof. In a perfect crystal, atoms have no place to move and no change in the order of atoms relative to each other is seen; only a total expansion of the material, termed *thermal expansion*. However, no material is perfect. All solid-state materials contain defects of some sort that will enable movement of atoms both within and between materials. This movement of atoms is called *solid-state diffusion* and is the main reason we see changes in properties of a material during usage at high temperatures. In this chapter, the basic principles of solid-state diffusion are presented along with examples from the field of thermoelectricity. Emphasis will be put on diffusion processes that lead to degradation in performance of thermoelectric materials and modules. In addition, the specific example of high temperature oxidation is described following the Wagner model of diffusion through a growing layer, as this is highly relevant for oxidation studies also for thermoelectric materials.

3.1 Solid-state diffusion

3.1.1 Defects

"Crystals are like people, it is the defects in them which tend to make them interesting!"
\- *Colin Humphreys*

Defects makes room for atomic movement within the lattice and are therefore key for understanding diffusion in crystalline materials. We find defects on several scales:

- Point defects (0D), such as an unoccupied lattice position, which we call a *vacancy*.
- Line defects (1D) forming a regular stacking fault in the lattice, such as a *dislocation.*
- Plane defects (2D) such as *grain boundaries* and *external surfaces.*

Defects are formed in the material when it is synthesized, or during usage due to thermal vibrations or mechanical strain. Vacancies, grain boundaries and dislocations are examples of *intrinsic defects* – representing atomic disorder in the lattice. Foreign atoms in the lattice, termed *solute* if desired and *impurities* if undesired, are examples of *extrinsic defects*. These can occupy both *substitutional* and *interstitial* positions within the lattice. A schematic overview over some of the most common defects is found in Figure 3.1.

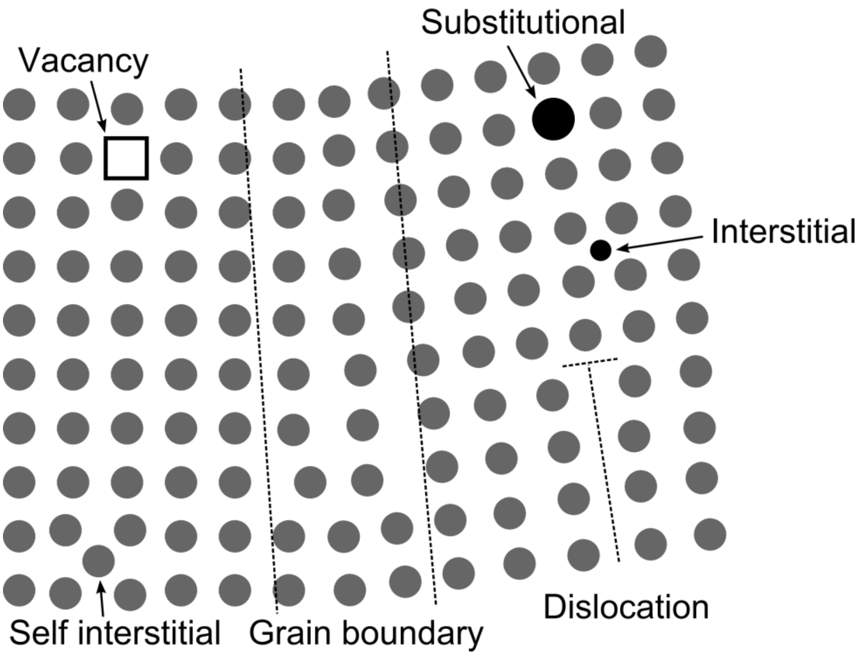

Figure 3.1 Overview over different kind of defects in crystalline materials. Point defects can be either intrinsic (vacancy, self-interstitial) or extrinsic (solute atoms in substitutional or interstitial position). Line defects (dislocations) and surface defects (grain boundaries) are also shown.

In a pure metal, vacancies are the predominating intrinsic point defect. The concentration of vacancies is temperature-dependent and given by the Gibbs free energy of formation of vacancies, G_v^F, or the entropy (S_v^F) and enthalpy (H_v^F) of formation according to

$$C_v = \exp\left(-\frac{G_v^F}{k_B T}\right) = \exp\left(\frac{S_v^F}{k_B}\right)\exp\left(-\frac{H_v^F}{k_B T}\right) \tag{3.1}$$

where k_B is the Boltzmann constant. Also self-interstitials are possible, where a similar expression applies, although self-interstitials normally have higher formation energy, and thus lower concentration than vacancies [100 p.80]. The concentration of defects is thus seen to follow an Arrhenius type of temperature dependency.

In a stoichiometric crystal A_xB_y, simultaneous formation of vacancy of both A and B atoms at free surfaces ensuring charge neutrality is called *a Schottky disorder*. An atom can also form *vacancy* by moving into an *interstitial* position between other atoms (*Frenkel disorder*).

Almost all stoichiometric crystals have some degree of *non-stoichiometry*, that is, deviation from the integer ratio between elements in the lattice. This is due to either extra interstitial or vacancies of one type and is typically indicated with δ such as $A_xB_{y-\delta}$.

3.1.2 Diffusion

According to the continuum description of diffusion, the flux of atoms or molecules can be described as being proportional to the concentration gradient. This is what we know as Fick's first law and is given (for linear flow in x-direction) as

$$J = -D\frac{dC}{dx} \tag{3.2}$$

Combining equation (3.2) with the conservation law (the net flux of atoms in and out of a control volume is zero), Fick's second law can be derived showing the temporal evolution of the concentration

$$\frac{dC}{dt} = D\frac{d^2C}{d^2x} = \frac{d}{dx}\left(\widetilde{D}(C)\frac{dC}{dx}\right) \tag{3.3}$$

where D is the concentration-independent diffusion coefficient, while $\widetilde{D}$ is concentration-dependent, such as interdiffusion between two species, often referred to as the interdiffusion or chemical diffusion coefficient. Furthermore, the diffusion coefficients have an Arrhenius temperature dependency

$$D = D^0\exp\left(-\frac{\Delta H}{k_BT}\right) \tag{3.4}$$

where ΔH is the *apparent* activation energy of diffusion, D^0 the preexponential factor and k_B is the Boltzmann constant.

These fundamental laws do however only give a phenomenological description of diffusion. They state the laws diffusion follows but do not give us any deeper insight into what is actually going on. What defines the diffusion coefficient of a material or system?

Diffusion mechanisms

From an atomistic point of view, diffusion is found when atoms move through defects in the crystal. Each movement is normally limited to the nearest neighbor, where the atom needs to break existing bonds and squeeze through other atoms before it reaches the neighboring vacancy or interstitial site. This implies an activation energy that the atoms need to overcome to be able to move. Thermal vibrations in the lattice will at some points be large enough so that individual atoms receive enough energy to make the jump. The jump frequency is thus given by

$$\omega = v^0 \exp\left(-\frac{G^M}{k_B T}\right) = v^0 \exp\left(\frac{S^M}{k_B}\right) \exp\left(-\frac{H^M}{k_B T}\right) \tag{3.5}$$

where v^0 is the *attempt frequency* and G^M, S^M and H^M are the gibbs free energy, entropy and enthalpy of *migration*, respectively.

Several diffusion mechanisms exist such as *interstitial mechanisms*, where an interstitial atom moves between adjacent atoms, or the *vacancy mechanism*, where an atom in the host lattice jumps into a neighboring vacancy, leaving a new vacancy behind into which new atoms can move. In the latter case, the diffusion process can thus more easily be understood as movement of the vacancy.

Grain boundaries, free surfaces and dislocations are examples of aggregates of defects stretching out in several dimensions which make it much easier for atoms to move (lower activation energy). These are therefor often called *high diffusivity paths* and are in many cases the dominating diffusion mechanism. They can severely affect durability of materials. An example is grain boundaries in diffusion barrier layers, which act as shortcuts for diffusion that otherwise would be prevented [100 p. 547].

Diffusion coefficient

From random walk theory the diffusion coefficient is given by the distance the atoms move by every jump, d, multiplied with the jump rate, Γ, and the number of neighboring sites, Z and divided by 6 (all directions in a three dimensional lattice)

$$D = \frac{1}{6} d^2 Z\Gamma \tag{3.6}$$

The diffusion under a chemical potential gradient can, simplified, be understood as the product of number of available sites in the lattice for movement (defects) and the jump frequency yielding the jump rate, $\Gamma \sim \omega C_v$. Comparing the expression of D from equations (3.4), (3.5) with (3.6), a similar Arrhenius temperature dependency is found, with the activation energy, ΔH, representing either the enthalpy of formation of defects (H^F), enthalpy of migration (H^M) or a combination of both. Other enthalpies related to the formation or migration of defects can also appear in this expression. The pre-exponential factor, D^0, can be expressed as

$$D^0 = gfv^0a^2\exp\left(\frac{\Delta S}{k_B}\right) \tag{3.7}$$

where g is a geometrical factor, f is the correlation factor, a is some lattice parameter and ΔS is the diffusion entropy. For the vacancy mechanism, the diffusion entropy is given by the sum of the formation and migration entropy, $\Delta S = S^F + S^M$, and similarly for the activation enthalpy, $\Delta H = H^F + H^M$. For interstitial atoms, the diffusion only depends on the migration enthalpy, since the concentration of interstitial positions is constant in a given crystal.

Several diffusion mechanisms can occur simultaneously, for example simulations diffusion of several elements or diffusion through both vacancies and grain boundaries. In diffusion experiments, the observed diffusion coefficient will be the sum of all the diffusion coefficient of the participating diffusion processes

$$\begin{aligned} D = D_I + D_{II} + \cdots = D_I^0 \exp\left(-\frac{\Delta H_I}{k_B T}\right) + D_{II}^0 \exp\left(-\frac{\Delta H_{II}}{k_B T}\right) + \cdots \\ = D_{Eff}^0 \exp\left(-\frac{\Delta H_{Eff}}{k_B T}\right) \end{aligned} \tag{3.8}$$

The observed activation energy, or enthalpy of diffusion ΔH_{Eff}, can be expressed as a function of the diffusion coefficients and enthalpy of diffusion for each diffusion mechanism

$$\Delta H_{Eff} = \Delta H_I \frac{D_I}{D_I + D_{II} + \cdots} + \Delta H_{II} \frac{D_{II}}{D_I + D_{II} + \cdots} + \cdots \tag{3.9}$$

At a given temperature, normally one diffusion mechanism predominates. In most multicrystalline materials, grain boundary diffusion will dominate up to 2/3 of the melting temperature of the material. The diffusion coefficient of several mechanisms are therefore often found to follow the relationship

$$D \ll D_d \leq D_{gb} \leq D_s \tag{3.10}$$

where D is the bulk (lattice) diffusion coefficient, D_d along dislocation, D_{gb} in grain boundaries and D_s at free surfaces.

3.1.3 Interdiffusion and Kirkendall effect

In a system with more than one component, the simultaneous diffusion of two or more diffusing species gives rise to an *interdiffusion coefficient*. Since a diffusing species will move from one type of crystal to another, often with gradual zones in between, the diffusion coefficient will depend on the concentration of defects. According to the theory of Darken, the interdiffusion coefficient can be defined as

$$\widetilde{D} = C_B \tilde{V}_B D_A + C_A \tilde{V}_A D_B \tag{3.11}$$

where $C_{A,B}$ denotes the concentration, $\tilde{V}_{A,B}$ the partial molar volumes and $D_{A,B}$ the intrinsic diffusion coefficient of atoms A and B respectively. A typical example is the diffusion between two different materials A and B in a diffusion couple as seen in Figure 3.2. If A and B are fully soluble, the diffusion of A into B and B into A will lead to a gradual intermixing of the two materials. In most cases the diffusion coefficients of the atoms will be different, in other words one type of atom will move more quickly into the other material. This will lead to an accumulation of vacancies at the fastest diffusing compound side (Kirkendall voids) and a build-up of new lattice planes at the opposite side. A shift in the position of the so called Kirkendall plane (the initial interface between A and B) towards the material with the lowest diffusion coefficient is observed as shown in Figure 3.2.

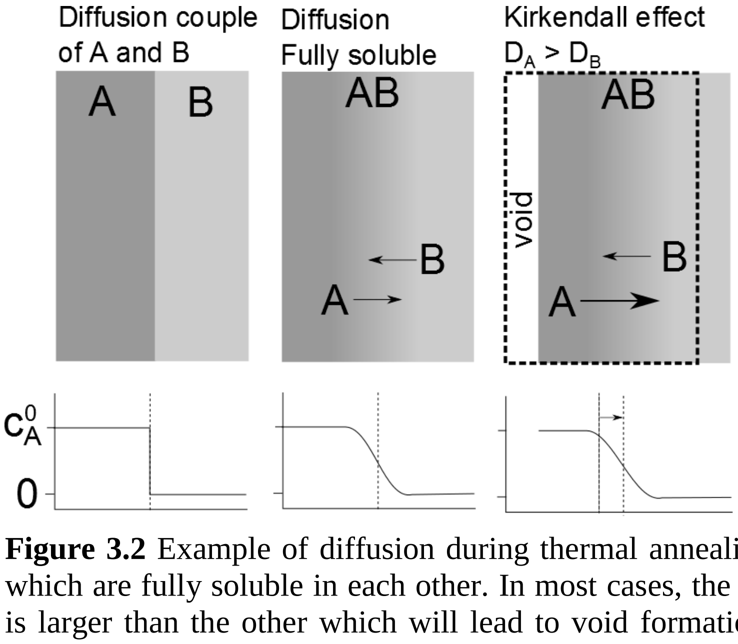

Figure 3.2 Example of diffusion during thermal annealing of the diffusion couple A and B, which are fully soluble in each other. In most cases, the diffusivity of one of the components is larger than the other which will lead to void formation at the side of the faster diffusing species (Kirkendall effect).

The theoretical description of Darken of such systems has later been shown to have small practical relevance, as they require local equilibrium of the vacancy concentration, which is often not the case. Instead, the non-equilibrium situation can be described by an additional force-factor in the flux equations for species *i*

$$J_i = -D_i \frac{dC_i}{dx} + \frac{C_i D_i^*}{k_B T} F \tag{3.12}$$

where D_i^* is the tracer diffusion coefficient and F is an external force, in this case arising from the non-equilibrium vacancy gradient. From this general equation, a new interdiffusion coefficient can be found which will be true for any external forces

$$D = \frac{D_1 D_2}{C_1 D_1 + C_2 D_2} \tag{3.13}$$

where the subscript 1 and 2 represents the two interdiffusing species.

3.1.4 Layer growth and parabolic kinetics

In many cases, A and B have very limited solubility in each other. Instead, intermetallic compounds (IMC) form, with a stoichiometric relationship A_xB_y, see Figure 3.3. In this case, the thickening of the IMC will be in the direction of the more slowly diffusing species. It must be emphasized that some non-stoichiometry needs to be present to allow for diffusion through A_xB_y – if not, there would not be a concentration gradient that could drive diffusion. A typical example of layered growth is found during oxidation and the formation of oxide scales. In this case, however, B is gas phase (O_2). This will be further treated in section 3.3.

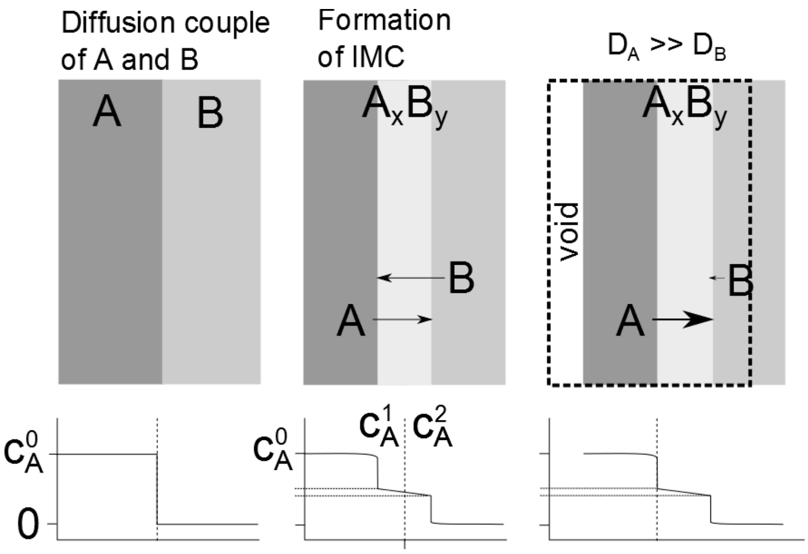

Figure 3.3 Example of formation of intermetallic phase (IMC) during aging of the diffusion couple A and B. In case the diffusion coefficient of one of the components is much faster than the other, void formation will also be seen (Kirkendall effect). The growth of the IMC will in most cases follow parabolic kinetics.

A general expression of the kinetics of such a diffusion-controlled thickening of an intermediate layer is found by solving Fick's first law (equation (3.2)) for the one-dimensional case. If we assume that $D_A >> D_B$ we have a simplified situation where only A atoms will diffuse through A_xB_y and react at the A_xB_y/B interface to form more A_xB_y. If we furthermore assume a constant diffusivity throughout the AB layer along with a constant flow of A to the A/ A_xB_y interface so that the consentration of A at the interface, C_A^1, is constant, we get

$$\frac{dx}{dt} = V_{AB}J_A = -n\frac{M_{\mathrm{AB}}}{\rho_{\mathrm{AB}}}D_A\frac{dC}{dx} \tag{3.14}$$

where V_{AB} is the volume of A_xB_y formed per mole A, n is the number of A_xB_y formed per A and M_{AB} and ρ_{AB} are the molar mass and density of A_xB_y respectively. The concentration gradient within A_xB_y is assumed to be constant and equal to $dC/dx = (C_A^2 - C_A^1)/x$, which is a fair assumption as long as the diffusion to the interfaces is not rate limiting. Integrating equation (3.14), we get

$$x^2 = k_P t \tag{3.15}$$

where k_P is the parabolic rate constant, in this case equal to $k_P = 2D_A n\frac{M_{\mathrm{AB}}}{\rho_{\mathrm{AB}}}(C_A^1 - C_A^2)$. The parabolic rate law is found when studying the kinetics in many different systems where diffusion is the rate limiting process. Even though the parabolic rate constant will vary depending on system, the general equation (3.15) will in most cases apply.

3.1.5 External driving forces

So far, the discussion has been limited to diffusion due to a concentration gradient. However, the real force acting on the individual atoms leading to a net flux of atoms from one position to another is the difference in *chemical potential* due to concentration differences. In addition to the driving force of a concentration gradient, other forces can contribute to atomic diffusion. *Electric potential gradients* can interact with atoms either in ionic systems where the atoms have effective electric charges, or in metals where the momentum in moving electrons can be transferred to the atoms, leading to a net flux in the direction of the flow of electrons (electromigration, see section 3.2.4). A *temperature gradient* can also act as an external force leading to diffusion of atoms (Thermomigration, see section 3.2.5). In addition, *stress gradients* can lead to movement of atoms (creep, see section 3.2.6) [100, p. 179-185]. In a thermoelectric system, all of these driving forces can be present and should therefore be considered when analyzing the relevance of solid-state diffusion in this field. This is the topic of the following section.

3.2 Diffusion in thermoelectric systems

As already stated, in a thermoelectric system several different diffusion processes are of interest, all the way from synthesis to long-term stability. The meaning of diffusion is here *atomic diffusion*, not the diffusive movement of heat and electricity, which of course also is highly relevant for thermoelectric systems, but not specifically related to material degradation processes. Below follows an overview of relevant diffusion processes with examples from the field of thermoelectricity along with reference to experimental work carried out in this thesis, with the exception of oxidation, which will be covered in section 3.3.

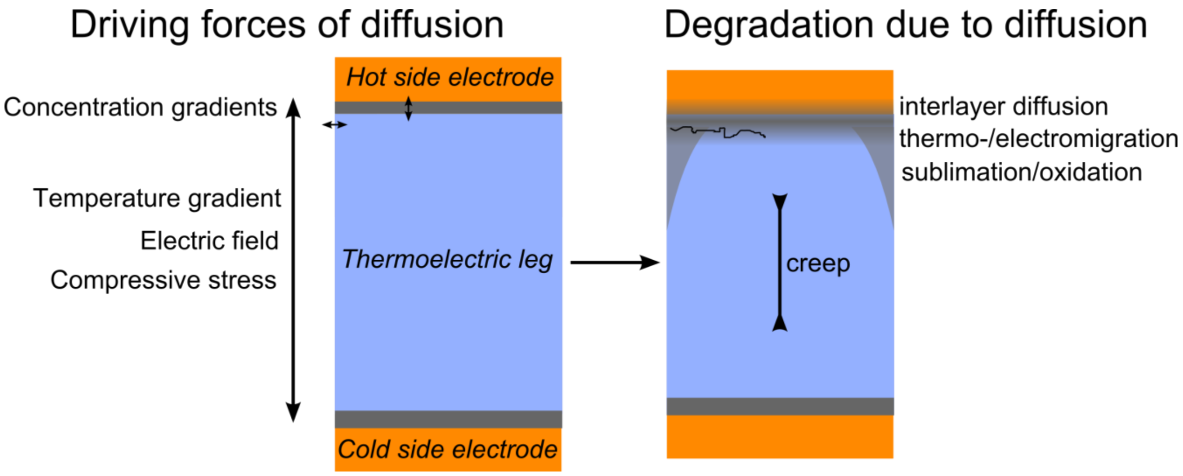

Figure 3.4 Overview over typical degradation processes in thermoelectric systems driven by diffusion at high temperatures.

3.2.1 Phase stability

The thermodynamics of the system will decide which phases are in thermodynamic equilibrium at a certain temperature, pressure, etc., but in many cases, true equilibrium is inhibited by kinetics, since atoms need to diffuse from one position to another. In the solid-state, these diffusion processes can be slow, leading to non-equilibrium materials with a high amount of secondary phases which have not reacted fully yet. This can be a problem during synthesis of thermoelectric material where the wanted phase with good thermoelectric properties can be hard to achieve due to slow kinetics limited by diffusion [101].

An example of a slow phase transition is the formation of peritectic phases. A peritectic system is characterized by a transition from one solid phase in equilibrium with a liquid phase into a new separate solid phase (peritectic reaction, $\alpha + L = \beta$)

[102]. In other words it solidifies *incongruently*. During solidification, α will first nucleate and grow until the peritectic temperature of β is reached, see Figure 3.5. β will first form at the surface of α-particles until the whole α is covered by a layer of β. New β will now form only at the surface of the remaining α which is accomplished through diffusion of B-atoms through the growing layer of β. Therefore, the kinetics of the transformation into the equilibrium phase β is limited by solid-state diffusion and thus follows parabolic kinetics similar to that described by equation (3.15).

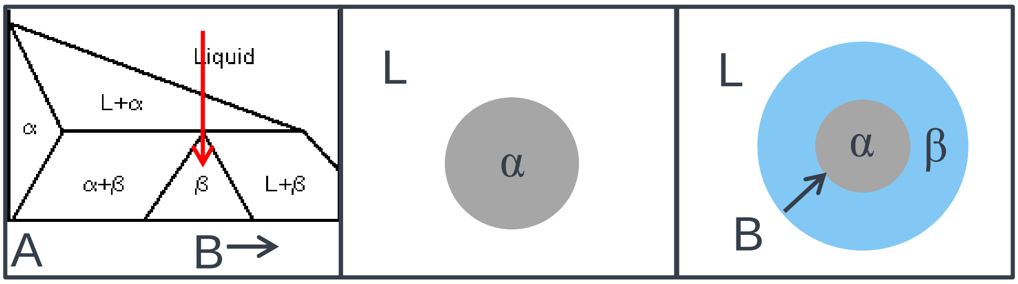

Figure 3.5 Example of solidification of a peritectic phase (β). First α nucleates and grows. When the peritectic temperature of β is reached, it first forms at the α-L interface according to α+L=β until all α is covered. Further formation of β is controlled through diffusion of B atoms through the growing β-phase towards the α-β interface where α slowly transforms into β.

Skutterudite ($CoSb_3$) is an example of a peritectic phase in the Co/Fe- Sb system. A more detailed description of the peritectic transformation of skutterudite is presented in more detail in section 4.1 and Paper 2. Also in the Mg_2Si-Mg_2Sn system, peritectic phases are found (see phase diagram in figure Figure 2.7). This results in a dendritic microstructure of Si-rich phases in a Sn-rich matrix. The details of the synthesis of Mg_2(Si-Sn) solid solutions are not discussed in this thesis but can be found elsewhere [103, 104]. However, the resulting microstructure will affect both thermoelectric properties and stability of the material. An example is the effect of the ratio of Sn/Si on the oxidation mechanisms, which is thoroughly discussed in Paper 3.

3.2.2 Decomposition and sublimation

A solid or liquid material will exchange atoms or molecules with its environment. The vapor pressure of a material is the equilibrium pressure of the gas formed as a result of decomposition of the original material, R, into one or more gas phases

$$R(s/l) = A(s/g) + B(g) \tag{3.16}$$

The *kinetic rate* of vaporization, or sublimation rate of the sublimating species material, can be described by the Hertz-Langmuir equation

$$J_{sub} = \frac{\alpha p N_A}{\sqrt{2\pi MRT}} \tag{3.17}$$

where α is the sticking coefficient of the gas molecules onto the surface, p is the surrounding pressure, M the molar mass of the sublimating species, N_A the Avogadro constant and R the gas constant. From this expression, the sublimation is seen to be modeled as time invariant and reflects that the rate-governing step is that of reaction (3.16). A constant sublimation rate is normally a good approximation at low temperatures, but at higher temperatures, the depletion of the sublimating species at the surface will limit the reaction. The system now enters a regime where the sublimation is governed by diffusion through a growing layer of already reacted material [105, 106]. The kinetics of the diffusion-controlled regime will be given by a parabolic rate equation similar to equation (3.15)

$$\Delta m^2 = k_S t \tag{3.18}$$

where Δm is the weight loss per unit area and k_S is the parabolic rate constant for sublimation. The parabolic rate constant has an Arrhenius temperature dependency, $k_S = k_0 exp\left(\frac{\Delta H_S}{RT}\right)$, where ΔH_S is the activation energy of sublimation, in this case closely related to the enthalpy of diffusion given by migration and formation enthalpies depending on the diffusion mechanism.

In thermoelectric systems for space applications, sublimation has been one of the main degradation mechanisms due to high temperatures and the vacuum of space [81]. The knowledge and control of the sublimation rate has been of great importance to determine the lifetime of RTGs. Sublimation will lead to a reduction in the cross sectional area of unreacted thermoelectric material near the hot side of a module which will increase the electrical resistance. The Seebeck coefficient of the affected zone will also be drastically affected, leading to a decrease in the total efficiency of the module. For simplicity, sublimation rates are often given as linear constants. For thermoelectric materials they range from around 1 g cm^{-2}h^{-1} for TAGS (500°C), 10^{-2} -10^{-4} g cm^{-2}h^{-1} for skutterudites (600–700°C) and 4.8x10^{-5} g cm^{-2}h^{-1} for SiGe (1000°C) [33]. Since the sublimation rate according to NASA should be less than around 10^{-7} g cm^{-2}h^{-1} to keep the area reduction below 5% after 10 years of operation [81], it is clear that the sublimation rates needs to be significantly lowered. The SiGe materials used in NASA RTGs up to now have been coated with Si_3N_4 to suppress sublimation, with great success [107]. With the new generation of RTGs based on skutterudite, renewed attention has been given to sublimation of these systems, as antimony has a relatively high vapor pressure at the application temperatures (up to 600°C) [108]. Also for waste heat recovery purposes, limiting the sublimation rate is key if the preferred option to avoid oxidation is encapsulation and use of inert gases. Parabolic kinetics is found with a parabolic rate constant of $8.7\times10^{-12}g^2cm^{-4}s^{-1}$ at 600°C in vacuum [34] and an activation energy of 44.5kJ/mol. It is a result of decomposition of $CoSb_3$ according to

$$CoSb_3 = CoSb_2 + Sb \tag{3.19}$$

and subsequent diffusion of Sb to the surface, where the vapor pressure of pure Sb is high enough to accompany significant sublimation. Decomposition and sublimation of antimony during synthesis of skutterudites is also important to consider as the synthesis temperatures often are very high and annealing times very long. The sublimation of Sb during synthesis is normally compensated for by adding a few percent additional antimony.

3.2.3 Interlayer diffusion and formation of IMC

As seen in section 2.3, in a thermoelectric module with hundreds of thermoelectric legs, there exist twice as many interfaces between thermoelectric material, metallization and electrodes. On the hot side of the module, the temperatures will in most cases be high enough to enable significant interdiffusion between the materials. Intermetallic compounds (IMC) will typically form between the materials as a result of the diffusion processes. The IMC can have a very different coefficient of thermal expansion (CTE) from the original material, leading to crack formation during thermal cycling. If the diffusion is large, it can lead to formation of Kirkendall voids and further cracks between the layers. This is of course detrimental to the durability of the module. In addition, diffusion from the metallization into the thermoelectric material could lead to drastic changes in the charge carrier densities near the hot side, which furthermore would affect the thermoelectric properties and lead to a reduction in overall zT.

In low-temperature thermoelectric modules based on Bi_2Te_3 the thermoelectric material is typically directly soldered to copper electrodes [109]. When using lead-free solders with high amounts of tin (Sn), Sn will at temperatures around 200–250°C diffuse into the thermoelectric material and form a thick IMC layer of SnTe which in turn will lead to reduction in device performance [110]. To reduce degradation, diffusion barriers of for example Ni-P are used. Also in this system, different Ni-Te

IMC will gradually form and can in the end also lead to failure of the device. The growth of NiTe is diffusion-controlled and grows nearly parabolically [111, 112]. The use of Ni as intermediate layer reduces the contact resistance from around $10^{-4}\Omega cm^2$ for unmetallized elements to $10^{-5}\Omega cm^2$ or even less.

Formation of IMC between contact layers and thermoelectric material has also been reported for systems based on skutterudite. Zhao et al. used titanium as intermediate layer between skutterudite and copper [113, 114]. The formation of Ti-Sb IMC were pronounced and grew according to parabolic kinetics. A slight increase in contact resistance was observed up to $3x10^{-5}\Omega cm^2$. However, no cracks formed and the IMC formed a stable and adherent contact layer. The estimated lifetime of the systems was more than 8000 days at a temperature of 500°C.

In Paper 5 of this thesis the diffusion of copper into skutterudite is reported, where the deposited nickel and titanium layers clearly are inadequate to suppress diffusion. The use of nickel electrodes, on the other hand, seems to be much more stable, with no diffusion of nickel into the thermoelectric material. Different metallization concepts and the durability of these are also investigated as part of this thesis. Interdiffusion between solder, metallization and Mg_2(Si-Sn) material is reported in Paper 4. The effect of the diffusion process on module characteristics such as inner resistance and open circuit voltage is discussed in section 4.5.

3.2.4 Electromigration

In section 3.1.5, the influence of external fields on lattice (bulk) diffusion was mentioned. The electric field will act in two ways on the atomic diffusion: direct interaction with ions (positive or negative effective charge) or through momentum transfer from electrons to ions ("electron wind"), see Figure 3.6.

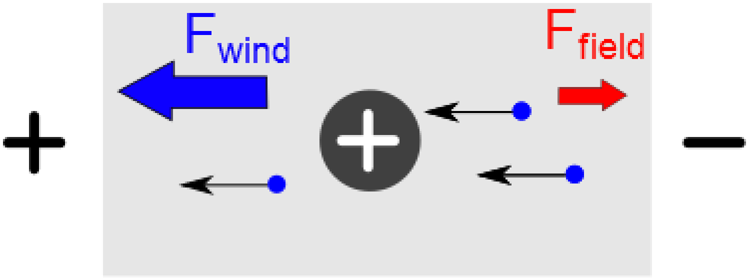

Figure 3.6 Schematic illustration of how ions are affected both by the electric field (F_{field}) and the electron "wind" (F_{wind}) due to monumentum transfer from moving electrons.

The diffusive force from an electric field is predominant in ionic systems, which included in the general flux equation (3.12) leads to the well-known Nernst-Einstein equation relevant for electrochemical systems with large contributions from ionic conduction. For metals, the effective charge of the ions can be neglected and the main contribution of an electrical field on atomic diffusion is that of the electron wind. This is called Electromigration (EM). The flux of ions due to EM can be found to follow the relationship

$$J_{EM} = C\left(\frac{D}{k_B T}\right)(z^* e)\left(\frac{j}{\sigma}\right) \tag{3.20}$$

where C is the concentration, D the diffusion coefficient and z the effective charge of the affected ions; while j is the electric current density, σ the electric conductivity and k_B the Boltzmann constant. The main parameter affecting EM is the current density [115]. EM has received renewed attention the last decade as microcircuits become smaller and smaller with increasing current densities where it can reach very high values. The critical current densities for EM are typically in the order of 10^6-10^7A/cm^2 which is far beyond those found in thermoelectric systems (typically 10^3-10^4 A/cm^2). However, some evidence of the phenomenon also occurring in thermoelectric devices is reported even at relatively low current densities. Liao et al found signs of EM at a current density of 700A/cm^2 in Bi_2Te_3 based modules [116]. Diffusion of Sn from Sn-Ag-Cu solder alloy into the underlying p-type Bi_2Te_3 was observed in contrast to no diffusion into the n-type material as seen in Figure 3.7. Compared to isothermally annealed samples at 200°C, the diffusion was significant. They concluded that EM caused enhanced diffusion in the direction of electron flow could explain the observed anomalies.

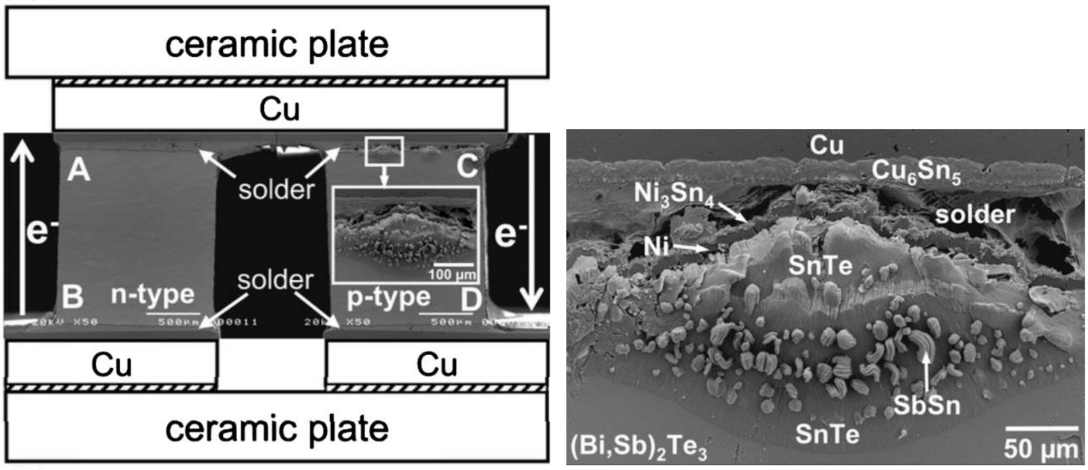

Figure 3.7 Effect of electromigration on the solder joint between copper electrode and Bi_2Te_3 in a thermoelectric module. A current density of 700A/cm^2 seems to cause significant increase in diffusion rate compared to samples isothermally annealed. Illustrations from *[116]*.

EM has also been observed during direct current-assisted sintering of both Bi_2Te_3 [117] and Zn_3Sb_4 [118] thermoelectric materials. This leads to inhomogeneities in the sintered material and reduction in performance. The current densities of such synthesis methods should therefor be limited when EM of elements in the system is known to occur.

3.2.5 Thermomigration

First discovered in gas and liquids, diffusion of atoms over a temperature gradient was described by Charles Soret in 1879, therefor often referenced as the Soret effect [119]. In solids, the terms *thermal diffusion* or thermomigration (TM) are used. The phenomenological description is given as an additional term in the flux equation (3.12) where a thermal gradient will result in a diffusion of atoms according to

$$J_{TM} = \frac{CD}{k_B T} \frac{Q^*}{T} \left(-\frac{dT}{dx} \right) \tag{3.21}$$

where Q^* is the *heat of transport*, C the concentration of atoms, D the diffusion coefficient and k_B the Boltzmann constant. In solids this effect was for decades ignored due to low driving forces (low temperature gradients), but has later been shown to have a large effect in small scale electronic devices under certain conditions such as using flip chip solder joint [120]. TM is reported to occur in solder joints where Joule heating in the chip/substrate induces a thermal gradient over the solder. A temperature gradient of 1000°C/cm is sufficient to cause significant elemental redistribution in the solder [121].

In thermoelectric devices, with a typical hot side temperature of 500°C, a cold side temperature of 50°C and thermoelectric element lengths of 3–5mm, temperature gradients in the range 1000°C/cm are to be expected. Therefore, the driving force for TM could in theory be large enough to lead to dissolution of both thermoelectric as well as hot side interface materials and solders. However, there exists very little literature on the effect of TM on thermoelectric systems. An exception is the work by Huang et al., who analyzed different diffusion processes around lateral “dark bands” near the hot side joints of a Bi_2Te_3 module [122]. They concluded that both TM and EM would contribute in accelerating performance degradation of the device.

TM could also play a role in direct current-assisted sintering where a large local temperature gradient exists between grains during sintering, especially at high temperatures and small particle size of materials with low thermal conductivity [123].

Care should therefore be taken when using such methods in synthesis of thermoelectric material, as it can lead to de-mixing and inhomogeneous materials.

3.2.6 Creep

The final external driving force that can drive diffusion is that of an externally applied pressure. Creep is also very temperature-dependent, as are most other diffusion processes. At temperatures above the softening point of the materials (normally above 0.5 times the melting temperature), creep is strong, activated by diffusion and slide along grain boundaries and dislocations [124]. The strain rate of the material is

$$\dot{\varepsilon}_{ss} = A_0 \exp\left(\frac{\Delta H_c}{k_B T}\right)\frac{{\sigma_{ss}}^{n}}{d^{m}} \tag{3.22}$$

where A_0 is a constant, ΔH_c an activation energy of creep, σ_{ss} the applied stress, d the average grain size and n and m are constant depending on the mechanism of creep. For so-called diffusion creep (Nabarro-Herring creep), n=1 and m=2 and ΔH_c will be similar to the diffusion enthalpy of the majority defect mechanism.

In a thermoelectric system, the material is sandwiched between two plates that are pressed together to achieve good thermal transfer between the interfaces. Thermoelectric materials with low compression strength are therefore vulnerable to creep. An example is GeTe-MnTe-SnTe materials which show creep in the order of 7% under 2 MPa pressure during 100 hours at 600°C [125]. However, the addition of Nb seemed to reduce the creep to 0.4% under the same conditions. Nb will increase the softening point of the material and thus increase resistance to dislocation glide in the material, effectively reducing creep.

3.2.7 Nanosize materials

Defects are not only key to understand atomic diffusion, they will also affect other material properties such as electric and thermal transport through the material. As seen in section 2.2.3, nano-effects can have a huge benefit for increasing the efficiency of thermoelectric materials where transport is restricted to certain dimensions in the material. For bulk materials, the main contribution of confined transport on zT is related to phonon interaction with defects in the systems such as small precipitates/phases and grain boundaries [15].

The effect of nanocrystals on diffusion is mainly linked to the high amount of grain boundaries, which are high diffusivity paths (see section 3.1.2). The effect of many of the above-mentioned diffusion-controlled degradation mechanisms can therefore be enhanced in nanostructured materials. In addition, the stability of the nano-materials is a question [38, 126, 127]. Nanocrystals formed during synthesis (often powder metallurgical processes including sintering) are in many cases metastable, where subsequent structural relaxation and grain growth can lead to the effects of nanosize crystals disappearing over time [63]. In the project ThermoMag [20], which supported parts of this thesis, it was concluded that the effect of nanosize particles on the thermoelectric properties Mg_2Si was limited to around 10–15% increase, and that the thermal stability of these "nanomaterials" could be questioned [128]. Still, examples are plentiful of other material systems such as LAST [129] and SiGe [130] that show great benefits of nanostructuring and still show significant thermal stability.

3.3 High temperature oxidation

Why is this relevant for thermoelectricity? Most applications using thermoelectric materials up to our time have been at relatively low temperatures (bismuth telluride restricted to ~300°C) or in inert atmospheres (for space application). Little emphasis has therefor been put on the resistance to oxidation of thermoelectric materials. But as we want to use novel thermoelectric materials also at higher temperatures in atmospheric conditions, care must be taken to avoid severe degradation due to oxidation of the material. Two obvious solutions are either protection of the surface through encapsulating the whole thermoelectric module, or applying a thin layer of coatings on the material surface. The latter option is discussed in Paper 1 and Paper 5 of this thesis. However, this complicates the production process and leaves the module more vulnerable to damage, so the best case would be to make material with little to no oxidation up to the application temperature. In fact, some thermoelectric materials do not oxidize at all (such as oxides) and some do so very little, due to formation of near passivating layers up to certain temperatures (such as SiGe [131]). Skutterudites on the other hand are known to oxidize severely [52], which puts a clear limit to how high temperatures skutterudites can be used under without protection. In any case, it is important to have a good understanding of the underlying mechanisms and kinetics of the oxidation process that can be of assist in the design of the system.

Oxidation can be defined as *"The conversion of the surface portions of metal to oxide on heating in air or oxygen"* [35, pp. 2]. When oxygen reaches the surface, the strong affinity of oxygen forming bonds with the metal (or other elements) will in many cases cause a reaction between the surface and the oxygen. When this reaction occurs over a longer period of time, an oxide scale will build up. A schematic picture of this process is found in Figure 2.8.

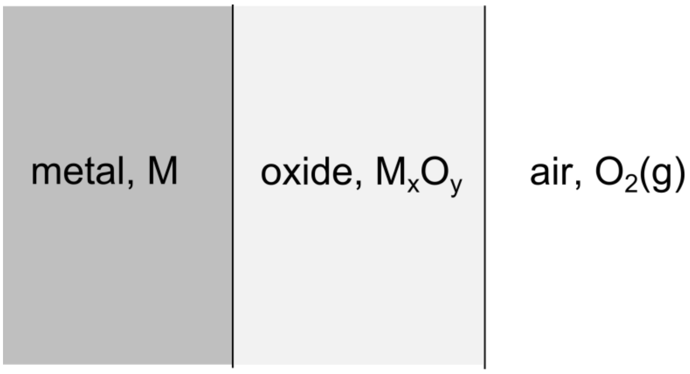

$$\frac{x}{y}M + \frac{1}{2}O_2 \rightarrow \frac{1}{y}M_xO_y$$

Figure 3.8 Schematic representation of oxidation of solids through oxide scale formation at the surface.

Oxidation is a highly temperature-dependent process. The oxidation of metallic elements is therefore often divided into different regimes depending on the oxidation temperature [35, pp. 28] (Figure 3.9):

- **Very low temperature:** Chemisorption/adsorption of O_2 on surface forming monolayer of O^-/O^{2-} ions. The low temperature hinders movement of either oxygen into the solid or atoms from the solid to the surface, effectively hindering further oxidation.
- **Low to medium temperatures:** At a sufficiently high temperature, some movement of atoms through the interlayer is allowed, although normal thermal movement of ions through lattice defects is prohibited. The kinetics governing this type of oxidation are generally termed log-laws, as after an initial buildup of an oxide layer, they will quickly be passivated, as the oxide layer hinders any more motion of ions either way through.
- **High temperature:** Movement of atoms through the lattice (metal/oxide) at these temperatures is sufficiently high to contribute to the oxidation. The growth of the oxide layers now follows parabolic laws typical for diffusion-controlled reactions. Also faster growth rates (linear, “breakaway”) can be seen depending on the governing oxidation mechanism. This is the temperature regime most relevant for thermoelectric materials and will be further discussed in the following.

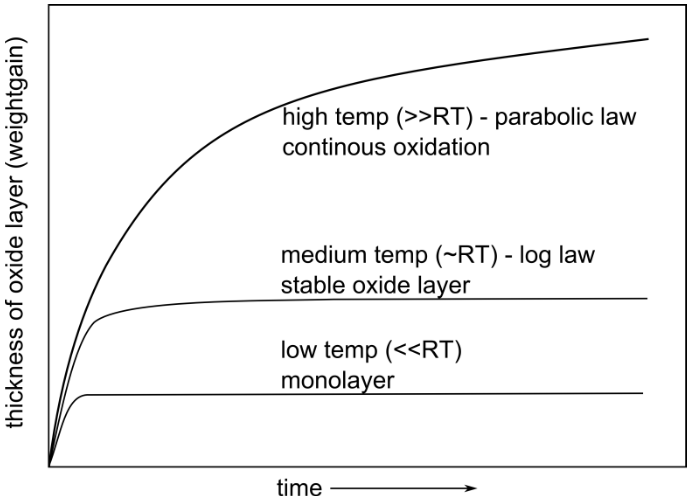

Figure 3.9 Typical oxidation rates at different temperature regimes.

3.3.1 Oxidation mechanism

The movement of ions is due to existence of lattice defects as seen in section 3.1. During oxidation, there are two types of main movement: metal ions outwards or oxygen ions inwards. The governing mechanism depends on the degree of non-stoichiometry in the oxide; if metal vacancies or interstitials are the main defect, then outward movement of metal ions will be dominating, or if oxygen vacancies or interstitials are the main defect, inward movement of oxygen ions will be dominating. Also mixed ion transport with nearly equal contribution of the two diffusion processes is possible. In addition, other defects such as grain boundaries, pores or cracks can contribute significantly to the oxidation process, especially transport of molecular oxygen into the core of the material.

Spallation of the outer oxide layer is also of great importance for many oxidation processes, as the oxide layer will typically be strained in both parallel and normal directions to the oxidized surface. Typically, solids which experience movement of oxygen ions inwards will inherit the stresses of the oxidized material, while solids with outwards movement of metal ions will only build up stresses related to the relative volume-change. If the metal ions are moving outwards during oxidation, this will leave vacancies in the lattice. These vacancies can then diffuse together and form larger pores and holes, which in the end can lead to larger cavities and crack formation between the metal and oxide layer. This was discussed by Pilling and Bedworth in their famous paper published in 1923 on high temperature oxidation of metals [132]. They formulated the *Pilling-Bedworth Principle*, which divides metals developing oxide layers in two separate classes:

1. **ultra-light metals** which form oxides occupying a smaller volume than the pure metal, ex.: Na, K, Ca, Mg
2. **other metals** which form oxides occupying a larger volume than the pure metal, ex.: Fe, Cu, Pb, Sn, Al, Ti, …

Group 1 should be porous and non-protective while Group 2 should form a protective layer. Group 1 metals will typically experience a self-propagating oxidation over certain temperatures, where the heat produced in the oxidation reaction will not be fully removed, and therefore increase the oxidation rate exponentially. In other words it will "burn in air" [35, p41]. This is exactly what we see for the Mg_2(Si-Sn) thermoelectric material of which oxidation mechanisms are thoroughly studied in Paper 3 of this thesis. Group 2 oxidation reactions could also produce extra heat, but since the oxide layer is denser, this local increase in heat will not speed up the total process. The *Pilling-Bedworth Ratio* (PBR) is furthermore defined as

$$PBR = \frac{V_{oxide}}{V_{metal}} = \frac{M_{oxide} \cdot \rho_{metal}}{n \cdot M_{metal} \cdot \rho_{oxide}} \tag{3.23}$$

where V is the volume, M the molar mass and ρ the density of oxide or metal, while n is the number of metal atoms per number of oxygen molecules. A PBR of less than unity represents the metals of Group 1 above, while a PBR above should form more protective oxide layers. However, a very high PBR (>2) will cause large stress build-up between the metal matrix and oxide layer, eventually causing spallation. Thus, ideal conditions are found for those materials that form oxides at a PBR of between 1 and 2. A typical example is aluminum, which quickly forms a passivating thin layer of Al_2O_3 with a PBR of 1.28.

3.3.2 Oxidation rates

A general formula of the oxidation of a substance M can be written as:

$$\frac{x}{y} M + \tfrac{1}{2} O_2 \rightarrow \frac{1}{y} M_x O_y \tag{3.24}$$

To allow for oxidation, the most important thing is of course that oxygen is present. It also needs to be present in such an amount that the oxidation is thermodynamically favorable, in other words that the Gibbs free energy of formation of the reaction is negative. The equilibrium constant, K, of the reaction above is given as

$$K = exp\left(\frac{\Delta G^{\circ}}{RT}\right) = \frac{a_{M_xO_y}^{1/y}}{a_M^{x/y} \cdot a_{O_2}^{1/2}} \tag{3.25}$$

where a is the activity of each reaction species and $\Delta G^{\circ}$the Gibbs free energy of formation. Assuming that both the solid phases, M and M_xO_y, are separated and non-interacting, their activities will be 1. The activity of oxygen can be assumed to equal the partial pressure in the surrounding atmosphere, p_{O_2}. The equilibrium pressure of oxygen can therefore always be calculated from tabulated values of the ΔG° as a function of temperature (assuming constant total pressure). This value of the partial pressure of oxygen is often termed the *dissociation pressure***,** giving the minimum value for the oxidation reaction to occur.

The growth of the oxide layer will follow a kinetic law given by:

$$\frac{dn_{M_xO_y}}{dt} = f(t) \tag{3.26}$$

where n denotes the number of moles of the oxide M_xO_y and f(t) is a function of time that can take many forms depending on the oxidation mechanism involved. It could also be rewritten with respect to either the metal or the oxygen consumption:

$$dn_{M_xO_y} = -\frac{2dn_{O_2}}{y} = -\frac{dn_M}{x} \tag{3.27}$$

The oxidation rate is related to the observed increase in thickness of the oxide layer, X, or the weight, W, of the oxidized sample. Assuming the only weight gain is from incoming oxygen, the weight change per unit area can be expressed as:

$$\frac{dW}{A} = -\frac{dn_{O_2}M_{O_2}}{A} = \frac{y\, dn_{M_xO_y}M_{O_2}}{2A} \tag{3.28}$$

where M_{O_2} is the molar mass of oxygen, 32g/mol, and A the surface area. The weight change per unit area is also proportional to the increase in oxide thickness dX (with ρ_{ox} denoting the density and M_{ox} the molar mass of the oxide layer)

$$dX = \frac{dW}{A}\frac{2M_{ox}}{y\,\rho_{ox}\,M_{O_2}} \tag{3.29}$$

These relations can be useful when looking at the type of reaction kinetics and how this is related to the observable changes of the oxidized species. Regardless of what is measured (e.g. thickness of oxide layer or weight gain), the kinetic rate laws have the same appearance. Equation (3.25) is thus often reformulated as a function of the oxide thickness or specimen weight, as this is a more visual concept

$$\frac{dX}{dt} = f'(t) \ or \ \frac{dW}{dt} = f''(t) \tag{3.30}$$

The reaction rates, f’(t) and f’’(t) are the same as that of equation (3.25), only with different constants involved, and the exact form of these reaction rates depends on the main oxidation mechanism involved, which will result in very different oxidation rates. The measured oxidation rate can thus give insight into the governing oxidation mechanism or rate limiting step.

Linear kinetics

In situations where the oxidation is limited by the flow of reactants to the reaction zone (e.g O_2 to the oxide/air or oxide/metal surface), it can be assumed that the reaction follows a linear law where the rate is independent of oxidation time

$$\frac{dX}{dt} = k_l \ \rightarrow \ X = k_l t \tag{3.31}$$

Linear kinetics can result when the forming scale is porous, i.e. PBR less than one. Near linear kinetics can also be seen in cases of spallation of the growing oxide layers, which is described in more detail in section 3.3.4

Parabolic kinetics

The case of a metal oxide scale growing as a result of diffusion through metal vacancies is sketched in Figure 3.10.

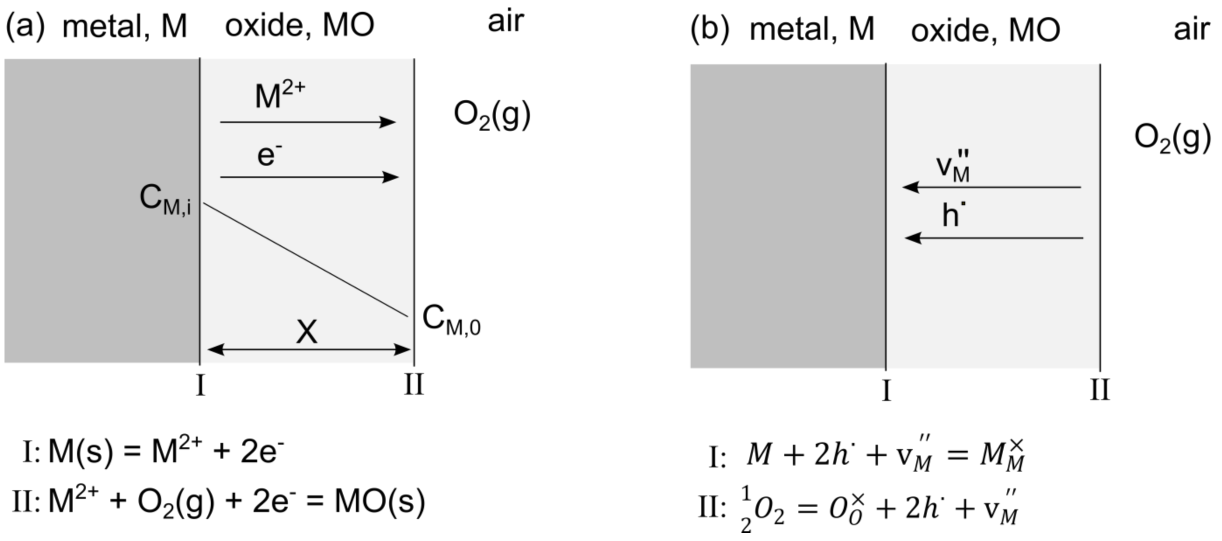

Figure 3.10 (a) Schematic representation of oxidation governed by outward lattice diffusion of divalent metal ions (M^{2+}). (b) Alternative representation of the process by corresponding majority lattice defects, in this case metal vacancies (v''_M) and electron holes ($h^{\cdot}$).

According to the principles of solid-state diffusion discussed in section 3.1.2, the concentration of the diffusion species is a linear function of the distance from the original surface. Adopting Fick’s first law (equation (3.2)), the flux through the oxide layer can be written as

$$J = -D\frac{C_{M,i} - C_{M,0}}{X} \tag{3.32}$$

The flux, J, represents the number of metal ions passing and area A per time unit. Since this amount of ions all contributes to the thickening of the oxide scale at the oxide/gas surface, J will be proportional to dX/dt. If the concentration are kept constant (given equilibrium at any moment in time) then equation (3.32) becomes

$$J \propto \frac{dn_{M_xO_y}}{dt} \propto \frac{dX}{dt} = \frac{k_{p,ox}}{X} \tag{3.33}$$

where $k_{p,ox}$ is the parabolic rate constant for oxidation. It can be expressed as

$$k_{p,ox} = \Omega D(C_{M,i} - C_{M,0}) \tag{3.34}$$

where Ω is the volume of oxide forming per unit quantity of diffusing species. The thickness at any moment of time is thus

$$X^2 = 2k_{p,ox}t \tag{3.35}$$

which is the same expression for the parabolic rate law for interdiffusion found in equation (3.15).

In an oxide, there exist two main types of point defects, cation or anion lattice site vacancies (i.e. $v_M'', v_O^{\cdot\cdot}$) and interstitial species (i.e. $M_i^{\cdot\cdot}, O_i''$). The total charge of the compounds needs to be sustained and thus generation of ionic defects will always result in simultaneous generation of electronic defects. Carl Wagner was the first to develop the theory of parabolic kinetics based on the assumption of a reaction governed by lattice diffusion of ions (or defects) through the growing oxide layer [133]. The main result of his work was that the oxidation thus is controlled by the respective ionic and/or electronic conductivity of the oxide layer. This also means that only small changes in the defect structure of the oxide (i.e. through dopants) will strongly affect the oxidation rate. A more rigorous treatment of Wagner's original description and analysis of the parabolic growth of oxide layers can be found in [134]. Here, a simplified picture is given to show how the parabolic rate constant is connected to the ionic diffusivities.

In the case of metal-deficit compound such as shown in Figure 3.10, where transport through the growing oxide scale is enabled through cation vacancies, there exist an equilibrium at the scale-gas surface given by

$$\tfrac{1}{2}O_2 = O_O^\times + 2h^\cdot + V_M'' \tag{3.36}$$

and similarly at the metal-oxide interface vacancies are consumed according to the equilibrium

$$O_O^\times + 2h^\cdot + V_M'' = \tfrac{1}{2}O_2 \tag{3.37}$$

The driving force for diffusion can thus be seen as the chemical potential gradient over the oxide layer due to differences in oxygen activity at the respective interfaces. Alternatively, this can be expressed as a concentration gradient of the metal ions as already discussed. This chemical potential gradient will be opposed by an electric potential due to the flow of electronic defects. Solving for this electrochemical equilibrium the parabolic rate constant can be shown to equal

$$k_{p,ox} = \frac{1}{2}\int_{p_{O_2}^i}^{p_{O_2}^0} \left(\frac{z_{cat}}{2} D_M + D_O\right)\, d\ln p_{O_2} \tag{3.38}$$

where D_M and D_O are the diffusivity of metal and oxide ions respectively, z_{cat} is the charge of the metal ions (cations) and $p_{O_2}^{i}$ and $p_{O_2}^{0}$ are the partial pressure (activity) of oxygen at the metal-oxide and oxide-air interface respectively.

The temperature dependency of the parabolic rate constant, and thus the oxidation rate, can from this analysis be understood as a function of the activation energy of diffusion due to formation and migration of defects discussion in section 3.1.2. In other words

$$k_{p,ox} = k_o \exp\left(-\frac{Q}{RT}\right) \tag{3.39}$$

where the activation energy, Q, mainly depends on the diffusion coefficient ($D = D_0 \exp(-Q/RT)$, see section 3.1.2) and the oxygen activity at either of the interfaces (depending on the major defect). In case of metal transport outwards, the partial pressure at the metal-oxide interface will be governing. The total activation energy of oxidation is often determined experimentally through thickness or weight change measurement as a function of time, temperature and partial pressure of oxygen, and can yield valuable insight into the governing oxidation mechanism.

Volatilization

In high temperature oxidation, the oxidation species can sometimes be volatile. In addition to the increasing weight due to oxygen take-up in the scale (parabolic kinetics), there is also a metal loss that will lead to decrease in weight at a constant rate (linear kinetics). Combining these to mechanisms the total oxide layer thickness is given by

$$\frac{dX}{dt} = \frac{k_{p,ox}}{X} - k_v \tag{3.40}$$

The scale will thus reach a limiting thickness, $X_s = k_{p,ox}/k_v$, while the total weight of the sample first will increase until the limiting thickness is reached and then start to decrease again as the weight change due to sublimation of oxide species overtakes that of oxidation reaction. This is partly what we see from oxidation of Mg_2(Si-Sn) in Paper 3, and also for skutterudite at temperatures above 600°C, as shown in Paper 1.

3.3.3 Influence of a second element in the metallic phase

So far the discussion have been limited to pure compounds. Addition of other elements in smaller (dopant) or larger (alloy) amounts can significantly affect the oxidation behavior. A second element can influence the oxidation in two main ways: (1) it may evenly distribute itself among the primary oxide phases where it will either accelerate or decelerate the oxidation but still follow the parabolic law; (2) form a new oxide layer on the outer surface of the oxide which either could protect the inner layer from further oxidation (log law) or cause spallation. How it will alter the main oxide phases depends on the valence of the constituent ion compared to that of the bulk ions and also the type of vacancies involved in oxidation (anion or cation vacancies). In a metal with anion vacancies, second elements with *higher* valency will leave fewer anion vacancies and therefor *diminish* the oxidation rate, and vice versa (Valency rule, according to Wagner-Hauffe) [135, p. 38].

In oxidation of alloys, the less noble element will oxidize first. As long as its oxide is stable, it will hinder formation of any other oxide products. Therefore, formation of an oxide scale containing just one of the elements that will protect the rest of the material from oxidizing is often seen. One example is Cr_2O_3 formation on stainless steel. A possible result of preferential oxidation of one element is depletion of this at the metal-oxide interface, i.e. the flux of metal ions through the oxide layer is higher than flux from bulk metal to the interface. Eventually, the activity of other elements to oxidize will be high enough so that these will start to oxidize as well**.** This effect can in the end lead to breakaway oxidation, or at least significant change in the oxidation rate after a certain induction period [134, p.237-241, 136].

3.3.4 Spalling of oxide scales

When an oxide layer forms on the surface of the bulk material, differences in molar volume can cause stresses to build up between the oxide layer and the bulk material. As the scale grows, more and more stress is accumulated, until it finally cannot withstand and will end with either cracking of the oxide scale or creep of the bulk material causing deformation and in many cases spallation of the oxide scale. The difference in thermal expansion (CTE) between the oxide and bulk material is the main factor that governs high temperature and cyclic oxidation. The less this difference is the better. Also other causes exist, such as epitaxial stresses, type of diffusion species and direction (anionic inwards, cationic outwards) and geometry of sample and composition of the scale [135, p. 202-219]. Typically, an oxide layer has lower CTE than the oxidized material [134, p. 74]. A quantitative expression of the internal stresses induced in an oxide with lower CTE than the bulk material is given by:

$$\sigma_{Oxide\ (compressive)} = \frac{E_{ox}\Delta T(\alpha_{ox} - \alpha_m)}{1 + 2(\frac{E_{ox}}{E_m})(\frac{t_{ox}}{t_m})} \qquad (3.41)$$

where E_{ox} and E_m are the Young's moduli of the oxide and the bulk material respectively, α_{ox} and α_m the CTE and t_{ox} and t_m the thickness. The ductility of the oxide layer is also important related to scale spallation, as a more ductile oxide would be able to release stresses through plastic deformation. This behavior can be further enhanced by leaving the oxide at high temperatures for longer times, instead of very short thermal cycles. In a thermoelectric device, the material will undergo many thermal cycles, so the stress behavior in the oxide shell during thermal cycling is of great importance.

3.3.5 Oxidation of skutterudites

The general oxidation mechanism of $CoSb_3$ has been investigated by several authors in the last years, and a good level of understanding has been reached [52, 137, 138]. However, p-type material containing Fe has shown much higher oxidation rates also at much lower temperatures, and the usability of these materials in application at earth is questioned [139-143]. The reason why these exceptionally high oxidation rates are seen for Fe-containing skutterudites is still not fully understood. The oxidation of p-type skutterudites seems to vary significantly depending on both Fe-content and filler type. In the following, the general picture of oxidation of skutterudites of both n and p-type will be presented.

Unfilled $CoSb_3$

Some initial oxidation experiments of undoped, pure skutterudite $CoSb_3$ is presented in Paper 1. The results from these experiments confirm much of the same picture that have been shown in [52, 137, 138]. Oxidation of $CoSb_3$ follows parabolic kinetics, with simultaneous outward diffusion of Sb and inward diffusion of O. Depending on temperature, several layers of oxidation products will grow at the surface. The outermost layer is a relatively thin Sb-O layer. There is a discrepancy in the literature as to whether this is primarily Sb_2O_3 or Sb_2O_4. A mixture of the two is probably the case, where the ratio depends strongly on temperature. At temperature above 450°C, Sb_2O_3 can react to form Sb_4O_6 (g) which leads to sublimation at the outer part of the oxide layers. At sufficiently high temperatures (above ~600°C), the mass-loss due to sublimation will outweigh the mass gain due to oxidation, leading to a net mass loss.

Under the Sb-O layer, $CoSb_2O_4$ will form at temperatures above 380°C degrees. At higher temperatures (>450-500°C), an intermediate layer of $CoSb_2O_6$ is also found. The oxidation is divided into two stages. First, all oxides will grow simultaneously until they reaches a certain thickness (first stage), after which the oxides will order themselves in layers (second stage, see Figure 3.11). These layers tend to be dense and stick well to the surface, and are the main reason we observe parabolic weight gain. However, there are uncertainties related to which layer and what diffusion species (Sb^{3+} or O^{2-}) are rate controlling. The parabolic rate constants have been found to vary between 3 and 3000 $\mu m^2/h$, and the activation energy likewise shows high variations between 37 and 262 kJ/mol. A summary of values reported in the literature is found in Table 3.1. Some reasons for the large discrepancy between the values for pure, undoped $CoSb_3$ could be differences in microstructure, such as pores and grain size, in addition to degree of non-stoichiometry, which all are a results of different synthesis routes and possibly also difference in experimental configurations.

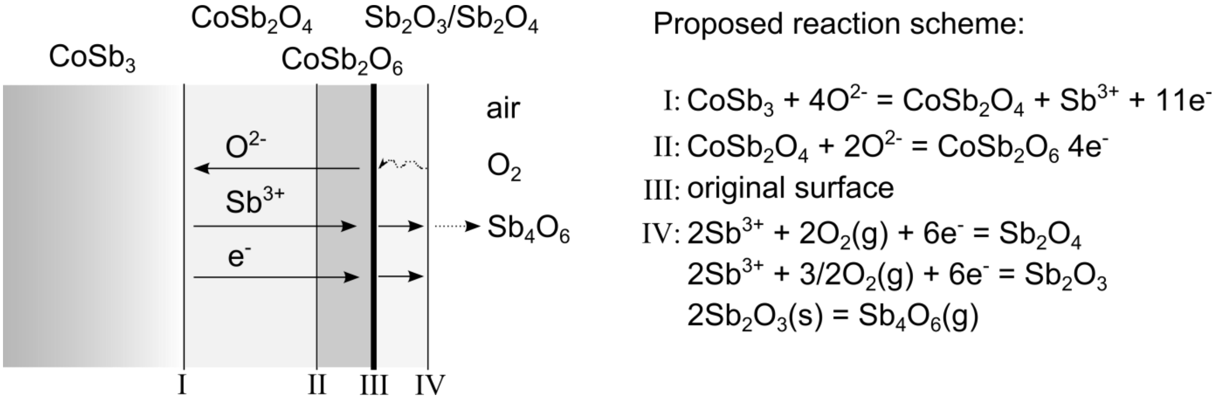

Figure 3.11 Schematic illustration of the different oxide layers on top of skutterudite ($CoSb_3$) after prolonged exposure to air at elevated temperatures, in addition to proposed oxidation reactions *[52]*. The relative thickness of the layers depends strongly on temperature.

Table 3.1 Skutterudite oxidation rates and estimated activation energies comparing literature values with own work. An oxide density of 5 g/cm^3 was used when conversion from weight to thickness according to equation (3.9).

Author	Sample type and composition	Temperature [°C]	oxidation rate / parabolic rate constant [μm^2/h]	activation energy [kJ/mol]
Paper 1 of this thesis	$CoSb_3$, bulk	550	1st: ~7.3 2nd: ~1.3	
		600 – 650	*weight loss*	
Zhao et al. [137]	$CoSb_3$, bulk	500 – 600	100 – 200	37.4
		650	*weight loss*	
Godlewska et al. [138]	$CoSb_3$, bulk	500 – 600	0.33 – 22	197
		700	*weight loss*	
Leszczynski et al. [52]	$CoSb_3$, powder	410 – 550	*two stages*	1st: 161 2nd: 106
Xia et al. [144]	$Yb_yCo_4Sb_{12}$, bulk	377	*higher than pure* $CoSb_3$	90 – 170
Xia et al. [142]	$CeFe_4Sb_{12}$, bulk	327	*breakaway*	
Park et al. [141]	$In_{0.25}Co_3FeSb_{12}$, bulk	350 – 450	6 – 3000	262
		550	*stable InSb layer*	
Sklad et al. [139]	$CeFe_4Sb_{12}$, powder	300	*breakaway*	
Peddle et al. [140]	$EuFe_4Sb_{12}$, powder	360	*breakaway*	
Qiu et al. [143]	$Ce_{0.9}Fe_3CoSb_{12}$, bulk	377 – 527	45 – 4500	
		577 – 627	*900 – 45*	

Filled and Fe-containing skutterudites

A small addition of filler atoms will significantly affect the oxidation mechanisms. Filling with small amounts of Yb reduces the activation energy of oxide growth and leads to a more linear type of oxidation mechanisms characterized by stress-build up and release, crack formation and new layer formation in cycles [144]. When Fe is added to the system, providing p-type material (see section 2.2.3), the oxidation rate is further enhanced. For fully filled $CeFe_4Sb_{12}$, oxidation is seen already at 300°C, where amorphous Fe-oxides and Sb-oxides along with ordered Ce_7O_{12} form [139]. At higher temperatures, Sb_2O_4 is found, but the Fe-oxides remain amorphous. As a result of this, no protective layers will form for skutterudites resulting in breakaway oxidation in contrast to more protective parabolic oxidation kinetics. However, the material tested in [139] contained small amounts of secondary phase $FeSb_2$ already at the outset, which could affect the oxidation, but this was not considered when the oxidation mechanisms were discussed. This is further discussed in section 4.2. Work by Xia et al. on bulk samples with the same composition found that Ce oxidizes preferentially, leading to decomposition of $CeFe_4Sb_{12}$ into $FeSb_2$ and Sb, before $FeSb_2$ and Sb further oxidizes after prolonged exposure [142].

For mixtures of Co and Fe skutterudites, the effect of Fe seems less detrimental. Co will stabilize the oxides, forming more dense layers, as seen for $In_{0.25}Co_3FeSb_{12}$ [141]. They will nonetheless oxidize much faster than unfilled $CoSb_3$ without Fe as seen in Table 3.1. An exception is found at higher temperatures (~500–550°C), where the formation of an intermediate InSb layer will significantly slow down the oxidation. A similar effect is seen for oxidation of $Ce_{0.9}CoFe_3Sb_{12}$ [143]. At temperatures up to 525–550°C, the oxide layer is dominated by Fe^{3+} oxides with significant difference in volume from the underlying material, thus resulting in very high oxidation rates. But at even higher temperatures, the oxidation slows down due to ordering of crystallized $FeSb_2O_4/FeSb_2O_6$ layers in addition to $CoSb_2O_4/CoSb_2O_6$ leading to near parabolic oxide growth.

From the above discussion, it can be observed how the oxidation of filled, p-type skutterudites is a very complex process, where the oxidation mechanisms and kinetics strongly depend on factors such as Fe-ratio and type and amount of filler element. Generally, the preferential oxidation of filler elements will increase oxidation rates of skutterudites. In the case of skutterudites with high Fe-content, the oxidation of filler elements will lead to decomposition of the skutterudite matrix into β-phase ($FeSb_2$) and Sb since "$FeSb_3$" cannot exist without any filler to stabilize the Fe-Sb bonds (see section 2.2.3 and 4.1.4). This will furthermore enhance oxidation rates significantly.

3.4 Thermo-mechanical failure

In addition to diffusion, an increase in temperature of a solid material will cause the atomic lattice to expand. The relative change in size over the change in temperature is called the coefficient of thermal expansion (CTE) and is often given in µm $m^{-1}K^{-1}$. It is one of the most important material properties considered when designing electronics that will operate at higher temperatures. This is because all materials have different thermal expansion coefficients, so that the same temperature increase will cause a difference in expansion of the materials leading to high mechanical stresses induced between them, similar to those seen between an oxide layer and oxidized material, given in equation (3.41). The relative difference in thickness and Young's modulus of the material is seen to affect the stresses and should be optimized for the given conditions, in addition to reducing the mismatch in CTE. Matching the Young modulus of the materials in contact are almost as important for reliable operation. In Table 3.2, CTE and Young's modulus of different materials typically found in a thermoelectric module is shown. Different substrate, electrode and contact materials will have to be chosen so that they match the CTE and Young's modulus of the thermoelectric material. These properties can vary considerable also between n- and p-type materials, which furthermore complicates the module assembly and choice of contact materials.

Table 3.2 Coefficient of thermal expansion (CTE) and Young's modulus of some materials often used in thermoelectric modules.

Material	Function	CTE [$10^{-6}K^{-1}$]	Young's modulus [GPa]
Alumina	Substrate	5.4 [145]	340 [146]
Copper	Electrode	16 [147]	110 [146]
Molybdenum	Metallization	5 [147]	330 [146]
Nickel	Metallization	13 [147]	207 [146]
Sn-Pb solder	Solder	25 – 28 [147]	9 – 48 [148]
Bi_2Te_3	TE material	12 – 16 [65]	32 [149]
$CoSb_3$	TE material	9 - 13 [66]	100 – 160 [150, 151]
Mg_2Si	TE material	7.5 [152]	117 [153]

For thermoelectric application where repeated rapid heating and cooling cycles is seen, the effect of thermo-mechanical degradation will be much higher than stationary application with stable interface temperatures [154]. This furthermore requires very good CTE matches and design of the contact layers that minimizes the stresses produced during heating and cooling [33]. Hori et al. found large tensile stresses building up between metallization and thermoelectric legs which lead to crack formation and failure after 400 cycles [155]. In Paper 4, the whole design of the silicide-based module revolves around using springs beneath each TE-leg to encompass the difference in CTE between the n- and p-type materials.

In addition to (adhesive) stresses between different materials layers as discussed above, cohesive stresses within the material can results in disintegration of the thermoelectric material itself. High fracture strength and toughness of the material is thus of key importance for long term operation in cycling conditions.

In the electronic industry, as a rule of thumb, the homologous temperature (operating temperature divided by the melting temperature) should be kept below 0.67 (using Kelvin scale) [156]. At higher temperatures, the mechanical properties gradually worsens. This is also relevant for thermoelectric systems which necessarily have to operate at as high temperature as possible to achieve good efficiencies.

4 Main findings

Five papers have been written as part of this thesis, and their summaries are given below. The full-length versions of the papers are found at the end of this thesis.

1. **Methods of enhancing thermal durability of high temperature thermoelectric materials for waste heat recovery** *(published)*

   In this article the basic oxidation of both skutterudite and Mg_2(Si-Sn) are discussed, along with initial studies on anti-oxidation coatings. These initial oxidation studies complemented data in the literature, and were used as a basis for further oxidation studies. In addition, a very promising candidate coating based on Al was found that protected both skutterudite and Mg_2(Si-Sn) up to 500–600°C in air.

2. **Influence of synthesis procedure on the microstructure and thermoelectric properties of p-type skutterudite $Ce_{0.6}Fe_2Co_2Sb_{12}$** *(published)*

   The microstructure is affected by the synthesis route. This again affects the TE properties and the stability of the material, especially towards oxidation. In this work, material with the same composition was synthesized with four different methods, and the resulting microstructure was investigated. Special focus was given to peritectic solidification and transformation, as this is one of the key factors influencing the formation of secondary phases and resulting microstructure. In addition, the thermoelectric properties were measured and discussed on basis of the microstructure.

3. **High temperature oxidation of Mg_2(Si-Sn)** *(submitted)*

   The thermoelectric properties Mg_2(Si-Sn) vary significantly with the ratio of Sn/Si. A ratio of between 0.4–0.6 yields the best thermoelectric properties. However, the addition of Sn can severely affect the stability of the compound. In this work, we performed a thorough study on oxidation mechanisms and kinetics for $Mg_2Si_{1-x}Sn_x$ as a function of x. We found that these compounds form a stable oxide layer of MgO below a certain threshold temperature above which breakaway oxidation is initiated. This threshold temperature is therefore identified as an ignition temperature, and this again decreases with increasing Sn-content. A mechanism for this breakaway oxidation was furthermore proposed.

4. **Design, assembly and testing of silicide based thermoelectric modules** *(published)*
   This article covers the design, assembly and testing aspects of three modules made of Mg_2(Si-Sn) and $MnSi_{1.75}$. The best-performing module gave power of 3.24W and efficiencies of 5.3%, which is the highest efficiency reported to date on modules solely based on silicides. Characterization of the modules after long long-term testing and cycling showed several different degradation mechanisms. Especially, it showed how important it is to avoid even small amounts of oxygen in the surrounding atmosphere to avoid oxidation at hot side interconnects.

5. **Novel method for evaluating thermoelectric performance and durability of functionalized skutterudite legs** *(to-be-submitted)*
   In this paper, a new method for measuring several skutterudite functionalized legs simultaneously is presented. It differs from standard methods in its ability to individually measure electric characteristics of each leg during long term thermal cycling and may thus be used to compare different metallization and coating concepts. Furthermore, post-characterization of the legs after thermal cycling was performed to form a relation between different temperature-activated degradation processes and the electrical performance of the functionalized skutterudite legs.

The content of the papers can be seen to vary from synthesis to long term testing and post-characterization. This holistic approach is chosen based on the assumption that **the long term stability of a thermoelectric material is a function of all the processes leading up to the final use in a module.** The remainder of this chapter will therefore summarize and discuss the different aspects all the way from synthesis to module testing and by this form a framework for future exploration of thermal durability of thermoelectric materials, in an attempt to answer the following questions:

- What thermal degradation processes are most relevant for thermoelectric systems?

- How do different thermal degradation processes affect the long-term performance?
- What compromise must be made between efficiency and durability to ensure best lifetime performance?

In addition to references to the five papers, unpublished experiments carried out during the work on this thesis that are relevant for this discussion will also be presented. The first two sections, 4.1 and 4.2, are therefore in a manuscript form with more details on the experimental, results and discussion part that are not found in Paper 1 and 2, while the remaining sections, 4.3, 4.4 and 4.5 forms a more comprehensive summary of the other three papers. In particular, section 4.5 concludes this work by discussing how the different degradation processes affect the performance of the thermoelectric device over time.

4.1 Formation and annihilation of secondary phases in skutterudite

A short introduction on skutterudites and the crystal lattice was given in section 2.2.3. It was seen how the zT value of the skutterudite is optimized primarily by adjusting the type and amount of filler element in addition to the ratio of Fe and Co. In addition, in-situ formation of nano-scale precipitates of the secondary phases such as $FeSb_2$ [157] or InSb [158] have shown to significantly enhance thermoelectric properties, mainly by a reduction in lattice thermal conductivity. However, the choice of filler element and Fe-content, in addition to any secondary phases, will also greatly affect the thermal stability of the material. For example, secondary phases will generally have different thermal expansion and Young's modulus than the skutterudite phase, consequently lowering the fracture strength and toughness of the material. During usage, stress build-up along phase boundaries can result in crack formation and disintegration of the grains. We thus get a situation where we do not only want to optimize for the best thermoelectric properties, but also for long-term stability. This will become clearer from the arguments presented at the end of this section.

It was therefore of interest to investigate the effect of different filler elements on microstructure and the thermoelectric properties of p-type skutterudite. While Paper 2 only discusses the case of filling with Ce, a more general formulation of the observations will be presented here, including results also for other filler elements.

4.1.1 Experimental methods

Material synthesis

Raw materials were weighed in according to stoichiometry of $Fi_{0.6}Fe_2Co_2Sb_{12}$ where Fi = In, Ca, Ce or Yb. Stoichiometric quantities of Co (pellets, 99.99%, Goodfellow), Fe (pellets 99.99%, Goodfellow), Sb (shot, 99.999%, Alfa Aesar) and Ce (99.9%, Alfa Aesar) were mixed and sealed under vacuum in a quartz tube. The material was heated up to 1150 °C for 2 hours. Subsequently the sample was ground manually using a mortar and a pestle.

The phase transformation into skutterudite was achieved by compacting the obtained powders with a direct current assisted sintering device (DSP 510, Dr. Fritsch) at 48 MPa and 630 °C for 60 min. Annealing of the sample was performed in an evacuated chamber backfilled with argon at 630 °C for 48 h. The finished pellets had a diameter of 12.7 mm and a thickness of approximately 4 mm, see Figure 4.1.

Characterization

Samples were analyzed with powder X-ray diffraction (XRD, Bruker D8 Advance), Potential Seebeck Microprobe (PSM), which measures the spatially distributed value of Seebeck coefficient at a surface, scanning electron microscopy (SEM) and energy dispersive X-ray spectroscopy (EDS, both with Zeiss Ultra 55). The actual composition of the skutterudite phase was calculated as an average between 7–10 points over the sample analyzed with EDS. The thermoelectric properties were measured using an in-house device (DLR, Cologne) to sense the Seebeck coefficient and the electrical conductivity simultaneously as a function of temperature [159]. Thermal diffusivity measurement was carried out by a laser flash analyzer (LFA, Netzsch) together with density measurements by the Archimedes method. The thermal capacity c_p was calculated using the Dulong-Petit law ($c_p = 0.23\ Jg^{-1}K^{-1}$).

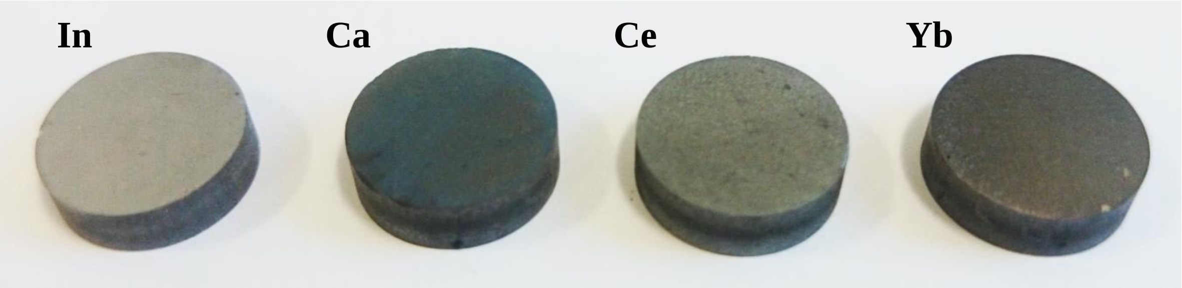

Figure 4.1 Picture of the four skutterudite samples prepared with different filler elements.

4.1.2 Results

In Figure 4.2, SEM images of the four samples after sintering and annealing for two days are shown. The microstructure clearly contains several different phases, primarily $Co_{1-x}Fe_xSb_2$ (β, dark), skutterudite (γ, grey) and $FiSb_x$ (white). Combining EDS measurement of the phases shown on the surface with XRD measurements (not shown here), the different phases could be identified with a high degree of certainty. The grain size can also be clearly seen, with varying greytones of the individual grains. The area fraction of each phase was calculated based on several of the SEM images and is found in Table 4.1.

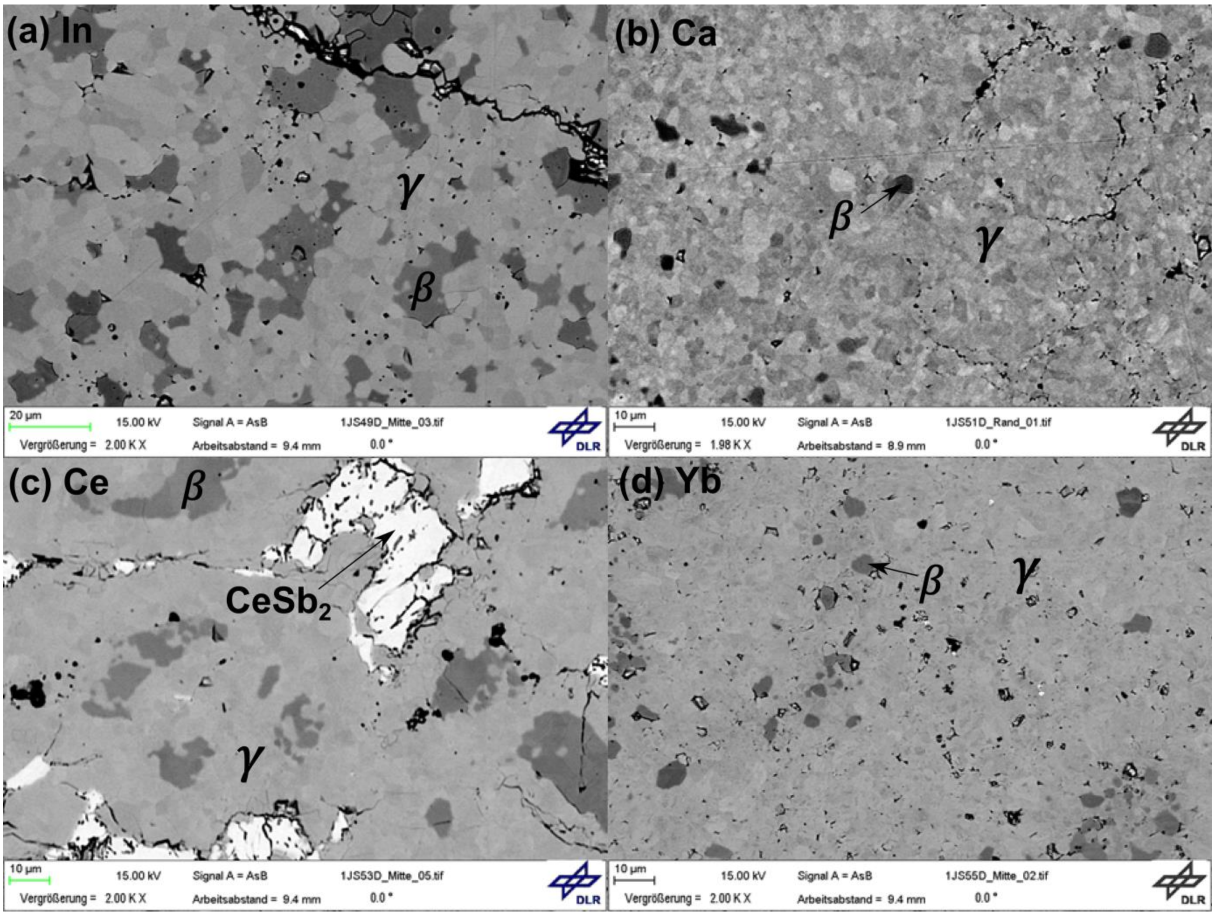

Figure 4.2 SEM images of samples with different filler elements after synthesis and annealing. Different phases are clearly observed: dark FeSb$_2$/CoSb$_2$ (β), grey skutterudite (γ, typically darker grey → higher filling fraction/iron content) and white: Fi$_a$Sb$_b$ phase of filler elements – a lot in Ce, very small grains in Yb.

Table 4.1 Area fraction (%) of different phases calculated from SEM images.

Sample	γ (skutterudite)	β ($Co_{1-x}Fe_xSb_2$)	Fi_aSb_b	Pores
In	74.2	22.1	-	3.7
Ca	94.4	4.4	-	1.2
Ce	70.6	23.5	3.3 ($CeSb_2$)	2.6
Yb	87.5	10.9	< 0.1 (Yb_2Sb_3)	1.6

The chemical composition of each grain varies considerably, which is evident from the plot of Filler-ratio (y) against Fe-content (x) of several different skutterudite grains shown in Figure 4.3. Especially the Ca and Yb filled samples show large variations. However, these variations seem very systematic, where y has a near linear dependence on x (or vice versa). The In sample shows on the other hand almost no variations.

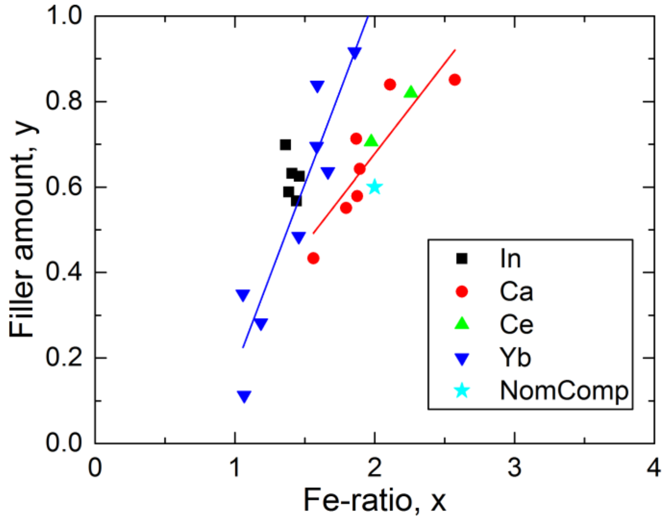

Figure 4.3 Filling ratio m of element M as a function of Fe content y in $M_mFe_yCo_{4-y}Sb_{12+\delta}$. Higher filling ratio → Higher iron content for all filler types except In.

PSM maps of the samples before and after annealing are shown in Figure 4.4. The frequency plots of these measurements are furthermore found in Figure 4.5. From these measurements, the effect of filler type and microstructure on Seebeck coefficient is quite clear. The In sample shows lowest Seebeck coefficient, with average values of 56 and 64 µV/K before and after annealing respectively, while the Ca sample show the highest average values of 85µV/K. Annealing will in general cause a higher and narrower distribution of Seebeck coefficients over the sample.

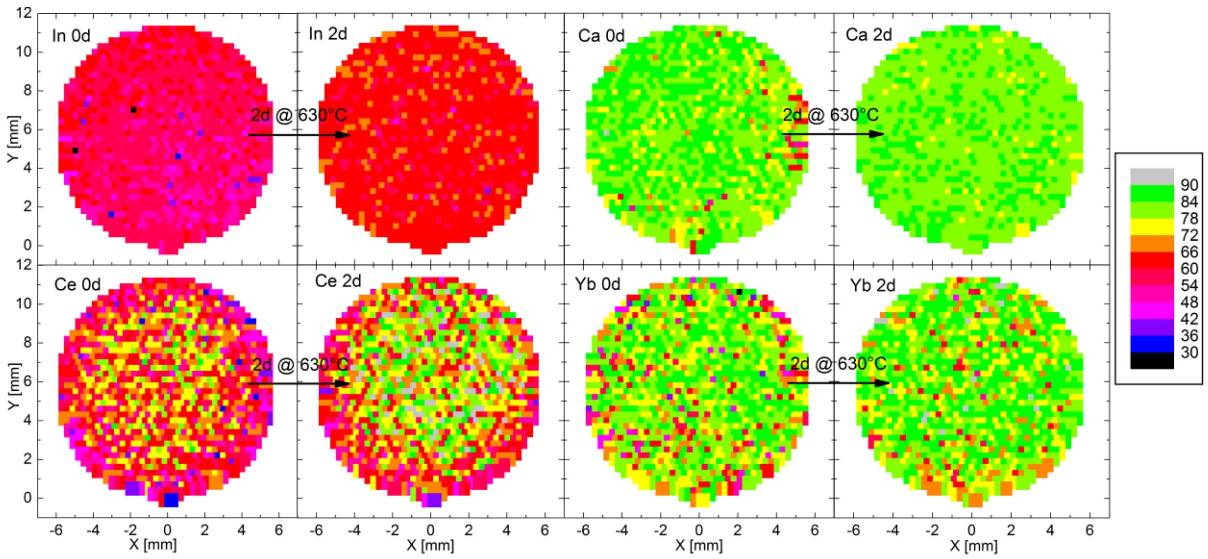

Figure 4.4 PSM scans of the four samples with different fillers before and after annealing.

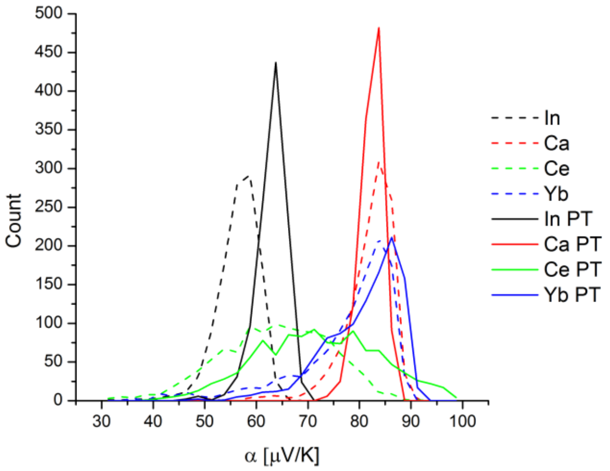

Figure 4.5 Frequency plot of Seebeck coefficient from PSM maps in Figure 4.4 of samples with different filler elements before and after 2 days annealing at 630°C (PT).

Where the PSM measurements give valuable insight into the variation of Seebeck coefficient over the sample, and thus the homogeneity of the samples, the measurement of all thermoelectric properties shows variations in average properties over a temperature range. Figure 4.6 shows the thermoelectric properties of the samples after 2 days of annealing, in addition to values of near phase pure Ce samples (from Paper 2). The Seebeck coefficient at room temperature has similar values as found by PSM, and the relative value between the samples is similar, also at higher temperatures. Of the four samples, the Ca-sample shows very high electrical conductivity compared to the other samples, leading to the best zT values. The samples with the highest amount of secondary phases, In and Ce, also have the lowest zT values, mainly due to the lower Seebeck coefficient. In contrast, the near phase pure, homogenous Ce sample shows excellent Seebeck coefficient, in addition to very low thermal conductivity, which leads to much better zT values compared to all the other samples. In the following section, the cause of the large variations in microstructure and thermoelectric properties will be discussed.

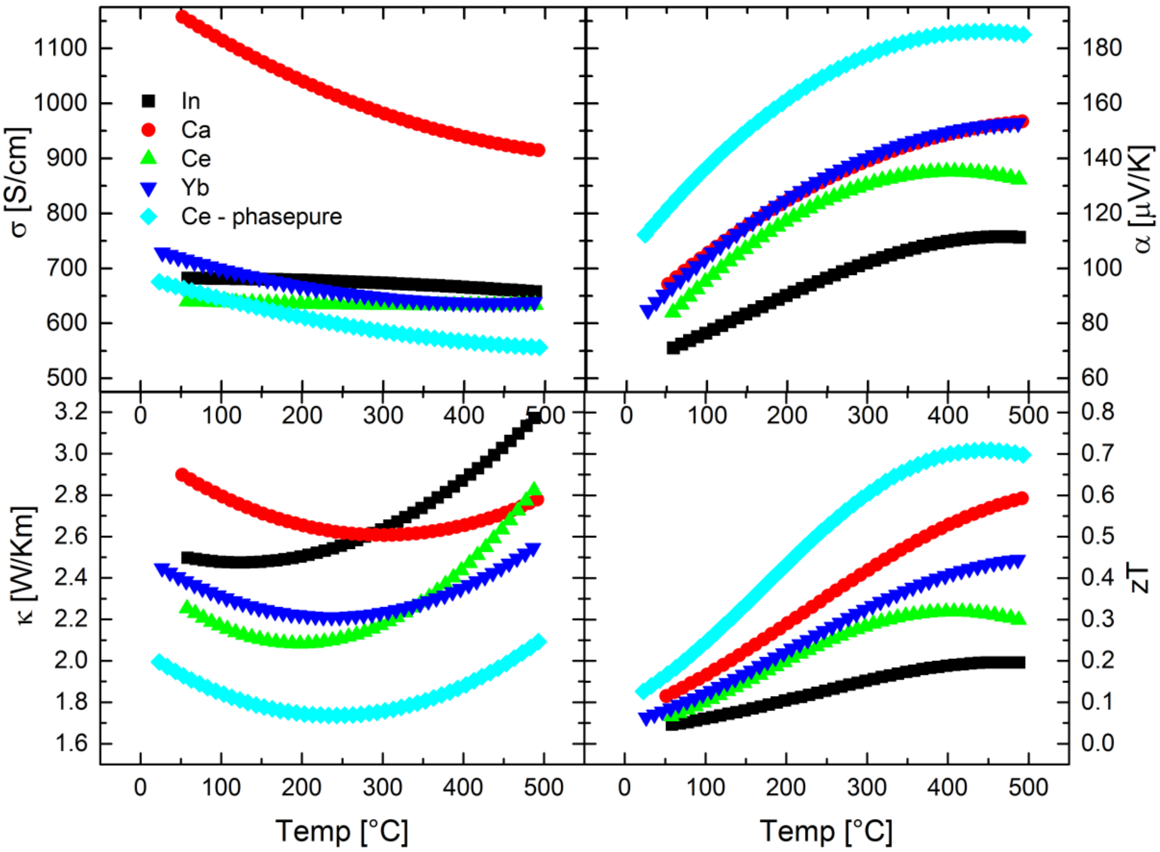

Figure 4.6 Thermoelectric properties of the four samples after sintering and annealing. A phase pure skutterudite, Ce-filled sample from Paper 2 is shown for comparison.

4.1.3 Effect of microstructure and filler element on thermoelectric properties

As is evident from Figure 4.4 and Figure 4.6, the Seebeck coefficients along with the other thermoelectric properties are clearly influenced by the filler element and particularly the microstructure and homogeneity of the sample. However, since all samples are synthesized in the same manner, the filler element is clearly the main contribution to the difference also in microstructure. This will be further discussed in Section 4.1.4. The metastability of these samples would probably lead to a change in properties upon prolonged annealing. Especially the Ce-sample would increase in skutterudite content upon further annealing, as shown in Paper 2. The following discussion on thermoelectric properties therefore only reflects the situation of the samples in the metastable, multiphase state.

Seebeck Coefficient

As shown in section 2.2.1, the Seebeck coefficient depends to a large degree on the charge carrier density – more charge carriers results in lower Seebeck coefficient. For these samples, the charge carrier density mainly depends on the amount of Co substituted with Fe forming holes. In addition, the valence of the filler atoms will affect the charge carrier density. In these experiments, the valence of each filler is In^{+}, Ca^{2+}, Yb^{2+} and Ce^{3+}, which would contribute one, two and three electrons respectively, effectively reducing the total amount of charge carriers [160]. Since the Fe content is similar for all samples, the Seebeck coefficients should therefore be highest for the Ce samples (lower amount of holes) and lower for In (higher amount of holes). However, as we see from both SEM images (Figure 4.2) and EDS analyses (Figure 4.3), the samples show large variations in amount of secondary phases and in the elemental composition of the skutterudite grains, which also will contribute to the total Seebeck coefficient. The Seebeck coefficients of the Ca and Yb samples are almost identical, both at room temperature and at higher temperature, which is expected, since they have the same valence and low amount of secondary phases. The Seebeck coefficients of the secondary phases are evidently much lower than of the skutterudite phase. This is reflected in the spatial distribution of Seebeck coefficient values across a sample (Figure 4.4 and Figure 4.5), where the mean value increases and the variation is reduced with annealing for all samples (i.e. less secondary phases). The variation is especially strong for the Ce samples, which clearly stems from the high amount of secondary phases, mainly β and $CeSb_2$. Similarly, the In sample has a low Seebeck coefficient due to the high amount of remnant β-phase. For the Ce samples, it is also seen how the sample has an outer ring with a lower Seebeck coefficient. This is probably due to sublimation of Sb during synthesis, leading to a higher amount of remnant secondary phases. Furthermore, this could results in more Sb vacancies in the lattice, balanced by an increased amount of holes according to the defect equilibrium $Sb_{Sb}^{\times} = v_{Sb}' + h^{\cdot} + Sb(g)$ that will decrease the Seebeck coefficient. For an n-type material, an opposite effect could be expected, i.e. a net decrease in charge carrier density and thus increase in Seebeck coefficient near the edge.

Electrical conductivity

In contrast to the Seebeck coefficient, the electrical conductivity increases with the number of charge carriers. Little information is available on the electrical conductivity of the secondary phases, but from comparison between the inhomogeneous and homogenous (phasepure) Ce samples, it seems that the electrical conductivity decreases with increasing amount of skutterudite. This is however more than compensated for by the increase in Seebeck coefficient, thus resulting in higher power factors for more phase pure material. Of the four samples, Ca filling seems to have a particularly good effect on the electrical conductivity of the samples and is the main reason these samples show the better zT values than the other samples (except the homogenous Ce). The difference between the Ca and Yb samples seems strange, since both possess a valence of 2 and have similar Seebeck coefficients (similar charge carrier densities). As seen from equation (2.4), the second factor affecting electrical conductivity is the charge carrier mobility μ. In this case it could be that slightly higher hole motilities in the Ca-sample due to the effect of light Ca fillers have lower effective mass than heavier filler elements such as Yb, thus increasing the mobility [161].

Thermal conductivity

The samples with the lowest thermal conductivities are the Ce- and Yb-samples, i.e. the samples with the heaviest/largest filler elements. This is as expected, since the main role of the filler element in a skutterudite is to reduce lattice thermal conductivity and higher filler mass relative to the skutterudite cage tends to lead to lower values [162]. It can also be seen how the phase pure Ce samples have even lower thermal conductivity, indicating a negative influence of secondary phases, probably due to higher thermal conductivities of these phases compared to the filled skutterudite. The effect of this is however limited, giving a slight increase of 10–20%. Furthermore, the Ca-sample has high electrical conductivity, which would imply a high electronic contribution to the thermal conductivity, while the In-sample contains a lot of secondary phases further increasing the thermal conductivity. Finally, the filler-ratio (Figure 4.3) and Fe-content will also affect the thermal conductivity. This is however hard to judge, since the samples are metastable and would probably change significantly upon prolonged annealing.

4.1.4 Peritectic formation of p-type Skutterudite

How can we explain the observed microstructure seen in Figure 4.2? How do the secondary phases form? And how can we get rid of them? Synthesizing skutterudites generally requires mixing and melting of a stoichiometric amount of the elements at temperature above the liquidus lines indicated in the phase diagrams of Co-Sb and Fe-Sb in Figure 4.7 (typically >1100°C). Upon cooling, several phases will form at different temperatures. The main phases are (Co,Fe)Sb (α), marcasite (Co,Fe)Sb_2 (β) and skutterudite (γ), which only exist as $CoSb_3$ (equal to x=0 in equation (2.7)). $FeSb_3$ will however form with the addition of filler atoms that will contribute with valence electrons to stabilize the Fe-Sb bonds, e.g. $CeFe_4Sb_{12}$ which is reflected in equation (2.7).

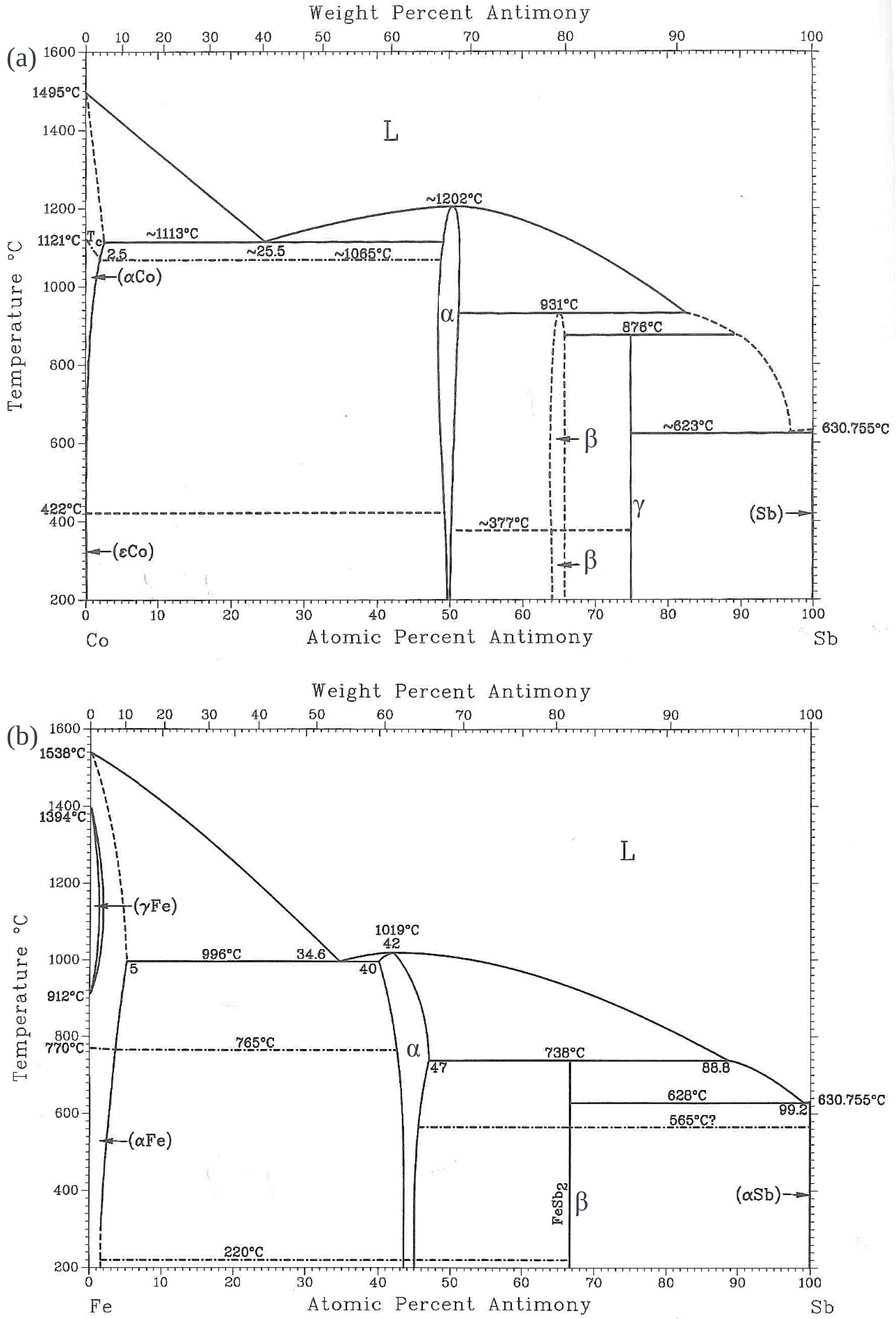

Figure 4.7 Phase diagram of (a) Co-Sb [163] and (b) Fe-Sb [164]. The skutterudite phase (γ) is only found for $CoSb_3$, while two secondary phases, CoSb/FeSb (α) and $CoSb_2$/$FeSb_2$ (β) with slightly different degree of non-stoichiometry, are found in both systems.

Below the liquidus temperature at 75 at% Sb (~1050°C for Co and ~920°C for Fe) α will nucleate and grow. The resulting morphology will depend on external factors such as cooling rate and filler element type, but typically, a dendritic growth is found (see Paper 2). The phase diagrams shows how both β and γ are *peritectic phases* - that is it will form as a result of the peritectic reactions

$$\alpha + L = \beta \tag{4.1}$$

$$\beta + L = \gamma \tag{4.2}$$

When temperature reaches the peritectic temperature of β (931°C for Co and 735°C for Fe), β will start to form at the surface of α according to equation (4.1). This is followed by diffusion-controlled peritectic transformation, with formation of additional β at the α/β interface by Sb diffusion from the liquid through the growing β layer (see section 3.2.1). Similarly, γ should in theory form when the peritectic temperature of γ is reached with further cooling. However, in the experiments published in Paper 2, no γ were found after solidification. From this it is proposed that *diffusion phase competition* [165] could play a major role in synthesis of skutterudites, inhibiting the formation of γ until all α is consumed. This assumption is also believed to hold for other filler elements and amounts.

The solidification of skutterudites with different Fe/Co-ratios will strongly affect the resulting microstructure, due to both thermodynamic as well as kinetic effects. In the isopleth section of the Co-Fe-Sb system at 75 at% Sb shown in Figure 4.8, it can be seen how the peritectic temperatures will change with Fe-content for $Co_{4-x}Fe_xSb_{12}$ (where 25 at% Fe equals x=4) [166]. The maximum Fe-content to form skutterudite without fillers is roughly 5 at% or x=0.8. At higher Fe-content, filler elements are needed (reaction (2.7)). The formation of skutterudite will in this case no longer follow the general reaction (4.2), but an additional term representing the filler elements must be included $Fi + \beta + Sb = \gamma$, or more specifically

$$\frac{y}{a} Fi_a Sb_b + Co_{4-x}Fe_xSb_8 + \left(4 - y\frac{b}{a}\right) Sb = Fi_y Co_{4-x}Fe_xSb_{12} \tag{4.3}$$

Most filler elements form antimonides with relatively high melting points that will solidify simultaneously with the other phases, which could for example affect the nucleation and growth of the other secondary phases. $CeSb_2$ will for instance nucleate at a temperature between 1000-1100°C depending on the Sb-content of the liquid [167], and could act as nucleation center for α phase upon solidification. This is a very complicated system with many degrees of freedom and is not discussed further here. Instead, we observe that these types of mechanisms could be used to control the final microstructure of the skutterudite. For example, instead of nucleating few large α-particles at initial stages of solidification, many smaller α particles could be made, which would significantly speed up the transformation into phase pure skutterudite.

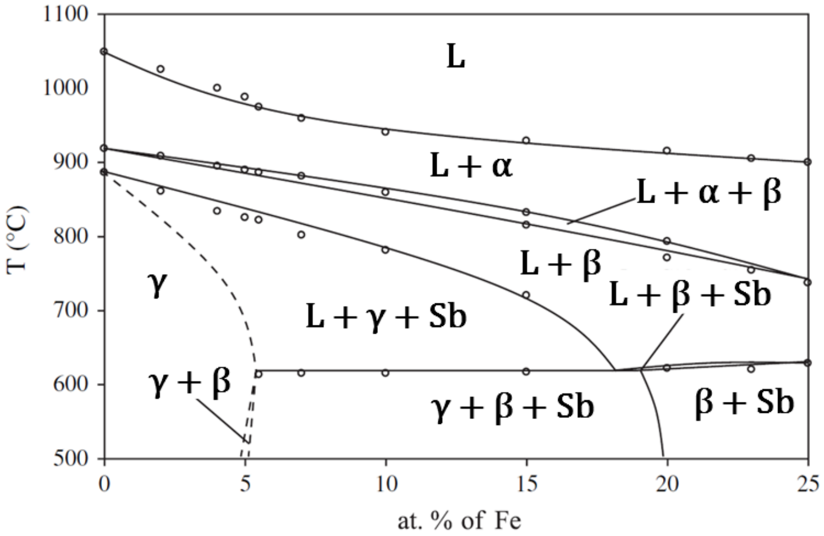

Figure 4.8 Isopleth section of the Fe-Co-Sb phase diagram at a constant Sb concentration of 75 at%, modified version from [166].

Equation (4.3) shows that the skutterudite phase will nucleate and grow only at zones where the three precursor phases co-exist. This will definitely affect the transformation kinetics. The further growth of the γ phase will be governed by solid-state diffusion between the Fi-containing phase and the β phase through the growing γ phase. Primarily the filler element and Sb will diffuse, but since the Fe-content (x) depends on the filler ratio (y), redistribution and diffusion of Fe and Co could also play a role. In Paper 2, annealing experiments were conducted, and confirmed that the fraction of the material transformed into γ, α_γ , fitted well with a three dimensional diffusion kinetics of the Ginstling –Brounshtein model [168]

$$f(\alpha_\gamma) = 1 - (2/3)\alpha_\gamma - \left(1 - \alpha_\gamma\right)^{2/3} = k_{GB}t \tag{4.4}$$

where k_{GB} is the parabolic rate constant. For any diffusion-controlled reaction, the rate constant depends on the diffusion coefficient (D), the concentration of the diffusion species (C_0) and is inversely proportional with the distance squared (see section 3.1.4). In this case, this is seen from the parabolic rate constant which is $k_{GB} = 2DC_0/\epsilon R^2$, where R is the *initial* radii of the reactants. This is of course an oversimplification, since the material consists of non-spherical grains, as well as several different phases, but nonetheless shows how important it is to control the grain size when synthesizing skutterudites to speed up the time it takes to reach phase pure skutterudite. For example, a decrease in grain size by a factor of 10 will reduce the transformation time 100-fold.

The diffusion coefficient is related to the type of governing diffusion mechanism. Since several elements need to diffuse to form γ phase, the slowest diffusion species will control the transformation rate. In Paper 2, it was concluded that diffusion of the filler element is the most important factor determining the transformation time. This is based upon results when comparing synthesis of skutterudites with composition $Fi_{0.6}Co_2Fe_2Sb_{12}$ with Fi = In, Ca, Ce and Yb (Figure 4.2). After sintering and annealing, the Ca sample had an area fraction of 94.4% skutterudite phase, the Yb sample 87.5%, In sample 74.2% and the Ce sample 70.6% (Table 4.1). XRD refinements showed similar values. For the two latter, In contained only β as secondary phase, while the Ce sample also contained large amounts of $CeSb_2$. The reason In could not transform into γ is most probably due to too low In fill fraction to support formation of γ with high Fe-content [169]. Therefore, the main reason the Ce sample has a low amount of γ and a high amount of remnant $CeSb_2$ is due to slow diffusion of Ce in γ. Similarly, the Ca sample has the highest amount of γ due to fast diffusion of Ca compared to Yb and Ce, probably due to much smaller atomic radii.

4.1.5 Summary

The long term stability of a skutterudite depends on a homogenous material without secondary phases to avoid severe changes in thermoelectric properties during usage. To achieve such material in a fast and efficient way some general principles are given for the synthesis of skutterudites:

- The thermoelectric properties of skutterudite are highly dependent on phase purity. Even though smaller amounts of nanosized secondary phases have been shown to be beneficial, higher amounts of secondary phases greatly influence the thermoelectric properties negatively, especially the Seebeck coefficient.
- There exists an upper and lower limit to the fill fraction (y) of any $Fi_yCo_{4-x}Fe_xSb_{12}$ skutterudite, which depends on the Fe-content (x). Below or above this level, secondary phases sustain, regardless of annealing time.
- The kinetics of Skutterudite formation is diffusion-controlled and depends on two main parameters: The grain size and the diffusion coefficient. Small grains

and large diffusion coefficients result in shorter annealing times to reach phase pure skutterudite during synthesis.

- Main factors influencing the diffusion coefficient are the Fe-content and filler type. For example, Ce will diffuse much more slowly in skutterudites than Yb, which furthermore diffuses more slowly than Ca, resulting in longer annealing times for the former.
- The grain size is highly dependent on the synthesis route. Smaller grains can be achieved through, e.g. rapid solidification or ball milling.

It is important to state that the general principle of manufacturing homogenous and stable material is a very important aspect for any thermoelectric material. In cases where the durability of the material is set up against increased thermoelectric efficiency, a compromise should be sought, so that both of these requirements can be met.

4.2 Oxidation of skutterudites

The general theory of oxidation of both unfilled and filled skutterudites was given in section 3.3.5. In Paper 1 of this thesis, the oxidation kinetics of unfilled $CoSb_3$ was furthermore studied and confirmed the underlying theory and will therefore not be discussed further here. Instead, the oxidation kinetics of p-type skutterudites is of interest to investigate due to the very high oxidation rates. The samples presented in the previous section were therefore used to study oxidation mechanisms and kinetics and how they depend on filler element and secondary phases and will be discussed in the following paragraphs.

4.2.1 Experimental methods

Samples presented in section 4.1 with composition $Fi_{0.06}Co_2Fe_2Sb_{12}$, where Fi = In, Ca, Ce or Yb (all p-type), were used for oxidation experiments, In addition, two reference materials used in the thermal cycling experiments of Paper 5 were tested for comparison. The compositions of these are $In_{0.25}Co_4Sb_{12}$ (n-type) and $In_{0.25}Co_3FeSb_{12}$ (p-type).

Thermogravimetric Analysis (TGA) and Differential Scanning Caliometry (DSC), Mettler Toledo TGA/DSC 1, were used to measure the weight change and heat exchange with the environment during heating in laboratory air with flow 100ml/min. Experiments with a constant heating rate of 10°C/min between room temperature and 800°C as well as isothermal soaking in the range 400–450°C were performed. Scanning Electron Microscopy (SEM) and Energy Dispersive X-ray Spectroscopy (EDS) of type Zeiss Merlin were used to examine cross-sections of the oxidized samples.

4.2.2 Results

In Figure 4.9, the weight change (TG) and differential weight change (DTG) as a function of temperature at a constant heating rate of 10°C/min is shown for all the samples. From these curves, a large difference in terms of oxidation is clearly seen. The Ce sample is by far the most easily oxidized sample, with rapid oxidation starting at around 350°C; the In sample has the second highest oxidation rate, while the Yb and Ca sample have lower and similar oxidation rates. In comparison, the two reference samples have somewhat different TG and DTG curves. The p-type reference sample (P-ref) with lower Fe and In content than the In-sample, and without any secondary phases, have similar oxidation behavior as the Yb and Ca sample up to 600°C, after which the weight suddenly starts to decrease. The n-type reference samples (N-ref) with no Fe have the slowest oxidation.

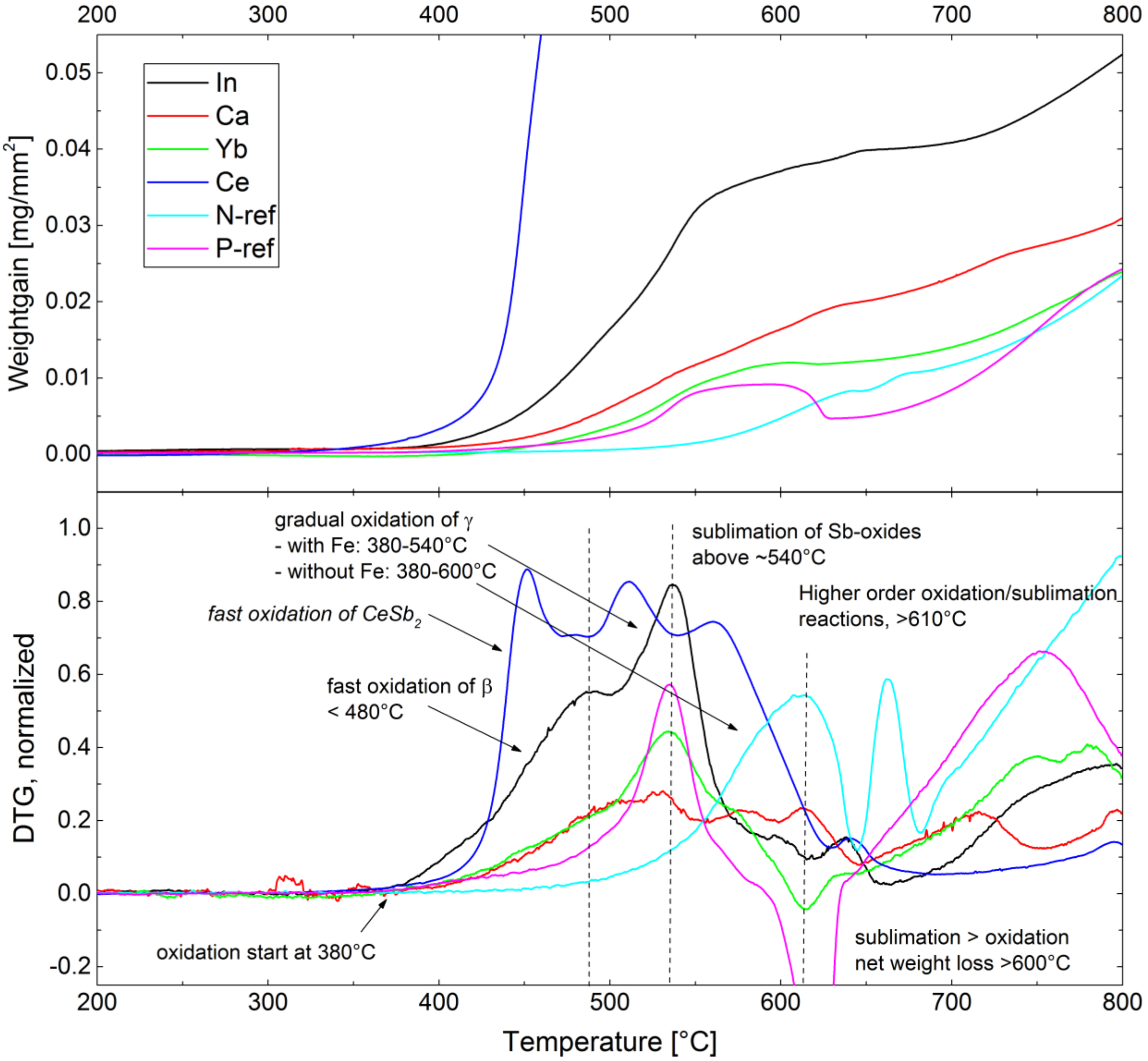

Figure 4.9 Weight gain (upper) and differential weight gain (DTG, lower) for constant heating rate of 10°C/min in air of bulk samples.

In Figure 4.10, the weight gain at isothermal oxidation at 450°C is shown for the same samples. The Ce sample has not been included, since its oxidation is so fast at this temperature that it cannot be used for any meaningful discussion of oxidation mechanism and rates. Not surprisingly, the In-sample shows much faster oxidation than any of the other samples, with near linear kinetics up to complete oxidation after around 6 hours. The Ca and Yb samples show similar oxidation rates with an initial period of linear growth and then transitioning into parabolic growth after 8 and 11 hours respectively. The P-ref also shows parabolic kinetics, but in two stages, where the first 3 hours is fast and then transitioning into much slower oxidation rate for the remaining oxidation time. Rather surprisingly, the N-ref sample has a limited period of parabolic growth during the first 6 hours before it transitions into a very rapid catastrophic oxidation regime. The kinetic rate fits well with a power law, $x = kt^n$, with n=3. Thus, after 24 hours the N-ref sample has oxidized the same amount as the Ca and Yb samples. The kinetic rate constants for all samples are found in Table 4.2.

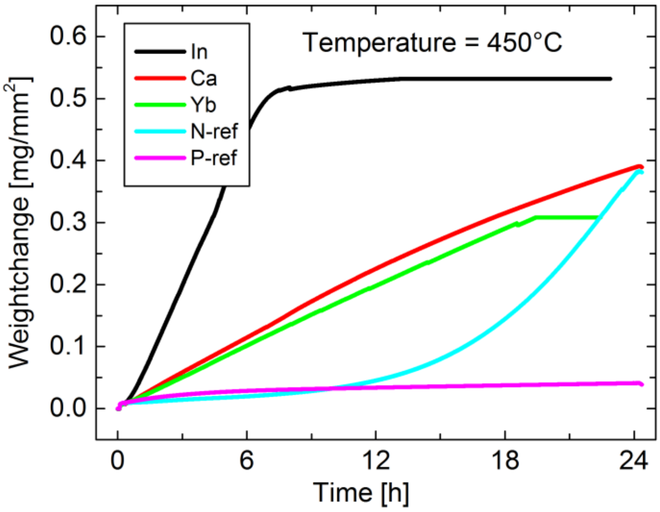

Figure 4.10 Weight gain per area of bulk samples at constant temperature during oxidation in air.

Table 4.2 Kinetic rate law and corresponding rate constant for isothermal oxidation at 450°C in air. For most of the samples, the oxidation is divided into different stages with rate laws. An oxide density of 5 mg/mm^3 was used to convert the units into oxide layer thickness according to equation (3.29). The values are only given for a single measurement and should only be used as indicating the relative difference between the samples.

Sample	**Time**	**Kinetic rate law**	**k_L [mg/(mm^{2}h)] / k_P [mg^2/(mm^{4}h)]**	**[µm/h] / [µm^2/h]**
In	1-6h	Linear (completely oxidized)	8.06E-02	92
Ca	1-8h	Linear	1.91E-02	22
	8-24h	Parabolic	1.30E-02	17001
Yb	1-11h	Linear	1.67E-02	19
	11-24h	Parabolic	1.43E-02	18650
N-ref	1-6h	Parabolic	5.01E-05	66
	6-24h	Power law, N=3 (catastrophic)	-	-
P-ref	1-3h	Parabolic stage 1	1.41E-04	185
	8-24h	Parabolic stage 2	2.41E-05	32

In Figure 4.11, the isothermal oxidation of N-ref and P-ref samples is shown for several temperatures between 400 and 450°C. Corresponding SEM images of the samples after 24h oxidation is found in Figure 4.12 and Figure 4.14. Oxide thickness is furthermore estimated by employing equation (3.29) and assuming an oxide of composition $CoSb_2O_4$ and density of 5g/cm^3.[8]

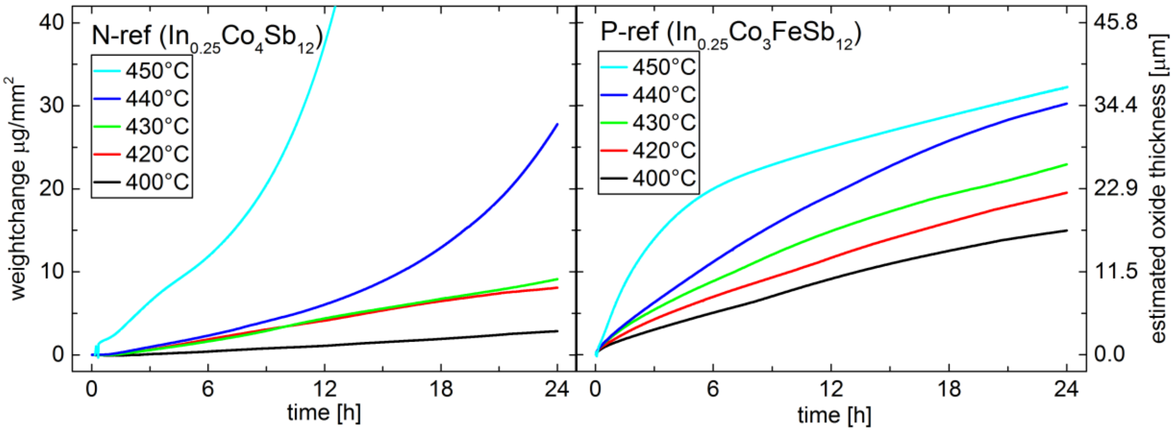

Figure 4.11 Isothermal TG measurement at different temperatures over 24h for the N-ref and P-ref samples.

The N-ref sample shows near linear kinetics at temperatures between 400 and 430°C. But at higher temperatures it will, after an initial period of steady weight gain, transition into breakaway oxidation. This is also reflected in the SEM images in Figure 4.12 and Figure 4.13, which shows clear signs of large crack formation inside and under the oxide layer, especially at the corners. From EDS measurements it is found that the oxide layer contains only one layer of $CoSb_2O_4$. No layers of $CoSb_2O_6$ or Sb_2O_3 are seen at these relatively low temperatures, in contrast to Figure 3.11.

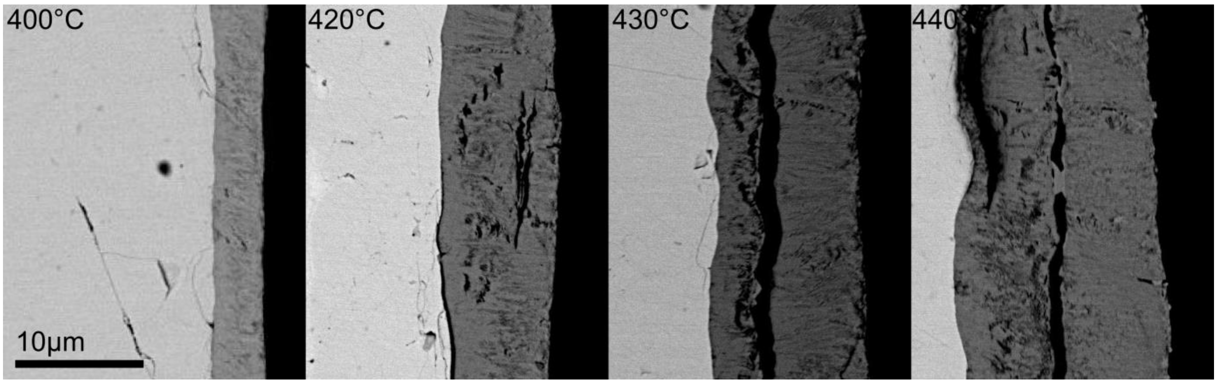

Figure 4.12 SEM images of N-ref samples after 24 hours oxidation in air at indicated temperatures.

---

[8] The theoretical density of $CoSb_2O_4$ and $Fesb_2O_4$ is 5.7g/cm^3 and 5.53 g/cm^3 respectively [170, 171]. A density of 5g/cm^3 is used, since some porosity is seen for the oxide layers, and is found to fit well when comparing weight change with thickness measurements in SEM. Since the molar mass and density of these two oxides are so similar, the same conversion factor is used for both.

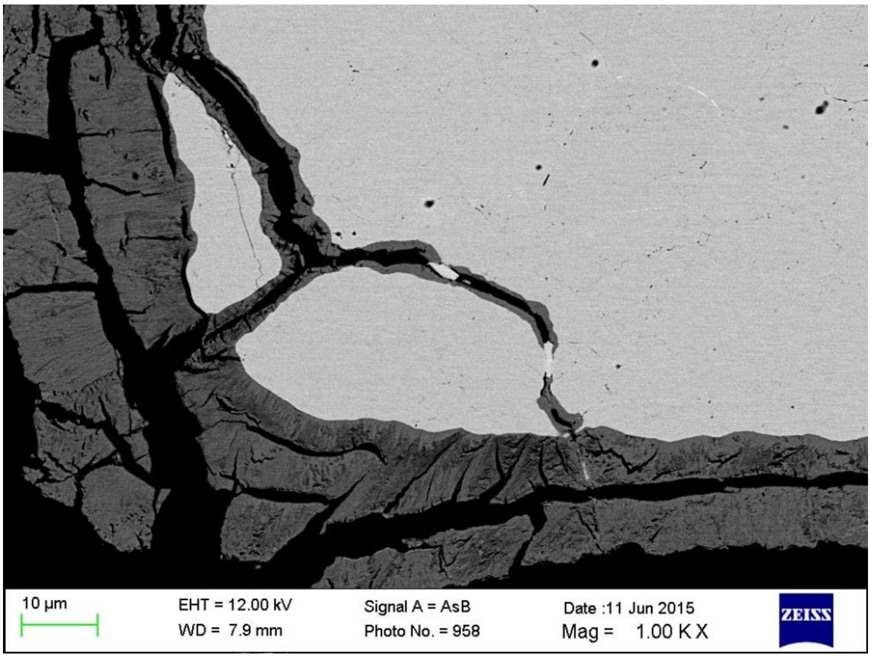

Figure 4.13 SEM images showing cracks in oxide layer and through grain boundaries in the skutterudite after oxidation of N-ref sample at 430°C for 24h in air.

In contrast to the N-ref sample, the P-ref sample has a higher initial oxidation rate, but never enters a breakaway regime at any temperature. Instead, the weight gain seems to stabilize and slow down at 450°C compared to lower temperatures. A closer look at the SEM images in Figure 4.14 shows formation of an intermediate InSb layer of a few microns at 450°C. Also at 440°C this layer is identified with SEM and EDS, however much thinner. According to EDS analysis, the oxide layer has an approximate composition of $Co_{0.75}Fe_{0.25}Sb_2O_4$.

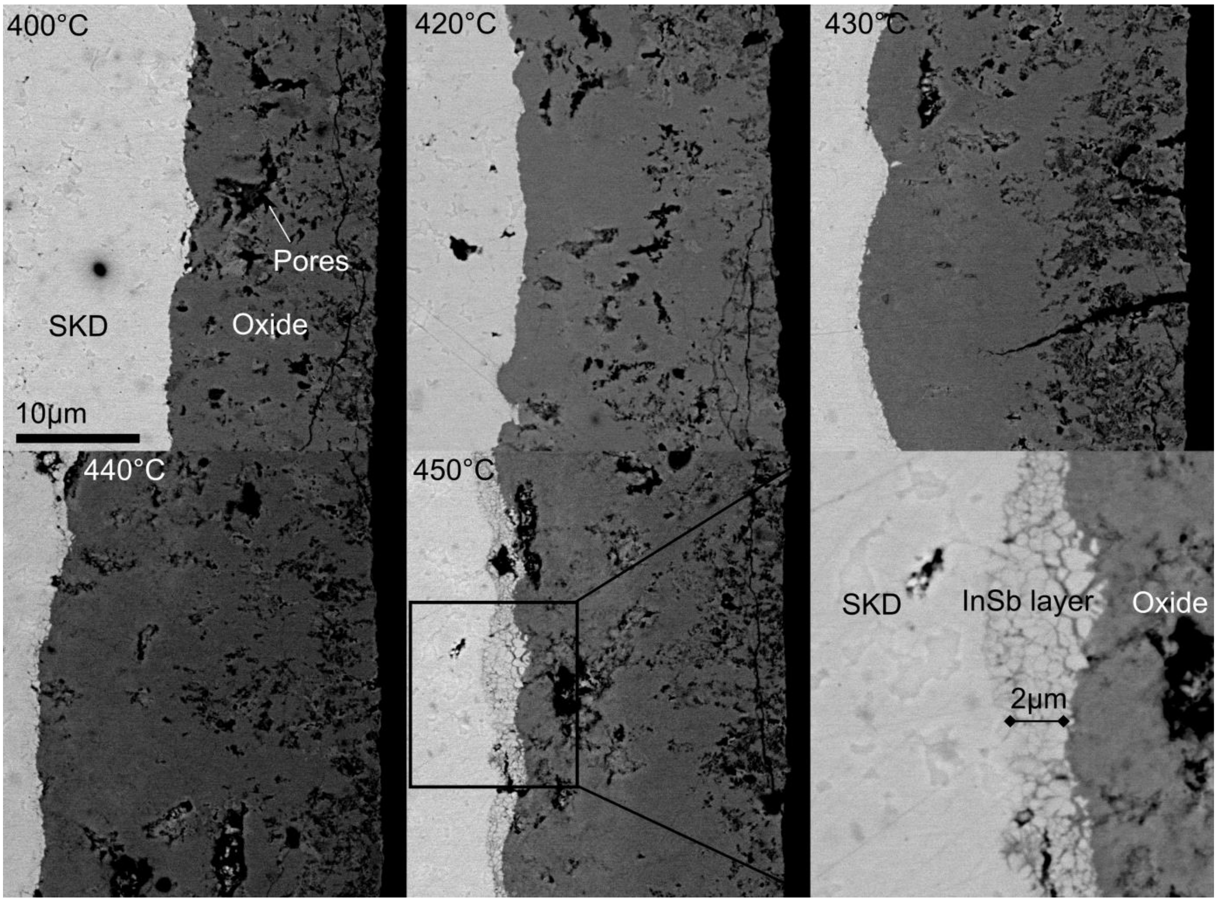

Figure 4.14 SEM images of P-ref samples after 24h oxidation in air at indicated temperatures.

4.2.3 Effect of filler element and microstructure

From the TG and DTG curves in Figure 4.9, several peaks are found, each of which represents changes in the oxidation rate due to gradual changes in dominating oxidation reactions at different temperatures. Especially the peaks at around 480°C, 540°C and 610°C are of interest, since they are common to most of the samples. With the knowledge of difference in microstructure, secondary phases and filler elements and amount between the samples, these peaks can be interpreted as representing oxidation of different phases. The temperatures themselves are on the other hand not representative for the temperatures at which these reactions really start, since these measurements are carried out under a constant heating rate and therefore never reach thermal equilibrium.

The Ce-sample shows several peaks at temperatures between 400 and 600°C that are not found for any of the other samples and can thus be interpreted as oxidation of the $CeSb_2$ phase found in large amounts (see Figure 4.2 and Table 4.1). The peak at 480°C is most clearly seen for the In-sample, but a “shoulder” is also seen for the Ca and Yb-samples, while the two reference samples do not show any increase in oxidation rate around this temperature. Since the In-sample contained by far the most remnant β-phase ($Co_{1-x}Fe_xSb_2$), while the Ca and Yb-samples only contained very small amounts and the reference sample none, this peak is found to represent the initial and rapid oxidation of β.

All samples except the N-ref show a peak in the DTG-curve at around 540°C. This is most likely linked to the oxidation of the skutterudite phase containing Fe, since the N-ref sample without Fe does not show any peak at this temperature, but instead at around 610°C. The same effect is also found in literature presented in section 3.3.5, where p-type skutterudites containing Fe typically undergo rapid oxidation starting at lower temperatures than the n-type skutterudites without any Fe. This has been attributed by various authors to formation of amorphous, non-protective, Fe-oxides at these temperatures [143].

At 610°C, also some samples show a downward peak, most clearly for the P-ref sample, which even has large net weight losses at this temperature. Sublimation of Sb_2O_3 is known to occur at temperatures above 450°C and increase rapidly with increasing temperature [172]. Net weight loss was observed in Paper 1 for isothermal oxidation of $CoSb_3$ above 600°C due to higher sublimation than oxidation rate. This effect is most likely the reason for the downward peaks in the DTG curve in Figure 4.9.

At an even higher temperature, the oxidation mechanisms now become very complex and hard to analyze without any complementary experimental work on oxidation states and phases of the oxidation products. This is also a much higher temperature than typical application temperatures for skutterudites and will therefore not be treated further here. Instead, a more careful look at the oxidation kinetics at intermediate temperatures shown in Figure 4.10, Figure 4.11 and Table 4.2 is of interest. The kinetic rate not only gives information about the oxidation kinetics but also the governing oxidation mechanism, as discussed in section 3.3.2.

Linear kinetics

Linear kinetics, which is seen for several of the samples, indicates that the rate-controlling step is reaction at the respective interfaces, i.e. the oxide layers are non-protective and O_2 transport to “fresh” interfaces is fast. The linear oxidation rate found for the initial stage of Ca and Yb sample is much lower than that of the In sample and is most likely linked to the high amount of the secondary β-phase in the In sample. A net weight gain during this period of 0.2mg/mm^2 corresponds to an oxide thickness of approximately 200µm. It is thus obvious that the β-phase is highly unbeneficial, as it leads to formation of porous, non-protective oxide layers. Combined with the results shown in Figure 4.9 at a constant heating rate, this clearly shows how important it is to avoid secondary phases, most prominently $CeSb_2$ and β, so that the oxidation resistance of the skutterudite is not severely reduced.

It is furthermore likely that the linear regime indicates growth of thin layers, which quickly crack and spall off due to stress build-up as a result of large differences in volume of the samples and the growing oxide layer, which has been observed for oxidation of skutterudites with composition $Yb_yCo_4Sb_{12}$ [144]. This is exactly what is observed for the N-ref sample in Figure 4.12. The N-ref sample shows very low oxidation rates between 400°C and 430°C. At first glance, the kinetics seems linear, but a closer look reveals that the linear curves are comprised of two or more parabolic regimes as seen exemplified in Figure 4.15. From the SEM images, a dense oxide layer of approximately 3µm is observed at 400°C, and similarly roughly 7µm at 420°C, which would indicate diffusion-controlled oxidation leading to parabolic kinetics. However, at 430°C and 440°C, the oxide layer is seen divided by a large crack with an outer layer of around 7µm. This type of parabolic growth, crack formation and growth of a new layer will in the long-term lead to near linear growth, which is also what we observe for all the N-ref samples initially. Estimations of the thickness based on weight change, as shown in the right axis in Figure 4.15, shows a change in rate at roughly 4.6µm, which is lower than the observed thickness in SEM of the outer cracked-off oxide layer. Nevertheless, considering irregularities in oxide thickness around the sample, along with corner effects, the combination of SEM and weight change show very much the same effect and explain well the overall linear kinetic rate.

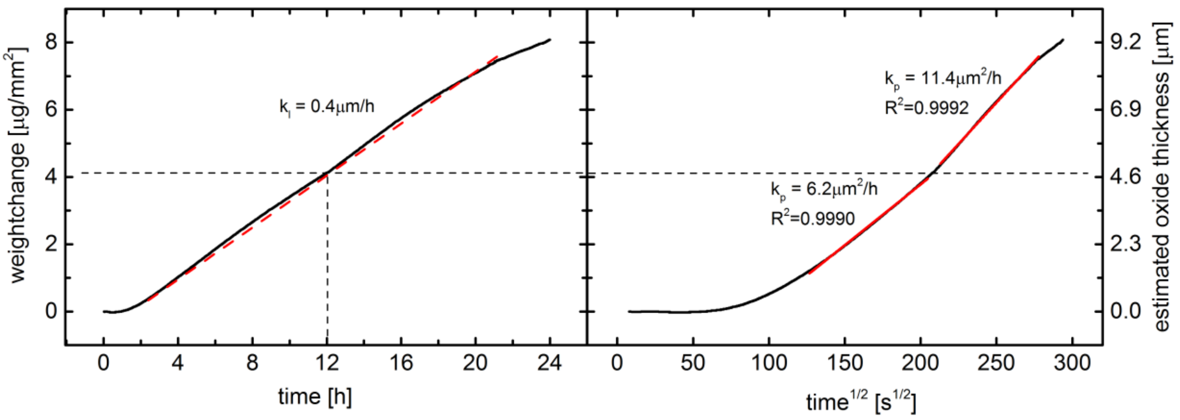

Figure 4.15 Weight change and estimated oxide thickness of N-ref sample isothermally oxidized in air at 420°C. The left graph shows that the near linear weight increase in fact consists of two parabolic weight gains as evident from the right graph where the same weight change is plotted against the square root of time.

The oxidation kinetics of the samples oxidized at 440°C and 450°C transitions into catastrophic oxidation after a certain amount of time, as already discussed. This is in part due to very strong corner effects, of which an example is readily seen in Figure 4.13. Crack-formation due to stress build-up, especially at the corners, leads to rapid oxidation. Furthermore, oxidation in cracks forming along grain boundaries is found to strongly influence the oxidation mechanism of the N-ref samples at temperatures above 430°C. This is a good example formation of cohesive stresses between grains as discussed in section 3.4, resulting in a material prone to thermo-mechanical failure and thus also even faster oxidation. It is likely that this effect also could be seen at lower temperatures over longer exposure times, since the oxide thickness will eventually reach a critical thickness of spallation of approximately 5-7µm. Comparing these results with literature data of unfilled $CoSb_3$ with very much slower parabolic kinetics, In-filling seems to have a highly unbeneficial effect on oxidation resistance. However, the large crack formation, especially at the corners following grain boundaries could also be linked to the synthesis method and to unsatisfactory sintering. The same crack-formation at corners can also clearly be identified in the thermal cycling experiments in Paper 5 after prolonged exposure to air at high temperature.

Parabolic kinetics

In contrast to linear growth, parabolic kinetics is a result of oxidation limited by diffusion through the growing dense oxide layer. This has been found to be the governing oxidation mechanism for most skutterudites of both n- and p-types (see section 3.3.5). Comparing the values of the parabolic rate constant with literature values of similar compounds and temperatures (Table 4.2), we see that the Ca (17000 µm^2/h) and Yb (18650 µm^2/h) samples lie higher than the literature data of both $In_{0.25}Co_3FeSb_{12}$ (~3000 µm^2/h) [141] and $Ce_{0.9}Fe_3CoSb_{12}$ (~2000 µm^2/h) [143]. Furthermore, the P-ref sample with the same nominal composition as [141] has a significantly lower rate constant of around 32 µm^2/h after the initial stage, but still several orders of magnitude higher than for unfilled $CoSb_3$ (around 0.04 µm^2/h at 450°C).[9]

The main factor governing the parabolic rate constant is the diffusion coefficient of the governing diffusing species through the layer(s). For skutterudites, at temperatures around 450°C, the main oxide layer is *schafarzikite*, with the chemical formula $CoSb_2O_4$, $FeSb_2O_4$ or a solid solution of the two, $Co_{1-x}Fe_xSb_2O_4$ [173]. In $CoSb_2O_4$ the main diffusing species is found to be inward diffusion of O^{2-} [52], and this is most likely the case also for the Fe-containing oxides. In this respect, Fe could potentially affect the oxidation rates in two ways: either increasing the O^{2-} diffusivity, for example by increasing the oxygen vacancy concentration, since Fe has a lower valence than Co (Valency rule, see section 3.3.3) or by forming secondary non-protective Fe-oxides with much higher diffusivities of O^{2-} or even O_2 molecules, which has also been reported by other authors [139, 142, 143].

The P-ref sample has parabolic kinetics. Formation of an intermediate InSb layer at temperatures above 440°C seems to strongly influence the kinetics, and is clearly responsible for the slow growth of the oxide layer. The existence of two parabolic regimes at 450°C (see Table 4.2) could be caused first by fast formation of the outer oxide layer until a dense InSb layer has formed, and then slower growth limited by diffusion through the InSb layer. From this we can conclude that diffusion through the InSb layer is rate controlling, which was also found by Park et al. for the same nominal composition, $In_{0.25}Co_3FeSb_{12}$ [141], however at much higher temperatures (550°C). At 450°C the P-ref sample shows two orders of magnitude lower parabolic rate constant (32µm^2/h) than for Park et al. (~3000µm^2/h), due to no formation of the rather protective InSb in the latter case. Why formation of the thin intermediate InSb-layer is observed in this work at as low temperatures as 440°C, while Park et al. only observed them at much higher temperatures, cannot be fully understood by these experiments alone, but is likely linked to synthesis methods, or small differences in actual composition or non-stoichiometry.

---

[9] Estimated from a parabolic rate constant of 0.33 µm^2/h at 500°C and an activation energy of 197 kJ/mol [138].

Another peculiar observation is that this InSb-layer in not found in the N-ref sample, with nominal composition $In_{0.25}Co_4Sb_{12}$. Since the only difference between P-ref and N-ref is the Fe-content of the P-ref sample, it is likely that this is the main reason for the protective behavior of the P-ref samples, compared to the breakaway behavior of the N-ref sample. In other words, the mechanism of the InSb layer formation is linked to the Fe-content of the skutterudite. Further investigations are needed to establish the underlying mechanisms of this effect.

The In-sample with composition $In_{0.6}Co_2Fe_2Sb_{12}$ contained high amounts of secondary phases that with its high and heterogeneous oxidation rates, prevented formation of any protective InSb-layer. However, there is reason to believe that a phase pure sample with higher Fe and In-content than the P-ref sample also would form an InSb "diffusion barrier", which would be highly beneficial for the oxidation resistance of the skutterudite. Whether the other filler-elements could form similar protective layers can unfortunately not be decided by this work, due to the unbeneficial effect of secondary phases upon oxidation, but would be very interesting to investigate further in future work.

4.2.4 Summary

From these measurements, it can be concluded that the parameters that affect the oxidation rate of p-type, Fe-containing skutterudite the most are first and foremost the amount and type of secondary phases. A content of a few percent of is enough to cause the material to show very high linear oxidation rates at relatively low temperatures (450°C). Furthermore, p-type skutterudite with high Fe-content shows much higher oxidation rates at much lower temperatures than unfilled skutterudite, $CoSb_3$. Also, In-filling in n-type skutterudite without any Fe has highly unbeneficial effects on the oxidation resistance, causing crack-formation and spallation of the oxide layers, especially at the corners. However, in combination with Fe, In can form intermediate layers of InSb, which seems to slow down oxidation significantly, leading to relatively low oxidation rates. It could therefore be possible that the right combination of filler elements and Fe-content could be used to optimize the skutterudite also for oxidation resistance, in addition to thermoelectric and mechanical properties. In the end, the oxidation of skutterudites should be limited as much as possible, to ensure stable performance of the thermoelectric device over time. This will be one of the topics of Sections 4.4 and 4.5.

4.3 Oxidation of $Mg_2(Si-Sn)$

In contrast to the extensive literature that exists on oxidation of skutterudites, little work has been done on the oxidation of silicide-based thermoelectric materials. Silicides generally have very good resistance towards oxidation due to formation of a protective layer of SiO_2 [174, 175]. An example is the good p-type thermoelectric material made of higher manganese silicide (HMS) that shows excellent protective behavior against oxidation [58]. In contrast, Mg_2Si shows much more severe oxidation and at high enough temperatures will ignite, and burning-like behavior is seen, much like other high Mg-containing alloys [175, 176].

The best silicide-based thermoelectric materials to date are those based on a solid solution of Mg_2Si and Mg_2Sn forming $Mg_2Si_{1-x}Sn_x$ compounds, and zT values of 1.4 have been reached [55]. However, the addition of Sn will also affect the high temperature stability. Early experiments on material made within the ThermoMag project are presented in Paper 1 of this thesis and show how already at temperatures as low as 400°C, $Mg_2Si_{0.4}Sn_{0.6}$ will oxidize severely.

The zT of $Mg_2Si_{1-x}Sn_x$ with three different Sn contents is presented in Figure 4.16. The synthesis and thermoelectric characterization of these materials were perfomed at the Ioffe Institute (St. Petersburg, Russia) and details can be found elsewhere [177]. It is clearly seen from the figure that the average zT drastically increases with increasing Sn-content. The question is now: how will the Sn-content affect the resistance towards oxidation? In other words, is there a need for a compromise between efficiency and thermal durability?

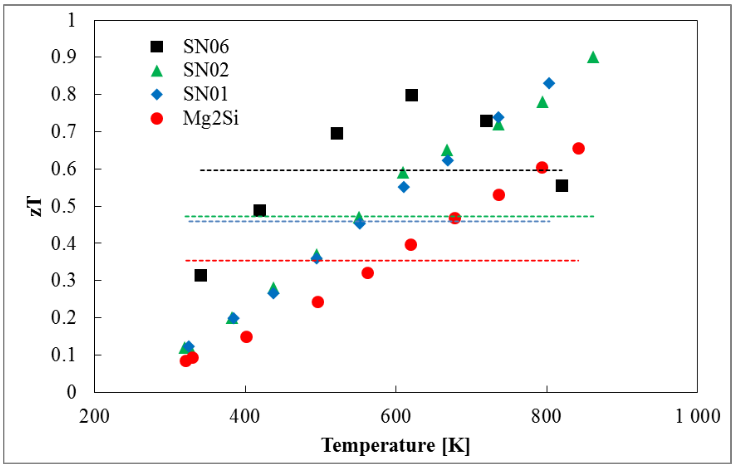

Figure 4.16 zT values of thermoelectric material for different Sn-content of Mg2Si1-xSnx. The dotted lines show the average zT value in the whole temperature range. Courtesy of Ioffe Institute.

Paper 4 thoroughly examines the effects of Sn on the oxidation rate in addition to proposing a more general scheme for oxidation mechanisms of Mg_2(Si-Sn) material. The main findings of this work are:

- At x>0.1, $Mg_2Si_{1-x}Sn_x$ is a two-phase material with Sn-rich and Si-rich phases
- Initially, a thin MgO layer quickly builds up at the surface of the $Mg_2Si_{1-x}Sn_x$, protecting it from further oxidation at lower temperatures
- Above a critical temperature (ignition temperature), the oxidation of the material will eventually enter a breakaway regime, with very rapid, exothermic oxidation
- The ignition temperature is higher for lower Sn-content (see Figure 4.17(b))
- The main mechanism affecting the transition from protective to breakaway regime is the decomposition of Sn-rich $Mg_2Si_{1-x}Sn_x$ forming liquid Sn underneath the oxide layer
- In addition, the Pilling-Bedworth is below 1 for Sn-content above 0.4, which results in porous, non-protective oxide layers (see Figure 4.17(a))

It was thus concluded that Sn-content greatly influences the temperatures at which Mg_2(Si-Sn) can be used in oxidizing atmospheres without protection. It also gives valuable insights into the basic mechanisms governing oxidation that can also be useful during synthesis, especially when employing these materials in large-scale mass production facilities. In this case, the production complexity should be as low as possible to keep production costs down. Therefore, the environmental conditions (temperatures and atmosphere) should be controlled according to the results given in Paper 4.

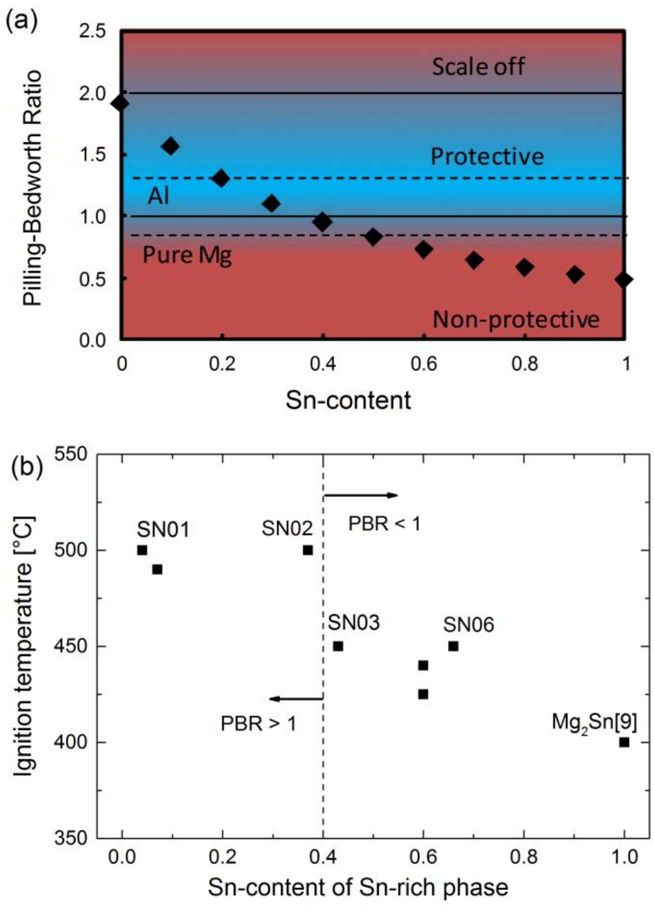

Figure 4.17 (a) Pilling Bedworth Ratio (PBR) of MgO on Mg2Si1-xSnx for different Sn-content, x. (b) Ignition temperature for different samples for different Sn-content of the Sn-rich phase (SN01 equals x = 0.1 etc.). A higher Sn-content yields lower ignition temperatures.

4.4 Protection from oxidation

As is evident from the two preceding sections, protection from oxidation is of uttermost importance to realize thermoelectric devices at medium to high temperatures. There exist only a few thermoelectric materials that can work satisfactorily alone in an oxidizing environment at high temperatures, such as oxides and some silicides, but also for these materials, the hot side interconnects can be prone to oxidation, and they also have significantly lower zT than, e.g. skutterudites. Work has therefore been carried out as part of this thesis to try to investigate and test some promising coating alternatives on skutterudite and magnesium silicide thermoelectric material. The experiments have been conducted on single thermoelectric legs of both silicides and skutterudites (Papers 1 and 5).

4.4.1 Coating tests on single legs

In Paper 1, several different commercially available coating alternatives were tested, but only one was found that showed promising capabilities of protecting from oxidation. This consisted of micron-sized aluminum flakes suspended in an organic slurry with small amounts of silica. Upon exposure to high temperature in air (>500°C), the thin aluminum flakes quickly oxidized forming alumina, Al_2O_3, and sintered together on the surface of the thermoelectric material, forming a non-porous, protective layer of 5 – 10 µm thickness or more. A sample of coated undoped skutterudite, $CoSb_3$, thermally cycled 180 times between 150°C to 600°C (holding for 1 hour) in air, showed almost no sign of oxidation (see Figure 4.18), while uncoated sample annealing at 550°C for 24 hours formed a thick oxide layer of more than 10 µm.

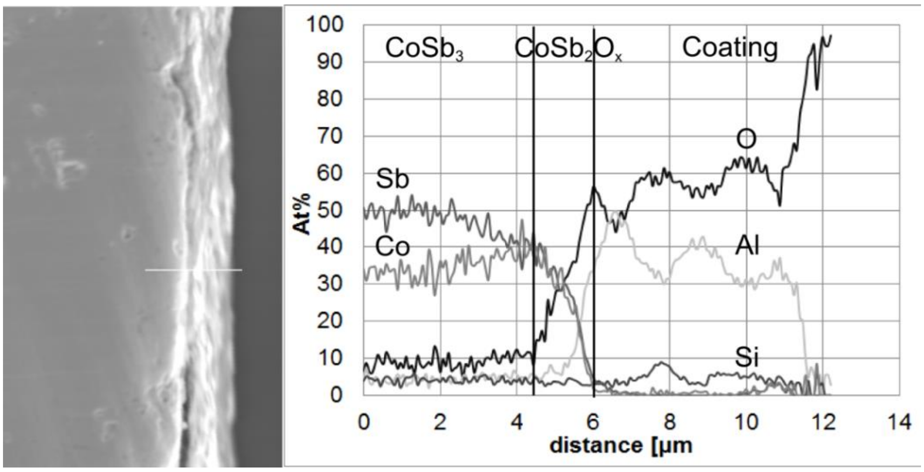

Figure 4.18 Cross section of undoped skutterudite, $CoSb_3$, coated with Al-coating after 180 cycles up to 600°C in air.

4.4.2 Effect of coating on thermoelectric performance

If coatings are going to be implemented on the surface of thermoelectric legs in a real thermoelectric device, it will need to sustain many rapid temperature variations. Both diffusion processes mechanical strain due to mismatch in CTE can cause the coating to break down after a certain amount of time. A new test method presented in Paper 5 was used to assess the performance of the Al-based coating over time. The electric performance of single legs, both coated and uncoated, where measured continuously during thermal cycling. An example is found in Figure 4.19, where the coated leg 1 shows much smaller increase in inner resistance over time compared with the other uncoated legs. However, also for the coated leg an increase in resistance was seen due to oxidation and post characterization showed how also for this leg oxygen had penetrated in between electrode and coating near the hot side forming a thin oxide layer near the edge of the leg. Work is currently ongoing for optimizing coating and developing a method for applying it on thermoelectric modules.

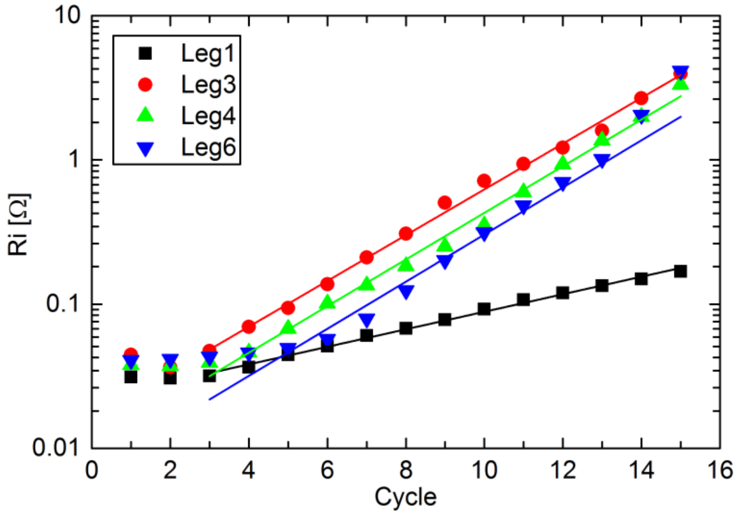

Figure 4.19 Inner resistance (logarithmic scale) of a single skutterudite leg and nickel electrode during thermal cycles between 150 and 500°C. Leg 1 is coated and shows relatively much lower increase in resistance than the other uncoated legs.

The most critical aspect of the coating, aside from its protective capabilities, is its simplicity to apply in a mass production industrial process. In this regard, a slurry based coating such as this have many benefits. Many other promising coating types have been developed, as mentioned in section 2.3.2, however all of these requires relatively complex production methods. It is thus believed that further development of such Al-based slurry coating (or other slurry based coatings) is important for implementation of new thermoelectric materials at medium to high temperature applications.

4.5 Degradation vs performance

There exist numerous ways to express the performance of a thermoelectric device, depending on both thermoelectric properties, and properties of the thermal and electrical contacts and interfaces [24, 89, 178]. In the following discussion, it is chosen to look only at the maximum power output of a module with set dimensions, which is given by the simple equation (2.15), repeated here for convenience: $P_{max} = V_{OC}^2/4R_i$. The thermal properties of the device are at first glance not considered here. However, since V_{OC} is dependent on the temperature difference over the thermoelectric material, an increase in the total thermal resistance (or impedance) of the interface materials, or a reduction in thermal resistance of the thermoelectric material, will result in a reduction in V_{OC} thereby reducing the maximum power and consequently the efficiency. Since V_{OC} and R_i are straightforward to measure in all practical purposes, it is therefore of interest to see how V_{OC} and R_i change during operation.

Any observed changes in V_{OC} or R_i can be linked to physical degradation processes within the device (as long as external fluctuations in heat supply and electric load can be accounted for). This means that it should be possible to determine the mechanisms that are causing the observed changes in electrical properties of the material or device over time. This type of failure mode – failure mechanism investigations is commonly found in the electronics industry and used in optimizing device reliability and durability [179]. It gives valuable input when we evaluate our device design concept. Is it the metallization that fails? Is it a result of changes in the thermoelectric material itself? Or can it be influenced by reaction with the environment, such as oxidation or sublimation? Papers 4 and 5 present performance studies of modules based on silicides and a novel test method for testing thermometric functionalized legs respectively. A detailed description of the apparatus can be found in Appendix II. The results from these studies will be included in the following discussion.

Figure 4.20 lists some typical degradation processes (failure mechanisms) and how they could possibly affect the electrical characteristics of the device (failure modes). Since a thermoelectric device works without any moving parts, the degradation processes are mostly limited to solid-state mechanisms such as diffusion and mechanical failure. These processes are again all thermally activated, either through thermo-mechanical stresses (due to thermal expansion) or through Arrhenius-like temperature dependencies (diffusion). Understanding the fundamental processes related to degradation is crucial to optimizing device durability. In the following, the relationship between the temperature activated degradation processes introduced in Chapter 3 and the performance of the device given by V_{OC} and R_i is discussed.

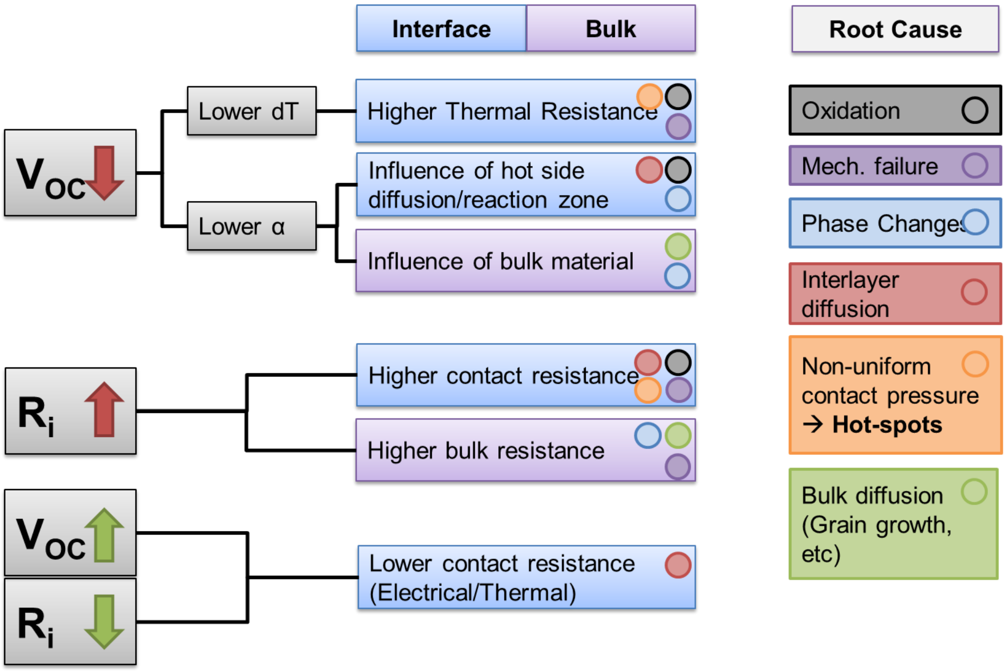

Figure 4.20 Possible root causes for the observed changes in V_{OC} and R_i during thermal cycling in air.

4.5.1 Reduction in V_{OC}

Equation (2.8) shows that a reduction in V_{OC} is either due to a lower temperature difference (ΔT) over the thermoelectric material, or a result of changes in the Seebeck coefficient (α) *within* the thermoelectric material. An example on how the V_{OC} changes with thermal cycles is found in Figure 4.21 (from Paper 5, see Appendix II for more details).

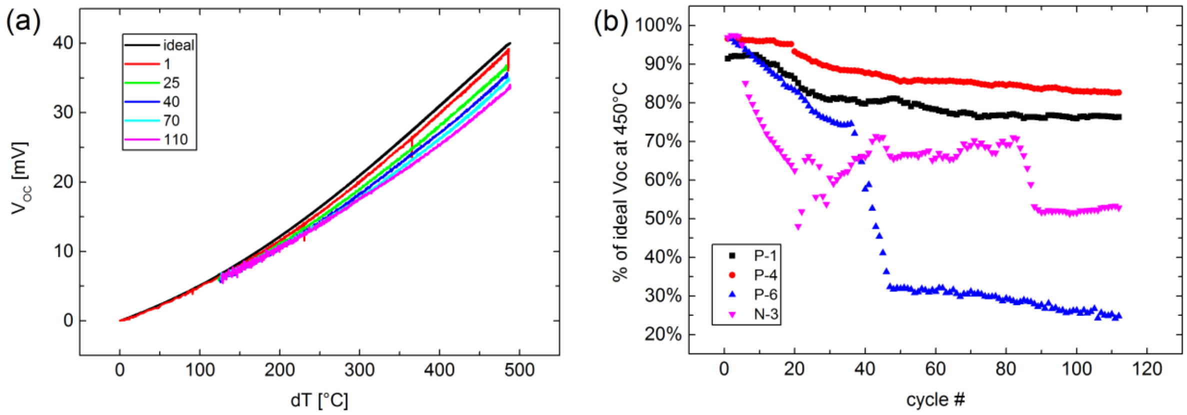

Figure 4.21 (a) V_{OC} of a skutterudite thermoelectric leg as a function of temperature difference at different cycles. (b) Relative change in V_{OC} compared to ideal conditions (calculated from equation (2.8)) during thermal cycling up to hot side temperature of 500°C

of four different functionalized thermoelectric legs (three p-type and one n-type, see Paper 5 for more details).

Thermal conductivity

The total thermal conductance of a thermoelectric module was given in equation (2.11). A lowering of ΔT over the thermoelectric material is either caused by an increase in thermal conductivity of the thermoelectric material (κ), or due to a reduction in the interface thermal conductance (increase in thermal contact resistance).

The thermal conductivity is a sum of the electronic (κ_{el}) and the lattice (κ_{ph}) part (see section 2.2.1). An increase in κ_{el} is caused by an increase in charge carrier density and/or mobility. Diffusion and segregation of dopants or other lattice defects will cause changes in these properties and thus lead to a change in κ_{el}. An increase in κ_{ph} is influenced by factors such as grain size and boundaries, (nano)precipitates and phase changes, which can all change significantly with increased temperatures. Any conclusive effect of high temperatures on thermal conductivity cannot be given here, since this will depend to a large degree on the material in question and the stability of this over time. Both an increase and decrease in thermal conductivity is possible. Nevertheless, as long as the thermoelectric material is relatively homogenous and stable at the running hot-side temperatures, other contributions to the total thermal conductance on the thermoelectric device are much higher.

Thermal Contact Resistance

In a real thermoelectric device, the influence of interface thermal resistivity can be significant [180, 181]. As shown in Paper 4, a thermal contact resistance of 0.1 cm^2K/W for a heat flux of 50W and cross sectional area of thermoelectric material of $1cm^2$means a temperature drop of 5K over the interface, clearly affecting V_{OC}.

Most of the degradation processes leading to an increase in thermal interface resistance will however have even more pronounced impact on the electric contact resistance. One typical example is the formation of oxide layers as exemplified in Figure 4.22 on the hot side of skutterudite legs thermally cycled in air. Oxides have thermal conductivities in the order of 1 to 10 W/(m K), which is in the same range as good thermoelectric materials (2-3 W/(m K)), and one or two orders of magnitude lower than most metals (~100 W/(m K)). The electrical conductivity on the other hand, is in most cases many orders of magnitude lower for oxides than for both thermoelectric materials and metals. A growing layer of oxygen will thus affect the inner electric resistance of the module much more than the open circuit voltage.

Another example is void and crack formation near the interface. This can either be due to interdiffusion (Kirkendall Effect, section 3.1.3), or thermo-mechanical stresses causing lateral crack formation, as seen in Paper 4. In contrast to diffusion phenomena such as oxidation, crack propagation happens fast and will lead to abrupt changes in the contact resistance. Instead of a gradual decrease in V_{OC} we will see this as a much steeper decrease over a short time period. However, also this will affect the electrical contact resistance much more than the thermal contact resistance.

In the tests carried out in this thesis, the effect of interface thermal resistance was found to be one of the highest contributions to changes in V_{OC} during performance testing. Both oxidation (skutterudite) and weak mechanical bonds and crack formation ($Mg_2(Si\text{-}Sn)$) were found to have substantial negative effects resulting in a significant reduction in V_{OC}.

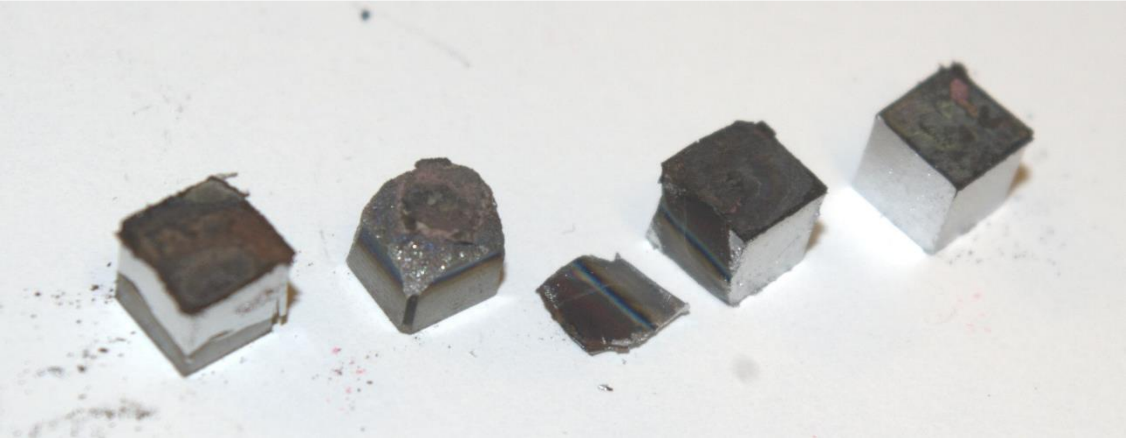

Figure 4.22 Skutterudite leg s after thermal cycling in air up to 500°C on the hot side. The coated sample (right) is seen to have little damage to the top side, while the uncoated sample (2nd from left) shows clear signs of oxidation and spallation near the edges.

Seebeck coefficient

Finally, a decrease in V_{OC} can be caused by a change in the Seebeck coefficient, either by formation of new phases such as intermetallic compounds (IMC) forming between metallization and thermoelectric leg, or changes in the thermoelectric material itself. In the first case, these layers tend to be so thin that the temperature gradient over them is equally small and therefore does not contribute any significant amount to the total V_{OC}, at least compared to any effect of thermal or electrical contact resistance. However, if no adequate diffusion barrier is used and atoms from the metallization or electrode are allowed to diffuse into the thermoelectric material, the Seebeck coefficient can change dramatically. This was clearly observed in Paper 5 by using PSM to measure the spatial variation of the Seebeck coefficient (at room temperature) over the cross section of a thermally cycled sample. An example is shown in Figure 4.23(a) of leg 1 from run 2 (see reduction in V_{OC} in Figure 4.21) where copper from the electrodes diffuses through both the Ag and Ti metallization layers and several hundred µm into the thermoelectric leg. The Seebeck coefficient decreases from an initial value of around 50 µV/K to near metallic value between 4 and 30 µV/K due to formation of Cu_2Sb phases in pores in the original material. This is also seen in the SEM images in Figure 4.23(b), although only the uppermost region is clearly identified here. Very high diffusivities of Cu is also seen in typical IC-materials such as silicon and silicon dioxide and is a “lifetime killer” [182]. Clearly, much better diffusion barriers are needed for hindering Cu-diffusion at these high temperatures (450-500°C). Alternatively, other electrode materials with lower diffusion rates need to be used, such as Nickel (Paper 5) or Molybdenum (Paper 4).

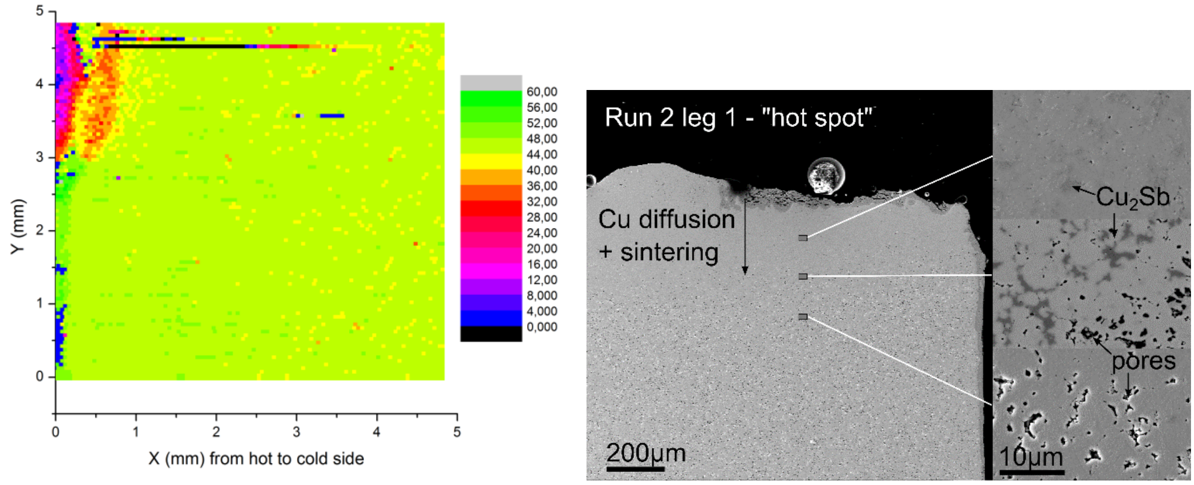

Figure 4.23 (a) PSM map of leg1 from run 2 (Paper 5) showing a large reduction in Seebeck coefficient near the hot side. (b) SEM images of the upper affected corner in (a), showing diffusion of Cu into the skutterudite, forming Cu_2Sb in pores.

In addition to the diffusion of metallic atoms into the thermoelectric material, some diffusion and segregation of atoms within the thermoelectric material itself is possible. The driving force of diffusion can be of different origins. Even though the concentration gradient over the material is the same initially, sublimation or interlayer diffusion near the hot side can give rise to concentration gradients causing substantial diffusion. In addition, the temperature and electric field gradient can also act as driving forces for diffusion, as discussed in sections 3.2.4 and 3.2.5, termed thermomigration and electromigration respectively. Even though there exists limited observation of the effect of these phenomena in thermoelectric systems, they could play a role, especially at high temperatures with temperature gradients close to 1000 °C/cm or current densities of more than 1000 A/cm^2.

In Paper 5, a gradient in the Seebeck coefficient is seen between the hot and cold sides of the skutterudite legs after thermal cycles (dT = 900K/cm). The Seebeck coefficient increases with a few percent towards the hot side, except very close to the hot side where it is substantially lower again. Clearly, changes in the charge carrier density are also found several millimeters into the material, not only near the hot side, which furthermore indicates temperature-dependent diffusion processes also *within* the bulk material. Since these tests were done in open circuit (no current flowing), electromigration can be excluded. The effect closest to the hot side is linked to In and Fe diffusion towards the interface, in addition to accumulation near pores as clearly identified in EPMA measurements. However, at distances more than 100µm from the hot side, the changes in composition are so small that they cannot be identified by EPMA. Since the Seebeck coefficient is very sensitive towards changes in charge carrier densities, small gradients in the concentration of, e.g. filler element across the cross-section invisible to other methods can be sensed with PSM. This is furthermore a sign that the diffusion and segregation of atoms reach several millimeters into the skutterudite and potentially contribute significantly to changes in overall performance over prolonged time. It remains unclear whether thermomigration plays a role in this diffusion process, or if it is a result of more local diffusion processes, e.g. diffusion/accumulation at pores.

4.5.2 Increase in R_i

The inner resistance of the thermoelectric device is given by equation (2.9). It is comprised of the resistance of the thermoelectric material and the electrodes connecting them, in addition to the contact resistance that arises at all metal/metal and metal/thermoelectric junctions. The resistivity of the electrode material is many orders of magnitude lower than the thermoelectric material, so that normally it can be ignored. In Figure 4.24 (from Paper 5), an example is shown of a gradual increase in the inner resistance of thermoelectric silicide module.

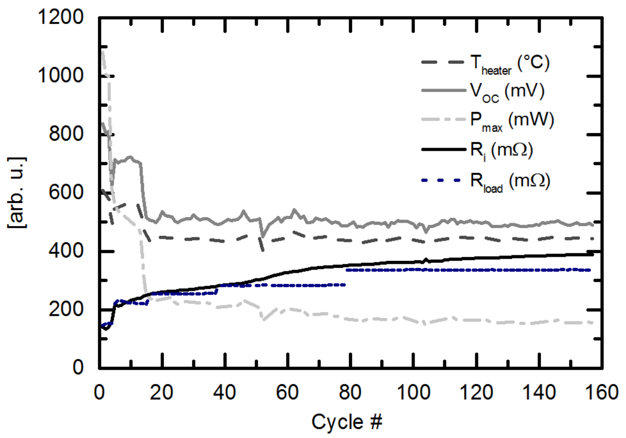

Figure 4.24 Evolution of V_{OC} and R_i during thermal cycling of a silicide module in argon atmosphere. P_{max} is the resulting power at a given load resistance, R_{load}, and the hot side temperature is given by T_{heater}. Taken from Paper 4.

Electrical contact resistance

Increase in electrical contact resistance is in most cases the main cause of degradation of TE-device performance over time. An increase of 30% in contact resistance results in a 20% reduction in performance [181]. Many of the same mechanisms causing an increase in thermal contact resistance will cause an even higher increase in electrical contact resistance, as already discussed. Oxidation and crack formation at the interface between electrode, metallization and thermoelectric material are some of the main causes of the increase. Uncontrolled growth of IMC's (no diffusion barrier), electromigration, and other diffusion processes can lead to a steadily increasing contact resistance over time. Furthermore, as mentioned in section 3.2.2, reduction in the cross-sectional area due to sublimation can also contribute negatively, as found for long term testing of RTG materials by NASA [81].

The increase in inner resistance seen in Figure 4.24 was identified as mainly caused by crack formation near the hot side of the n-type thermoelectric material (see Figure 4.25). The material was found to be too brittle to withstand the thermo-mechanical stress during thermal cycling testing. In Paper 5, oxidation was found to be the main cause of the observed increases in inner resistance over time (see Figure 4.19). While the open circuit voltage only decreased by a few percent, the inner resistance rose by several orders of magnitude.

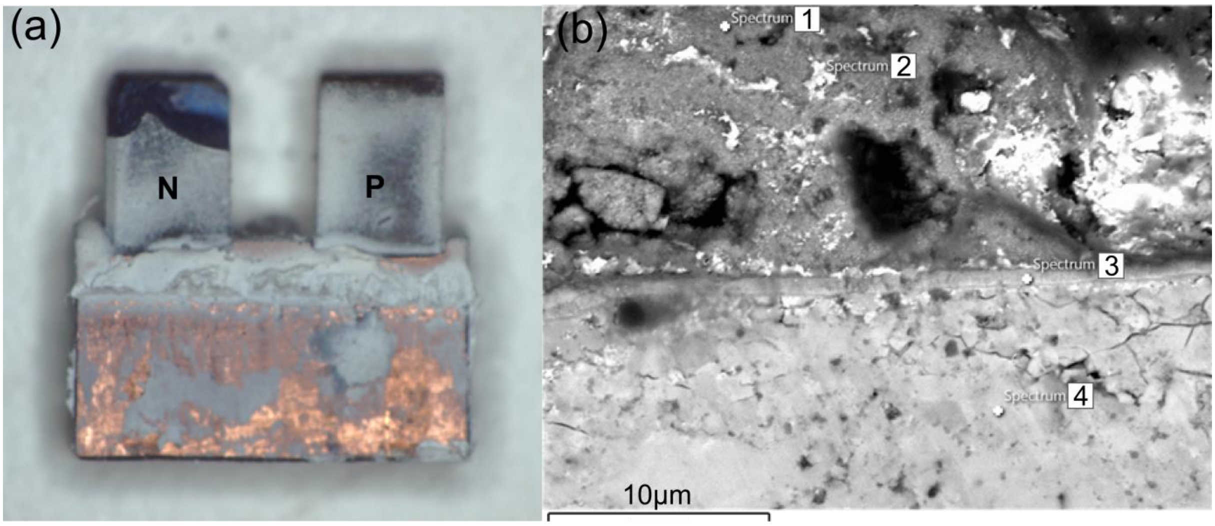

Figure 4.25 (a) Unicouple taken from Module 3 in Paper 4 after testing, with n-type ($Mg_2Si_{0.53}Sn_{0.4}Ge_{0.05}Bi_{0.02}$) and p-type ($MnSi_{1.75}Ge_{0.01}$) thermoelectric legs soldered on a cold side copper block. Cracks have caused a large part of the hot side of the n-type leg to chip off, while small cracks near the hot side interface of the same leg is seen in (b).

Bulk electrical resistivity

Similarly as in the discussion on influence of changes in bulk thermal conductivity and Seebeck coefficient, the bulk electrical resistivity is of less importance than the interface properties. Generally, the same mechanisms that will lead to changes in Seebeck coefficient will also affect electrical resistivity, since both properties are dependent on charge carrier density. For example, the reduction in Seebeck coefficient near the hot side in Figure 4.23 will also lead to much lower electrical resistivity. However, the overall effect in power factor ($\alpha^2\sigma$) will most likely be negative, since the charge carrier density of the original thermoelectric material is normally optimized for high power factors and any change will just reduce the value. A reduction in the cross sectional area near the hot side due to sublimation and oxidation from the sides will increase the bulk resistance. Also, crack formation will clearly increase the bulk resistance. The effect of other types of failure mechanisms is more unclear, just as with bulk thermal conductivity and Seebeck coefficient, and should be the topic of further studies.

4.5.3 Enhancement of performance

In sharp contrast to the reduction in performance discussed so far, in some cases an increase in performance is to be expected. This is especially true for the hot side interconnects in any setup where initial diffusion resulting in better bonding will cause a decrease in both thermal and electrical contact resistance. In this case, we will observe both increases in V_{OC} as well as decreases in R_i, of which the latter will be of most significance. In Figure 4.26 such a scenario is shown, where diffusion bonding between the metallized skutterudite element and nickel electrode is seen at a hot side temperature above 440°C. Another example is found for the initial diffusion bonding of silicide-based thermoelectric module 1 found in Paper 5. Other mechanisms will not play any significant role in enhancement of performance over time, but only contribute to degradation.

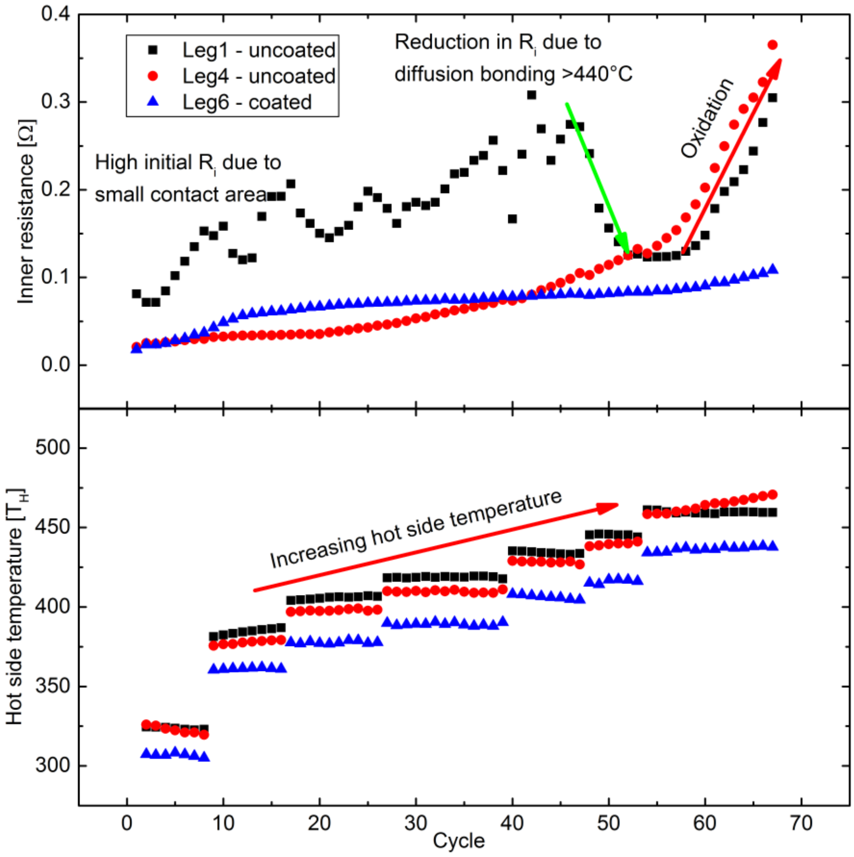

Figure 4.26 Inner resistance of three functionalized skutterudite legs (upper) as a function of cycles between 150°C and steadily increasing hot side temperatures (lower), holding for one hour for each cycle. Cold side temperature is kept at 25-30°C. Details of the setup found in Appendix II.

4.5.4 Summary

Based on the presented results and discussion, the most common failure modes and mechanisms typically found in thermoelectric systems, the relative effect on the performance of the device is shown in Table 4.3. This table intends to show which failure mechanisms are most severe when it comes to a thermoelectric device's performance over time, i.e. its *durability*. The analysis is based on literature data (Section 3.2), as well as own work on silicide and skutterudite legs and modules. It is meant as a guide to design of thermoelectric systems, and clearly shows where focus should be kept in order to facilitate optimum lifetime performance. However, since the specific failure mechanisms can differ severely between material and design concept, the relative weight between them can be different from that given in Table 4.3 .

Table 4.3 Most common failure modes and mechanisms found in thermoelectric devices and their relative impact on the performance over time, given by number of +’s. Modes leading to *increase* in performance also included.

FAILURE MODES		**FAILURE MECHANISMS**						
		Oxida-tion	**Mech. Failure (CTE-mismatch)**	**Phase Change**	**Interlayer diffusion**	**Non-uniform contact pressure (hot spots)**	**Subli-mation**	**Bulk diffusion**
Decrease in V_{OC}	Higher th. cont. resistance	+	++		+	++	++	
	Lower α at interface	+			+	+	+	
	Lower α in bulk			+			+	+
Increase in R_i	Higher el. contact resistance	+++	+++		+	++	++	
	Higher el. Bulk resistance	+	+	+			+	+
Increase in V_{OC}	*Lower th. contact resistance*				++			
Decrease in R_i	*Lower el. contact resistance*				++			

5 Final conclusions and perspectives

The main objective of this thesis has been threefold: (I) Investigate thermal degradation processes in skutterudites and silicides both during processing and end-use, (II) assess how these degradation processes affect the long-term performance of a thermoelectric device and finally (III) identify compromises that must be taken between efficiency and durability to achieve the best life-time performance and thus cost per kWh of the final system. In what degree has these objectives been achived? And where should the focus of future research lay?

In chapter 3, a survey of different thermal degradation processes relevant for thermoelectric systems revealed many potential sources of degradation all the way from material processing to assembly and end-use of thermoelectric devices. These degradation processes were furthermore assessed in skutterudite and silicides, in particular high temperature oxidation. In both these oxidation studies, it was found that alloying elements and dopants had a huge influence on the oxidation rate.

For $Mg_2Si_{1-x}Sn_x$, a higher Sn-content generally results in higher efficiency due to lower thermal conductivity, and the highest efficiency silicides based materials are therefore found in this system. In this work it has been shown how a higher Sn-content also results in significantly lower oxidation resistance. Furthermore, testing of thermoelectric modules made of this material with relatively high Sn content gave record high power and efficiency output of 3W and 5.1% respectively, but also revealed how only small amounts of oxygen in the environment significantly contributed to degradation and performance reduction during usage. In other words, during use the material with higher Sn-content will be more prone to oxidation that will lead to faster reduction in performance. Even though the initial efficiency is high, it quickly deteriorates and leads to short life-times, whereas lower efficiency material with lower Sn-content can show better stability over time resulting in better total performance over its lifetime. In addition, weak and brittle materials in combination with interdiffusion and formation of intermetallic faces at the interface between thermoelectric material and metal contact, lead to crack formation and further increase in inner electric and thermal resistance of the system. There is evidently a need for more knowledge around how other parameters than the thermoelectric properties evolve in the Mg_2(Sn-Si-Ge) system, not only in relation to oxidation, but also mechanical properties.

The effect of filler elements on microstructure, thermoelectric properties and oxidation resistance were investigated for different filled skutterudites. In particular, different synthesis methods were used to produce $Ce_{0.6}Co_2Fe_2Sb_{12}$. The best zT value of 0.7 was found for the most homogenous sample which was produced using the fastest of the applied synthesis methods by first preparing precursor phases of the intermediate products found in synthesis of skutterudites. This precursor method could therefore be beneficial also for industrial mass production. From literature it is already clear that both filler elements and Fe content significantly reduces oxidation resistance of skutterudites, and this was also found for the compositions studied in this work. Furthermore, it was shown how only small amounts of secondary phases, particularly $CeSb_2$ and $FeSb_2$, can reduce oxidation resistance of skutterudites further. From this work it was clear that knowledge of the pathway from a multitude of secondary phases up until their transformation into phase pure skutterudite is key for optimizing both the processing time and homogeneity, thus achieving better thermoelectric properties and durability of the final thermoelectric device. This should be studied further.

Not only does the thermoelectric material need to be optimized for durable operation. Also the other components of a thermoelectric device need to be chosen so they do not cause any degradation and performance loss. Especially the metallization and potential coatings needs to be developed in such a way that interface degradation processes between thermoelectric materials and metals/coatings are minimized. In this thesis, a new method of assessing different types of metallization and coating were developed. Preliminary results shows how this type of testing could be beneficial both in developing new metallization and coating as well as get a more fundamental knowledge how the different degradation processes affect the performance during usage. More work will be needed to optimize the method such as detailed control of surrounding atmosphere and faster heating and cooling rates to mimic end-use applications.

To summarize, for adaption of novel thermoelectric materials such as skutterudites and silicides into waste heat recovery application, more work is clearly needed in the field of optimizing material and system properties that shows better stability over time. Relevant thermal degradation processes needs to be studied further so that continuous improvement of materials and the systems they are implemented in take these factors into consideration.

6 References

1. IEA, *World Energy Outlook.* 2012.
2. BP, *BP Energy Outlook 2030*, 2012: London.
3. *EU Energy Strategy* [cited 2016 Jan 15th]; Available from: https://ec.europa.eu/energy/en/topics/energy-strategy.
4. Library, L.L.N. *U.S. Energy Flow*. 2014 [cited 2015 25. October]; Available from: https://flowcharts.llnl.gov/.
5. Yang, J. and F. Stabler, *Automotive Applications of Thermoelectric Materials.* Journal of Electronic Materials, 2009. **38**(7): p. 1245-1251.
6. Energi, N. and NEPAS, *Potensialstudie for utnyttelse av spillvarme fra norsk industri*, 2009, Enova.
7. Enova. *Enova støtter storsatsing på energigjenvinning ved Elkem Salten*. 2013 [cited 2013 31.10]; Available from: http://www.enova.no/finansiering/naring/aktuelt/enova-stotter-storsatsing-pa-energigjenvinning-ved-elkem-salten/250/975/.
8. EERE, *Waste Heat Recovery: Technology and Opportunities in U.S. Industry*, 2009.
9. Rowe, D.M., *Thermoelectric Waste Heat Recovery as a Renewable Energy Source.* International Journal of Innovations in Energy Systems and Power, 2006. **1**(1).
10. Zervos, H., *Thermoelectric Energy Harvesting 2013-2023: Devices, Applications, Opportunities*, 2013, IDTechEx.
11. EERE, *ITP Materials: Engineering Scoping Study of Thermoelectric Generator Systems for Industrial Waste Heat Recovery*, 2013.
12. Astrain, D., et al., *Study of the influence of heat exchangers' thermal resistances on a thermoelectric generation system.* Energy, 2010. **35**(2): p. 602-610.
13. LeBlanc, S., et al., *Material and manufacturing cost considerations for thermoelectrics.* Renewable and Sustainable Energy Reviews, 2014. **32**(0): p. 313-327.
14. Snyder, G.J. and E.S. Toberer, *Complex thermoelectric materials.* Nature Materials, 2008. **7**(2): p. 105.
15. Martín-González, M., O. Caballero-Calero, and P. Díaz-Chao, *Nanoengineering thermoelectrics for 21st century: Energy harvesting and other trends in the field.* Renewable and Sustainable Energy Reviews, 2013. **24**(0): p. 288-305.
16. Uher, C., *Skutterudite-Based Thermoelectrics*, in *Thermoelectrics Handbook, Macro to Nano*, D.M. Rowe, Editor. 2006, CRC Press: Boca Raton, Florida, p. 34.1-34.17.
17. Shi, X., et al., *Multiple-Filled Skutterudites: High Thermoelectric Figure of Merit through Separately Optimizing Electrical and Thermal Transports.* Journal of the American Chemical Society, 2011. **133**(20): p. 7837-7846.
18. Zaitsev, V.K., et al., *Thermoelectrics on the Base of Solid Solutions of* Mg_2B^{IV} *Compounds* (B^{V} *= Si, Ge, Sn)*, in *Thermoelectrics Handbook, Macro to Nano*, D.M. Rowe, Editor. 2006, CRC Press: Boca Raton, Florida, p. 29.1-29.11.
19. Liu, W., et al., *Enhanced thermoelectric properties of n-type* $Mg_{2.16}(Si_{0.4}Sn_{0.6})_{1-y}Sb_y$ *due to nano-sized Sn-rich precipitates and an optimized electron concentration.* Journal of Materials Chemistry, 2012. **22**(27): p. 13653-13661.
20. ESA. *ThermoMag Homepage*. 2011 [cited 2013 15. March]; Available from: http://www.thermomag-project.eu/index.html.
21. *ThermoMag, Final description of Work*, in *Seventh Framework Program NMP-2010-1.2-3* 2010.
22. Biswas, K., et al., *High-performance bulk thermoelectrics with all-scale hierarchical architectures.* Nature, 2012. **489**(7416): p. 414-418.
23. McDonald, A. and L. Schrattenholzer, *Learning rates for energy technologies.* Energy Policy, 2001. **29**(4): p. 255-261.
24. Rowe, D.M. and G. Min, *Evaluation of thermoelectric modules for power generation.* Journal of Power Sources, 1998. **73**(2): p. 193-198.
25. Rowe, D.M., *Introduction*, in *CRC Handbook of Thermoelectrics*, D.M. Rowe, Editor. 1995, CRC Press, Tylor & Francis group: Boca Raton, Florida.

26. Rowe, D.M., *General principles and conciderations*, in *Thermoelectrics Handbook, Macro to Nano*, D.M. Rowe, Editor. 2006, CRC Press, Tylor & Francis group: Boca Raton, Florida, p. 1.1-1.13.
27. Abelson, R.D., *Space Missions and Applications*, in *Thermoelectrics Handbook, Macro to Nano*, D.M. Rowe, Editor. 2006, CRC Press, Tylor & Francis group: Boca Raton, Florida, p. 56.1-56.27.
28. Hicks, L.D. and M.S. Dresselhaus, *Effect of quantum-well structures on the thermoelectric figure of merit.* Physical Review B, 1993. **47**(19): p. 12727-12731.
29. Hicks, L.D. and M.S. Dresselhaus, *Thermoelectric figure of merit of a one-dimensional conductor.* Physical Review B, 1993. **47**(24): p. 16631-16634.
30. Goldsmid, H.J., *Thermoelectric Properties of Metals and Semiconductors*, in *Introduction to Thermoelectricity*, H.J. Goldsmid, Editor. 2009, Springer, p. 23-41.
31. ThermoMag, *D1.1 End-User Design Requirements*, 2011, ESA. p. 44.
32. *Engineering Toolbox: Coefficients of Linear Thermal Expansion*. [cited 2013 4. November]; Available from: http://www.engineeringtoolbox.com/linear-expansion-coefficients-d_95.html.
33. Liu, W., et al., *Current progress and future challenges in thermoelectric power generation: From materials to devices.* Acta Materialia, 2015. **87**: p. 357-376.
34. Zhao, D., et al., *High temperature sublimation behavior of antimony in CoSb3 thermoelectric material during thermal duration test.* Journal of Alloys and Compounds, 2011. **509**(6): p. 3166-3171.
35. Evans, U.R., *The corrosion and oxidation of metals: Scientific Principles and Practical Applications*. 1960: St. Martin's Press.
36. Belov, Y.M., S.M. Maniakin, and I.V. Morgunov, *Review of Methods of Thermoelectric Materials Mass Production*, in *Thermoelectrics Handbook, Macro to Nano*, D.M. Rowe, Editor. 2006, CRC Press, Tylor & Francis group: Boca Raton, Florida, p. 20.1-20.7.
37. Book, B.A. and J.L. Harringa, *Solid-State Synthesis of Thermoelectric Materials*, in *Thermoelectrics Handbook, Macro to Nano*, D.M. Rowe, Editor. 2006, CRC Press, Tylor & Francis group: Boca Raton, Florida, p. 19.1-19.15.
38. Li, J.-F., et al., *High-performance nanostructured thermoelectric materials.* NPG Asia Mater, 2010. **2**: p. 152-158.
39. Li, X., et al. *Mo/Ti/*$CoSb_3$ *joining technology for* $CoSb_3$ *based materials*. in *24th International Conference onThermoelectrics*. 2005.
40. Schlesinger, M. and M. Paunovic, *Modern Electroplating*. 2011: Wiley.
41. Miner, A., *The Industrialization of Thermoelectric Power Generation Technology,* U.S.D.o.E.T.A. Workshop, 2012.
42. Mancheri, N.A., *Chinese Monopoly in Rare Earth Elements: Supply–Demand and Industrial Applications.* China Report, 2012. **48**(4): p. 449-468.
43. UNEP, *Assessing the environmental impacts of consumption and production: Priority Products and Materials*, A Report of the Working Group on the Environmental Impacts of Products and Materials to the International Panel for Sustainable Resource Management., Hertwich, E., van der Voet, E., Suh, S., Tukker, A., Huijbregts M., Kazmierczyk, P., Lenzen, M., McNeely, J., Moriguchi, Y, Editor 2010.
44. Scherrer, H. and S. Scherrer, *Thermoelectric Properties of Bismuth Antimony Telluride Solid Solutions*, in *Thermoelectrics Handbook, Macro to Nano*, D.M. Rowe, Editor. 2006, CRC Press, Tylor & Francis group: Boca Raton, Florida, p. 27.1-27.17.
45. Xie, W., et al., *Unique nanostructures and enhanced thermoelectric performance of melt-spun BiSbTe alloys.* Applied Physics Letters, 2009. **94**(10): p. 102111.
46. Slack, G.A., *New Materials and Performance Limits for Thermoelectric Cooling*, in *CRC Handbook of Thermoelectrics*, D.M. Rowe, Editor. 1995, CRC Press, Tylor & Francis group: Boca Raton, Florida, p. 407-439.
47. Alam, H. and S. Ramakrishna, *A review on the enhancement of figure of merit from bulk to nano-thermoelectric materials.* Nano Energy, 2013. **2**(2): p. 190-212.

48. Liessmann, W., *Der Bergbau und die Mineralien von Modum-Skutreud, Norwegen*, in *Emser Hefte*1994, Doris Bode Verlag GMBH: Haltern, Germany.
49. Sales, B.C., D. Mandrus, and R.K. Williams, *Filled Skutterudite Antimonides: A New Class of Thermoelectric Materials.* Science, 1996. **272**(5266): p. 1325-1328.
50. Sesselmann, A.J., *Investigation on the Thermoelectric and Structural Properties of Cobalt-Antimony based Skutterudites and Modifications with Indium and Rare-Earth Elements*. PhD thesis Universität Augsburg, 2012
51. Bérardan, D., et al., *Existence, structure and valence properties of the skutterudites CeyFe4−xCoxSb12.* Journal of Alloys and Compounds, 2003. **350**(1–2): p. 30-35.
52. Leszczynski, J., K. Wojciechowski, and A. Malecki, *Studies on thermal decomposition and oxidation of CoSb3.* Journal of Thermal Analysis and Calorimetry, 2011. **105**(1): p. 211-222.
53. Zaitsev, V.K., et al., *Highly effective* $Mg_2Si_{1-x}Sn_x$ *thermoelectrics.* Physical Review B, 2006. **74**(4): p. 045207.
54. Bashir, M.B.A., et al., *Recent advances on Mg2Si1−xSnx materials for thermoelectric generation.* Renewable and Sustainable Energy Reviews, 2014. **37**(0): p. 569-584.
55. Khan, A.U., et al., *Thermoelectric properties of highly efficient Bi-doped Mg2Si1−x−ySnxGey materials.* Acta Materialia, 2014. **77**(0): p. 43-53.
56. Tani, J.-i., M. Takahashi, and H. Kido, *Fabrication of oxidation-resistant β-*$FeSi_2$ *film on* Mg_2Si *by RF magnetron-sputtering deposition.* Journal of Alloys and Compounds, 2009. **488**(1): p. 346-349.
57. Jung, I.-H., et al., *Thermodynamic modeling of the Mg–Si–Sn system.* Calphad, 2007. **31**(2): p. 192-200.
58. Fedorov, M.I. and V.K. Zaitsev, *Thermoelectrics of Transition Metal Silicides*, in *Thermoelectrics Handbook, Macro to Nano*, D.M. Rowe, Editor. 2006, CRC Press, Tylor & Francis group: Boca Raton, Florida.
59. Fedorov, M.I., *Thermoelectric Silicides: Past, Present and Future.* Journal of Thermoelectricity, 2009. **2**: p. 51-60.
60. Rogl, P., *Formation and Crystal Chermistry of Clathrates*, in *Thermoelectrics Handbook, Macro to Nano*, D.M. Rowe, Editor. 2006, CRC Press, Tylor & Francis group: Boca Raton, Florida, p. 32.1-32.17.
61. Nolas, G.S., *Structure, Thermal Conductivity, and Thermoelectric Properties of Clathrate Compounds*, in *Thermoelectrics Handbook, Macro to Nano*, D.M. Rowe, Editor. 2006, CRC Press, Tylor & Francis group: Boca Raton, Florida, p. 33.1-33.7.
62. Sakurada, S. and N. Shutoh, *Effect of Ti substitution on the thermoelectric properties of (Zr,Hf)NiSn half-Heusler compounds.* Applied Physics Letters, 2005. **86**(8): p. 082105.
63. Schlecht, S., C. Erk, and M. Yosef, *Nanoscale Zinc Antimonides: Synthesis and Phase Stability.* Inorganic Chemistry, 2006. **45**(4): p. 1693-1697.
64. Yin, H., et al., *Thermal Stability of Thermoelectric Zn4Sb3.* Journal of Electronic Materials, 2010. **39**(9): p. 1957-1959.
65. Pavlova, L.M., Y.I. Shtern, and R.E. Mironov, *Thermal expansion of bismuth telluride.* High Temperature, 2011. **49**(3): p. 369-379.
66. Rogl, G., et al., *Thermal expansion of skutterudites.* Journal of Applied Physics, 2010. **107**(4): p. 043507-10.
67. Falmbigl, M., et al., *Thermal expansion of thermoelectric type-I-clathrates.* Journal of Applied Physics, 2010. **108**(4): p. 043529-35299.
68. Gahlawat, S., et al., *Elastic constants determined by nanoindentation for p-type thermoelectric half-Heusler.* Journal of Applied Physics, 2014. **116**(8): p. 083516.
69. Jung, D.-y., et al., *Thermal expansion and melting temperature of the half-Heusler compounds: MNiSn (M = Ti, Zr, Hf).* Journal of Alloys and Compounds, 2010. **489**(2): p. 328-331.
70. Gałązka, K., et al., *Phase formation, stability, and oxidation in (Ti, Zr, Hf)NiSn half-Heusler compounds.* physica status solidi (a), 2014. **211**(6): p. 1259-1266.

71. Baranowski, L.L., G. Jeffrey Snyder, and E.S. Toberer, *Effective thermal conductivity in thermoelectric materials.* Journal of Applied Physics, 2013. **113**(20): p. 204904.
72. Hogan, T.P., *Modeling and Characterization of Power Generation Modules Based on Bulk Materials*, in *Thermoelctrics Handbook, Macro to Nano*, D.M. Rowe, Editor. 2006, CRC Press: Boca Raton, Florida, p. 12.1-12.23.
73. Baranowski, L.L., G. Jeffrey Snyder, and E.S. Toberer, *Response to "Comment on 'Effective thermal conductivity in thermoelectric materials'" [J. Appl. Phys. 113, 204904 (2013)].* Journal of Applied Physics, 2014. **115**(12): p. 126102.
74. Rowe, D.M. and G. Min, *Design theory of thermoelectric modules for electrical power generation.* IEE Proceedings: Science, Measurement & Technology, 1996. **143**(6): p. 351-356.
75. Min, G., *Thermoelectric Module Design Theories*, in *Thermoelectrics Handbook, Macro to Nano*, D.M. Rowe, Editor. 2006, CRC Press: Boca Raton, Florida, p. 11.1-11.15.
76. Datta, M., T. Osaka, and J.W. Schultze, *Microelectronic Packaging*. 2004: CRC Press.
77. Tollefsen, T.A., *Metallization of Thermoelectric Materials*, 2014: Thermoelectric materials (THELMA) workshop, Oslo.
78. Saber, H.H., M.S. El-Genk, and T. Caillat, *Performance Test Results of a Skutterudite-Based Unicouple with a Metallic Coating.* AIP Conference Proceedings, 2005. **746**(1): p. 584-592.
79. Dong, H., et al., *Improved oxidation resistance of thermoelectric skutterudites coated with composite glass.* Ceramics International, 2012(0).
80. Park, Y.-S., et al., *Protective enamel coating for n- and p-type skutterudite thermoelectric materials.* Journal of Materials Science, 2015. **50**(3): p. 1500-1512.
81. Yang, J. and T. Caillat, *Thermoelectric Materials for Space and Automotive Power Generation.* MRS Bulletin, 2006. **31**(03): p. 224-229.
82. Kambe, M., T. Jinushi, and Z. Ishijima, *Encapsulated Thermoelectric Modules for Advanced Thermoelectric Systems.* Journal of Electronic Materials, 2014. **43**(6): p. 1959-1965.
83. de Boor, J., et al., *Fabrication and characterization of nickel contacts for magnesium silicide based thermoelectric generators.* Journal of Alloys and Compounds, 2015. **632**: p. 348-353.
84. Xiao, H., *Introduction to semiconductor manufacturing technology*. 2001, Upper Saddle River, NJ: Prentice Hall.
85. Li, H., et al., *Interface evolution analysis of graded thermoelectric materials joined by low temperature sintering of nano-silver paste.* Journal of Alloys and Compounds, 2016. **659**: p. 95-100.
86. Xia, H., et al., *Bonding and interfacial reaction between Ni foil and n-type PbTe thermoelectric materials for thermoelectric module applications.* Journal of Materials Science, 2013. **49**(4): p. 1716-1723.
87. Chuang, T.-H., et al., *Improvement of bonding strength of a (Pb, Sn)Te–Cu contact manufactured in a low temperature SLID-bonding process.* Journal of Alloys and Compounds, 2014. **613**: p. 46-54.
88. Sakamoto, J., et al., *Improving thermoelectric technology performance and durability with aerogel*, 2005, Jet Propulsion Laboratory, National Aeronautics and Space Administration: Pasadena, CA.
89. Buist, R.J., *Methodology for Testing Thermoelectric Materials and Devices*, in *Handbook of Thermoelectrics*, D.M. Rowe, Editor. 1995, CRC Press: Boca Raton, Florida, p. 18.1-18.11.
90. Ahiska, R. and K. Ahiska, *New method for investigation of parameters of real thermoelectric modules.* Energy Conversion and Management, 2010. **51**(2): p. 338-345.

91. Mengali, O.J. and M.R. Seiler, *Symposium on Thermoelectric Energy Conversion - Contact resistance studies on thermoelectric materials.* Advanced Energy Conversion, 1962. **2**: p. 59-68.
92. Thimont, Y., et al., *Design of Apparatus for Ni/Mg2Si and Ni/MnSi1.75 Contact Resistance Determination for Thermoelectric Legs.* Journal of Electronic Materials, 2014. **43**(6): p. 2023-2028.
93. Kim, Y., G. Yoon, and H.S. Park, *Direct Contact Resistance Evaluation of Thermoelectric Legs.* Experimental Mechanics, 2016: p. 1-9.
94. Rauscher, L., et al., *Efficiency determination and general characterization of thermoelectric generators using an absolute measurement of the heat flow.* Measurement Science and Technology, 2005. **16**(5): p. 1054.
95. Takazawa, H., et al. *Efficiency measurement of thermoelectric modules operating in the temperature difference of up to 550K*. in *25th International Conference on Thermoelectrics*. 2006.
96. Esarte, J., G. Min, and D.M. Rowe, *Modelling heat exchangers for thermoelectric generators.* Journal of Power Sources, 2001. **93**(1–2): p. 72-76.
97. Snyder, G.J., *Thermoelectric Power Generation: Efficiency and Compatibility*, in *Thermoelectrics Handbook, Macro to Nano*, D.M. Rowe, Editor. 2006, CRC Press: Boca Raton, Florida, p. 9.1-9.22.
98. Kristiansen, N.R., et al., *Waste Heat Recovery from a Marine Waste Incinerator Using a Thermoelectric Generator.* Journal of Electronic Materials, 2012. **41**(6): p. 1024-1029.
99. Hendricks, T.J. and D.T. Crane, *Thermoelectric Energy Recovery Systems: Thermal, Thermoelectric and Structural Considerations*, in *Thermoelectrics and its Energy Harvesting - Modules, Systems and Applications in Thermoelectrics*, D.M. Rowe, Editor. 2012, CRC Press: Boca Raton, Florida, p. 22.1-22.30.
100. Mehrer, H., *Diffusion in Solids*. Solid-State Sciences, ed. M. Cardona, et al. 2010, Berling, Heidelberg: Springer.
101. Chen, N., et al., *Macroscopic thermoelectric inhomogeneities in (AgSbTe2)x(PbTe)1−x.* Applied Physics Letters, 2005. **87**(17): p. 171903.
102. Kerr, H.W. and W. Kurz, *Solidification of peritectic alloys.* International Materials Reviews, 1996. **41**(4): p. 129-164.
103. Bourgois, J., et al., *Study of electron, phonon and crystal stability vs. thermoelectric properties in* Mg_2X *(X=Si, Sn) compounds and their alloys.* Functional Material Letters : Frontier of Thermoelectrics, 2013. **6**(5): p. 1340005.
104. Luo, W., et al., *Fabrication and thermoelectric properties of Mg2Si1−xSnx (0 ≤ x ≤ 1.0) solid solutions by solid state reaction and spark plasma sintering.* Materials Science and Engineering: B, 2009. **157**(1–3): p. 96-100.
105. L'vov, B.V., *Thermal Decomposition of Solids and Melts*. Hot Topics in Thermal Analysis and Calorimetry, ed. J. Simon. 2007: Springer Netherlands. 247.
106. Martinson, I.G., *Evaporation of substances under kinetic or diffusion control in sublimation in a vacuum.* Russian Journal of Applied Chemistry, 2006. **79**(8): p. 1230-1237.
107. Saber, H.H., M.S. El-Genk, and T. Caillat, *Tests results of skutterudite based thermoelectric unicouples.* Energy Conversion and Management, 2007. **48**(2): p. 555-567.
108. El-Genk, M.S., et al. *Life tests of a skutterudites thermoelectric unicouple (MAR-03)*. in *22nd International Conference on Thermoelectrics*. 2003.
109. Liao, C.-N., C.-H. Lee, and W.-J. Chen, *Effect of Interfacial Compound Formation on Contact Resistivity of Soldered Junctions Between Bismuth Telluride-Based Thermoelements and Copper.* Electrochemical and Solid-State Letters, 2007. **10**(9): p. 23-25.
110. Chen, S.-w. and C.-n. Chiu, *Unusual cruciform pattern interfacial reactions in Sn/Te couples.* Scripta Materialia, 2007. **56**(2): p. 97-99.

111. Lin, T.Y., C.N. Liao, and A. Wu, *Evaluation of Diffusion Barrier Between Lead-Free Solder Systems and Thermoelectric Materials.* Journal of Electronic Materials, 2012. **41**(1): p. 153-158.
112. Lo, L.-C. and A. Wu, *Interfacial Reactions Between Diffusion Barriers and Thermoelectric Materials Under Current Stressing.* Journal of Electronic Materials, 2012. **41**(12): p. 3325-3330.
113. Zhao, D., et al., *Interfacial evolution behavior and reliability evaluation of CoSb3/Ti/Mo–Cu thermoelectric joints during accelerated thermal aging.* Journal of Alloys and Compounds, 2009. **477**(1–2): p. 425-431.
114. Zhao, D., H. Geng, and X. Teng, *Fabrication and reliability evaluation of CoSb3/W–Cu thermoelectric element.* Journal of Alloys and Compounds, 2012. **517**: p. 198-203.
115. Lienig, J. and G. Jerke. *Electromigration-aware physical design of integrated circuits*. in *18th International Conference on VLSI Design*. 2005.
116. Liao, C.-N., W.-T. Chen, and C.-H. Lee, *Polarity effect on interfacial reactions at soldered junctions of electrically stressed thermoelectric modules.* Applied Physics Letters, 2010. **97**(24): p. 241906.
117. Liao, C.-N. and L.-C. Wu, *Enhancement of carrier transport properties of BixSb2−xTe3 compounds by electrical sintering process.* Applied Physics Letters, 2009. **95**(5): p. 052112.
118. Dasgupta, T., et al., *Electro-migration of Zinc during current-assisted pressure sintering of β-Zn4Sb3 – effect of process parameters and its influence on the thermoelectric properties.* MRS Online Proceedings Library, 2011. **1325**.
119. Rahman, M.A. and M.Z. Saghir, *Thermodiffusion or Soret effect: Historical review.* International Journal of Heat and Mass Transfer, 2014. **73**: p. 693-705.
120. Ye, H., C. Basaran, and D. Hopkins, *Thermomigration in Pb–Sn solder joints under joule heating during electric current stressing.* Applied Physics Letters, 2003. **82**(7): p. 1045-1047.
121. Basaran, C., S. Li, and M.F. Abdulhamid, *Thermomigration induced degradation in solder alloys.* Journal of Applied Physics, 2008. **103**(12): p. 123520.
122. Huang, C. and A. Christou, *Diffusion controlled degradation analysis of high temperature (Bi,Sb)2(Te,Se)3 semiconductor thermoelectric power modules.* Materials Science and Engineering: B, 1995. **29**(1–3): p. 233-236.
123. Olevsky, E.A. and L. Froyen, *Impact of Thermal Diffusion on Densification During SPS.* Journal of the American Ceramic Society, 2009. **92**: p. S122-S132.
124. Kassner, M.E. and M.-T. Pérez-Prado, *Chapter 1 - Introduction*, in *Fundamentals of Creep in Metals and Alloys*, M.E.K.-T. Pérez-Prado, Editor. 2004, Elsevier Science Ltd: Oxford, p. 3-9.
125. Zhang, L., et al., *Thermoelectric Performance and High-Temperature Creep Behavior of GeTe-Based Thermoelectric Materials.* Journal of Electronic Materials, 2011. **40**(5): p. 1057-1061.
126. Goldstein, A.N., C.M. Echer, and A.P. Alivisatos, *Melting in Semiconductor Nanocrystals.* Science, 1992. **256**(5062): p. 1425-1427.
127. Aminorroaya Yamini, S., et al., *Fabrication of thermoelectric materials - thermal stability and repeatability of achieved efficiencies.* Journal of Materials Chemistry C, 2015. **3**(40): p. 10610-10615.
128. ThermoMag, *Periodic Report Summary 2*, 2014, ESA.
129. Sootsman, J.R., D.Y. Chung, and M.G. Kanatzidis, *New and Old Concepts in Thermoelectric Materials.* Angewandte Chemie International Edition, 2009. **48**(46): p. 8616-8639.
130. Joshi, G., et al., *Enhanced Thermoelectric Figure-of-Merit in Nanostructured p-type Silicon Germanium Bulk Alloys.* Nano Letters, 2008. **8**(12): p. 4670-4674.
131. Margalit, S., et al., *Oxidation of silicon-germanium alloys.* Journal of Crystal Growth, 1972. **17**: p. 288-297.
132. Pilling, N.B. and R.E. Bedworth, *The Oxidation of Metals at High Temperatures.* Journal of the Institute of Metals, 1923. **29**: p. 529-291.

133. Wagner, C., *Beitrag zur theorie des anlaufvorgangs.* Z. Phys. Chem. B, 1933. **21**: p. 25-41.
134. Young, D., *High temperature oxidation and corrosion of metals*, ed. D. Young. 2008, Oxford: Elsevier.
135. Khanna, A.S., *Introduction to High Temperature Oxidation and Corrosion*. 2002: ASM International.
136. Swaminathan, K. and O.M. Sreedharan, *Potentiometric determination of stabilities of NiSb2O4 and NiSb2O6.* Journal of Alloys and Compounds, 1999. **292**(1–2): p. 100-106.
137. Zhao, D., et al., *High temperature oxidation behavior of cobalt triantimonide thermoelectric material.* Journal of Alloys and Compounds, 2010. **504**(2): p. 552-558.
138. Godlewska, E., et al., *Degradation of CoSb3 in Air at Elevated Temperatures.* Oxidation of Metals, 2010. **74**(3-4): p. 113-124.
139. Sklad, A.C., M.W. Gaultois, and A.P. Grosvenor, *Examination of CeFe4Sb12 upon exposure to air: Is this material appropriate for use in terrestrial, high-temperature thermoelectric devices?* Journal of Alloys and Compounds, 2010. **505**(1): p. 6-9.
140. Peddle, J.M., M.W. Gaultois, and A.P. Grosvenor, *On the Oxidation of EuFe4Sb12 and EuRu4Sb12.* Inorganic Chemistry, 2011. **50**(13): p. 6263-6268.
141. Park, K.-H., et al., *High-Temperature Stability of Thermoelectric Skutterudite In0.25Co3FeSb12.* Journal of Electronic Materials, 2012. **41**(6): p. 1051-1056.
142. Xia, X., et al., *Oxidation Behavior of Filled Skutterudite CeFe4Sb12 in Air.* Journal of Electronic Materials, 2014. **43**(6): p. 1639-1644.
143. Qiu, P., et al., *"Pesting"-like oxidation phenomenon of p-type filled skutterudite Ce0.9Fe3CoSb12.* Journal of Alloys and Compounds, 2014. **612**: p. 365-371.
144. Xia, X., et al., *High-Temperature Oxidation Behavior of Filled Skutterudites YbyCo4Sb12.* Journal of Electronic Materials, 2012. **41**(8): p. 2225-2231.
145. Auerkari, P., *Mechanical and physical properties of engineering alumina ceramics*. 1996: Technical Research Centre of Finland.
146. *MatWeb.com*. [cited 2016 5th January]; Available from: http://www.matweb.com/index.aspx.
147. Cverna, F. and A.S.M.I.M.P.D. Committee, *ASM Ready Reference: Thermal properties of metals*. 2002: ASM International.
148. Basaran, C. and J. Jiang, *Measuring intrinsic elastic modulus of Pb/Sn solder alloys.* Mechanics of Materials, 2002. **34**(6): p. 349-362.
149. Zhao, L.-D., et al., *Thermoelectric and mechanical properties of nano-SiC-dispersed Bi2Te3 fabricated by mechanical alloying and spark plasma sintering.* Journal of Alloys and Compounds, 2008. **455**(1–2): p. 259-264.
150. Case, E.D., *Thermomechanical Properties of Thermoelectric Materials*, in *Modules, Systems, and Applications in Thermoelectrics*. 2012, CRC Press, p. 16.1-16.29.
151. Rogl, G., et al., *New p- and n-type skutterudites with ZT>1 and nearly identical thermal expansion and mechanical properties.* Acta Materialia, 2013. **61**(11): p. 4066-4079.
152. Mondolfo, L.F., *Al–Mg–Si Aluminum–Magnesium–Silicon system*, in *Aluminum Alloys*. 1976, Butterworth-Heinemann, p. 566-575.
153. Schmidt, R.D., et al., *Room-Temperature Mechanical Properties and Slow Crack Growth Behavior of Mg2Si Thermoelectric Materials.* Journal of Electronic Materials, 2012. **41**(6): p. 1210-1216.
154. Ferrotech. *Reliability of Thermoelectric Coolers*. Thermoelectric Technical Reference [cited 2016 Jan. 26th]; Available from: https://thermal.ferrotec.com/technology/thermoelectric/thermalRef10.
155. Hori, Y., et al. *Analysis on thermo-mechanical stress of thermoelectric module*. in *Thermoelectrics, 1999. Eighteenth International Conference on*. 1999.
156. Buttay, C., et al., *State of the art of high temperature power electronics.* Materials Science and Engineering: B, 2011. **176**(4): p. 283-288.

157. Zhou, C., et al., *Thermoelectric properties of Co0.9Fe0.1Sb3-based skutterudite nanocomposites with FeSb2 nanoinclusions.* Journal of Applied Physics, 2011. **109**(6): p. 063722.
158. Li, H., et al., *High performance InxCeyCo4Sb12 thermoelectric materials with in situ forming nanostructured InSb phase.* Applied Physics Letters, 2009. **94**(10): p. 102114.
159. Boor, J., et al., *High-Temperature Measurement of Seebeck Coefficient and Electrical Conductivity.* Journal of Electronic Materials, 2013. **42**(7): p. 1711-1718.
160. Qiu, P.F., et al., *High-temperature electrical and thermal transport properties of fully filled skutterudites RFe4Sb12 (R = Ca, Sr, Ba, La, Ce, Pr, Nd, Eu, and Yb).* Journal of Applied Physics, 2011. **109**(6): p. 063713.
161. Dahal, T., et al., *Effect of triple fillers in thermoelectric performance of p-type skutterudites.* Journal of Alloys and Compounds, 2015. **623**: p. 104-108.
162. Zebarjadi, M., et al., *Effect of filler mass and binding on thermal conductivity of fully filled skutterudites.* Physical Review B, 2010. **82**(19): p. 195207.
163. Ishida, K. and T. Nishizawa, *The Co-Sb (Cobalt-Antimony) system.* Bulletin of Alloy Phase Diagrams, 1991. **11**(3): p. 243-248.
164. Okamoto, H., *Phase diagrams of binary iron alloys*. 1993: ASM International.
165. Gusak, A.M., *Diffusion Phase Competition: Fundamentals*, in *Diffusion-controlled Solid State Reactions: in Alloys, Thin-Films, and Nanosystems*. 2010, John Wiley & Sons, p. 37-60.
166. Amornpitoksuk, P., et al., *Experimental determination of phase equilibrium in the Fe-Co-Sb ternary system.* Intermetallics, 2007. **15**: p. 475-478.
167. Predel, B., *Ce-Sb (Cerium-Antimony)*, in *Ca-Cd – Co-Zr*, O. Madelung, Editor. 1993, Springer Berlin Heidelberg, p. 1-3.
168. Khawam, A. and D.R. Flanagan, *Solid-State Kinetic Models: Basics and Mathematical Fundamentals.* Journal of Physical Chemistry B, 2006. **110**(35): p. 17315-17328.
169. Park, K.-H., et al., *Synthesis and Thermoelectric Properties of In z Co4−x Fe x Sb12 Skutterudites.* Journal of Electronic Materials, 2010. **39**(9): p. 1750-1754.
170. de Laune, B.P. and C. Greaves, *Structural and magnetic characterisation of CoSb2O4, and the substitution of Pb2+ for Sb3+.* Journal of Solid State Chemistry, 2012. **187**: p. 225-230.
171. *FeSb2O4 Crystal Structure*, M.P.D.S.M. Pierre Villars, Editor 2014, SpringerMaterials: CH-6354 Vitznau, Switzerland (ed.).
172. Agrawal, Y.K., A.L. Shashimohan, and A.B. Biswas, *Studies on antimony oxides: partI Thermal Analysis of Sb203 in air, nitrogen and argon.* Journal of Thermal Analysis, 1975. **7**: p. 635-641.
173. Cumby, J., B.P. de Laune, and C. Greaves, *The structures and magnetic properties of FexCo1-xSb2O4 and MnxCo1-xSb2O4, 0≤x≤1.* Journal of Materials Chemistry C, 2016. **4**(1): p. 201-208.
174. Lie, L.N., W.A. Tiller, and K.C. Saraswat, *Thermal oxidation of silicides.* Journal of Applied Physics, 1984. **56**(7): p. 2127-2132.
175. Brause, M., et al., *Surface electronic structure of pure and oxidized non-epitaxial Mg2Si layers on Si(111).* Surface Science, 1998. **398**(1–2): p. 184-194.
176. Kim, Y.M., et al., *Key factor influencing the ignition resistance of magnesium alloys at elevated temperatures.* Scripta Materialia, 2011. **65**(11): p. 958-961.
177. Fedorov, M.I., V.K. Zaitsev, and G.N. Isachenko, *High effective thermoelectrics based on the Mg2Si-Mg2Sn solid solution.* Solid State Phenomena, 2011. **170**: p. 286-292.
178. Wang, H., et al., *Determination of Thermoelectric Module Efficiency: A Survey.* Journal of Electronic Materials, 2014. **43**(6): p. 2274-2286.
179. Ohring, M. and L. Kasprzak, *Chapter 1 - An Overview of Electronic Devices and Their Reliability*, in *Reliability and Failure of Electronic Materials and Devices (Second Edition)*, M.O. Kasprzak, Editor. 2015, Academic Press: Boston, p. 1-38.
180. Min, G. and D.M. Rowe, *Optimisation of thermoelectric module geometry for 'waste heat' electric power generation.* Journal of Power Sources, 1992. **38**(3): p. 253-259.

181. Bjørk, R., *The Universal Influence of Contact Resistance on the Efficiency of a Thermoelectric Generator.* Journal of Electronic Materials, 2015. **44**(8): p. 2869-2876.
182. Lloyd, J., *Reliability of copper metallization*, 1998, Reports from Lloyd Technology Associates, Inc.

Appendix I. Papers

Paper 1: Methods for Enhancing the Thermal Durability of High-Temperature Thermoelectric Materials

Journal of ELECTRONIC MATERIALS, Vol. 43, No. 6, 2014
DOI: 10.1007/s11664-013-2917-0

Methods for Enhancing the Thermal Durability of High-Temperature Thermoelectric Materials

GUNSTEIN SKOMEDAL,[1,3,4,5] NILS R. KRISTIANSEN,[1]
MARIANNE ENGVOLL,[2] and HUGH MIDDLETON[1]

1.—University of Agder, Kristiansand, Norway. 2.—Tegma AS, Kristiansand, Norway. 3.—Department of Engineering Sciences, Jon Lilletuns vei 9, 4898 Grimstad, Norway. 4.—e-mail: gunstein.skomedal@uia.no. 5.—e-mail: gunstein@gmail.com

Thermoelectric materials, for example skutterudites and magnesium silicides, are being investigated as promising materials for medium-to-high-temperature waste heat recovery in transport and in industry. A crucial aspect of the success of a thermoelectric material is its stability over time when exposed to rapid heating and cooling. In this work different aspects of the degradation of these thermoelectric materials at high temperature were examined. Initial thermal durability was studied, and several candidate coatings were evaluated to enhance durability by protecting the materials from oxidation and sublimation during thermal cycles in air for up to 500 h and up to 873 K. The samples were characterized by SEM and EDS. The results showed it is possible to reduce degradation of the thermoelectric material without compromising overall thermoelectric efficiency.

Key words: Skutterudite, magnesium silicide, oxidation, durability, coating

INTRODUCTION

Global energy consumption is increasing rapidly. Better ways of producing and using this energy are needed for a sustainable future. A large portion, >60%, of the energy already produced is lost as heat.[1] Thermoelectric generators (TEG) are good options for recovery of heat in transport and in industry, in which large temperature gradients are available and space is sometimes limited, so other heat-recovery technology cannot be used. Several good thermoelectric (TE) materials, for example PbTe and TAGS, are available for exploiting this potential,[2] but price, production complexity, and environmental issues, among others, have prevented large-scale industrial commercial development of these materials.

Skutterudite (SKD; $CoSb_3$) has attracted much attention over the last decade because of its relatively high ZT values (>1) [3,4] in the medium-to-high-temperature range, 250–650°C. Magnesium silicide-based alloys (MGS) also have very good ZT values (>1) in this temperature range.[5] MGS alloys can be made from inexpensive, abundant, and non-toxic raw materials and are very light compared with other well-known TE materials.

Some of the main challenges with these materials are oxidation and sublimation of the substrate, which reduce the lifetime of the TE material. Oxidation and sublimation of SKD are well known, and have been studied thoroughly over the last decade.[6–12] Even at 380°C oxidation begins to result in a two-layer Sb_2O_3–Sb_2O_4 structure on the outside and $CoSb_2O_4$–$CoSb_2O_6$ on the inside. At temperatures up to approximately 600°C both layers are fairly stable and continue to grow in accordance with a parabolic rate law typical of a diffusion-controlled process, with opposing diffusion of Sb outwards and O inwards. When the inner layer reaches a specific thickness it splits into two distinct layers of $CoSb_2O_6$ and $CoSb_2O_4$. At higher temperatures, because of their relatively high vapor pressures, the antimony oxides begin to evaporate more quickly than the bulk material can be oxidized, so weight loss is observed. The antimony oxide layer is also very brittle and tends to form scales which spall off the surface when they reach a critical thickness, further enhancing degradation.

(Received June 30, 2013; accepted November 19, 2013;

For MGS a wide variety of different alloys are available, for example the solid solution $Mg_2Si_{1-x}Sn_x$, so the oxidation and sublimation behavior of such species is related to the particular composition of the material. Although there is relatively little published literature on this topic, some examination of pure Mg_2Si has been conducted.[13,14] TGA measurements showed that Mg_2Si remains unreacted in air up to 450–500°C, but above these temperatures reacts with O_2 to form MgO and Si. This is also a diffusion-controlled reaction; it is, therefore, important to limit the O_2 flow toward the surface of the bulk material. Recent studies using temperature-dependent x-ray diffraction showed that $Mg_2Si_{1-x}Sn_x$ starts to decompose in air at temperatures as low as 400°C.[15] MgO, Si, Sn, and other $Mg_2Si_{1-x}Sn_x$ solid solutions will separate as distinct phases on the surface of the bulk material and form a porous layer which does not hinder further oxidation and decomposition.

It is clear that to enable use of both SKD and MGS as high-temperature (>350–400°C) TEGs some form of protection against oxidation and sublimation is needed. One widely used method is full encapsulation in units which are filled with an inert gas, for example argon. Alternatively an aerogel can be cast around an entire leg assembly;[16,17] this also reduces parasitic heat loss. This module-level protection does, however, require more material in addition to the TE material, adding to the total cost. They are also fairly vulnerable to mechanical damage. Last, even if oxidation is hindered, unit-level protection is not sufficient to prevent sublimation on the surface of the TE material. Because a module is made of several TE legs connected in series, leg-level protection could have advantages with regard to price and simplicity of design and assembly and at the same time hinder both oxidation and sublimation. This could be achieved by addition of a protective layer during leg production.

Several coatings for leg-level protection, ranging from thin metal layers to thicker composite glass coatings, have already been evaluated for use on SKD.[18–25] The most important properties of a coating, in addition to hindering oxidation and sublimation of the TE material, should be low electrical and thermal conductivity, a coefficient of thermal expansion (CTE) matching that of the TE material, good adhesion to the substrate, and chemical inertness. It should also be applied by use of an inexpensive and reliable method of deposition which could be readily adapted for mass-production of legs.

In this work the thermal stability and degradation of $CoSb_3$ and $Mg_2S_{1-x}Sn_x$ were evaluated with candidate coatings for protection of the surface of TE legs in a module. The coatings have been tested by both aging and thermal cycling in air.

METHODS AND MATERIALS

For studies on SKD materials, undoped skutterudite, $CoSb_3$, supplied by TEGma, was cut into 2.94 mm cubes. The samples used for the coating tests were as-cut, whereas samples used for the oxidation tests were further polished with 1 μm diamond suspension. For experiments on magnesium silicide compounds, $Mg_2(Si_{0.4}Sn_{0.6})_{0.99}Sb_{0.01}$, produced at the Ioffe Institute (St Petersburg) through the ThermoMag program, were used. These samples also were polished by use of 1 μm diamond suspension. Oxidation experiments were conducted in a Lenton (UK) LTF 16/50/180 tube furnace with air-flow through the tube during thermal aging at 550°C, 600°C, and 650°C for SKD and 350°C, 370°C, and 400°C for MGS. The weight change of the samples were noted for aging times between 1 h and 333 h for SKD and from 1–48 h for MGS. Changes in surface structure were noted during the aging process. Several different types of coating were applied to the samples. These could be grouped into different oxide and metal coatings, silicone-Zn from KBS-coatings (US), boron nitride spray from Saint Gobain (France), and several glass ceramic coatings supplied by Advanced Technical Products Supply (USA).

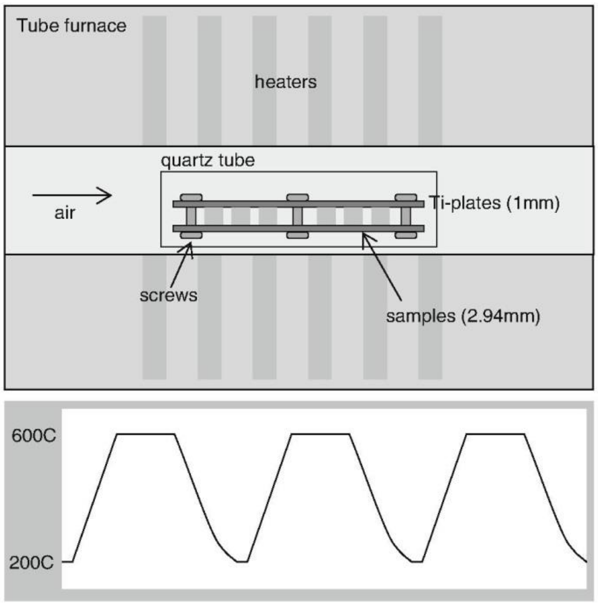

Fig. 1. Experimental set-up for thermal cycling of $CoSb_3$.

A small tube furnace made by Hugh Middleton at the University of Agder optimized for running with faster heating/cooling rates was used for the thermal cycling experiments. Two rows of six SKD samples, coated and uncoated, were fastened between two titanium plates 1 mm thick (Fig. 1) and placed inside a quartz tube located in the center of the furnace in the uniformly heated zone. Titanium was chosen as the clamp material because of its good CTE match (9 versus 10–11 for SKD). The furnace was then run in cycles between 200°C and 600°C with a dwell time at 600°C of 1 h and a ramp

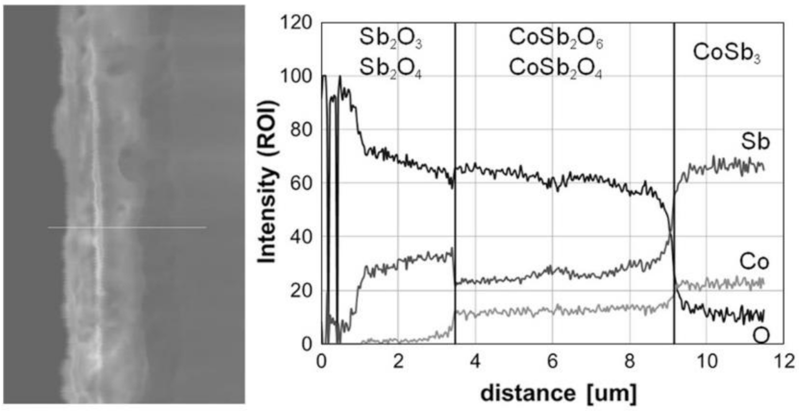

Fig. 2. Cross section of oxidized surface $CoSb_3$ after aging in air at 550°C for 24 h.

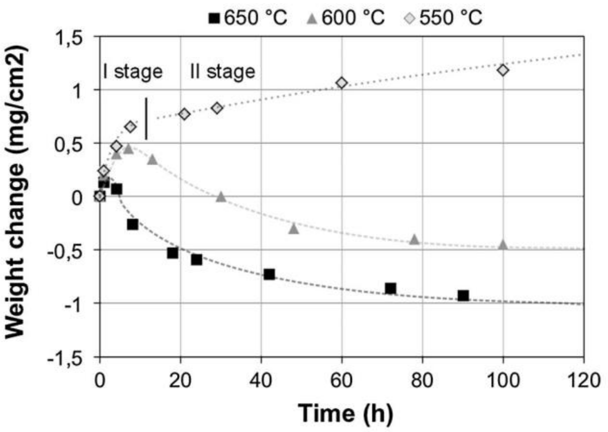

Fig. 3. Weight change of bulk $CoSb_3$ in air as a function of time and aging temperature. *Dotted lines* are included for illustration only.

rate of 10°C min^{-1}. The experiment lasted for a total of 180 cycles in 500 h. To identify reaction products, surfaces and cross sections of all samples from both aging and thermal cycling experiments were analyzed by use of a Jeol SEM 6400 with EDAX.

RESULTS AND DISCUSSION

Oxidation of $CoSb_3$

An example of the oxidation of $CoSb_3$ is given in Fig. 2. The oxide forms two distinct layers, an outer Sb_2O_3–Sb_2O_4 layer and an inner $CoSb_2O_4$–$CoSb_2O_6$ layer. It was difficult to identify the cobalt antimony oxides in the two separate layers; instead a more gradual decrease in oxygen content as a function of distance from the outer surface was observed.

Weight-change curves for oxidation of SKD are given in Fig. 3. At 550°C, oxidation of SKD follows a parabolic rate law in agreement with Refs. 9 and 10, i.e. $(\Delta m)^2 = k_p t$, where Δm is the change in mass per unit area and k_p the parabolic rate constant. The two different stages of oxidation described in Ref. 10 can also be seen; the first stage has a slightly higher k_p value than the second (5.6×10^{-6} kg^2 m^{-4} h^{-1} and 2.1×10^{-6} kg^2 m^{-4} h^{-1}, respectively). Both of these values are two orders of magnitude lower than reported in Ref. 9. This might be because of a coarser grain structure which would slow down the diffusion of both oxygen and antimony. The slight drop in mass between the two stages is possibly caused by scaling off of the outer oxide layers. At 600°C and 650°C a weight loss is observed. The first stage of the oxidation can still be seen, although only for the first 1–2 h of the oxidation process. The second stage behaves differently from that seen at lower temperatures. According to Ref. 10 an increase in oxidation rate is found at 583°C; this could be linked to the phase transition from α-Sb_2O_3 to β-Sb_2O_3 and a subsequent increase in evaporation, which would then be faster than the oxidation process resulting in a net mass loss.

Coatings and Thermal Cycling of $CoSb_3$

Most of the candidate coatings tested afforded little to no protection against oxidation and sublimation of SKD. The oxide coatings, silicone-Zn coating, and glass ceramic coatings were found to be either too porous or did not adhere sufficiently well to the SKD surface. The only coating product that hindered formation of the oxidation layer and simultaneously had good mechanical stability was an oxide–metal coating containing mostly Al_2O_3 (Fig. 4). The oxide layer was approximately 3.5 μm thick for the coated sample compared with 15–20 μm for the uncoated sample. No pure Sb_2O_4 layers formed; instead, the Sb diffused into the coating. The $CoSb_2O_4$ oxide adhered well to the unoxidized $CoSb_3$ thus precluding formation of $CoSb_2O_6$ and Sb_2O_4 layers; as a result the oxide layer was much more mechanically stable. The coating thus remained attached to the sample. The same coating was used on a sample during thermal cycling. In Fig. 5 it is apparent the coating eliminated oxidation almost completely; only a very thin intermediate layer approximately 1.5 μm thick

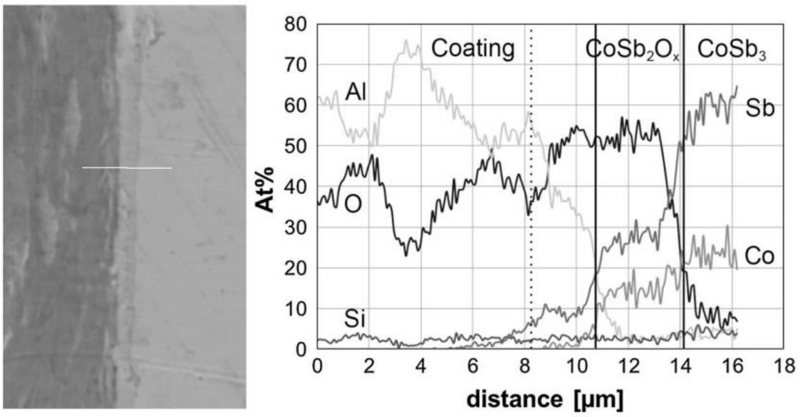

Fig. 4. Cross section of SKD with an Al–O coating after aging at 600°C in air for 48 h. The coating reduced oxidation of the SKD surface and hindered sublimation of Sb.

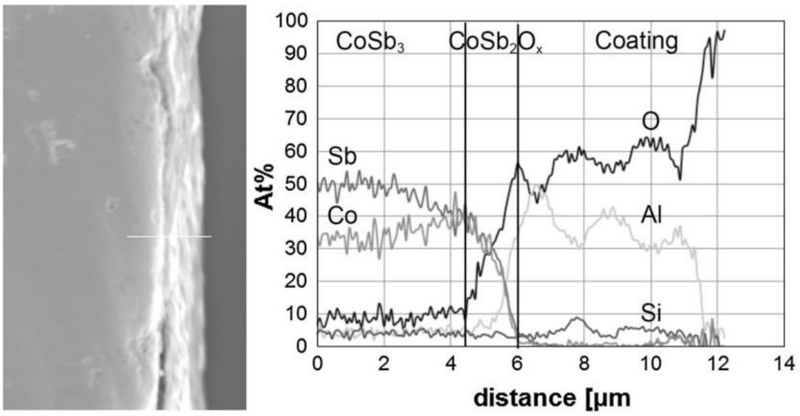

Fig. 5. Cross section of SKD with an Al_2O_3 coating after 180 cycles up to 600°C. The thin coating layer (~6 μm) seems to eliminate almost all oxidation of the SKD; only a thin layer of $CoSb_2O_4$ and $CoSb_2O_6$ approximately 1.5 μm thick, with a gradual transition into the coating layer, can be seen.

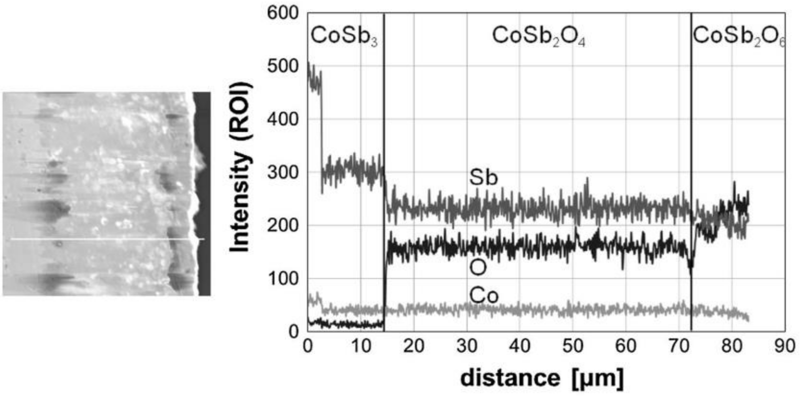

Fig. 6. Cross section of SKD coated with BN after 180 cycles up to 600°C. The BN coating peeled off during dismantling and preparation. A very thick (approx. 65–70 μm) oxide layer has formed.

formed after 180 cycles up to 600°C, a total of over 180 h at this temperature. On uncoated samples oxide layers were approximately 20 μm thick, which shows the coating effectively hindered both sublimation of Sb and oxidation of the bulk material. Another very important observation was that the coating layer was fully oxidized and both thermal losses and electrical conduction were kept to a minimum. Some cracks were observed between the substrate and the coating. This was most probably a result of sample preparation, because enhanced oxidation was not seen in places where visible cracks appeared. It was also found that thin layers were usually more mechanically stable than thick layers during thermal cycling. This was apparent for samples with thicker coating layers, on which oxide layers up to 10 μm thick were found.

A cross section view of an SKD sample coated with boron nitride (BN) after 180 cycles up to 600°C can be seen in Fig. 6. In this special case the oxide layer is three times thicker (65–70 μm) than that for uncoated samples. It is unclear whether this apparent increase in the amount of oxide is a result of the BN coating acting as a catalyst which increases the rate of oxidation or because the rate of oxidation was the same for the uncoated samples but the outer oxide layers evaporated and were not found in the cross sectional analysis. This can also be seen in Fig. 3, where mass loss is observed for samples exposed to temperatures >600°C. The BN coating is too porous to stop oxygen transport through the coating, but could still be dense enough to prevent sublimation and scaling of the outer oxide layers. This effect must be studied further, to enable understanding of the rate-limiting steps in the oxidation of $CoSb_3$ and how this knowledge could be used to manipulate the reaction kinetics.

Oxidation and Protection of Mg_2(Si–Sn)

No distinct oxidation layer was observed for the tested $Mg_2Si_{0.4}Sn_{0.6}$ sample, in contrast with $CoSb_3$. As is apparent from Fig. 7 the material was slightly inhomogeneous and contained some dark Si-rich regions with a composition approximating to $Mg_2Si_{0.7}Sn_{0.3}$.

After aging at 350°C for 24 h very little oxidation was observed; only for some parts of the surface was an increase of O content observed compared with room temperature. Slightly increased oxidation was observed for the sample heated for 48 h at 370°C. SEM and EDS analysis (using an acceleration voltage of 15 kV) of the surface facing the heat source revealed a uniform layer of MgO with some Sn content, but no Si was seen in the uppermost layer. On the other side of the sample, oxidation was more diverse and was related to phase composition, as is apparent from Fig. 6 and Table I. A general observation was that the higher the Sn content of the original phase, the higher the oxygen content.

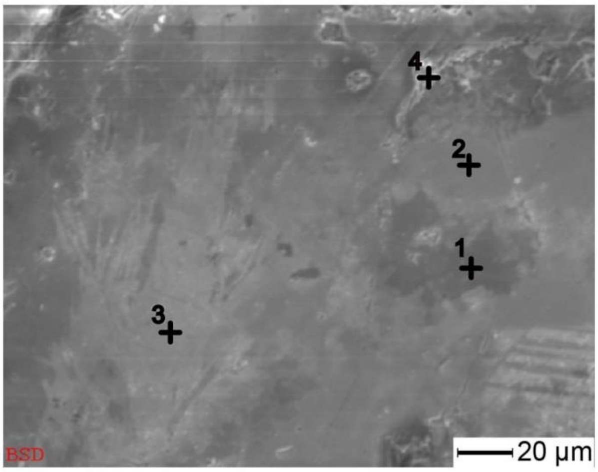

Fig. 7. Oxidized surface of $Mg_2Si_{0.4}Sn_{0.6}$ after 48 h at 370°C. Dark Si-rich regions have slightly lower MgO content than brighter Sn-rich regions. *Point 4* is almost fully oxidized.

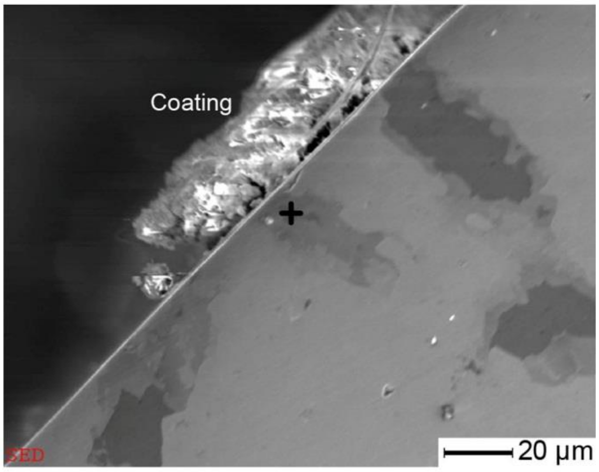

Fig. 8. Cross section of $Mg_2Si_{0.4}Sn_{0.6}$ coated with a Al_2O_3 coating after aging for 24 h at 400°C. No sign of degradation was observed.

Table I. Atomic percentage of each element present at points 1–4 in Fig. 7

	Mg	Si	Sn	O	Original phase
1	63.2	27.3	2.7	6.9	$Mg_2Si_{0.9}Sn_{0.1}$
2	53.0	6.3	14.0	26.7	$Mg_2Si_{0.32}Sn_{0.68}$
3	58.6	9.4	17.7	14.3	$Mg_2Si_{0.35}Sn_{0.65}$
4	44.6	2.6	4.3	48.6	$Mg_2Si_{0.38}Sn_{0.62}$
Average	57.3	10.3	13.9	18.5	$Mg_2Si_{0.43}Sn_{0.57}$

In other words, Sn-rich phases decompose much more quickly and at lower temperatures than Si-rich phases. The mechanism of evolution of the decomposition of Mg_2(Si–Sn) solid solution in air must be studied further.

Two samples of MGS, one uncoated and one completely coated with Al_2O_3, were aged in air at 400°C for 24 h. A high rate of decomposition was observed for the uncoated samples, with one half of the sample completely oxidized (seen as a black MgO porous layer). The decomposition and oxidation seems to self-propagate starting from one end of the sample and moving inwards. The highly exothermic oxidation of Mg could explain this "run-away" oxidation. The porous structure disintegrated almost completely on handling and so was difficult to analyze. No sign of Sn and Si were found in the outer layers. The coated sample showed no sign of degradation, as is apparent from Fig. 8. It is evident the coating must be very dense to avoid oxygen reaching the surface. Further work is required to determine if the coating can work at higher temperatures than those studied here.

CONCLUSION

Studies have been conducted on the thermal durability of pure $CoSb_3$ and pure $Mg_2Si_{0.4}Sn_{0.6}$ in air, and different coatings were tested in attempts to prevent degradation of the TE materials over time. Reaction kinetics and products of oxidation of $CoSb_3$ were studied. Oxide layers seemed fairly stable during thermal cycling; no increase in the rate of oxidation occurred as a result of cracking and/or scaling of the outer oxide layers. Although several coatings were tested, only Al_2O_3 afforded effective protection from oxidation. After 180 cycles up to 600°C, oxide layers were reduced from 20 μm for uncoated samples to 1.5 μm for coated samples. All the other coatings tested were either too porous, so O_2 and Sb diffusion was not hindered sufficiently, or did not adhere sufficiently well. Moreover, mechanical instability as a result of CTE mismatch with the substrate resulted in formation of cracks between coating and substrate.

Initial studies of the oxidation reactions of Mg_2(Si–Sn) solid solutions showed that onset and speed of oxidation were functions of the Sn content of the solid solution. Even at temperatures as low as 350–370°C $Mg_2Si_{0.4}Sn_{0.6}$ started to decompose into MgO, Sn, Si, and other solid solutions of $Mg_2Si_{1-x}Sn_x$. At 400°C the rate of reaction increases substantially and large black porous crystals of MgO grow rapidly from the bulk material in a self-propagating manner, because oxidation of Mg is highly exothermic. Addition of an Al_2O_3 coating effectively hindered oxidation and decomposition at this temperature. This coating is also believed to work at higher temperatures.

ACKNOWLEDGEMENT

The authors wish to acknowledge financial support from the ThermoMag Project, which is co-funded by the European Commission in the 7th Framework program (contract NMP4-SL-2011-263207), by the European Space Agency and by the individual partner organizations.

REFERENCES

1. L.L.N. Library, *U.S. Energy Flow* (2011) [cited 15 April 2013]. Available from: https://flowcharts.llnl.gov/energy.html#2011.
2. G.J. Snyder and E.S. Toberer, *Nat. Mater.* 7, 105 (2008).
3. H. Alam and S. Ramakrishna, *Nano Energy* 2, 190 (2013).
4. X. Shi, J. Yang, J.R. Salvador, M. Chi, J.Y. Cho, H. Wang, S. Bai, J. Yang, W. Zhang, and L. Chen, *J. Am. Chem. Soc.* 133, 7837 (2011).
5. V.K. Zaitsev, M.I. Fedorov, E.A. Gurieva, I.S. Eremin, P.P. Konstantinov, A.Y. Samunin, and M.V. Vedernikov, *Phys. Rev. B* 74, 045207 (2006).
6. R. Hara, S. Inoue, H.T. Kaibe, and S. Sano, *J. Alloy. Compd.* 349, 297 (2003).
7. J. Leszczynski, A. Malecki, and K.T. Wojciechowski, *International Conference on Thermoelectrics* (2007).
8. E. Godlewska, K. Zawadzka, A. Adamczyk, M. Mitoraj, and K. Mars, *Oxid. Met.* 74, 113 (2010).
9. D. Zhao, C. Tian, S. Tang, Y. Liu, and L. Chen, *J. Alloy. Compd.* 504, 552 (2010).
10. J. Leszczynski, K. Wojciechowski, and A. Malecki, *J. Therm. Anal. Calorim.* 105, 211 (2011).
11. D. Zhao, C. Tian, Y. Liu, C. Zhan, and L. Chen, *J. Alloy. Compd.* 509, 3166 (2011).
12. X. Xia, P. Qiu, X. Shi, X. Li, X. Huang, and L. Chen, *J. Electron. Mater.* 41, 2225 (2012).
13. M. Riffel and J. Schilz, *International Conference on Thermoelectrics* (1997), pp. 283–286.
14. J.-I. Tani, M. Takahashi, and H. Kido, *J. Alloy. Compd.* 488, 346 (2009).
15. H. Scherrer, F. Gascoin, Q. Recour, D. Berthebaud, P. Zwolenski, L. Chaput, B. Wiendlocha, J. Tobola, and J. Bourgeois, *Funct. Mater. Lett.* 06, 1340005 (2013).
16. J.S. Sakamoto, G.J. Snyder, T. Calliat, J.-P.S. Fleurial, M. Jones, and J.-A. Palk, US 7,461,512 B2, 9 Dec 2008.
17. J. Salvador, J. Cho, Z. Ye, J. Moczygemba, A. Thompson, J. Sharp, J. König, R. Maloney, T. Thompson, J. Sakamoto, H. Wang, A. Wereszczak, and G. Meisner, *J. Electron. Mater.* 42, 1389 (2012).
18. H.H. Saber and M.S. El-Genk, *Energy Convers. Manag.* 48, 1383 (2007).
19. H.H. Saber, M.S. El-Genk, and T. Caillat, *Energy Convers. Manag.* 48, 555 (2007).
20. E. Godlewska, K. Zawadzka, R. Gajerski, M. Mitoraj, and K. Mars, *Ceram. Mater.* 62, 490 (2010).
21. E. Godlewska, K. Zawadzka, K. Mars, R. Mania, K. Wojciechowski, and A. Opoka, *Oxid. Met.* 74, 205 (2010).
22. P. Wei, C.-L. Dong, W.-Y. Zhao, and Q.-J. Zhang, *J. Inorg. Mater.* 25, 577 (2010).
23. H. Dong, X. Li, X. Huang, Y. Zhou, W. Jiang, and L. Chen, *Ceram. Int.* 39, 4551 (2013).
24. H. Dong, X. Li, Y. Tang, J. Zou, X. Huang, Y. Zhou, W. Jiang, G.-J. Zhang, and L. Chen, *J. Alloy. Compd.* 527, 247 (2012).
25. K. Zawadzka, E. Godlewska, K. Mars, and M. Nocun, *AIP Conf. Proc.* 1449, 231 (2012).

Paper 2: The Influence of Synthesis Procedure on the Microstructure and Thermoelectric Properties of p-type Skutterudite $Ce_{0.6}Fe_2Co_2Sb_{12}$

Journal of ELECTRONIC MATERIALS
DOI: 10.1007/s11664-015-4046-4

The Influence of Synthesis Procedure on the Microstructure and Thermoelectric Properties of *p*-Type Skutterudite $Ce_{0.6}Fe_2Co_2Sb_{12}$

A. SESSELMANN,[1] G. SKOMEDAL,[2,4] H. MIDDLETON,[2] and E. MÜLLER[1,3]

1.—Institute of Materials Research, German Aerospace Centre (DLR), Linder Hoehe, 51147 Cologne, Germany. 2.—Faculty of Engineering and Science, University of Agder, 4879 Grimstad, Norway. 3.—Institute of Inorganic and Analytical Chemistry, Justus Liebig University Giessen, Heinrich-Buff-Ring 58, 35392 Giessen, Germany. 4.—e-mail: gunstein.skomedal@uia.no

We have investigated *p*-type skutterudite samples with the nominal composition $Ce_{0.6}Co_2Fe_2Sb_{12}$ synthesized from elementary constituents by gas atomization and conventional melting, and also those synthesized from ternary and binary phases such as $Fe_xCo_{1-x}Sb_2$ and $CeSb_2$, respectively, which were mixed and subsequently ball-milled. We conducted measurements of the temperature-dependent transport properties (Seebeck coefficient, thermal/electrical conductivity) and carried out scanning electron microscope analysis, electron probe micro-analysis and powder x-ray diffraction to obtain information about microstructure and elementary distribution of the phases. We show that the presented synthesis methods each possess particular strengths but ultimately, however, lead to different final compositions of the skutterudite phase and secondary phases, which significantly influence the thermoelectric properties of the material. Material prepared using an educt method gave the best thermoelectric properties with a peak ZT of 0.7. Furthermore, we show that even an apparent homogeneous skutterudite area within the material exhibits varying stoichiometry in each grain even though they conform to the solubility range of cerium in this *p*-type skutterudite. Moreover, we show that marcasite is preferred as an educt over the arsenopyrite phase and discuss the formation of the *p*-type skutterudite phase with these synthesis techniques.

Key words: *p*-Type skutterudite, synthesis, microstructure, peritectic reaction, transformation rate

INTRODUCTION

Filled skutterudites are today among the most efficient thermoelectric materials in the temperature range between room temperature and 500°C.[1] This is because this class of materials can exhibit a high Seebeck coefficient S, high electrical conductivity σ and a concomitant low thermal conductivity κ, which can be mathematically quantified as the figure-of-merit, $ZT = S^2\sigma T/\kappa$. The chemical composition of a filled skutterudite is $R_xT_4Pn_{12}$, (R = filler, T = transition metal, Pn = pnicogen) and high ZT is observed especially for antimonides (Pn = Sb), which can be synthesized as *n*- and *p*-type materials. The latter are usually obtained by introducing electron-deficient species on the transition metal site (e.g. Co substituted by Fe). The optimal filling fraction of R (e.g. Ce) is strongly dependent on the Co/Fe ratio and therefore complicates the synthesis of *p*-type skutterudites.

The conventional synthesis of skutterudites is usually done by mixing stoichiometric amounts of the constituents and subsequently heating the material in vacuum or inert atmosphere above 1050°C until an entire liquid phase is reached. This

---

(Received June 2, 2015; accepted September 7, 2015)

mixture is then rapidly cooled down to room temperature. Thereafter, no considerable amount of skutterudite phase has formed, but several secondary phases are obtained. To reach phase pure filled skutterudite, the samples are annealed for a prolonged time at temperatures significantly below the peritectic decomposition temperature of the specific skutterudite. There are further approaches such as melt spinning techniques,[2,3] gas atomizing[4] or high energy ball milling followed by SPS,[5] which reduce the annealing time drastically.

An alternative approach to the usual mixing of all materials is to make educts which are similar to the secondary phases reached by rapid cooling of the melt. Chen et al. used this method to prepare $Ba_xFe_yCo_{4-y}Sb_{12}$ samples by first making precursors of $BaSb_3$ and $Fe_xCo_{1-x}Sb_2$, then crushing and mixing them with Sb before pressing and sintering.[6,7]

In this work, we discuss the mechanisms and kinetics governing the formation of skutterudite after peritectic solidification and transformation of the secondary phases with a special focus on short-term synthesis routes which are interesting from a commercial point of view. We have chosen to synthesise material with a 1:1 ratio of Fe/Co, to observe secondary phases, which occur due to the Fe and Co fraction, respectively. We are aware that higher ZT has been reported for both lower and higher Fe content.[8,9] Ce was chosen as filler element and the filling fraction set at 0.6 as this is the maximum filling fraction for the given Fe/Co ratio.[10] We present and compare different synthesis routes of skutterudites with the nominal composition $Ce_{0.6}Fe_2Co_2Sb_{12}$, which are studied with regard to the evolution of microstructure, the impurity phases and the thermoelectric properties.

EXPERIMENTAL PROCEDURE

Four different synthesis routes were used to prepare polycrystalline $Ce_{0.6}Fe_2Co_2Sb_{12}$ skutterudites.

(1) Stoichiometric quantities of Co (pellets, 99.99%; Goodfellow), Fe (pellets 99.99%; Goodfellow), Sb (shot, 99.999%; Alfa Aesar) and Ce (99.9%; Alfa Aesar) were mixed and sealed under vacuum in a quartz tube. The material was heated to 1150°C for 2 h and rapidly air-cooled to inhibit peritectic decomposition. Subsequently the sample was ground manually using a mortar and a pestle.

(2) Precursor material containing Ce, Fe and Co was prepared by arc-melting under Ar atmosphere. Together with further Fe, Co and Sb the material was inductively melted at 1250°C for 30 min and then cooled in a vacuum. The main difference between sample (1) and (2) is thus the slower cooling rate for sample (2).

(3) Two educts, $CeSb_2$ and $Fe_{0.5}Co_{0.5}Sb_2$, were synthesized by arc-melting and induction-melting (at 1100°C), respectively. The educts together with an addition of Sb was ball-milled for 15 min with 400 rpm using steel balls (ball to sample ratio of 50:1). The net chemical reaction between the phases was $0.6\ CeSb_2 + 4\ Fe_{0.5}Co_{0.5}Sb_2 + 2.8\ Sb = Ce_{0.6}Fe_2Co_2Sb_{12}$ and was achieved by further sintering and annealing.

(4) The powder for sample (4) was obtained by gas atomizing of a melt from the elementary constituents at 1150°C under argon atmosphere. In all samples, an addition of 1 wt.% Sb were added to compensate for any sublimation losses.

The phase transformation into skutterudite was achieved by compacting the obtained powders from methods 1–4 with a direct current assisted sintering device (DSP 510; Dr. Fritsch) at 48 MPa and 630°C for 60 min. Annealing of the sample from method 1 was performed in an evacuated chamber backfilled with argon at 630°C for 48 h. Additionally, parts of sample (2) were also annealed immediately after solidification (without grinding and pressing) to analyze the peritectic solidification and transformation.

Samples were analyzed with powder x-ray diffraction (XRD; Bruker D8 Advance), scanning electron microscopy (SEM), energy dispersive x-ray spectroscopy (EDX; both with Zeiss Ultra 55) and electron probe micro-analysis (EPMA; JEOL JXA-8500F). The actual composition of the skutterudite phase was calculated as an average between 7 and 10 points over the sample analyzed with EPMA. The thermoelectric properties were measured using an in-house device to sense the Seebeck coefficient and the electrical conductivity simultaneously as a function of temperature. Thermal diffusivity measurement was carried out by a laser flash analyzer (LFA; Netzsch) together with density measurements by the Archimedes method. The thermal capacity c_p was calculated using the Dulong–Petit law ($c_p = 0.23\ \mathrm{Jg^{-1}\ K^{-1}}$). The lattice thermal conductivity κ_L data was calculated by using the relationship between the lattice and the electronic thermal conductivity κ_e ($\kappa = \kappa_L + \kappa_e$) and the Wiedemann–Franz law, ($\kappa_e = L\sigma T$), where T is the absolute temperature and L is the Lorenz number. Furthermore, L was obtained by using the single parabolic band model with $L = \left(\frac{k_B}{e}\right)^2 \frac{3F_0(\eta)F_2(\eta)-4F_1(\eta)^2}{F_0(\eta)^2}$, with k_B being the Boltzmann constant, e the electronic charge, F the Fermi–Dirac integral and η the reduced Fermi energy.[11]

RESULTS AND DISCUSSION

In Fig. 1, the diffractograms of the samples show predominantly skutterudite phase, except for sample (2) which only exhibits secondary phases. Electron probe micro-analyses reveal that the samples (1, 3 and 4) with identical starting composition, i.e.

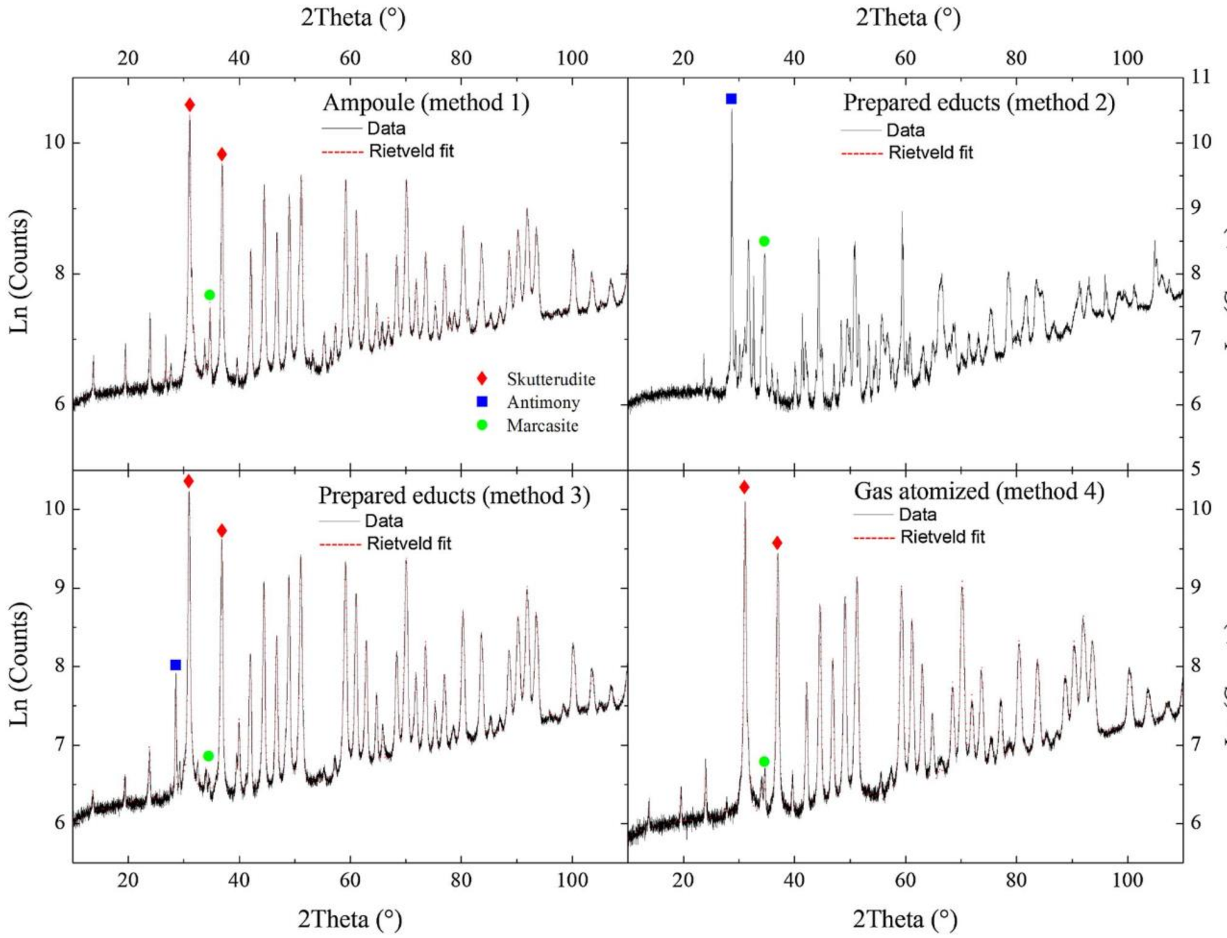

Fig. 1. X-ray diffractograms of $Ce_{0.6}Fe_2Co_2Sb_{12}$ samples from different synthesis routes after direct current-assisted sintering (except sample 1, which was annealed for 48 h at 630°C). The *y* scale is logarithmic to magnify the secondary phases. The red diamond indicates different (*hkl*) planes of the skutterudite phase. The impurity phases are marked with other symbols (Color figure online).

$Ce_{0.6}Fe_2Co_2Sb_{12}$, end up with different stoichiometry of the particular skutterudite phase (Table I).

Skutterudite Composition and Secondary Phases

Sample (1) shows a stoichiometry of $Ce_{0.47}Fe_{1.82}Co_{2.18}Sb_{11.89}$, and represents an overbalance of Co over Fe and a Ce and Sb deficiency of the target skutterudite composition. The lack of Ce is substantial and is around 28% when the maximum filling fraction of 0.6 at a 1:1 Fe/Co ratio is considered. The residual Ce forms oxides or a $CeSb_2$ phase, which was verified by SEM imaging. Phase analysis of the diffractograms also detected a significant amount of $FeSb_2$ marcasite phase, which is around 6% according to XRD refinement. Sample (1) is coarse-grained, which means that further skutterudite phase transformation is hindered by long diffusion paths of secondary phases. Even though no skutterudite was found in the diffractogram of sample (2), SEM/EDX and EPMA (Fig. 2) also shows significant amounts of skutterudite along with a multitude of secondary phases, foremost Sb, $Fe_xCo_{1-x}Sb_2$, $CeSb_2$, $Fe_xCo_{1-x}Sb$, and to a small extent oxides containing Ce. Due to the large inhomogenities in the skutterudite phase at this stage with very little annealing, the XRD peaks were broad and possibly overlap with other phases so it could not be accurately determined from the diffractograms. In fact, the local composition of the skutterudite phase according to EDX and EPMA ranged from almost fully filled $CeFe_4Sb_{12}$ to unfilled $Fe_{0.5}Co_{3.5}Sb_{12}$. This will be further discussed in the next section.

For sample (3), the Sb, $Fe_xCo_{1-x}Sb_2$ and $CeSb_2$ precursor phases were prepared and subsequently ball-milled and compacted, i.e. there is no melting step after the formation of the prepared phases. It has to be noted that the phase purity of $CeSb_2$ and $Fe_xCo_{1-x}Sb_2$ was not verified by XRD and was directly processed to further synthesize the skutterudite material. Due to the peritectic nature of both phases, it is possible that the phases partly decompose during arc-melting or further processing. Still, the final sample shows a much higher

Table I. Results of the electron microprobe measurements of the $Ce_{0.6}Fe_2Co_2Sb_{12}$ samples and Rietveld refinement results (volume fraction of the phases) with different synthesis routes

						(vol.%)					
#	Synthesis	EPMA	Density (g/cm^3)	r_{wp}, GOF	Lattice parameter of γ (Å)	skutterudite (γ)	$Fe_xCo_{1-x}Sb$ (α)	$Fe_xCo_{1-x}Sb_2$ (β)	Sb	$CeSb_2$	Other (C, oxides)
1	Elementary constituents (bulk)	$Ce_{0.47}Fe_{1.82}Co_{2.18}Sb_{11.89}$	7.77	5.14, 2.16	9.0931	88	1	6	–	<1	4
3	$CeSb_2 + Fe_{0.5}Co_{0.5}Sb_2$ + Sb	$Ce_{0.43}Fe_{1.97}Co_{2.03}Sb_{11.97}$	7.70	5.98, 2.45	9.0860	93	–	<1	5	<1	<1
4	Elementary constituents (gas atomized)	$Ce_{0.54}Fe_{2.03}Co_{1.97}Sb_{11.85}$	7.62	6.07, 2.28	9.0834	96	–	3	–	<1	<1

fraction of skutterudite (93%) than sample (1), and has much lower proportions of the marcasite $Fe_xCo_{1-x}Sb_2$ phase and significantly higher fractions of Sb (5 wt.%). According to EPMA, the composition of sample (3) is $Ce_{0.43}Fe_{1.97}Co_{2.03}Sb_{11.97}$, and thus is close to the initial composition for the Fe/Co ratio and the Sb content. The deficiency of Ce within the skutterudite stoichiometry is considerable and almost equal to sample (1). Sample (4), which was gas-atomized from elementary constituents, comprises the highest portion of skutterudite phase among the samples (96 wt.%). The final composition of sample (4) is $Ce_{0.54}Fe_{2.03}Co_{1.97}Sb_{11.85}$ and therefore does not suffer from a Ce deficit in comparison to the other routes. However, no elementary Sb was found in sample (4) and, furthermore, a deficiency of Sb within the skutterudite phase is detectable. The latter indicates that, during the synthesis/processing of the material, an evaporation of Sb takes place and that a surplus of Sb of around 1% of the initial weight would not be enough to compensate the loss of Sb. SEM images of sample (3) and (4) are found in Fig. 3.

For all samples, the relative short annealing time compared with traditional synthesis approaches (with typical 7 days annealing) is the main reason for the remnant secondary phases found in both XRD and SEM. The short annealing time also leads to non-homogenous samples with broad variations in composition over the sample (see Fig. 4). In the diffractograms, we can identify broader peaks, particularly at high angles, which can increase the uncertainty of the determination of the lattice parameter and phase purity, respectively. This is seen for samples (3) and (4) which exhibit almost the same lattice parameter of the skutterudite phase (Table I), but possess significantly different Ce filling fractions. The filler atom usually increases the lattice parameter, which can be easier separated in compositions with only one atom species on the 8c transition metal site (e.g. Co). Kitagawa et al. found a linear relationship between the lattice parameter and the Ce filling fraction of Fe-doped skutterudite.[12] The lattice parameters are in good agreement when the EPMA data is taken as source for the compositional values and the formula of the linear regression from Kitagawa et al.[12] is applied (max. 0.15% deviation). For the gas-atomized sample, a high strain of the lattice can be observed in the diffractograms which can explain the relatively low lattice parameter compared to the other samples when the EPMA composition is considered. It can be assumed that this high lattice strain is due to the rapid quenching of the material, and, subsequently, many defects induced in the powder, and that it may disappear with prolonged annealing. Marcasite phase (β) was found in all the samples, and additionally small portions of the structurally related arsenopyrite can also be found in the diffractogram. However, distinction between both phases is difficult in the multiphase diffractogram,

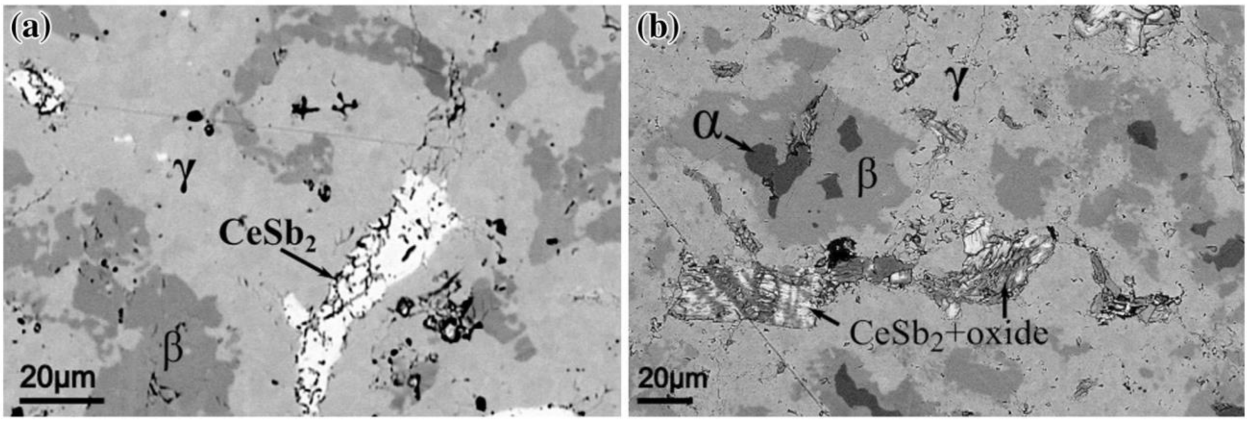

Fig. 2. SEM images of $Ce_{0.6}Fe_2Co_2Sb_{12}$ samples with different synthesis routes; image (a) represents method (1), image (b) represents method (2). Skutterudite (γ) is the main phase in both samples. Secondary phases are $Fe_xCo_{1-x}Sb$ (α), $Fe_xCo_{1-x}Sb_2$ (β), $CeSb_2$ and oxides, respectively.

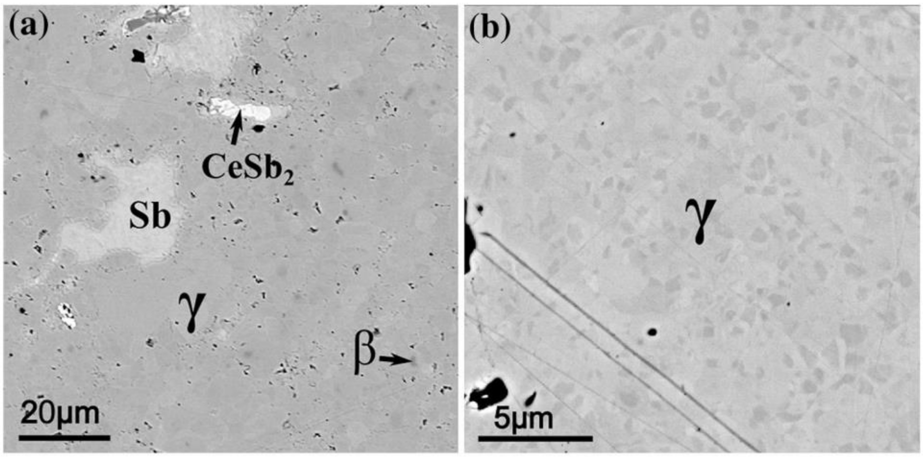

Fig. 3. SEM images of $Ce_{0.6}Fe_2Co_2Sb_{12}$ samples 3 (a) and 4 (b). In image (a) the main phase is skutterudite (γ), light areas are $CeSb_2$ and Sb and small dark grains are the remaining $Fe_xCo_{1-x}Sb_2$ (β). In image (b) the different grey tones represent varying orientation of skutterudite grains.

since the arsenopyrite crystal structure is a subgroup of the marcasite (and pyrite) type, i.e. a marcasite crystal can be mathematically described as an arsenopyrite crystal.[13] On the other hand, $FeSb_2$ does only occur as marcasite, whereas $CoSb_2$ (and $Fe_xCo_{1-x}Sb_2$, with $x > 0.5$[14]*) undergoes a phase transition from arsenopyrite to marcasite at around 650 K.[15] The electronic state of $CoSb_2$ as a marcasite phase seems to be energetically less favorable,[16–18] and it can be assumed that the marcasite structure is preferred over the arsenopyrite for the synthesis of the skutterudite phase.

Furthermore it should be noted that orthorhombic $CeSb_2$ was hardly detectable in XRD due to the high crystallinity of the skutterudite phase and overlap of several peaks with the skutterudite phase and other secondary phases. For this reason, it is recommended to also ensure phase purity with, e.g., SEM additional to XRD analysis (see Figs. 2 and 3).

Filling Fraction

In Fig. 4, the Fe content and Ce filling in the skutterudite phase based on EPMA measurements is plotted for different grains. Our data are normalized on the transition metal site (Co, Fe), i.e. it is assumed to be fully occupied. It is clearly observable that the Ce/Fe ratio follows a nearly linear relationship for all samples. Earlier work on the filling fraction limit (FFL) of Ce as a function of the Fe content in $Ce_yFe_xCo_{4-x}Sb_{12}$ is also shown for comparison. The FFL of Ce in $Ce_yCo_4Sb_{12}$ is around $y = 0.05$–0.08,[8–10,19,20] although recent reports have claimed that a much higher FFL is possible using solvothermal synthesis.[21] For unfilled material, $Fe_xCo_{4-x}Sb_{12}$, the maximum Fe content is $x = 0.8$,[22] while a minimum filling of 0.8 is found for $Ce_yFe_4Sb_{12}$,[23] thus a minimum filling fraction can be

---

*The transition temperature will be different in comparison to pure $CoSb_2$, if a phase transformation exists.

assumed to follow a straight line from $y = 0$ and $x = 0.8$ up to $y = 0.8$ and $x = 4$. All measured grains in our samples are found lying on lines inbetween this minimum and maximum filling fraction indicated in Fig. 4. The gas-atomized sample (4) is the one that best resembles the nominal composition ($y = 0.6$, $x = 2$), with very little spread. Sample (1) shows a higher spread of the grain composition along the line of the reported Ce/Fe ratio.[8] Sample (3) grain compositions lie on a line even further down close to the minimum filling fraction line. Generally, the average Ce filling fraction in our samples seems to be a little lower than the initial composition, with $y = 0.6$, and the Fe content is more (samples 3 and 4) or less (sample 1) balanced. Furthermore, we do not see any direct correlation between Ce (as a filling atom) and Sb (as the pnicogen) in the skutterudite phase. It is interesting that the gas-atomized sample possesses an apparent Sb deficit (or alternatively additional Fe/Co interstitials), which does not correlate with the Ce filling fraction. According to SEM and EPMA analyses, we conclude that in the case that the Ce content for a certain Fe content reaches the minimum line, the secondary phases $Fe_xCo_{1-x}Sb_2$ (β) are more stable (thermodynamically more favorable) and no phase pure material can be achieved. Longer synthesis time will therefore often result in more secondary phases if this is not compensated for by adding excess Ce and Sb above the stoichiometric composition. Besides a well-mixed state of the different secondary phases, it is advisable to work in the upper part of the solubility region, i.e. close to $\gamma + CeSb_2$, to ensure phase purity of the final compound. It should be emphasized that the samples presented here did not undergo a long annealing step, especially in the case of method 3 and 4. As a consequence, the inhomogeneities especially between the skutterudite grains may be metastable, which presents a topic to investigate in future studies.

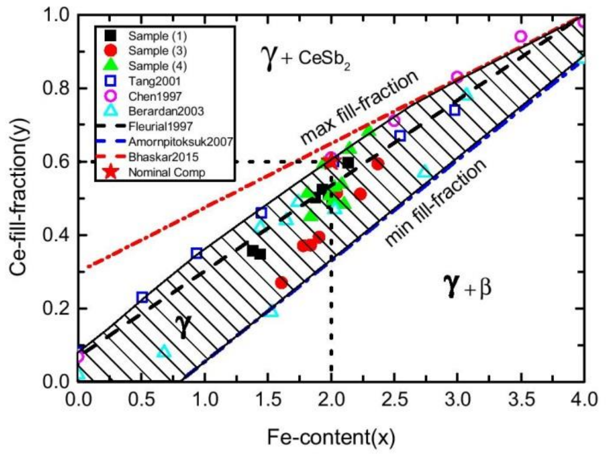

Fig. 4. EPMA point analyses of $Ce_{0.6}Fe_2Co_2Sb_{12}$ samples from different synthesis routes, compared to reported minimum and maximum Ce/Fe ratio. Stability zone of the skutterudite phase, γ, are indicated, as well as two (or more) phase zones directly above and below the max and min filling fraction.

Peritectic Solidification and Transformation

To get a better understanding of the peritectic solidification and transformation of p-type skutterudites, parts of sample (2) were annealed directly from solidified material at 610°C for 2 h and 6 h. In Fig. 5, the microstructure of sample (2) directly after solidification is shown. The microstrucure resembles the expected phases formed during a relatively slow peritectic solidification from the liquid state:[24]

- Peritectic solidification of $CeSb_2$ below liquidus temperature ($T_L^{CeSb_2} \approx 1000°C$) and Sb (solidifies below 630°C).[25]
- Nucleation of $Fe_xCo_{1-x}Sb$ (α) followed by dendritic growth between the liquidus temperature ($T_L^{\alpha} \approx 950°C$) of α and the peritectic temperature ($T_P^{\beta} \approx 850°C$) of $Fe_xCo_{1-x}Sb_2$ (β).[22]
- Nucleation of β on the α surface according to the peritectic reaction $\alpha + L = \beta$, followed by peritectic transformation of $\alpha \rightarrow \beta$ by diffusion of Sb through the β layer.

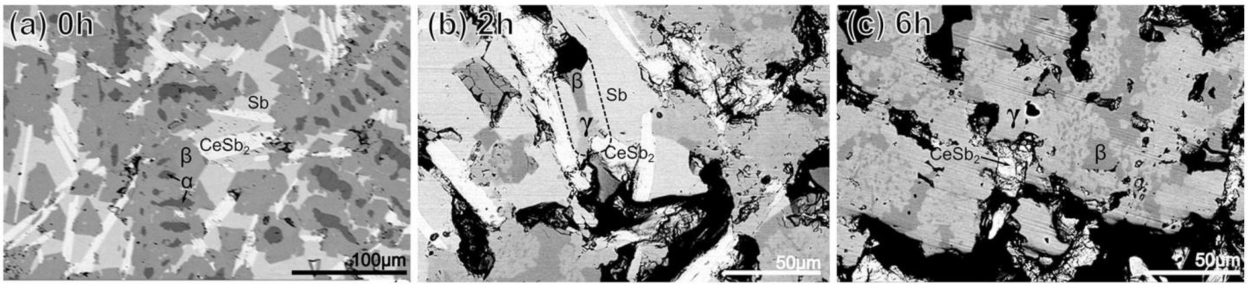

Fig. 5. SEM pictures of sample (2) taken directly after solidification (a) and after 2 h (b) and 6 h (c) of annealing at 610°C, respectively. For the non-annealed sample no skutterudite (γ) is found, but after 2 h of annealing γ is seen growing between $Fe_xCo_{1-x}Sb_2$ (β) and $CeSb_2$. Due to Sb sublimation, large pore structures form during solidification and the full peritectic transformation of β into γ is limited by Sb deficiency.

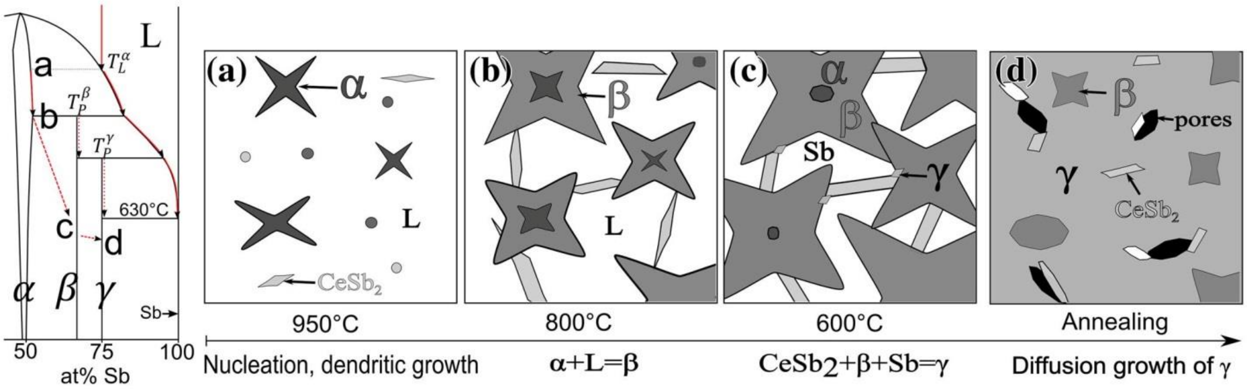

Fig. 6. Schematic drawing of the steps in formation of skutterudite phase (γ) during solidification (a–c) and annealing (d). A sketched phase diagram of the peritectic system Co/Fe-Sb is shown on the left. α and $CeSb_2$ nucleates and grow (dendritic and nodular, respectively) until T_P^β is reached. β forms first by the peritectic reaction $\alpha + L = \beta$, then by diffusion of Sb through β to the α/β interface. Upon further cooling, nucleation and growth of γ is inhibited by remnant α phase and relatively few nucleation spots. Additional annealing below T_P^γ is needed to form γ. The formation of γ is primarily governed by diffusion of Ce and Sb through the growing γ phase towards the γ/β interface, as well as opposite diffusion of Fe/Co. Pores appears due to a combination of Sb sublimation and density differences between the reactants and products of the annealing.

The resulting microstructure is then composed of these four phases with volume fractions estimated based on SEM data as 9.2% of $CeSb_2$, 22.7% of Sb, 59.2% of β and 8.3% of α phase. The filled skutterudite phase γ can in principle evolve from pure elements (diffusively) from an unfilled skutterudite phase plus filler (diffusively) or, as in our case, from several phases, which form due to a melting step within our different synthesis approaches:

$$y\mathrm{CeSb_2} + (4-2y)\mathrm{Sb} + \mathrm{Fe}_x\mathrm{Co}_{4-x}\mathrm{Sb}_8 = \mathrm{Ce}_y\mathrm{Fe}_x\mathrm{Co}_{4-x}\mathrm{Sb}_{12} \tag{1}$$

In sample (2), where an additional α phase has formed, no traces of skutterudite were found at the intersections between β, Sb and $CeSb_2$ directly after solidification, which indicates a slow transformation rate and/or a competitive process, such as the diffusion of Sb through β to fully transform the α phase. The latter is a known kinetic effect seen in diffusion phase competition during the formation of intermetallic compounds with a narrow solubility range over a concentration gradient.[26]

The final steps of the transformation into (almost) phase pure γ are seen in Fig. 5 after 2 and 6 h of annealing of sample (2). The intermediate product before complete phase transformation will appear as islands of remaining β and $CeSb_2$/Sb separated by γ. This is what we also observed in the SEM micrograph for sample (1) (see Fig. 2a). Based on the phase diagram of the Co-Fe-Sb and Ce-Sb system in addition to SEM pictures, the entire process from peritectic solidification to almost full transformation is sketched in Fig. 6. This scheme may be generalized to many other *p*-type skutterudites, where Ce is replaced by other filler atoms and the Fe/Co ratio is different. For other filler elements, the solubility in α or β could be higher, or form phases at lower temperatures. However, the general principle should remain the same for most of the common filler elements used in *p*-type skutterudite.

It is obvious that the formation of α greatly impedes the formation of a skutterudite phase and significantly changes the Co/Fe ratio. As a consequence, it is highly recommended to cool the melt as fast as possible between the temperature range of T_L^α and T_P^β which is a common strategy when syntehsising peritectic phases. This shows the advantages of methods 3 and 4, which did not exhibit any α phase, and can be attributed to the used educts and processing (method 3 with small grain size) and the extremely rapid cooling in the case of the gas-atomized sample (method 4), respectively.

The transformation from the different secondary phases into the filled skutterudite phase is diffusion-controlled and therefore can be put into a diffusion model to estimate the kinetics of the transformation.[27,28] We assume uniformly distributed spherical particles with average radii R_0 and employ the Ginstling–Brounshtein model which is frequently used to fit kinetic data for three dimensional diffusion:

$$f(\alpha_\gamma) = 1 - (2/3)\alpha_\gamma - \left(1-\alpha_\gamma\right)^{2/3} = kt \tag{2}$$

where k is the rate constant and α_γ is the degree of conversion which in our case represents the area fraction of the phase found by image analyses of SEM pictures. The rate constant k is defined as $k = 2DC_0/\varepsilon R_0^2$, where C_0 is the concentration of the diffusing species at the γ/β interface and ε is a proportionalty constant. By plotting $f(\alpha_\gamma)$ against t and using linear regression, k is found from the slope. In Fig. 7a, $f(\alpha_\gamma)$ is plotted for different times and temperatures and shows a relativly good fit to the model. Since k is the rate constant for a temperature activated process, the Arrhenius expression applies,

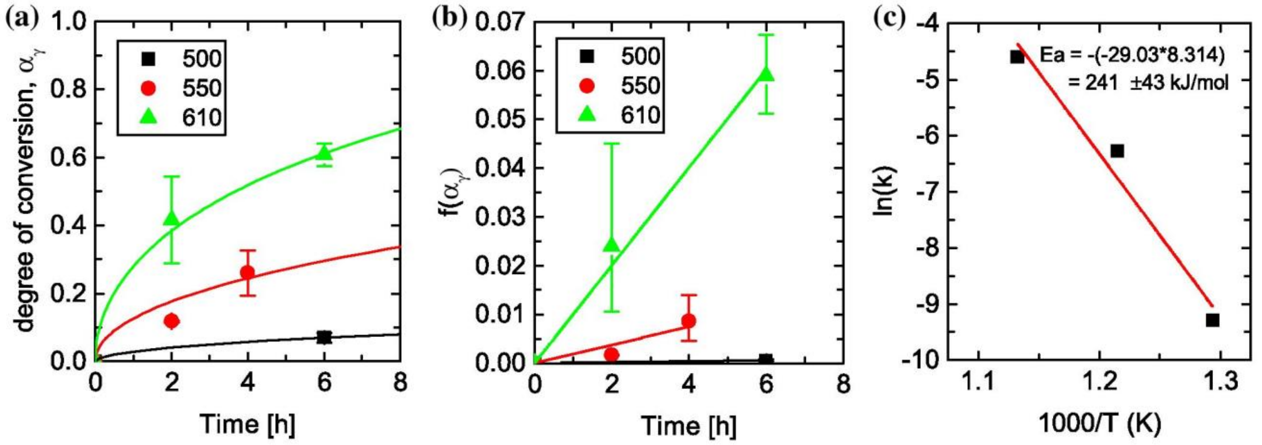

Fig. 7. (a) Results from annealing experiments of sample (2) directly after solidification showing degree of conversion into skutterudite phase as a function of time and temperature. (b) Linear regression of the Ginstling–Brounshtein kinetic model versus time shows a relatively good fit. The slope of the linear fit represent the rate constant k. (c) The activation energy of the total transformation is estimated from the slope of $\ln(k)$ versus $1/T$.

$k = k_0\exp(-E_a/RT)$, where k_0 is the preexponential constant, R the gas constant and E_a the activation energy. By plotting $\ln(k)$ versus $1/T$ and finding the slope(see Fig. 7b), we estimate an activation energy of 241 ± 43 kJ/mol for the total transformation. It must be stressed that this is not necessarily the activation energy of diffusion of a specific specis, but rather an average value for all the diffusion processes going on. Extrapolating the line in Fig. 7a at 610°C, we find 90% transformation after 18 h and full transformation after 33 h. The process dramatically slows down and almost half of the annealing time is used to convert the final 10% with this model. By including variation in grain size and distribution of the precursor phases, it can be speculated that the real transformation rate is even slower at the end, which is also indicated by numerical simulation of similar systems.[27]

For sample 1, which was synthesized from elements and subsequently crushed manually, we achieved a skutterudite phase fraction of around 88% after 48 h of annealing at 630°C. For the methods 3 and 4, the projected annealing times are much shorter and in the range of a few hours. Since these samples were made of much finer powder, the diffusion paths are also much shorter. From Eq. 2, it can be seen that the time to reach complete transformation (τ) is proportional to the square root of the grain size (R_0) and inversely proportional to the diffusion coefficient (D), $\tau \sim R_0^2/D$.[28] For a grain size of ~100 μm (ground) compared to ~10 μm (ball-milled), this equals a 100-fold decrease in the transformation time. Since we have several diffusive species during transformation, the slowest of these will govern the transformation time. Both diffusion of Sb and Ce is needed for the peritectic transformation to occur. It should be noted that the transformation into the filled skutterudite phase with other filler atoms, such as Yb, Ca and In, was significantly faster than for the p-type Ce-filled skutterudite. It can be speculated that the diffusion of the filler atom, i.e. from the secondary phase which contains the filler element for γ, is rate-limiting whereas diffusion of Sb is not. The diffusion of Ce is very apparent when looking at a cross-section between β-γ-$CeSb_2$ (see Fig. 8). The Ce content decreases over the γ domain from 5% to 6% neighboring $CeSb_2$ down to 3%. The peritectic transformation has taken place here at a Fe-rich β-phase ($Fe_{0.77}Co_{0.23}Sb_2$). The Fe/Co ratio (x) is

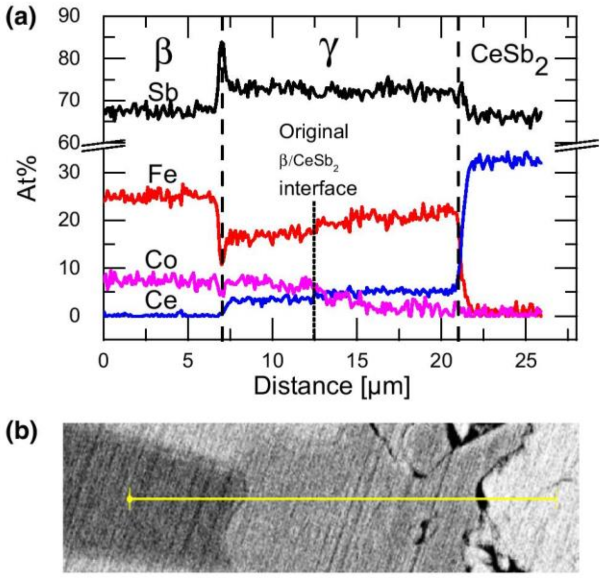

Fig. 8. Elemental distribution from EDX (a) over the line in (b) taken from the area indicated by a dashed square in Fig. 5(b), showing a skutterudite (γ) phase region forming between $Fe_xCo_{1-x}Sb_2$ (β, left) and $CeSb_2$ (right). A concentration gradient in Fe, Ce and Co is seen in γ according to a certain ratio y/x in $Ce_yFe_xCo_{1-x}Sb_{12}$, going from $CeFe_4Sb_{12}$ to $Ce_{0.54}Fe_{2.8}Co_{1.2}Sb_{12}$ from right to left. The concentration of Ce, Fe and Co changes abruptly inside γ at around 12.5 μm. This is likely the location of the former $\beta/CeSb_2$ interface.

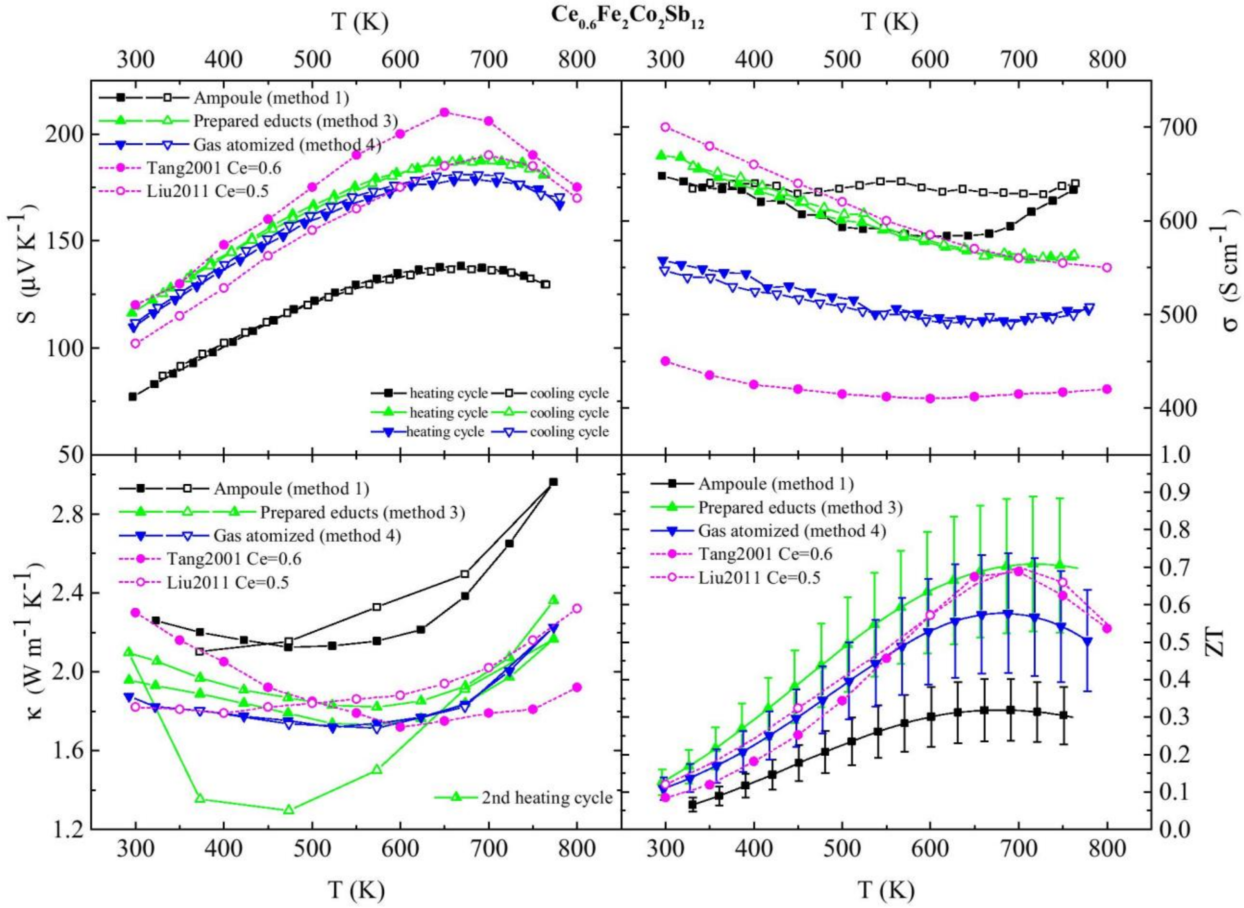

Fig. 9. Transport properties of the $Ce_{0.6}Fe_2Co_2Sb_{12}$ samples as a function of temperature: Seebeck coefficient S, electrical conductivity σ, thermal conductivity κ and thermoelectric figure of merit ZT; measurement points of the cooling down branch are indicated by open symbols. Literature data inserted for comparison.[6,29]

actually increasing from β towards $CeSb_2$ also indicating diffusion of Fe^{2+} and to a lower extent for Co^{3+}. We then end up with diffusion of Ce and Sb from right to left, and opposite diffusion of Fe and, to a lower extent, of Co. The surplus Sb requirement according to Eq. 1 will be transported in from the surrounding Sb phase. At the γ/$CeSb_2$ interface, we then see almost pure $CeFe_4Sb_{12}$ while at the β/γ interface we find $Ce_{0.54}Fe_{2.8}Co_{1.2}Sb_{12}$. Finally, a sharp change in the concentration of both Ce, Co and Fe is seen roughly halfway between β and $CeSb_2$. This is likely to be the location of the original β/$CeSb_2$ interface.

Thermoelectric Properties

The Seebeck coefficient, electrical and thermal conductivity and the calculated figure of merit ZT are shown in Fig. 9 as a function of temperature along with literature data of material with similar compositions.[9,29] The results vary significantly due to the fraction of impurity phases in the particular samples and the different skutterudite compositions, which are detected in the SEM images and x-ray diffractograms, respectively. Very little skutterudite phase was detected in sample (2), and as a consequence sample (2) was not considered in the thermoelectric characterization. We observed the thermoelectric properties right after synthesis or short annealing time to evaluate the applicability and a possible alteration of the material.

Here, sample (1) shows the lowest ZT among the samples, which is due to the lower absolute Seebeck coefficient and a higher thermal conductivity. Surprisingly, the electrical conductivity of sample (1) remains at relatively high values, albeit changes during the measurement. Most probably this can be attributed to a microstructural effect (e.g. grain growth, densification, and/or rearrangement of secondary phases) and does not indicate a change in the charge carrier density and/or no severe change in the phase composition (stoichiometry, proportion), since the Seebeck coefficient is stable during the measurement cycle. The high absolute value of sample (1) may be attributed to Sb as a secondary phase possessing significantly larger electron conductivity than the skutterudite material. The samples with a higher fraction of skutterudite phase

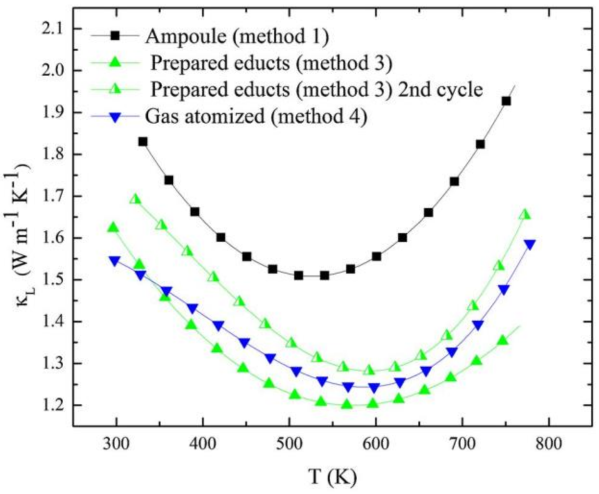

Fig. 10. Calculated lattice thermal conductivity κ_L of the $Ce_{0.6}Fe_2Co_2Sb_{12}$ samples as a function of temperature calculated using a single parabolic band model. The ascending values at higher temperatures are effects due to intrinsic behavior, which is not considered in the model.

[samples (3) and (4)] reveal excellent thermoelectric properties, with a considerably higher absolute Seebeck coefficient and a lower thermal conductivity compared to sample (1). Furthermore, sample (3) has a slightly higher Seebeck coefficient and especially higher electrical conductivity in comparison to the gas-atomized sample (4), and thus shows significantly greater ZT values, reaching a $ZT_{\max} = 0.71$ at 726 K which is comparable to literature data. It is remarkable that the lower phase purity and the slightly lower Ce filling of the skutterudite in sample (3) still achieves better thermoelectric properties compared to the gas-atomized sample (4). However, sample (3) is still metastable, which can be seen in the thermal conductivity data, where the cooling down measurement shows significantly different values and descends strongly. For the metastable sample (3), a change of the lattice thermal conductivity after the first measurement cycle can be detected and exhibits values in the second measurement, which are slightly above the values of the gas-atomized sample (4). In Fig. 10, the calculated lattice thermal conductivity is shown for all samples including the second cycle for sample (3).

In comparison to literature values, the samples in this study resembles best samples with nominal composition $Ce_{0.5}Fe_2Co_2Sb_{12}$,[29] which is not surprising when looking at the actual filling fraction of sample (3) and (4) of 0.43 and 0.54, respectively. An exception is the electrical conductivity of sample (4) which lies in between literature data of material with filling fractions of Ce = 0.6[9] and Ce = 0.5.[29]

As a reason for lower electrical conductivity of the gas-atomized sample (4) in comparison to the ball-milled sample (3), we first assume two major effects: firstly, the Sb deficiency and secondly a higher Ce content of the skutterudite composition of sample (4). It has to be noted that the electrical conductivity will also be influenced by the metallurgical state. In particular, the mobility of the sample might change with longer annealing times and will add to the compositional changes we already detected in the samples. The electronic state of the skutterudite can be written as $Ce^{3+}_{0.6}Fe^{2+}_2Co^{3+}_2Sb^{1-}_{12}$ (this simple assumption is more accurately discussed in[30,31]) and thus a deficiency of Sb means that the number of electron acceptors are lowered, which as a consequence decreases the electrical conductivity in a p-type material. This is also the case for higher Ce content, because more electrons have to be compensated by the electron acceptors. However, it is known that a higher filling fraction leads to higher effective band mass, which would normally lead to higher Seebeck coefficients.[30] A more likely reason for the lowered electrical conductivity was found in the diffractogram of the gas-atomized sample (4). Here, a high lattice strain was refined, which means a high number of defects in the lattice of the skutterudite. Thus, these defects can significantly decrease the charge carrier mobility and consequently the electrical conductivity. A closer look into the temperature-dependent Seebeck data verifies this assumption. Samples 3 and 4 exhibit a similar trend with almost identical Seebeck coefficients, which means that the charge carrier density should be almost the same as each other. As a consequence, it can be concluded that the gas-atomizing introduces many defects in the powder, which are still present after phase transition and heat treatment during the compaction process. It can be speculated that a higher electrical conductivity can be achieved by a further surplus of Sb in the initial weight and a further heat treatment (possibly at higher temperatures).

CONCLUSION

In this study, we synthesized polycrystalline p-type skutterudite from the initial composition $Ce_{0.6}Fe_2Co_2Sb_{12}$ using different synthesis approaches, including gas-atomizing. However, EPMA analysis revealed that the final stoichiometry of the skutterudite samples were all different. We present a model of the peritectic transformation from secondary phases into the skutterudite phase. Furthermore, it can be concluded that synthesis of p-type skutterudite from pure elements can be impeded by non-ideal mixing of the secondary phases (foremost $CeSb_2$, marcasite $Fe_xCo_{1-x}Sb_2$ and Sb) and the formation of $Fe_xCo_{1-x}Sb$, which also dramatically decreases the transformation rate into the skutterudite phase. The diffusion coefficients of the filler atom, along with the average grain size of the sintered powder, are the governing parameters for determining the transformation time to phase pure skutterudite. For the gas-atomized sample, we did not see any signs of $Fe_xCo_{1-x}Sb$ due to the excellent

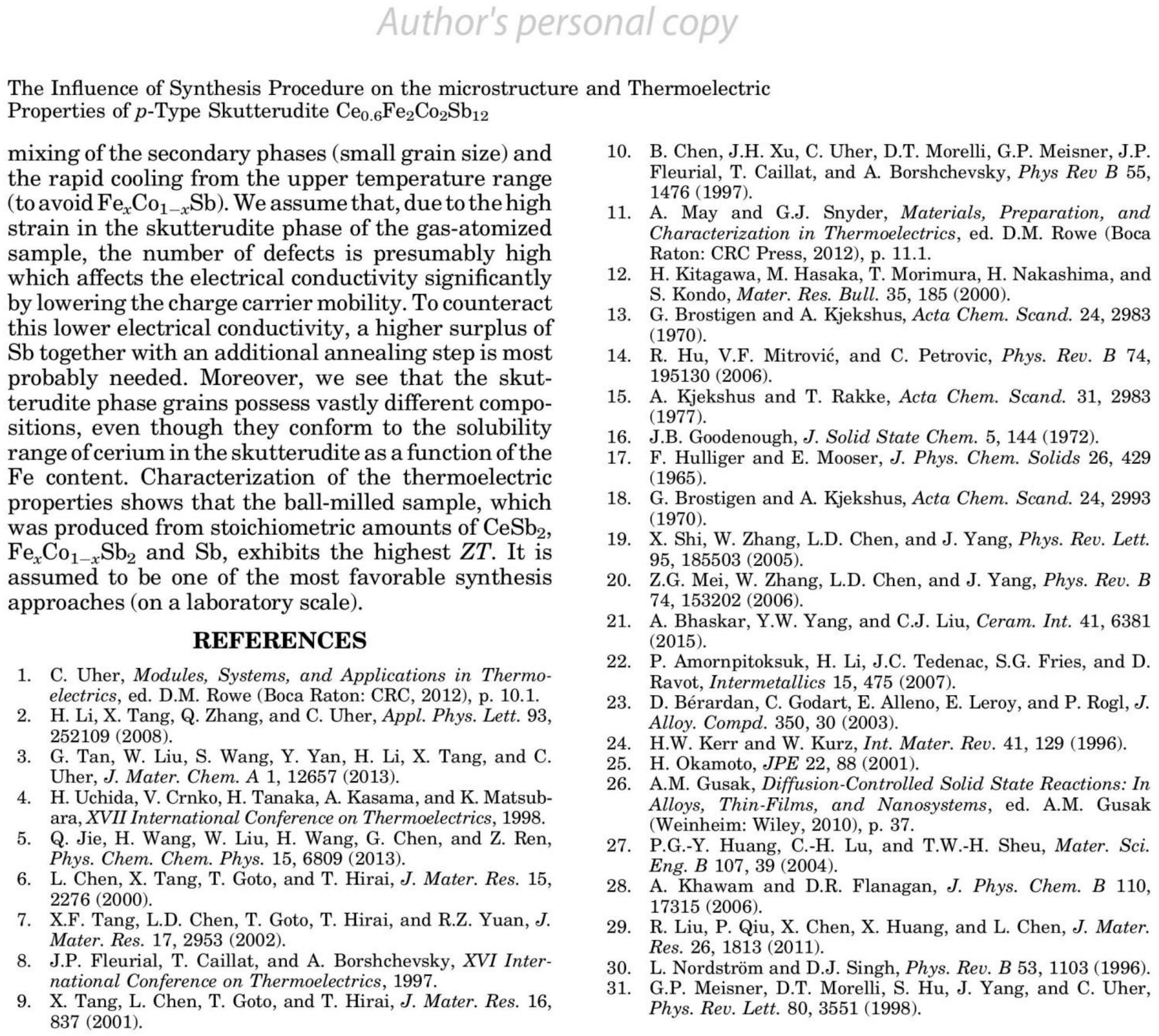

mixing of the secondary phases (small grain size) and the rapid cooling from the upper temperature range (to avoid $Fe_xCo_{1-x}Sb$). We assume that, due to the high strain in the skutterudite phase of the gas-atomized sample, the number of defects is presumably high which affects the electrical conductivity significantly by lowering the charge carrier mobility. To counteract this lower electrical conductivity, a higher surplus of Sb together with an additional annealing step is most probably needed. Moreover, we see that the skutterudite phase grains possess vastly different compositions, even though they conform to the solubility range of cerium in the skutterudite as a function of the Fe content. Characterization of the thermoelectric properties shows that the ball-milled sample, which was produced from stoichiometric amounts of $CeSb_2$, $Fe_xCo_{1-x}Sb_2$ and Sb, exhibits the highest ZT. It is assumed to be one of the most favorable synthesis approaches (on a laboratory scale).

REFERENCES

1. C. Uher, *Modules, Systems, and Applications in Thermoelectrics*, ed. D.M. Rowe (Boca Raton: CRC, 2012), p. 10.1.
2. H. Li, X. Tang, Q. Zhang, and C. Uher, *Appl. Phys. Lett.* 93, 252109 (2008).
3. G. Tan, W. Liu, S. Wang, Y. Yan, H. Li, X. Tang, and C. Uher, *J. Mater. Chem. A* 1, 12657 (2013).
4. H. Uchida, V. Crnko, H. Tanaka, A. Kasama, and K. Matsubara, *XVII International Conference on Thermoelectrics*, 1998.
5. Q. Jie, H. Wang, W. Liu, H. Wang, G. Chen, and Z. Ren, *Phys. Chem. Chem. Phys.* 15, 6809 (2013).
6. L. Chen, X. Tang, T. Goto, and T. Hirai, *J. Mater. Res.* 15, 2276 (2000).
7. X.F. Tang, L.D. Chen, T. Goto, T. Hirai, and R.Z. Yuan, *J. Mater. Res.* 17, 2953 (2002).
8. J.P. Fleurial, T. Caillat, and A. Borshchevsky, *XVI International Conference on Thermoelectrics*, 1997.
9. X. Tang, L. Chen, T. Goto, and T. Hirai, *J. Mater. Res.* 16, 837 (2001).
10. B. Chen, J.H. Xu, C. Uher, D.T. Morelli, G.P. Meisner, J.P. Fleurial, T. Caillat, and A. Borshchevsky, *Phys Rev B* 55, 1476 (1997).
11. A. May and G.J. Snyder, *Materials, Preparation, and Characterization in Thermoelectrics*, ed. D.M. Rowe (Boca Raton: CRC Press, 2012), p. 11.1.
12. H. Kitagawa, M. Hasaka, T. Morimura, H. Nakashima, and S. Kondo, *Mater. Res. Bull.* 35, 185 (2000).
13. G. Brostigen and A. Kjekshus, *Acta Chem. Scand.* 24, 2983 (1970).
14. R. Hu, V.F. Mitrović, and C. Petrovic, *Phys. Rev. B* 74, 195130 (2006).
15. A. Kjekshus and T. Rakke, *Acta Chem. Scand.* 31, 2983 (1977).
16. J.B. Goodenough, *J. Solid State Chem.* 5, 144 (1972).
17. F. Hulliger and E. Mooser, *J. Phys. Chem. Solids* 26, 429 (1965).
18. G. Brostigen and A. Kjekshus, *Acta Chem. Scand.* 24, 2993 (1970).
19. X. Shi, W. Zhang, L.D. Chen, and J. Yang, *Phys. Rev. Lett.* 95, 185503 (2005).
20. Z.G. Mei, W. Zhang, L.D. Chen, and J. Yang, *Phys. Rev. B* 74, 153202 (2006).
21. A. Bhaskar, Y.W. Yang, and C.J. Liu, *Ceram. Int.* 41, 6381 (2015).
22. P. Amornpitoksuk, H. Li, J.C. Tedenac, S.G. Fries, and D. Ravot, *Intermetallics* 15, 475 (2007).
23. D. Bérardan, C. Godart, E. Alleno, E. Leroy, and P. Rogl, *J. Alloy. Compd.* 350, 30 (2003).
24. H.W. Kerr and W. Kurz, *Int. Mater. Rev.* 41, 129 (1996).
25. H. Okamoto, *JPE* 22, 88 (2001).
26. A.M. Gusak, *Diffusion-Controlled Solid State Reactions: In Alloys, Thin-Films, and Nanosystems*, ed. A.M. Gusak (Weinheim: Wiley, 2010), p. 37.
27. P.G.-Y. Huang, C.-H. Lu, and T.W.-H. Sheu, *Mater. Sci. Eng. B* 107, 39 (2004).
28. A. Khawam and D.R. Flanagan, *J. Phys. Chem. B* 110, 17315 (2006).
29. R. Liu, P. Qiu, X. Chen, X. Huang, and L. Chen, *J. Mater. Res.* 26, 1813 (2011).
30. L. Nordström and D.J. Singh, *Phys. Rev. B* 53, 1103 (1996).
31. G.P. Meisner, D.T. Morelli, S. Hu, J. Yang, and C. Uher, *Phys. Rev. Lett.* 80, 3551 (1998).

Paper 3: High temperature oxidation of Mg2(Si-Sn)

High temperature oxidation of Mg_2(Si-Sn)

Gunstein Skomedal[1], Alexander Burkhov[2], Alexander Samunin[2], Reidar Haugsrud[3], Hugh Middleton[1]

1: University of Agder, Jon Lilletunsvei 9, NO-4879 Grimstad, Norway
2: Ioffe Institute, St. Petersburg, Russia
3: Department of Chemistry, University of Oslo, FERMiO, Gaustadalléen 21, NO-0349 Oslo, Norway

Abstract:

High temperature oxidation of $Mg_2Si_{1-x}Sn_x$ alloys (X = 0.1 - 0.6) has been investigated. The oxidation rate was slow for temperatures below 430°C. In the temperature range between 430 and 500°C all the alloys exhibited breakaway oxidation. The onset temperature of the breakaway region in general decreased with increasing level of Sn in the alloy. The breakaway behavior is explained by a combination of the formation of a non-protective MgO layer and the formation of Sn-rich liquid at the interface between the oxide and Mg depleted Mg_2Sn.

Highlights:

- $Mg_2Si_{1-x}Sn_x$ show little to no oxidation at temperatures below ignition temperature
- At higher temperatures it will enter a break-away regime with very rapid oxidation
- The ignition temperature for break-away oxidation is higher for lower Sn content

Keywords: Electronic materials; Magnesium; High temperature corrosion; Selective oxidation

INTRODUCTION

Mg_2(Si-Sn) alloys have been investigated extensively during the last decade due to promising thermoelectric properties and use of lightweight, non-toxic and abundant raw materials compared to today's state-of-the art thermoelectrics, such as PbTe and Bi_2Te_3 [1]. Mg_2Si has shown both high Seebeck coefficient and high electronic conductivity. Peak figure of merit, zT, of 0.6-0.7 has been reported [2], where $zT = \alpha^2\sigma/\kappa$, α is the Seebeck coefficient, σ the electrical conductivity and κ the thermal conductivity. Alloying with Sn, peak zT-values up to 1.4 have been reported for Mg_2Si-Mg_2Sn solid solutions [1, 3, 4] due to increased valley degeneracy and reduced lattice thermal conductivity in the alloys. However, only small amounts of oxygen in the surrounding atmosphere combined with elevated temperatures of about 400-600°C lead to oxidation of the material, which is detrimental to long-term stability and reduces the efficiency of thermoelectric devices [5-7]. Thin oxidation resistant coatings may solve this stability challenge, but understanding of the oxidation mechanism is essential to processing of the material in the different production steps.

The high temperature oxidation behavior of Mg_2Si was recently studied [5, 8]. In contrast to other silicides, Mg_2Si forms a rather thin surface layer of MgO with no SiO_2 or other oxides present [9]. The MgO layer is a few nm thick under ambient conditions and increases to approximately one micron at higher temperatures, protecting the material up to temperatures around 450°C in air. The oxidation follows parabolic kinetics, reflecting oxide growth controlled by outward Mg^{2+} diffusion in MgO. However, Mg_2Sn forms no passivating layer at high temperatures and the oxide layer grows linearly with time [10]. At 400°C and higher in temperature, "burning" of the samples commences after certain exposure times. In general, pure Mg and its alloys in most cases experience such catastrophic oxidation at temperatures above ~400°C [11, 12]. The onset (ignition) temperature of the catastrophic oxidation varies with the alloy constituents and their content - as clearly seen for the two systems of importance to the present contribution, Mg_2Si (~940°C) and Mg_2Sn (~400°C). For Mg_2Si, SiO_2 forms above 710°C and $MgSi_2O_4$ is observed in the oxide scale of the alloys oxidized above 940°C

Initial studies on the oxidation of Mg_2Si - Mg_2Sn solid solutions show similar behavior as for the pure compounds [7, 13]. For oxidation of $Mg_2Si_{0.4}Sn_{0.6}$ breakaway kinetics is encountered at temperatures as low as 400°C in air, while materials with lower Sn content are more resistive towards catastrophic oxidation.

In this work we have synthesized different compositions of $Mg_2Si_{1-x}Sn_x$, and investigated effects of the Sn content on the degradation of the materials in oxidizing atmospheres at high temperatures. The effect of time and temperature on the oxidation mechanisms was studied by performing thermogravimetric analysis followed by characterization of the microstructure of the alloys and corrosion products.

EXPERIMENTAL

$Mg_2Si_{1-x}Sn_x$ with contents of Sn varying from 0.1 to 0.6 and different levels of Sb and Bi (<1wt%) was synthesized with HF (High Frequency) induction melting of stoichiometric amounts of the elements followed by rapid cooling. Pure Mg_2Si (Yasunaga Corp., Japan) was used as the reference. Some of the compositions were annealed directly from the solidified ingot, while others were subsequently milled with millstones (sample grain size 0.04 – 0.3 mm) or ball-milled (grain size about 60 nm) and sintered into pellets using a hot press. The sintering was done under vacuum with pressure about 300-400 kg/cm^2, at temperatures varying from 873 K to 1173 K, depending on the solid solution composition. The composition and manufacturing procedure of the samples are presented in Table I.

The ingots/pellets were either cut into small pieces of approximately 1x5x5 mm^3 (bulk samples) or ground into powders for oxidation tests and further analysis. The surface of the bulk samples was grinded with P2400 SiC paper, ultrasonically cleaned in alcohol and placed in a desiccator before the oxidation experiments.

Thermogravimetric Analysis and Differential Scanning Calorimetry (Mettler Toledo TGA/DSC 1) were used to study the oxidation mechanism, applying the isoconversion method for powder samples (constant heating rate 2.5-20 K/min). Similar thermogravimetric measurements of the oxidation were performed on bulk samples with a constant heating rate of 1 K/min and isothermally in the temperature range 350-550°C with an airflow of 100 ml/min, laboratory air.

The microstructure and the composition of both, unoxidized and oxidized samples were examined with scanning electron microscope (SEM, Zeiss Merlin) and energy dispersive X-ray spectrometer (EDS). XRD (Bruker D8 Advanced) was used to identify the oxidation products.

Table I Samples used in the TGA/DSC tests.

ID	Composition	Doping	Synthesis
Mg_2Si	Mg_2Si	$Sb_{0.005}$	*Reference sample, Yusunaga Corp. Japan*
SN01	$Mg_2Si_{0.9}Sn_{0.1}$	$Bi_{0.02}$	HF melting, milling with millstones (0.04-0.315mm), hot pressing (1173 K)
SN01b	$Mg_2Si_{0.9}Sn_{0.1}$	$Sb_{0.015}$	HF melting, milling with millstones (0.04-0.315mm), hot pressing (1173 K)
SN02	$Mg_2Si_{0.8}Sn_{0.2}$	$Sb_{0.01}$	HF melting, milling with millstones (0.04-0.315mm), hot pressing (1123 K)
SN02b	$Mg_2Si_{0.8}Sn_{0.2}$	$Sb_{0.01}$	HF melting, ball milling (nanopowder ,~60nm), hot pressing (1123 K)
SN03	$Mg_2Si_{0.7}Sn_{0.3}$	$Sb_{0.001}$	HF melting and annealing
SN03b	$Mg_2Si_{0.7}Sn_{0.3}$	$Sb_{0.01}$	HF melting milling with millstones (0.04-0.315mm), hot pressing (1093 K)
SN04	$Mg_2Si_{0.6}Sn_{0.4}$	$Sb_{0.001}$	HF melting and annealing
SN06	$Mg_2Si_{0.4}Sn_{0.6}$	$Sb_{0.01}$	HF melting, milling with millstones (0.04-0.315mm), hot pressing (873 K)
SN06b	$Mg_2Si_{0.4}Sn_{0.6}$	$Sb_{0.01}$	HF melting and annealing

Finally, Environmental SEM (FEI Quanta 200 FEG-ESEM) equipped with a heating stage was used to study, in-situ, the evolution of the surface oxide scale during heating of a sample with composition $Mg_2Si_{0.4}Sn_{0.6}Sb_{0.01}$. The high temperature ESEM was done in a partial pressure of water vapor of $p_{H_2O} = 610Pa$ at temperatures up to 700°C.

RESULTS

Fig. 1 shows the microstructure of the samples with different Sn-content before oxidation. The materials with X>0.2 are two-phase composites with clearly identified Sn-rich (light) and Si-rich (dark) regions. In Table II the approximate composition of the two phases is shown based on EDS point analyses. It is clear that, at least with the present synthesis methods, the solid solutions of Mg_2Si and Mg_2Sn in the range 0.1 to 0.6 are not formed, probably due to the miscibility gap in the Mg_2Si-Mg_2Sn phase diagram [14]. The two-phase structure with a slightly varying composition resembles peritectic solidification: initially during cooling of the melt, Si-rich Mg_2Si dendrites grow followed by solidification of the Sn-rich phase with some transformation of the Si-rich phase (diffusion controlled) leading to an intermediate zone with gradually changing composition. This two-phase nature of the alloy matrix influences the high temperature oxidation mechanism of these materials. The composition of the different phases and their microstructure will be considered when discussing the oxidation mechanisms of this alloy system.

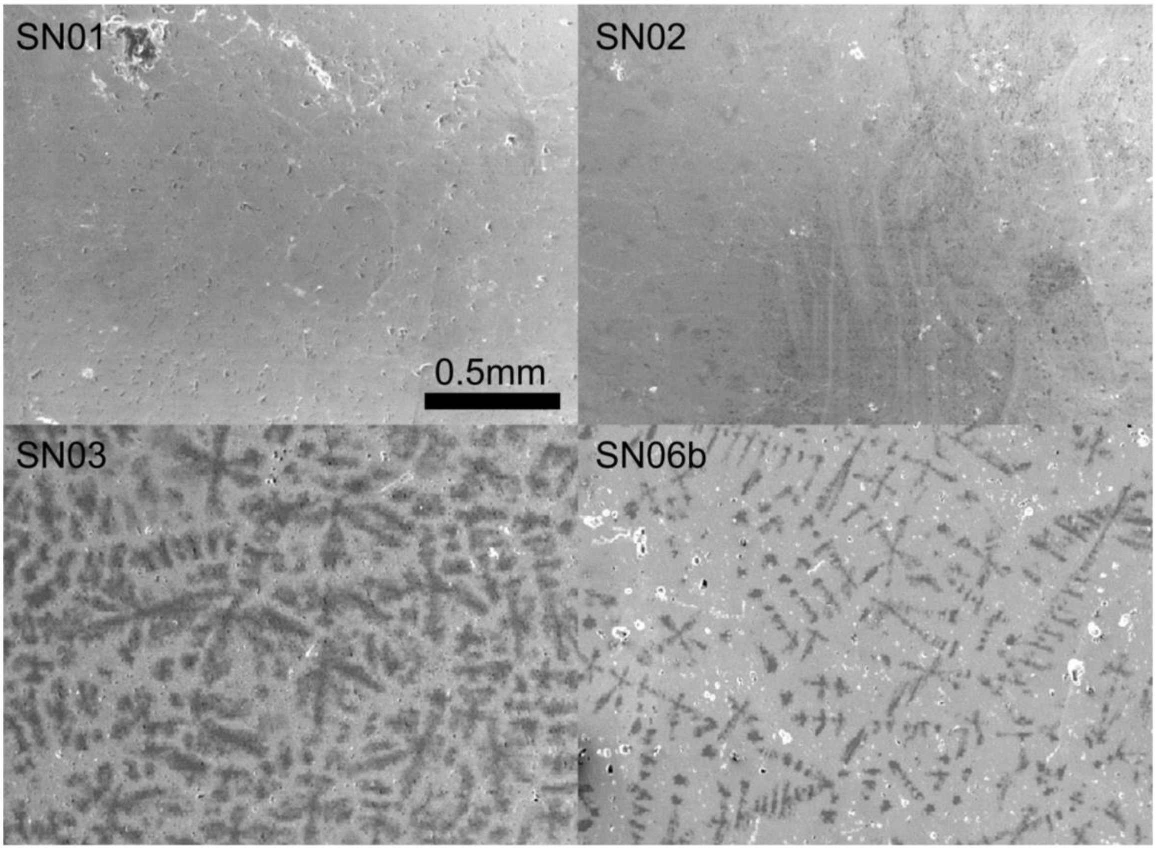

Fig. 1 SEM micrographs of the $Mg_2Si_{1-x}Sn_x$ samples before oxidation. Only the samples with the nominal Sn content of 0.1 (SN01) is single-phase, SN02 has small regions with precipitation of Sn-rich phases while all other samples contain a Si-rich phase (dark) and a Sn-rich phase (bright) in different quantities and with different chemical composition as seen in table II.

Table II $Mg_{2-y}Si_{1-x}Sn_x$ phase composition calculated from EDS analysis of the different phases found by SEM

Area	**Element**	**SN01**	**SN01b**	**SN02**	**SN02b**	**SN03**	**SN03b**	**SN04**	**SN06**	**SN06b**
Si-rich (Sn < 0.1)	Mg	1,94	1,93	1,91	1,92	1,98	1,86	1,98	2,00	1,99
	Si	0,96	0,93	0,89	0,90	0,97	0,97	0,96	0,93	0,92
	Sn	0,04	0,07	0,11	0,10	0,03	0,03	0,04	0,07	0,08
Mix (Sn 0.1 - 0.4)	Mg			1,99	1,30	1,95	1,83	1,92	1,88	1,92
	Si			0,63	0,72	0,84	0,82	0,86	0,83	0,75
	Sn			0,37	0,28	0,16	0,18	0,14	0,17	0,25
Sn-rich (Sn > 0.4)	Mg					1,94	1,82	1,95	2,15	1,88
	Si					0,57	0,61	0,50	0,40	0,34
	Sn					0,43	0,39	0,50	0,60	0,66

Oxidation under constant heating rate

The first oxidation tests were done with powder samples in air at constant heating rate, to get an overview of different effects as a function of temperature and to determine the heat flow associated with the respective processes. Fig. 2 presents the weight change and the heat flow encountered for the different Sn compositions when heated at the rate of 5 K/min in air. Generally, all samples containing Sn show two distinct temperature regions where the weight increases abruptly as a consequence of oxidation. Between 500°C and 550°C the samples oxidize heavily, with the onset temperature varying slightly with Sn content – decreasing with increasing levels of Sn. The step-like behavior is followed by a gradual weight increase up to about 850°C, where a new breakaway-like oxidation occurs. The two breakaway stages are most pronounced for the lower Sn contents ($x<=0.2$). Samples SN01b, SN02, SN02b gain at around 500°C between 20-30% of weight, with the final weight gain of 5-10% at 850°C. Tests with other heating rates (2.5, 10, 15 and 20 K/min) showed similar behavior, but the temperature regions of the different stages and the relative amount oxidized at each stage slightly varies. The Mg_2Si sample showed very little oxidation before it suddenly went through rapid oxidation at around 920°C. One may note from Fig. 2 that there are clear variations in the detailed behavior of materials with the same nominal composition but with different fabrication procedures.

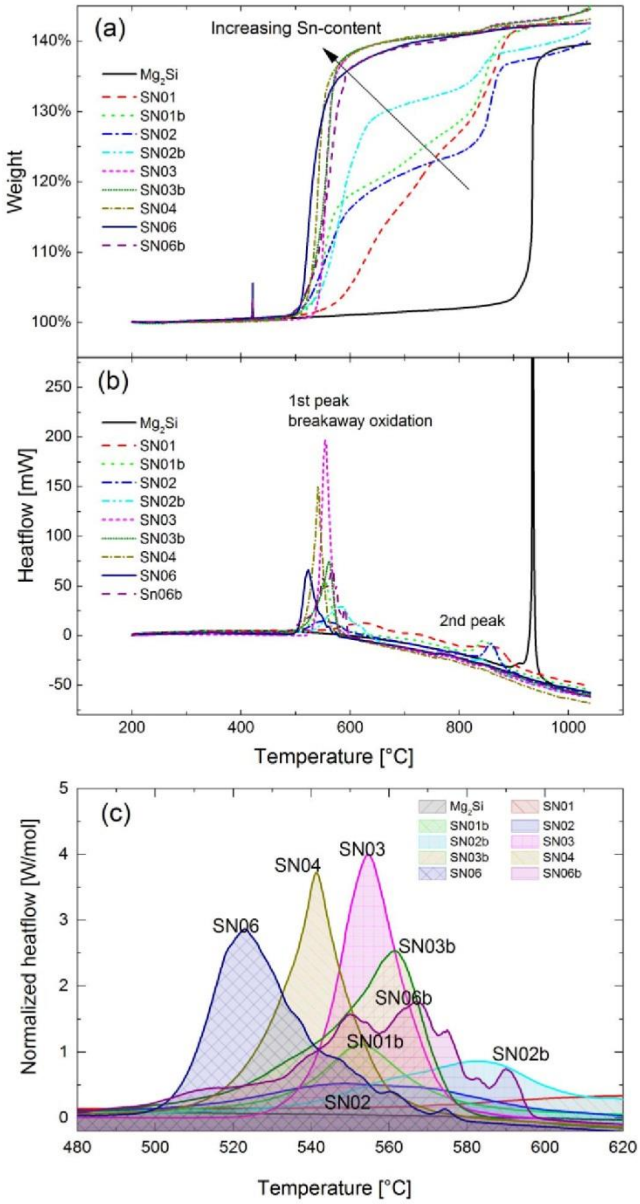

Fig. 2 TGA (a) and DSC (b) curves for different powder samples at constant heating rate of 5K/min in air. (c) shows normalized heat flow of the 1st peak (divided by the number of moles in the sample), where the area under graph equals to the enthalpy of the exothermic oxidation reaction.

Fig. 2(b) displays the DSC signals corresponding to the TG-curves, and the peaks occurring in the temperature range 480 to 620°C are further enlarged in Fig. 2(c). The onset temperature of the major DSC peaks indicates the beginning of the oxidation processes, while the heat-flow reflects essentially the enthalpy of the predominating reaction. The enthalpy associated with this first breakaway stage was estimated to be of order of 1000kJ/mol (500kJ/mol Mg) which indicates that the major oxidation reaction occurring at 500 °C is:

$$Mg_2Si_{1-x}Sn_x + O_2 = 2MgO + (1-x)Si + xSn \qquad (2)$$

since the formation enthalpy of MgO is 603kJ/mol [SI]. In addition, some Sn will oxidize to SnO_2, which also has a high enthalpy of 578kJ/mol [SI]. This is supported by the XRD results for samples after complete oxidation at 600°C showing the presence of MgO, SnO_2, Sn and Si, which is also in accordance with the literature data on oxidation of Mg_2Si [8] and other Mg-alloys [12]. The DSC signals observed at higher temperatures are less distinct, reflecting that several processes are in play and that they are smeared out over a large temperature region. Therefore, it becomes difficult to estimate thermodynamic values corresponding to specific processes. At temperatures above ~700°C silicon will oxidize faster, as seen for samples with Sn-content of 0.1 in Fig. 2. The enthalpy of the reaction occurring at 920 °C for Mg_2Si is difficult to estimate since the reaction is violent and the heat flow is difficult to measure accurately. However, taking an average of several runs the value is comparable with the enthalpy of the reaction at 500 °C, again indicating that oxidation of Mg is the predomination reaction.

After complete oxidation, the average weight change for all samples was around 37- 42 %, which corresponds to the weight gain expected when assuming complete oxidation of Mg and Sn into MgO and SnO_2 and essentially no oxidation of Si.

The experiments on the powder samples, presented above, give a general outline on the correlation of the oxidation resistance with Sn content. However, the reaction rate of these powders will, to a large degree, depend on the grain size and on the total surface area of the samples, both of which can vary considerably. This is reflected in the TGA/DSC results as the shifts in apparent onset temperatures and the width of the DSC peaks (e.g. broader peaks and higher temperatures for the larger particles). To elucidate further the different oxidation features, bulk samples with well-defined and similar surface area were exposed to constant heating rate of 1K/min. The samples were isothermally annealed to the complete oxidation at the temperatures above onset of the breakaway oxidation. TG curves from these experiments are presented in Fig. 3. Although a similar trend is encountered as for the powders (cf. Fig. 2), the apparent onset temperatures are now more strongly affected by the Sn content; it increases with decreasing Sn content from ~530 °C for SN06 to ~850°C for SN01b, i.e. varying by more than 300°C. Additionally, we observe differences in the oxidation behavior of the samples of the same nominal composition, illustrated by traces for SN03 and SN03b in Fig. 3.

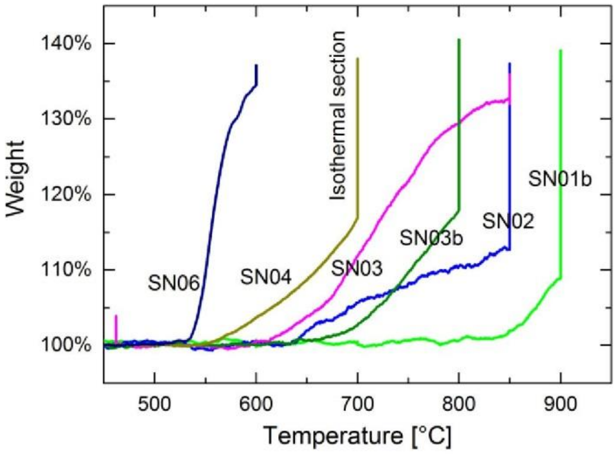

Fig. 3 TG curves of bulk samples (~1x3x3mm^3) in oxidizing atmosphere at constant heating rate of 1K/min to above the onset temperature of breakaway oxidation, followed by an isothermal section until complete oxidation (37-40% weight gain).

Isothermal oxidation

Earlier studies have shown that SN06 starts to oxidize heavily around 400°C upon prolonged exposure [7], whereas the TG and DSC (cf. Fig. 2 and 3) experiments at a constant heating rate, presented here, did not show significant weight gain at temperatures below ~500°C. To investigate this discrepancy, the materials were oxidized isothermally as a function of time to determine the oxidation kinetics and to further investigate the catastrophic oxidation and the reactions preceding this event. Fig. 4 shows TG-curves for some selected samples at different temperatures. For all samples the weight changes are only a few micrograms below a certain threshold temperature (ignition temperature) at which the breakaway oxidation (burning) is initiated. For samples of the same composition the breakaway process at higher temperature generally develops after a shorter duration. The duration of the complete oxidation also significantly depends on the sample composition. Below the onset temperature (see example in the inset for SN 06), the details of the TG data show both weight increase and decrease as a function of time, seemingly with no systematic variations with respect to composition, exposure time and reaction conditions. The weight changes never exceeds more than 2-4µg/mm^2. This translates into a 1.5-3µm thick MgO layer.

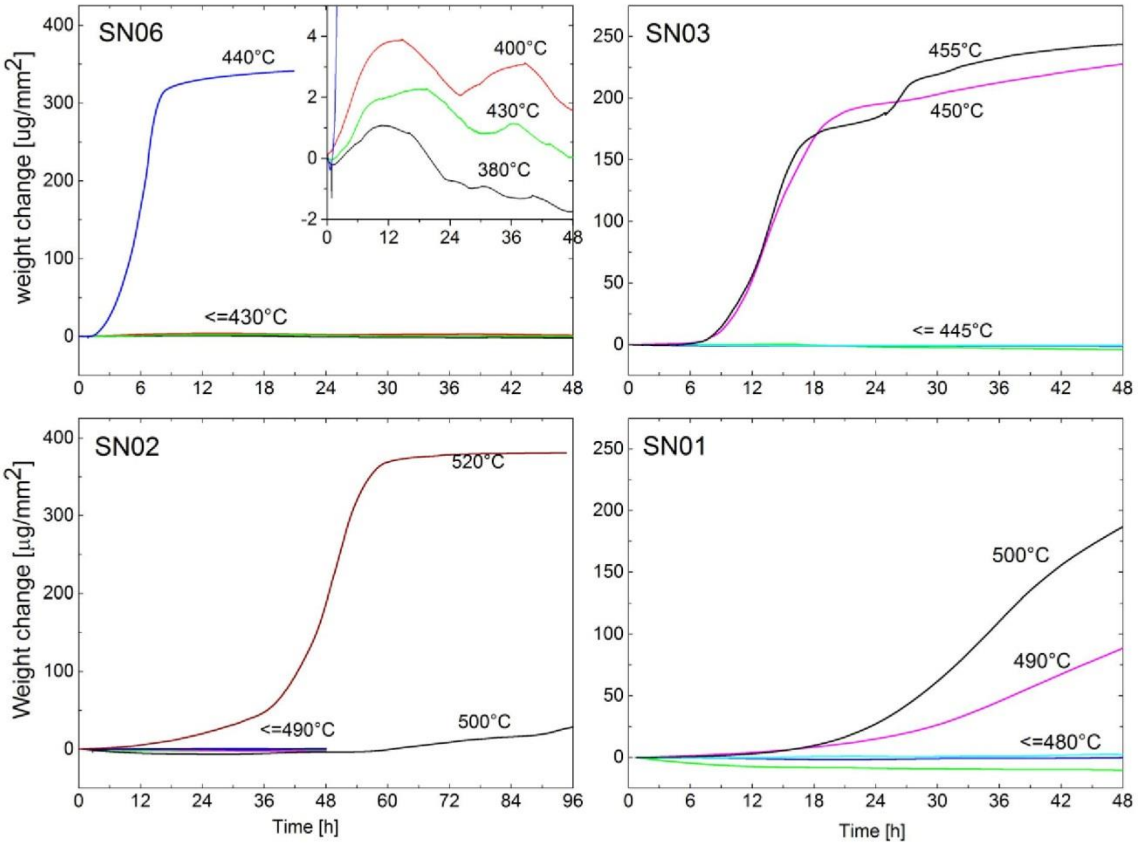

Fig. 4 Selected TG-curves from isothermal oxidation of samples with different Sn-content at different temperatures in air. The inset for SN06 shows a magnification of the very small weight changes at temperatures below the onset of breakaway oxidation (burning). The onset temperature is generally found higher for lower Sn-content. Be aware of different x- and y-scales between the graphs.

Composition and microstructure

The composition and the structure of the isothermally oxidized samples were investigated by means of XRD, with a representative example of the X-ray pattern displayed in Fig. 5. The major phases present in all samples were MgO (Periclase), SnO_2 (Cassiterite), Sn and Si. Not surprisingly, the SnO_2 content increases with increasing Sn content in the original material, and for the materials containing the most Sn, also SnO (Romarchite) was identified. One should note from these patterns that for SN01 there are residues of $Mg_2Si_{1-x}Sn_x$ (from Vegard's law we estimate a Sn-content of 0.07) since oxidation was stopped before completion . For SN03 also very small remnants of $Mg_2Si_{1-x}Sn_x$ with a rather broad spectrum corresponding to 0.2-0.5 in Sn-content can be seen. No SiO_2 was identified with XRD in these samples.

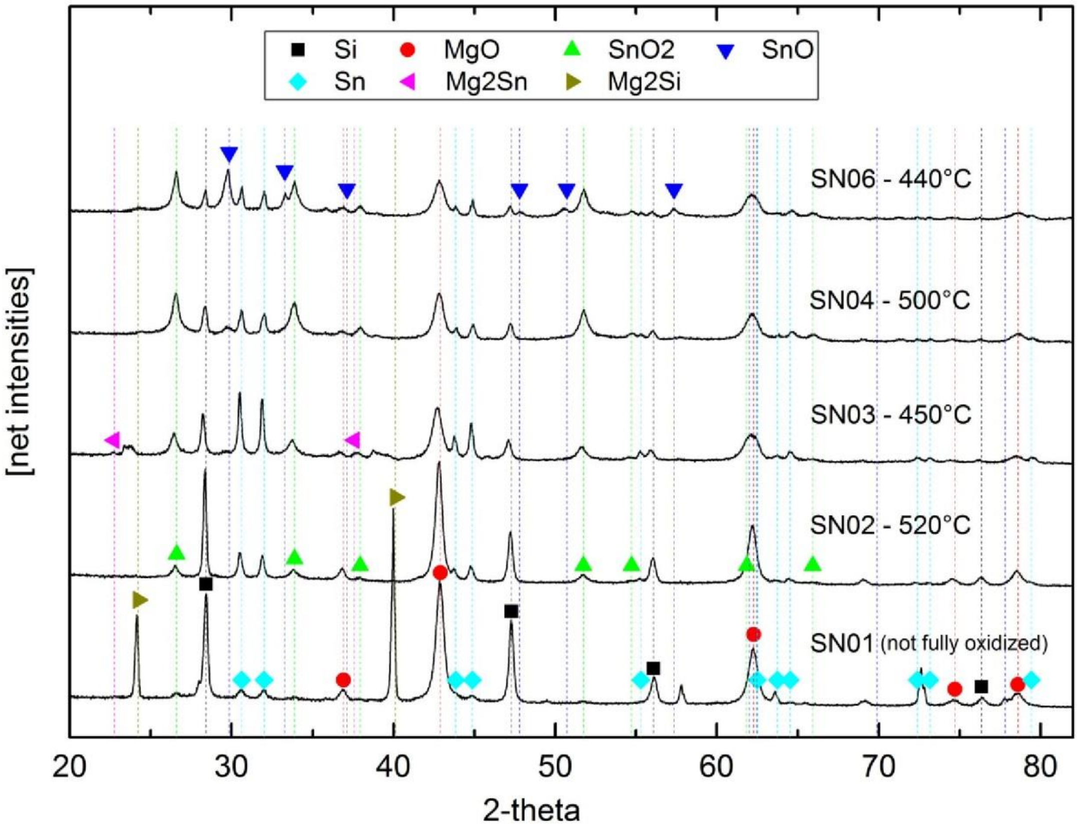

Fig. 5 XRD diffractograms of some samples after complete isothermal oxidation above the ignition temperature. The predominant phases are indicated.

SEM micrographs of the cross sections of the oxide layer of SN06 oxidized at 430°C for 48h is displayed in Fig. 6. Moreover, Fig. 7 shows the elemental distribution of the major alloy constituents (in addition to oxygen) across the oxide scale and a few micro meters into the underlying alloy matrix after oxidation at 400°C for 48 h. These last figures represent the situation prior to the point of breakaway: the outer scale consists of rather porous MgO. The EDS line scan reveals that the alloy is depleted in Mg close to the oxide-alloy interface.

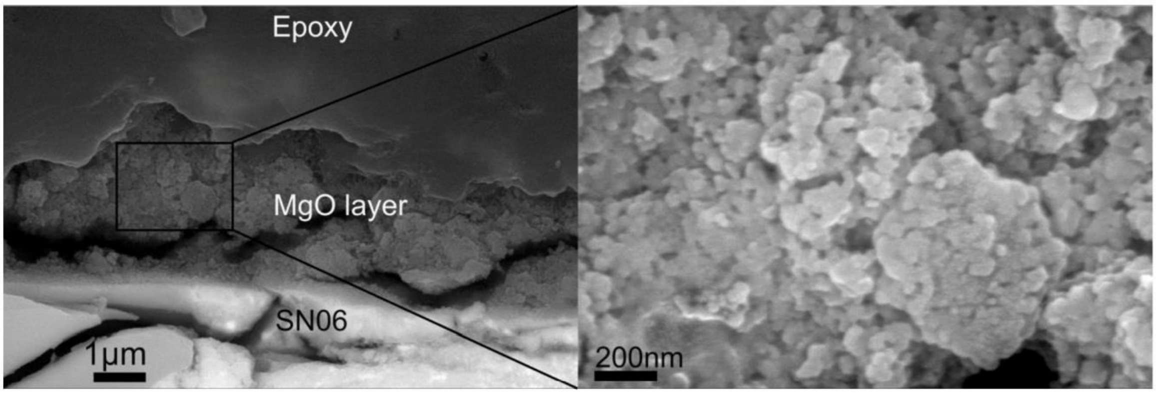

Fig. 6 SEM picture of cross section of MgO layer on top of SN06 after 48 h isothermal oxidation at 430°C. The picture shows a region of the sample where the epoxy has cracked off leaving a cracked surface open to inspection. Cracks are also found between MgO layer and underlaying SNO6 surface.

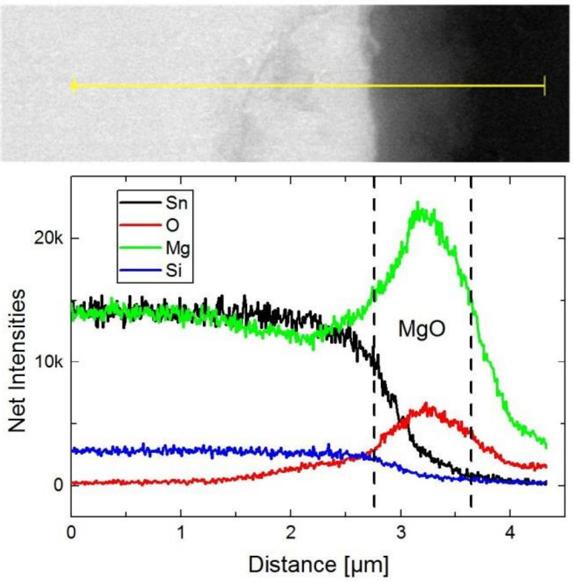

Fig. 7 EDS linescan of the dense, 1μm thick surface oxide layer of SN06 after 48h in air at 400°C. A depletion of Mg right beneath the oxide layer is clearly identified.

The oxidation of SN06 was studied in situ as a function of increasing temperature in an Environmental SEM (ESEM). A series of snap shots during heating of the SN06 sample are presented in Fig. 8. A movie of the oxidation process is available online [15]. Based on the location of the thermocouple inside the furnace, used for the oxidation experiment, it is reasonable to assume that the actual temperature on the surface of the samples is significantly lower than the furnace set point. A gradient in the temperature in the ESEM is also evident when comparing with onset temperatures from the TG measurements, which are significantly lower than observed in the ESEM. The temperatures, included in the micrographs, should therefore only be used as a relative reference. Nevertheless, this fascinating approach gives us rather unique insight of the degradation mechanism for this material: The initial oxide scale nucleates at surface defects such as pores and cracks and rapidly covers the entire surface. The oxidation propagate fast when the temperature increases and a porous surface scale is formed with a "cauliflower"- like structure, in line with the microstructure of the scale shown in Fig. 6. Interestingly, the ESEM reveals formation of large fast growing spherical particles on the surface of the sample above a specific temperature. Post characterization indicated that these spheres were liquid Sn, that may form at the oxide-alloy interface. The liquid does not wet the surface and penetrates outward through porosity forming spherical particles at the surface, where the surface of the spheres oxidizes to SnO/SnO_2.

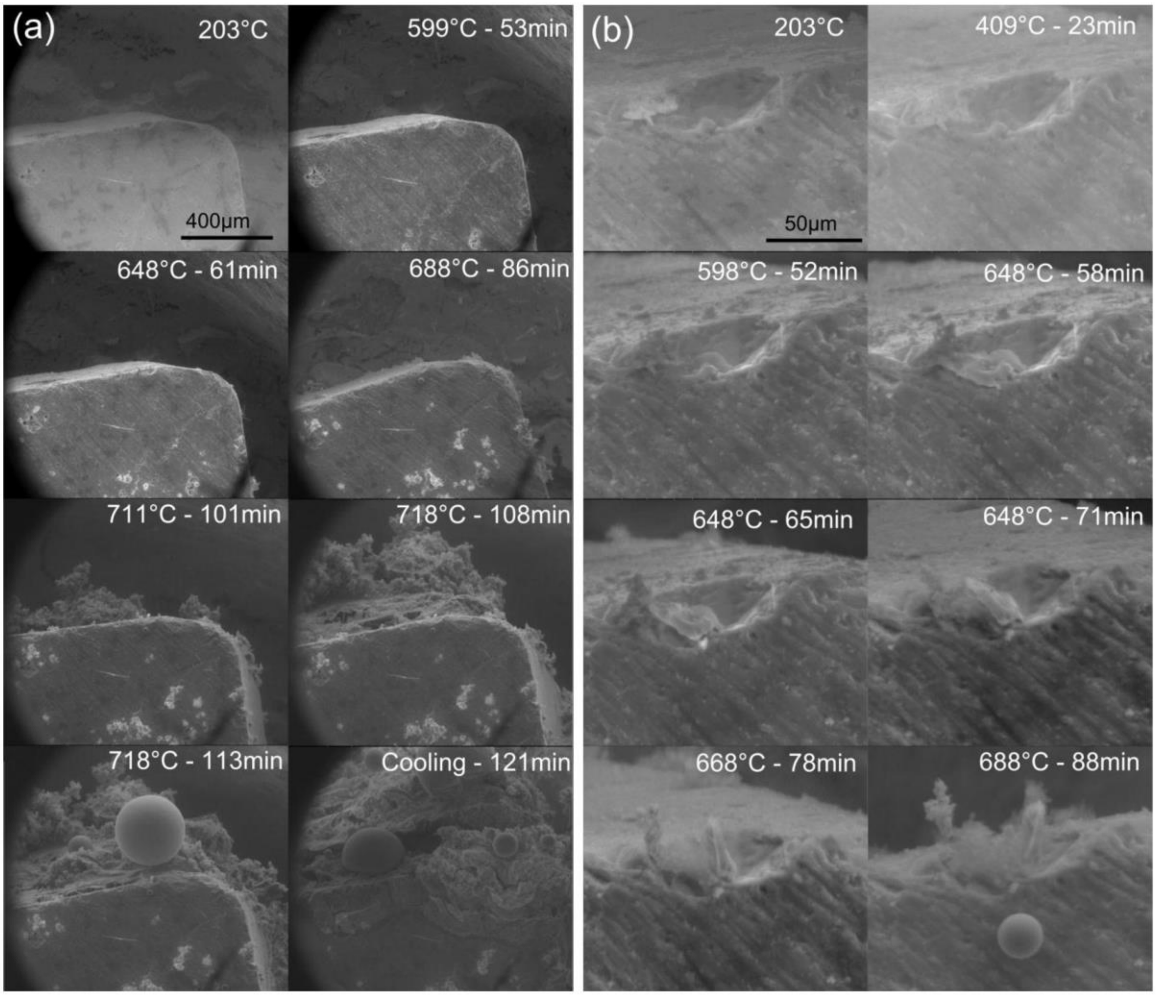

Fig. 8 SEM pictures of oxidation and decomposition of SN06. In (a) the rapid oxidation causing cauliflower like morphology is shown, while (b) shows the initial oxidation near cracks and defects at the exposed surface. The spheres are liquid Sn that do not wet the surface and therefore gathers as spheres on the surface before they eventually roll off.

DISCUSSION

Degradation of $Mg_2Si_{1-x}Sn_x$ is a complex process, consisting of several stages, which in combination yield the oxidation behavior and variations with composition, temperature and time, described in the previous sections. To get a quantitative understanding of the oxidation mechanism of such alloys requires an extensive experimental investigation. The main aim of this contribution is to get a qualitative understanding of the processes, contributing to the material degradation and their potential effect on the material applications.

Earlier investigations have shown that Mg_2Si is oxidation resistant at least up to about 500°C, above which the oxidation rate gradually increases and reaches a breakaway type behavior at a certain threshold (ignition) temperature. The reported threshold temperature varies significantly, from ~550°C for powder samples [5] to ~940 °C for thin films [8], the latter being close to the breakaway temperature of the reference Mg_2Si sample (powder), tested in this work (~920°C, see Fig. 2). The oxide scale will initially consist of an outer layer of MgO, whereas Si remains unaltered in the alloy. However, as the Mg component is consumed, Si is enriched close to the outer scale and will also eventually start to oxidize after prolonged exposure time and at the higher temperatures. When Sn is added to the Mg-Si system, forming $MgSi_{1-x}Sn_x$, the oxidation behavior remains more or less unchanged as long as the Sn level is low and the alloy matrix is single-phase. Although the oxidation rate increases slightly and the ignition temperature decreases, the effect of Sn on the degradation becomes far more pronounced once the composition reaches Sn levels (X>0.1), where a two-phase matrix of Si-rich and Sn-rich regions is formed. In a simplified picture one may treat the oxidation of the two phases separately. The initial oxidation of these two phases will be relatively similar consisting of the formation an outer layer of MgO. The Mg flux through the oxide layer will cause depletion of Mg (Mg vacancies) near the alloy-oxide interface. This is counterbalanced by a flux of Mg through the alloy, resulting in a certain concentration of Mg at the alloy-oxide interface, $C_{Mg,i}$, which depends on temperature (equilibrium concentration) and time (diffusion). The critical concentration of Mg, $C_{Mg,crit}$, to continue forming solely MgO depends on the maximum deviation from stoichiometric Mg_2X (X=Si,Sn). $C_{Mg,i}$ will either stabilize at values above $C_{Mg,crit}$ yielding protective behavior, or eventually become lower than $C_{Mg,crit}$, where Mg_2X will decompose and also Sn and Si will start to oxidize. This effect is shown schematically in Fig. 9. Similar effects are found in other alloy systems where the less noble element will be oxidized preferentially until depletion of this element causes other oxides to form [16]. An example is the out-diffusion of Cr in chromia-forming steel, where the depletion of Cr after a certain time can lead to breakaway oxidation [17]. In our case the oxidation behavior of Si-rich and Sn-rich phase will be rather different, since Si forms a protective scale whereas Sn does the strictly opposite. This is clearly reflected in the XRD diffractograms (Fig. 5), that shows no SiO_2 formation but large amounts of SnO_2 (and to some degree SnO for samples with high Sn-content) at temperatures just above the ignition temperature. Consulting the binary phase diagrams of the two systems, Mg-Si and Mg-Sn, another important difference appears: It is evident that a liquid phase is formed in the Mg-Sn system at temperatures above the eutectic point of Mg_2Sn-Sn at 203°C when the Mg-content is lower than that of Mg_2Sn. In contrast, the eutectic temperature between Mg_2Si and Si is 945°C. Consequently, liquids may form below the oxide layer on the Sn rich alloys when the oxide-alloy interface is Mg-depleted. This liquid will be detrimental to the protective behavior of the oxide scale and the oxidation turns into a break-away behavior. Our ESEM measurement (Fig. 8) confirms the formation of liquid Sn during oxidation.

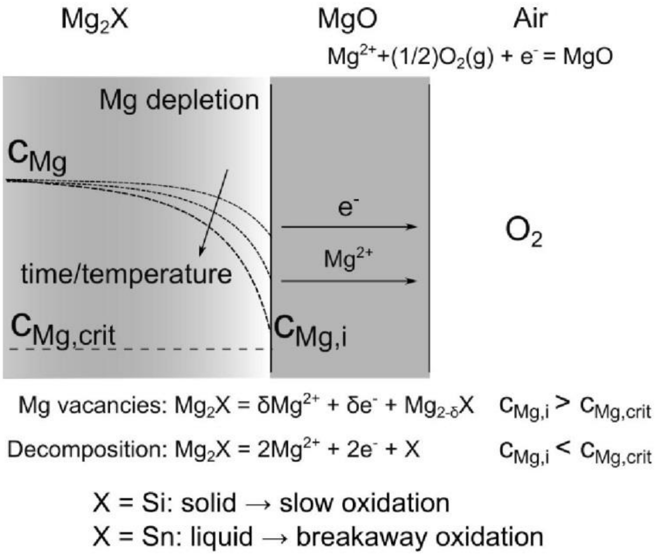

Fig. 9 Schematic illustration of the outward diffusion of Mg through the growing oxide layer (consumption), and the resulting concentration profile in the underlying matrix (depletion). The Mg concentration at the interface, $C_{Mg,}i$, is given by a balance of these two fluxes and depends on time and temperature. When $C_{Mg,}i$ become lower than a critical concentration $C_{Mg,crit}$, Mg_2X (X=Si,Sn) will decompose. At this point, Sn-rich phases will form liquid Sn under the oxide layer and result in breakaway oxidation.

Another material system property important to the effect of the composition on the oxidation mechanism is the gradual change of the so called Pilling Bedworth Ratio (PBR), defined as the ratio between the volume of the oxide layer and the volume of the original alloy [18], with Sn content. As a consequence of the buildup of strain and stress between the oxide and the underlying alloy matrix, cracked/porous (i.e. non-protective) oxide scales with weak adherence are formed when PBR<1 and PBR>2. With PBR values between 1 and 2, in theory, adherent protective oxide scales may be formed. Both, PBR and Gibbs free energy change connected to solute concentration, have been shown to affect the resistance towards breakaway oxidation for different Mg alloys [19]. Assuming that only MgO forms and by using experimentally determined values of density and molar mass [20], the PBR as a function of Sn-content has been estimated and is presented in Fig. 10(a). It is clear that for Sn content between 0 and 0.4, the PBR is between 1 and 2, being in the "protective region". For Sn content of 0.4 or above, the PBR is below 1, yielding "non-protective" scales. These changes in PBR correlate well with the cracking scales, observed for the alloys with higher Sn contents (cf. Fig. 6). Plotting the ignition temperatures (Fig. 4) against the Sn-content in the samples, a distinct border is found at the Sn-content of 0.4, corresponding to PBR of 1 (Fig. 10(b)). The formation of non-protective oxide scales accelerates the oxidation rate and, accordingly, the consumption of Mg. This leads to rapid formation of liquid phases, and thereby the catastrophic degradation of the alloys. The strongly exothermic nature of Mg oxidation could yield local "hot spots", that may also be important for the accelerated degradation of these materials. Indeed, the TG-curves in Fig. 4 resemble the sigmoidal-type of curves, expected for autocatalytic reactions, where the exothermic oxidation of Mg "catalyzes" further oxidation. This corresponds to the ESEM results seen in Fig. 8. Pores and other defects at the surface can act as the nucleation centers where oxidation is initiated. →Homogenous, defect-free surfaces are therefore important when preparing samples for testing as well as employing these materials for real applications.

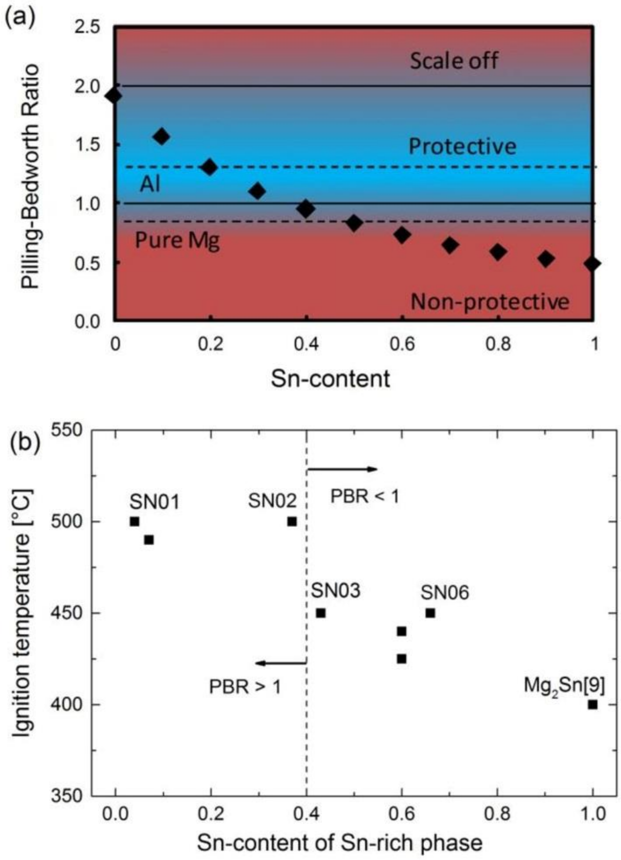

Fig. 10 (a) Pilling-Bedworth ratio (PBR) calculated from theoretical densities of $Mg_2Si_{1-x}Sn_x$ as a function of x assuming only MgO formation. (b) Comparing the ignition temperature to Sn-content (of the Sn-rich case for two-phase samples, see table II), a distinct border around Sn-content of 0.4 corresponding to PBR of 1 is found, where samples show significantly higher ignition temperatures at lower Sn-content.

This simplified picture qualitatively explains the observed degradation behavior. When the initial MgO forms it will remain relatively protective as long as it is thin, but when the scale grow thicker the stresses between the outer MgO and the alloy increases and the cracks start to propagate. The consumption of Mg increases and liquid phases may form due to the enrichment of Sn. These effects alone and, in particular combined, leads to the initial catastrophic oxidation, observed at temperatures around 430-500 °C. The alloys with lower Sn levels will require longer exposure time and/or higher temperatures to turn into the breakaway regime (cf. Fig. 4). Moreover, for these alloys (X<=0.2) a matrix of Si-rich phase may be preserved and its continuing oxidation yield the gradual weight increase, observed after the initial breakaway regime. The remains of the matrix are finally being fully oxidized in the second breakaway stage appearing above ~850 °C (cf. Fig. 2), resembling the behavior of Mg_2Si. Consulting the Mg_2Sn-Mg_2Si phase diagram, the peritectic temperature of the Sn-rich phase is 857°C which indicate an enhanced effect of peritectic decomposition.

A more detailed understanding of the development of the oxidation mechanism of these alloys with temperature would require knowledge on the activation energy of the processes important to the overall degradation. In particular the temperature dependence of the Mg consumption by oxidation vs. supply by diffusion (yielding the concentration of Mg at the alloy-oxide interface, $C_{Mg,i}$), but also the temperature dependence of the oxide scale deformation would be essential. Deformation processes are important to the scale microstructure and adherence to the alloy, and accordingly to the type of oxidation kinetics, e.g. parabolic ("protective") vs linear ("non-protective") time dependence. As such, the deformation processes may strongly influence the rate of Mg consumption at the oxide alloy interface.

The evolution of the oxidation behavior as a function of temperature is a delicate balance of at least these three major processes with correspondingly different activation energies. Consequently, the course of oxidation may, as we have seen here, change dramatically only with small differences in temperature and also with small differences in the alloy composition and microstructure (i.e. detailed fabrication route). Therefore the behavior of nominally the same composition may have rather different behavior. The complexity of the overall oxidation process is also reflected in the differences, observed between powders and bulk specimens, different heating rates and isothermal oxidation.

From this study, it is clear that thermoelectric systems made with silicide materials needs to operate at lower temperatures than the ignition temperature in the presence of oxygen (air). Since only small additions of Sn decrease the ignition temperature significantly, the benefit of increased zT values may be offset by the need to decrease the hot side temperature to avoid oxidation. In cases where high temperatures are available, encapsulation or use of protective coatings must be considered. However, as we have seen, oxidation well below the ignition temperature forms a protective layer leading to near zero oxidation rates during prolonged exposure to oxygen. For thermoelectric applications with lower hot side temperatures, $Mg_2Si_{1-x}Sn_x$ could possibly be used without special coatings or encapsulation. It also means that these materials can be easily handled in oxidizing conditions during processing and assembly as long as the temperature is kept below the ignition temperature. This simplifies the production process and shows the adequacy of employing $Mg_2Si_{1-x}Sn_x$ in industrial mass-production.

CONCLUSION

The high temperature oxidation mechanisms of $MgSi_{1-x}S_x$ resemble that of other Mg-alloys systems: low oxidation rates below a certain threshold (ignition) temperature, where a protective layer of MgO forms due to outward diffusion of Mg, followed by breakaway kinetics (burning) above the ignition temperature. The ignition temperature is strongly dependent on the alloy composition, which in our case is seen as a decrease in the ignition temperature of $Mg_2Si_{1-x}Sn_x$ from ~500°C at X=0.1 to ~430°C at X=0.6. For X>0.1 the alloy is two-phase with a balance between Si-rich and Sn-rich phases, which affects the oxidation mechanisms significantly. Two main mechanisms are suggested to explain the transition into breakaway oxidation: firstly, the depletion of Mg at the alloy-oxide interface causing the decomposition of the Sn-rich phase forming liquid Sn, and secondly, stress build-up between alloy and oxide, leading to crack formation and non-protective oxide layers. This process is enhanced at X>=0.4, when PBR is less than unity. In addition, the very exothermic oxidation of Mg leads to a fast, near autocatalytic reaction, which in the case of non-homogenous samples and presence of surface-defects can result in even lower ignition temperatures. The applicability of $Mg_2Si_{1-x}Sn_x$ in thermoelectric application is limited either to temperatures well below the ignition temperature for the given Sn-content, or requires the use of encapsulations and coatings.

ACKNOWLEDGEMENTS

The authors wish to acknowledge financial support from the ThermoMag Project, which was co-funded by the European Commission in the 7th Framework program (contract NMP4-SL-2011-263207), by the European Space Agency and by the individual partner organizations. Special thanks to colleagues from Centre for Materials Science and Nanotechnology (SMN) at University of Oslo for help with carrying out ESEM and TGA measurements.

REFERENCES

[1] V.K. Zaitsev, M.I. Fedorov, E.A. Gurieva, I.S. Eremin, P.P. Konstantinov, A.Y. Samunin, M.V. Vedernikov, Highly effective $Mg_2Si_{1-x}Sn_x$ thermoelectrics, Phys Rev B, 74 (2006) 045207.
[2] M. Akasaka, T. Iida, A. Matsumoto, K. Yamanaka, Y. Takanashi, T. Imai, N. Hamada, The thermoelectric properties of bulk crystalline n- and p-type Mg2Si prepared by the vertical Bridgman method, J. Appl. Phys., 104 (2008) 013703.
[3] A.U. Khan, N.V. Vlachos, E. Hatzikraniotis, G.S. Polymeris, C.B. Lioutas, E.C. Stefanaki, K.M. Paraskevopoulos, I. Giapintzakis, T. Kyratsi, Thermoelectric properties of highly efficient Bi-doped Mg2Si1−x−ySnxGey materials, Acta Mater, 77 (2014) 43-53.
[4] W. Liu, X. Tan, K. Yin, H. Liu, X. Tang, J. Shi, Q. Zhang, C. Uher, Convergence of Conduction Bands as a Means of Enhancing Thermoelectric Performance of n-Type Mg2Si1-xSnx Solid Solutions, Phys Rev Lett, 108 (2012) 166601.
[5] J.-i. Tani, M. Takahashi, H. Kido, Fabrication of oxidation-resistant β-$FeSi_2$ film on Mg_2Si by RF magnetron-sputtering deposition, J. Alloy Compd., 488 (2009) 346-349.
[6] R. Funahashi, Y. Matsumura, T. Barbier, T. Takeuchi, R. Suzuki, S. Katsuyama, A. Yamamoto, H. Takazawa, E. Combe, Durability of Silicide-Based Thermoelectric Modules at High Temperatures in Air, J. Electron. Mater., 44 (2015) 2946-2952.
[7] G. Skomedal, N. Kristiansen, M. Engvoll, H. Middleton, Methods for Enhancing the Thermal Durability of High-Temperature Thermoelectric Materials, J. Electron. Mater., 43 (2013) 1946-1951.

[8] D. Stathokostopoulos, D. Chaliampalias, E. Pavlidou, K.M. Paraskevopoulos, K. Chrissafis, G. Vourlias, Oxidation resistance of magnesium silicide under high-temperature air exposure, J. Therm. Anal. Calorim., 121 (2015) 169-175.
[9] M. Brause, B. Braun, D. Ochs, W. Maus-Friedrichs, V. Kempter, Surface electronic structure of pure and oxidized non-epitaxial Mg2Si layers on Si(111), Surface Science, 398 (1998) 184-194.
[10] W.D. Robertson, H.H. Uhlig, Chemical Properties of the Intermetallic Compounds Mg2Sn and Mg2Pb, Journal of The Electrochemical Society, 96 (1949) 27-42.
[11] V. Fournier, P. Marcus, I. Olefjord, Oxidation of magnesium, Surface and Interface Analysis, 34 (2002) 494-497.
[12] F. Czerwinski, Oxidation Characteristics of Magnesium Alloys, JOM, 64 (2012) 1477-1483.
[13] J. Bourgois, J. Tobola, L. Chaput, P. Zwolenski, D. Berthebaud, F. Gascoin, Q. Recour, H. Scherrer, Study of electron, phonon and crystal stability vs. thermoelectric properties in Mg_2X (X=Si, Sn) compounds and their alloys, Funct. Mater. Lett., 6 (2013) 1340005.
[14] I.-H. Jung, D.-H. Kang, W.-J. Park, N.J. Kim, S. Ahn, Thermodynamic modeling of the Mg–Si–Sn system, Calphad, 31 (2007) 192-200.
[15] G. Skomedal, Mg2(Si-Sn) oxidation (video), in: https://www.youtube.com/watch?v=AiPikp-3tgw, 2014.
[16] D. Young, High temperature oxidation and corrosion of metals, in: D. Young (Ed.), Elsevier, Oxford, 2008, pp. 237-241.
[17] H.E. Evans, A.T. Donaldson, T.C. Gilmour, Mechanisms of Breakaway Oxidation and Application to a Chromia-Forming Steel, Oxid. Met., 52 (1999) 379-402.
[18] C. Xu, W. Gao, Pilling-Bedworth ratio for oxidation of alloys, Mat Res Innovat, 3 (2000) 231-235.
[19] Y.M. Kim, C.D. Yim, H.S. Kim, B.S. You, Key factor influencing the ignition resistance of magnesium alloys at elevated temperatures, Scripta Materialia, 65 (2011) 958-961.
[20] W. Luo, M. Yang, F. Chen, Q. Shen, H. Jiang, L. Zhang, Fabrication and thermoelectric properties of Mg2Si1−xSnx ($0 \leq x \leq 1.0$) solid solutions by solid state reaction and spark plasma sintering, Mat Sci Eng B-Solid, 157 (2009) 96-100.

Paper 4: Design, assembly and characterization of silicide-based thermoelectric modules

Paper 4: Design, assembly and characterization of silicide-based thermoelectric modules

Energy Conversion and Management 110 (2016) 13–21

Contents lists available at ScienceDirect

Energy Conversion and Management

journal homepage: www.elsevier.com/locate/enconman

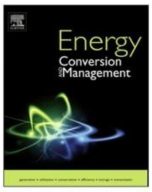

Design, assembly and characterization of silicide-based thermoelectric modules

Gunstein Skomedal [a,*], Lennart Holmgren [b], Hugh Middleton [a], I.S. Eremin [c], G.N. Isachenko [c,d], Martin Jaegle [e], Karina Tarantik [e], Nikolas Vlachos [f], Maria Manoli [f], Theodora Kyratsi [f], David Berthebaud [g], Nhi Y. Dao Truong [g], Franck Gascoin [g]

[a] *Department of Engineering Sciences, University of Agder, Jon Lilletunsvei 9, 4879 Grimstad, Norway*
[b] *Termo-Gen AB, Gotland, Sweden*
[c] *A.F. Ioffe Physical-Technical Institute, Saint Petersburg, Russia*
[d] *ITMO University, Saint Petersburg, Russia*
[e] *Fraunhofer IPM, Freiburg, Germany*
[f] *Department of Mechanical and Manufacturing Engineering, University of Cyprus, Nicosia, Cyprus*
[g] *Laboratoire CRISMAT, Caen, France*

ARTICLE INFO

Article history:
Received 10 September 2015
Accepted 30 November 2015

Keywords:
Thermoelectric module
Higher manganese silicide
Magnesium silicide
Degradation

ABSTRACT

Silicides have attracted considerable attention for use in thermoelectric generators due mainly to low cost, low toxicity and light weight, in contrast to conventional materials such as bismuth and lead telluride. Most reported work has focused on optimizing the materials properties while little has been done on module testing. In this work we have designed and tested modules based on N-type magnesium silicide Mg_2(Si–Sn), abbreviated MGS, and P-type Higher Manganese Silicide, abbreviated HMS. The main novelty of our module design is the use of spring loaded contacts on the cold side which mitigate the effect of thermal expansion mismatch between the MGS and the HMS. We report tests carried out on three modules at different temperatures and electric loads. At a hot side temperature of 405 °C we obtained a maximum power of 1.04 W and at 735 °C we obtained 3.24 W. The power per thermoelectric material cross section area ranged from 1 to 3 $W\,cm^{-2}$. We used the modeling tool COMSOL to estimate efficiencies at 405 and 735 °C and obtained values of 3.7% and 5.3% respectively – to our knowledge the highest reported value to date for silicide based modules. Post-test examination showed significant degradation of the N-type (MGS) legs at the higher hot side temperatures. Further work is underway to improve the lifetime and degradation issues.

1. Introduction

Silicides are among the most promising materials for thermoelectric generators (TEG) exploiting medium temperature waste heat recovery sources such as exhaust gas heat from internal combustion engines. Recent studies on novel thermoelectric material have shown that silicides offer considerable advantages over conventional materials for mass production and scale up due to their low cost, relatively high abundance and availability of raw materials and high thermoelectric efficiency [1–3]. However, module manufactures have had very limited experience with silicide based materials thus creating a paucity in performance data for modules based on silicides. Today the highest performing silicide thermoelectrics are based on Mg_2(Si–Sn) solid solutions and are all N-type with peak zT values up to 1.5 [4–7]. Typically, the efficiency improves with increasing Sn-content in $Mg_2Si_xSn_{1-x}$ to a peak value with x between 0.4 and 0.6, but will simultaneously reduce the stability to the extent that lower hot side temperatures must be used [8]. Decomposition due to fast oxidation of Mg is especially of concern [9,10]. In contrast to N-type silicides, there are few examples of P-type silicides and of these the Higher Manganese Silicides (HMS) exhibits the best performance with peak zT values in the range 0.6 to 0.8 [11]. One problem with combining both N-type and P-type materials as unicouples in a module construction is caused by their relative difference in coefficients of thermal expansion (CTE). Generally, N-type silicides have CTE in the range 16–18 $\cdot$ $10^{-6}\,K^{-1}$ for Mg_2(Si–Sn) whereas P-type HMS materials exhibit CTE's in the range of 9-13 $\cdot$ $10^{-6}\,K^{-1}$ [6,12–14]. This inevitably leads to stress build up as a result of the large

---

[*] Corresponding author. Tel.: +47 91113267.
E-mail address: gunstein.skomedal@uia.no (G. Skomedal).

http://dx.doi.org/10.1016/j.enconman.2015.11.068
0196-8904/

temperature gradient between the hot and cold sides of the module. This in turn can cause degradation of the legs and a reduction in performance over time. This effect is particularly observed with the N-type legs on the hot side of the module. Attempts by Nemoto et al. have been made to overcome this problem by constructing unileg modules based on N-type Mg_2Si only [15–17]. These modules shows very good stability and reliability but still have quite low efficiency, with power per module area of around 0.22 W/cm^2 at a temperature difference of 500 °C.

A very important consideration in module design is minimizing degradation of thermoelectric properties during long periods of time. This is especially the case for the hot side where interdiffusion and material loss is more prevalent. The general approach is to introduce functional layers between the thermoelectric leg material and the current collecting plate. This process is collectively referred to as "Metallization". These include a diffusion barrier layer, a contact layer, an adhesion layer and a compliant layer [18]. In order for these layers to function reliably there needs to be some interdiffusion between them but not a persistent amount that would otherwise spoil their effect. This requires careful selection of material and method of application. In the case of contact layers, one promising option is the use of other silicides such as $TiSi_2$, $CrSi_2$, CoSi and MnSi. The latter has been combined with HMS and exhibits low contact resistances in the order of 10^{-6}–10^{-5} $\Omega\,cm^2$ [19–22]. Another approach is to use pure metals such as Ni to form contacts. With HMS a diffusion barrier needs to be inserted between the leg and the contact layer in order to hinder reaction and crack formation. A thin layer of chromium seems to be a good option for this function mainly because it has a very close matching CTE ($\sim 10 \cdot 10^{-6}\,K^{-1}$) and relatively low contact resistance in the order of $10^{-5}\,\Omega\,cm^2$ [23–25]. The Iida group in Japan [22] has investigated the direct sintering of nickel powder on top of Mg_2Si giving a good contact layer, but even better contact can be achieved by pressing a thin nickel foil onto the surface of the leg instead of using nickel powder. In such experiments contact resistances in the region of $10^{-6}\,\Omega\,cm^2$ have been observed and this approach seems promising for long term stability [26]. Both these methods have been shown to work well within the ThermoMag project. However, concern has been raised on how stable the direct contact of Ni on Mg_2Si is due to the formation of NiSi, and whether or not a diffusion barrier is also needed in this case. In the case of $Mg_2(Si–Sn)$, we are not aware of any published work on contacts, but we assume that similar approaches used for other silicides and especially pure Mg_2Si could be used. However as stated previously in this article there is concern about the higher CTE of $Mg_2(Si–Sn)$ compared with Mg_2Si. The goal of the design presented in this article was to facilitate a versatile and simple test-module that could be easily fabricated, incorporating different N- and P-type materials with different CTE values. Several methods of metallization were also used as described in the experimental section.

2. Experimental

2.1. Material preparation

The thermoelectric material used within this work is a result of the effort of several partners within the ThermoMag project [27]. Details of the synthesis of the thermoelectric material can therefore be found in the references to the respective partners work and are not given in details in this report. General powder-compaction techniques where used to prepare cylindrical pellets ($\varnothing$ = 10–50 mm). These were then cut into legs of the size $3 \times 3 \times 4\,mm^3$ at Fraunhofer IPM. The material composition and thermoelectric properties of the materials used for the modules are listed in Table 1.

2.2. Module design

The construction of the module is shown in Fig. 1. The left illustration shows two legs (N and P) sandwiched between a copper block and a molybdenum plate both acting as current collectors (electrodes). The copper block is a structural element and also has recessed cavities into which springs are located; these provide compression to the legs to maintain contact while at the same time provide some compliance to mitigate the effect of thermal expansion mismatch between the N- and P-type material. The metallized legs are attached to the cold side by use of lead based solder foil as described in the module assembly. The right hand side of Fig. 1 shows the complete module with two rows of 3 pairs of unicouples containing 12 thermoelectric legs in total. The unicouples are held in position on the cold side by an anodized aluminum block of size $11.7 \times 32.8\,mm^2$. Heat transfer is effected through from the *side* of the copper blocks to the anodized aluminum, while the springs press the blocks up (∼1 mm) from the bottom. The current collection on the hot side was made using copper (module #1) and molybdenum (modules #2 and #3). The hot side was electrically isolated from the heating source using thin sheets of mica plates. The normal use of substrates attached to the hot side was considered unnecessary in this test setup.

2.3. Module assembly

The "as received" thermoelectric legs were subjected to a quality control involving matching of physical dimensions and checking of thermo power, electrical conductivity and evidence of cracking or chipping. Particular attention was given to select legs of equal height as this affects the quality of the electrical and thermal contact– only the closest matching legs were selected for module construction. The metallization was carried out by sputtering one or more metal layers onto the selected legs. Prior to this however there was a pretreatment stage in which the faces of the legs were polished and cleaned to remove any traces of surface oxidation and grease. Both N- and P-type materials were given the same metallization treatment and both hot and cold sides were metallized. After metallization the legs were placed in the correct orientation and soldered onto the cold side of the copper blocks using foils of a lead based solder allow. The solder operation was carried out in a vacuum tube back filled with argon at 450 °C. The hot side bonding was accomplished through diffusion bonding at the beginning of the performance testing.

2.4. Performance testing

The modules were tested in an evacuated chamber back filled with argon. The module was first placed onto a water cooled aluminum plate to maintain the cold side. An insulating sheet of mica was placed between the hot side of the module and a heater element. The whole setup was then clamped together using a spring loaded plate. The hot side temperature was measured with thermocouples placed both on the surface of the heater and on the surface of the hot side of the module. The cold side temperature of the module was not directly measured, but estimated from V_{OC} and the temperature of cooling water flow. Copper wires were soldered onto the two cold side current collecting electrodes for performance measurements of module voltage and current. Two test regimes were used – either the hot side was heated up to a fixed temperature while monitoring module behavior or the module was thermally cycled while measuring the performance. The measured open circuit voltage (V_{OC}) was compared with the theoretical value calculated from the integral of the Seebeck coefficients of the N- and P-type thermoelectric materials according to Eq. (1). The

Table 1
Material properties of the thermoelectric material used in the modules.

Material name	MGS-1	MGS-2	HMS
Composition	$Mg_2(Si_{0.4}Sn_{0.6})_{0.99}Sb_{0.01}$	$Mg_2Si_{0.53}Sn_{0.4}Ge_{0.05}Bi_{0.02}$	$MnSi_{1.75}Ge_{0.01}$
Producer	Ioffe Institute [28]	University of Cyprus [7]	Laboratoire CRISMAT [29]
Synthesis	Melt-annealing followed by hot pressing	Cold pressing and annealing, then ball milling and heating followed by SPS	Ball milling followed by SPS
Density (g/cm^2)	3	2.75	4.95
Seebeck coefficient (μV/K)	(−) 130–160	(−) 100–220	150–220
Electrical conductivity (S/cm)	800–1400	800–1600	300–500
Thermal conductivity (W/m K)	2–2.5	2–3	2.5–3
Peak zT	0.8 (600 K)	1.4 (800 K)	0.4 (800 K)

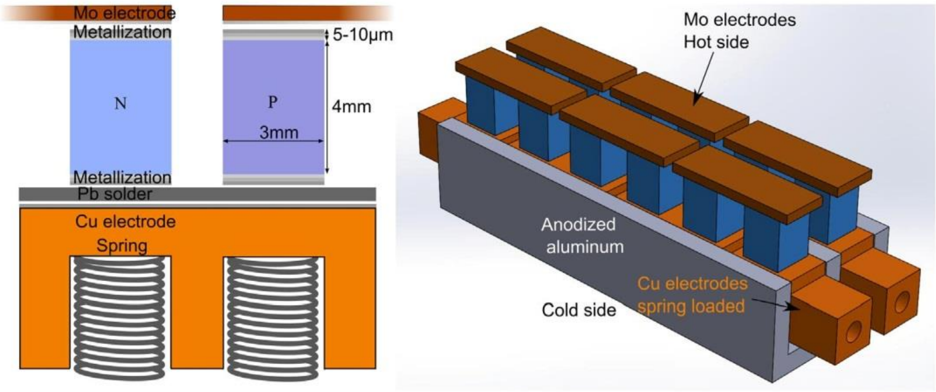

Fig. 1. Left: Sketch of unicouple with metallization and contact layers. Right: Sketch of finished assembled module with 6 unicouples. The heat conduction on the cold side is through the *side-walls* of the Cu electrodes which are layered with thermal paste.

Table 2
Summary of test results of the modules. Cold side temperature of module varies between 30 and 50 °C. R_i and P_{max} are calculated from Eqs. (2) and (3). For module #3 the values represents the initial conditions before cycling. K is the total thermal conductance of the thermoelectric elements.

Module	TE materials	Hot side contacts	Test temp (°C)	R_i legs (Ω)	V_{OC} ideal (V)	K legs (W/K)	R_i (Ω)	V_{OC} (V)	P_{max} (W)	$Z\overline{T}$ calc
#1	N: MGS-1 P: HMS	Cu-electrodes Ni/Pb/Ni	$T_{hot} \sim 735$ single run	0.09	1.34	0.067	8 → 0.1	1.16	3.24	0.26
#2	N: MGS-1 P: HMS	Mo-electrodes Ni/Pb/Ni/Cr	$T_{hot} \sim 405$ single run	0.08	0.73	0.069	0.1	0.65	1.04	0.24
#3	N: MGS-2 P: HMS	Mo-electrodes Ni/Pb/Ni/Cr	$T_{hot} \sim 450$ thermal cycling	0.08	0.82	0.069	>0.2	~0.5	<0.11	–

multiplication scaling factor of 6 corresponds to the number of thermoelectric legs making up the unicouples.

$$V_{OC} = 6\int_{T_{cold}}^{T_{hot}} (S_P(T) - S_N(T))dT \tag{1}$$

where S_P and S_N are the temperature dependent Seebeck coefficient of the N- and P-type material respectively. These were fitted to the measured seebeck coefficient values for the nominal materials as a 3rd degree polynomial function, $S(T) = aT^3 + bT^2 + cT + d$. The inner resistance of the module (R_i) was calculated by measuring the module in open circuit and load conditions using

$$R_i = \frac{V_{OC} - V}{I} \tag{2}$$

where V and I are the measured voltage and current under load conditions. From this the maximum power of the module at load-matching condition ($R_{load} = R_i$) can be calculated from

$$P_{max} = \frac{V_{OC}^2}{4R_i} \tag{3}$$

After testing the modules were disassembled and some of the unicouples taken out and cut in half to examine the cross section with scanning electron microscope (SEM, Zeiss Merlin) and energy dispersive X-ray spectrometer (EDS). A simple COMSOL model was developed to estimate heat transport and total efficiency of the system utilizing the built-in thermoelectric effect multiphysics package. The peak efficiency was found by maximizing $\eta_{TE} = P/Q_{in}$, where Q_{in} is the heat flow into the module from the hot side. Then the average ZT of the module was calculated by solving

$$\eta_{max} = \frac{T_H - T_C}{T_H} \cdot \frac{\sqrt{1 + Z\overline{T}} - 1}{\sqrt{1 + Z\overline{T}} + \frac{T_C}{T_H}} \tag{4}$$

where $\overline{T} = (T_H + T_C)/2$. The measured temperatures and I–V characteristics along with the nominal thermoelectric properties were used as input to the model to optimize the interface parameters such as electrical contact resistance and heat transfer coefficients. Since the module was tested in a chamber backfilled with argon and the module did not have any insulation, parasitic heat losses

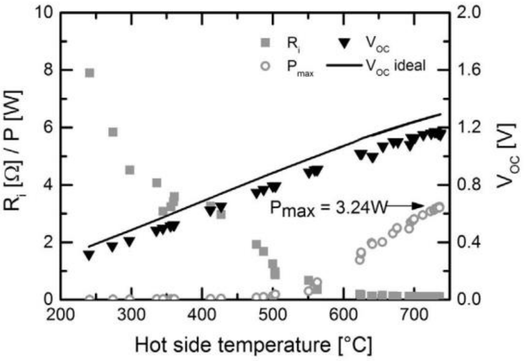

Fig. 2. V_{OC}, R_i and P_{max} of module #1 during the test when ramping up from RT to 735 °C on the hot side. The V_{OC} estimated from the Seebeck coefficient of the TE materials are also shown, approximately 10% higher than the measured value. The inner resistance R_i is reduced dramatically from 8 to 0.1 Ω indicating good diffusion bonding at elevated temperatures. This results in a peak P_{max} of 3.24 W at hot side temperature of 735 °C.

were estimated too. The radiative losses were estimated using a surface emissivity of 0.8 for all surfaces, and the convective losses using a surface convective heat transfer coefficient of 10 W/m^2 K in surroundings of 25 °C (values based on natural convection of air). To simplify things further the thermal contact resistances of the system were set to constant values which were found by fitting the calculated V_{OC} within ±1% of the measured V_{OC} at given hot side temperatures. The cold side heat transfer coefficient was estimated from measured temperature differences between cooling water and actual cold side temperature of module and set to a constant value of 2000 W/m^2 K and the cold side reservoir to 25 °C. This allows the cold side temperature of the module to vary within the model. It was evident from the post-characterization after testing that the P-type material showed very good stability and bonding at the hot side interconnect which contrasted the observed degradation of the N-type material. Therefore, the electrical contact resistance was set to $1 \times 10^{-5}\ \Omega\,\mathrm{cm}^2$ for the P-type elements while the N-type was varied to fit the measured series (inner) resistance of the module. On the cold side, the electrical contact resistance was set to zero as it was very small compared to the total series resistance.

3. Results and discussion

Several modules with different TE-materials, metallization and hot side electrodes were manufactured and three of them were chosen for further testing as shown in Table 2. The first two modules were only tested for a short period while the third module was tested for a prolonged time period.

The power-characteristics of module #1 are found in Fig. 2. The initial R_i of this module at room temperature was above 8 Ω but decreased rapidly as it was heated up to higher hot side temperatures. The decrease corresponds to the formation of a diffusion bond between the hot side electrode and the N- and P-type elements. As can be seen, R_i was reduced to a minimum value of 0.1 Ω at around 600 °C. The hot side temperature was further ramped up to 735 °C were a maximum power of 3.24 W was measured under load-matching conditions. Because the cold side temperature was not measured directly on the module, a deviation in the V_{OC} compared with the estimated values using Eq. (1) was to be expected. This is also seen in Fig. 2 where the V_{OC} was roughly 10% lower than estimates based on the measured hot side and cooling water temperatures. Most of this deviation was due to a 10% temperature difference over the cold side heat exchanger of the module, in addition to thermal contact resistances within the module. After the test the module was taken out and disassembled as shown in Fig. 3. The hot side electrodes could be removed by applying a small force. A black porous layer was clearly visible around the hot side of the N-type elements. By contrast, the P-type elements appeared to be intact. Subsequent SEM/EDS analysis showed that the black layer was a mixture of MgO and a Cu–Si phase, probably Cu_3Si. Cross sectional analysis also revealed a thick interdiffusion zone on the hot side of thickness 100–300 μm consisting of mixed phases of $Mg_2(Si–Sn)$ and Cu. No clear layers of

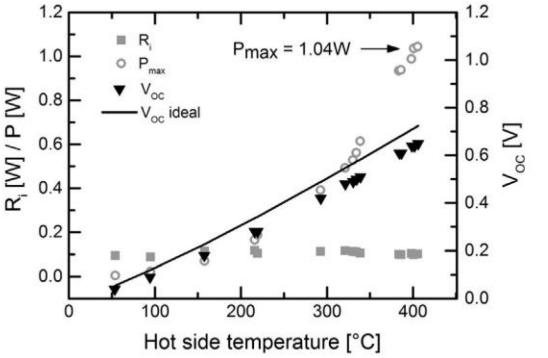

Fig. 4. Temperature and V_{OC} measurements of module #2. The calculated power curve is shown based on the V_{OC} and calculated R_i. The inner resistance is low and stable at approximately 0.1 Ω during the temperature programmed ramp. P_{max} with a hot side temperature of 405 °C is 1.04 W.

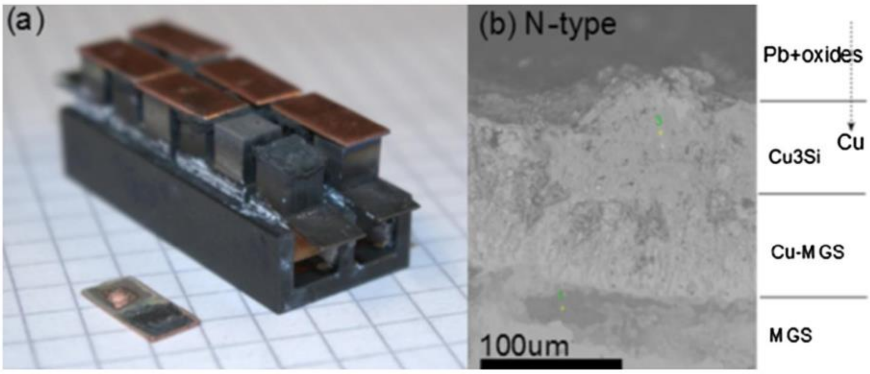

Fig. 3. (a) Module #1 after disassembly. A thick, black porous layer can be seen on the hot side of N-elements. EDS analysis showed high amount of oxygen indicating decomposition and MgO formation. (b) SEM picture of the hot side cross section of the N-element interconnect shows a thick diffusion zone of approximately 150–200 μm where Cu had diffused into the hot side of the element. Only traces of Pb and Ni are still evident.

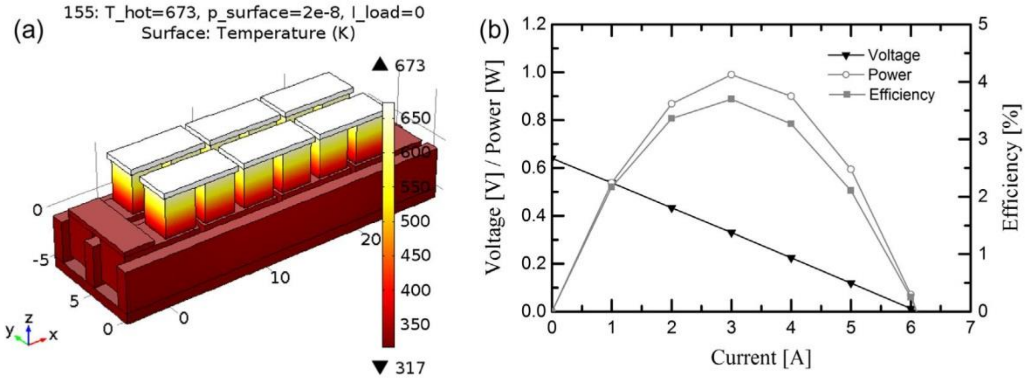

Fig. 5. (a) Surface temperature calculated using a COMSOL model of modules #1 and #2. (b) Voltage, power and efficiency of the module as a function of load current. All values calculated with a N-type contact resistance on the hot side of 2x10^{-4} Ω cm^2 and a hot side temperature of 400 °C.

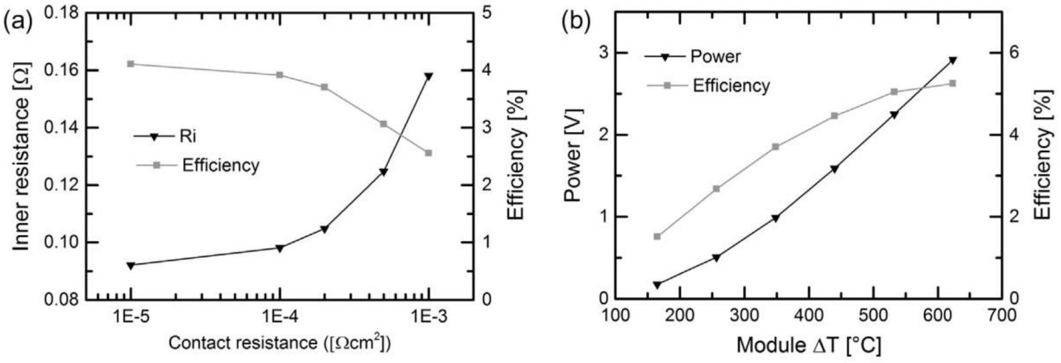

Fig. 6. Calculated results from COMSOL model for modules #1 and #2. (a) Total inner resistance and maximum efficiency of the module for different contact resistances of the hot side N-junction at a hot side temperature of 400 °C. (b) Maximum power and efficiency for different module ΔT at N-type contact resistance of 2×10^{-4} Ω cm^2.

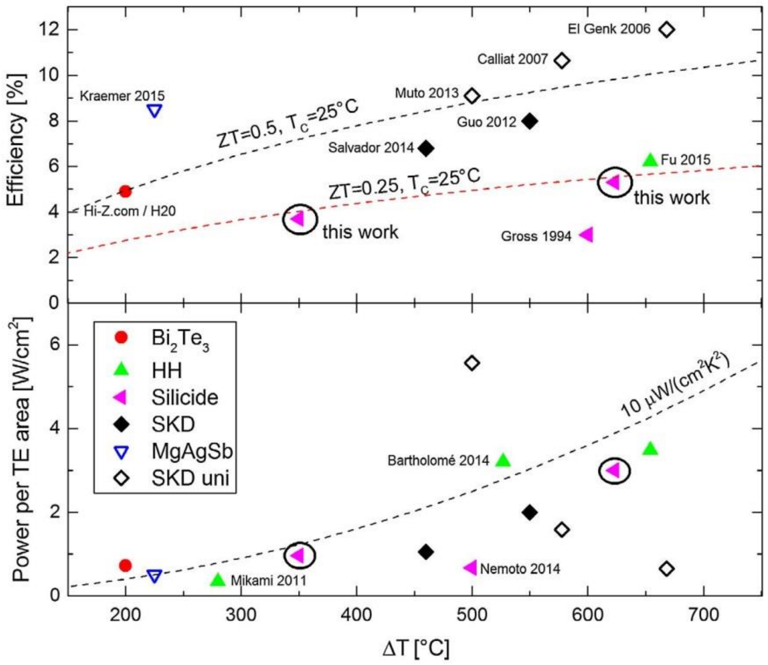

Fig. 7. Comparison of module efficiency (a) and power per area of thermoelectric material (b) for different modules (filled symbols) and unicouples (open symbols) as a function of temperature difference over the module, ΔT [17,19,30–38]. Efficiency curves calculated from Eq. (4) and power curves assuming constant power factor (i.e $P_{\max} \approx \text{const} \cdot \Delta T^2$) is shown for comparison between the different modules tested at different ΔT.

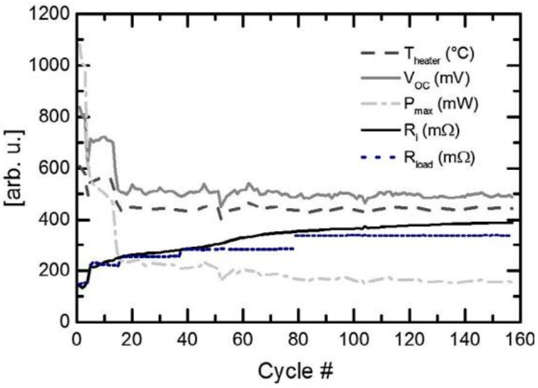

Fig. 8. T_{hot}, V_{OC}, R_i and $P_{\max}$ during thermal cycling of module #3 between 150 °C and 450 °C. The dwell time at 450 °C was 15 min while the ramp time was approximately 20 min for both up and down. The initial jump in R_i was caused by reinserting the module after initial diffusion bonding of hot side. It can be seen how R_i gradually decreases during the whole test-period.

the Ni and Pb sputtered layers were found. For the P-type elements no reactions between the electrode and the TE-material were found, showing the excellent stability of HMS. Even though the test were run in an evacuated chamber backfilled with industrial grade argon (99.95%), the presence of large amounts of MgO shows how also low partial pressure of oxygen present in the argon cylinder (typically ~10 ppm of O_2/H_2O) can cause fast oxidation and decomposition of $Mg_2(Si–Sn)$ solid solutions at high temperatures. The results show that using a copper current collector with a nickel diffusion barrier does not provide enough protection on the hot side for $Mg_2(Si–Sn)$. Therefore in further tests, molybdenum was used instead of copper and chromium used as diffusion barrier in addition to nickel.

The initial test results of module #2 are presented in Fig. 4. In contrast to module #1 this module showed at the outset a very low inner resistance R_i of just above 0.1 Ω at low temperature and did not change during testing. Similarly to module #1, the V_{OC} was stable and approximately 10% lower than the values estimated from the Seebeck coefficient given in Eq. (1). The module temperature was limited to 405 °C on the hot side to try to avoid the severe oxidation and decomposition seen for module #1 at higher temperatures. The maximum power recorded with a hot side temperature of 405 °C was 1.04 W. When this is divided by the total area of the module this equates to 0.28 W/cm^2, or when divided by the total thermoelectric area equates to 0.98 W/cm^2.

The total resistance of the electrical connections was estimated by subtracting off the electrical resistance of the thermoelectric material leaving a residual resistance of 20% or 0.02 Ω. Assuming that most of this is caused by the contact resistance on the hot side junctions between electrode and thermoelectric material this corresponds to 1.6 mΩ per element or $1.5 \times 10^{-4}\ \Omega\,\text{cm}^2$. This is around an order of magnitude higher than the contact resistance produced by other contacting methods [19–26]. However, the bonding method in this work was based on a pressure contact followed by in-situ diffusion bonding. This is a simple method not requiring any subsequent soldering. An increase in R_i caused by contacts of 20% is considered to be high, but from Eq. (3) we find that this equals to a $P_{\max}$ reduction of 17%. This may not necessarily be detrimental to the performance of the module so long as it can be stabilized over time and not increased any further.

The measured thermal and electrical values from the performance testing were used in a COMSOL model for estimating efficiency and how variations in electrical contact resistance would influence the performance. Both for modules #1 and #2 the inner resistance were similar around 0.1 Ω. A contact resistance of $2 \times 10^{-4}\ \Omega\,\text{cm}^2$ on the N-type hot side interfaces in the COMSOL model was found to fit well with this observation. At a temperature difference of 405 °C and a cold side reservoir temperature of 25 °C, the I–V characteristics was replicated in the model and the total power and efficiency of the module calculated and are found in Fig. 5. The max efficiency was estimated to 3.7% at this temperature, with corresponding ΔT over the module of 350 °C. This equals an average ZT of the module of 0.24 (see Table 2). In Fig. 6, the maximum efficiency is plotted against the contact resistance of the N-type (a) and the estimated module ΔT (b). As can be seen, the efficiency decreases from 4.1% to 2.6% for an increase in the contact resistance from $1 \times 10^{-5}\ \Omega\,\text{cm}^2$ to $1 \times 10^{-3}\ \Omega\,\text{cm}^2$. This equals an increase in inner resistance of the module of 73% (from 0.092 to 0.16 Ω). As expected, the maximum efficiency increases gradually with increasing hot side temperature and reaches 5.3% at a hot side temperature of 700 °C and module ΔT of 623 °C which is similar to the test-condition of module #3. The thermal contact resistance across the hot side junction between the thermoelectric material and the electrode is in the order of $1–2 \times 10^{-5}\ \text{m}^2\,\text{K/W}$. The total thermal conductance of the module is around 0.07–0.08 W/K of which 0.06–0.07 is ascribed to the thermoelectric material (as seen in Table 2) and the rest stems from electrode material and thermal interfaces. Optimizing the thermal interfaces in particular would offer a higher efficiency and power.

Fig. 7 compares our module data with literature sources for other high performing thermoelectric modules and unicouples

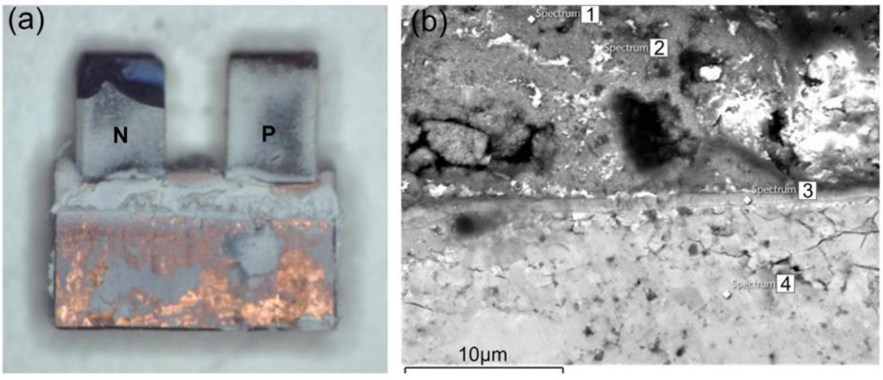

Fig. 9. (a) One unicouple of module #3 after testing. The N-element has visibly cracked in large chunks on the hot side. The P-element appears intact. (b) SEM/EDS of cross section of remnant parts of the hot side of the N-element. Many small cracks are also found right beneath the metallization layers. The EDS spectrum of the points indicated can be found in Table 3.

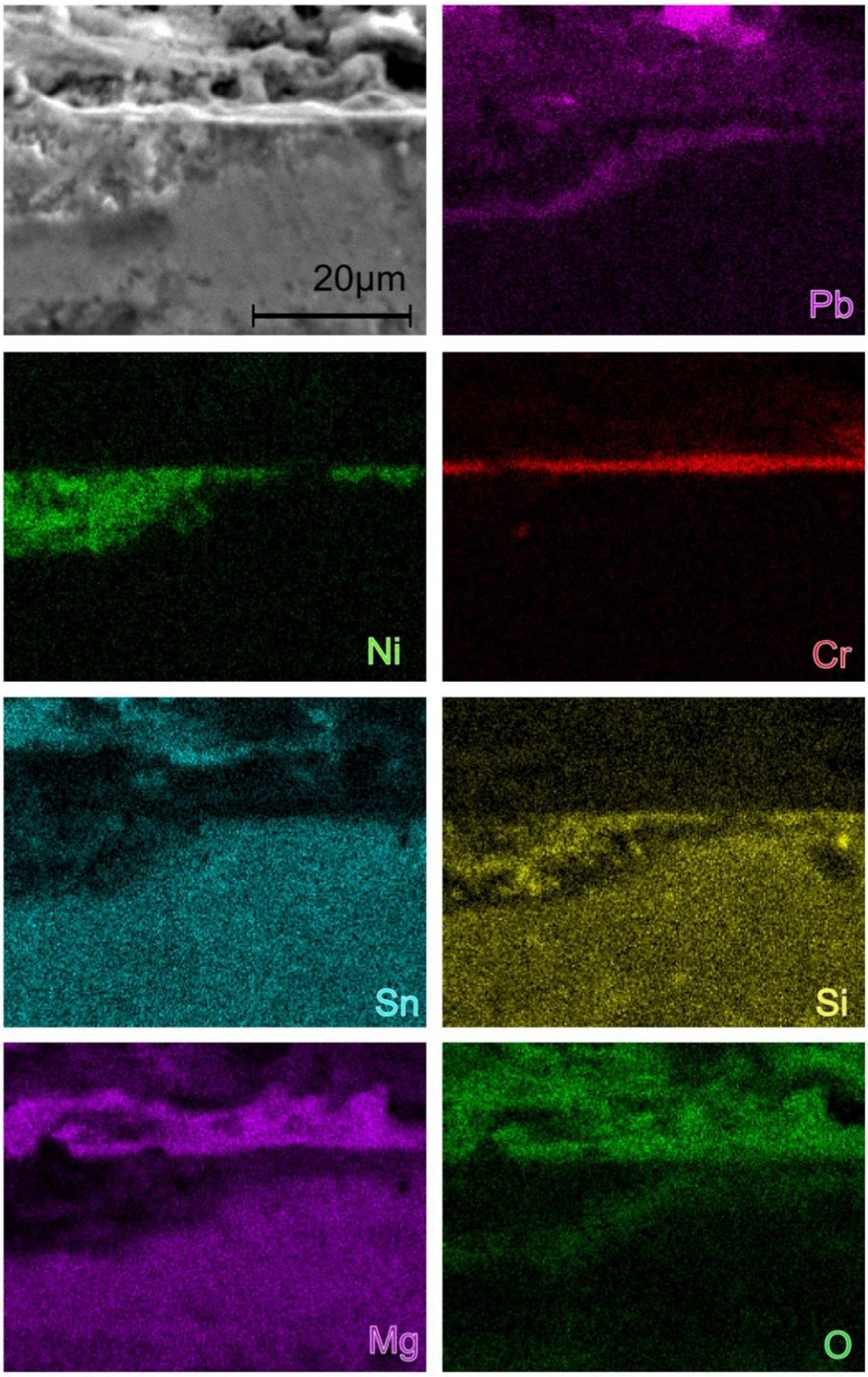

Fig. 10. SEM/EDS mapping of cross section of hot side interconnect of module #3. Diffusion of Ni and some Pb is seen through the Cr layer, especially at places where the Cr layers is very thin. Above the Cr-layer, Pb, Mg and Sn are found together with high amounts of O.

Table 3
EDS spectrum (at.%) for the points found in Fig. 9b. The phases proposed are only indicative.

Spectrum	O	Mg	Si	Cr	Ge	Sn	Pb	Bi	Phases
1	49.0	46.5	1.3	0.9	–	0.4	1.8	–	MgO
2	44.3	37.3	0.8	2.6	–	7.6	6.8	0.6	MgO + Pb/Sn
3	42.3	24.8	6.9	6.4	1.1	15.5	2.5	0.4	Cr (0.5 µm thick)
4	17.3	52.1	14.1	–	2.0	13.9	–	0.6	$Mg_2Si_{0.53}Sn_{0.4}Ge_{0.05}Bi_{0.02}$

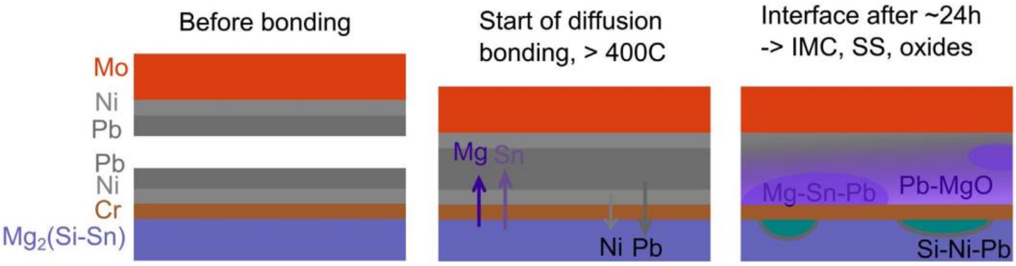

Fig. 11. Schematic sketch of the diffusion processes taking place on the hot side connection between the N-element and metallization during bonding/testing of module #2 and #3.

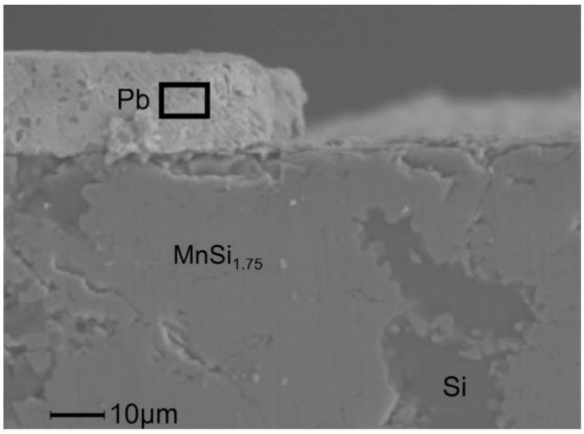

Fig. 12. SEM cross sectional analysis of a P-element from module #3 after testing. No interdiffusion was visible between the metallization and the P-element. Also very little oxygen was present compared to the N-element. The bulk material itself was on the other hand not homogenous and showed large areas consisting of pure Si which was attributed to imperfections in the synthesis method.

based on Half Heuslers (HH), Skutterudites (SKD), MgAgSb and a standard Bi_2Te_3 module [17,19,30–38]. Even though our silicide performance figures are somewhat lower that the literature values, we maintain that our values are the highest yet reported for modules based solely on silicides. Moreover, we advocate that our performance figures could have been improved by employing higher zT silicide materials and optimize contacts. When the heat is freely available as waste heat, sometimes power factor can be more important than efficiency from a cost perspective [39,40]. The rated power per area is thus another important parameter for a module and is also plotted in Fig. 7. The values have been normalized with respect to the cross sectional area of the thermoelectric elements as opposed the total area of the module. This allows a fair comparison to be made between unicouples and modules made from several unicouples. From this we can infer that our modules have comparatively high performance. In addition, the lower density of silicide material compared to other thermoelectric materials gives an advantage to the overall weight of the module, which for some applications such as vehicles could be important.

Although achieving high efficiency and power density is important, reliability over time is more practical importance. Therefore a new module #3 was made for long term testing to assess module stability. In addition, the N-type material was changed to a material with higher peak zT to assess its usability in a module. All other parts of the module were unchanged. Performance indicators as a function of thermal cycles are found in Fig. 8. The initial R_i was somewhat higher than for module #2 and temperature was therefore ramped up to 600 °C for a short period to try to accelerate the diffusion processes and reduce R_i further. The module was then removed from the vacuum chamber and then repositioned, as evidenced by the abrupt increase in R_i after 4 cycles. This revealed a weakness with the module design because the hot side bonds can easily be broken upon release of the pressure and thus cause an increase in contact resistance. Thermal cycles between 150 and 450 °C were then carried out, holding 15 min at 450 °C before ramping the temperature slowly up and down. It can be seen how V_{OC} remains relatively stable over time, while the R_i increases gradually from 0.2 to 0.4 Ω. Consequently, $P_{\max}$ is reduced from 0.11 to 0.07 W.

The performance of module #3 was far inferior to modules #1 and #2. Therefore, it was decided to disassemble module #3 and to examine the components by SEM/EDS. Fig. 9(a) shows clearly how the N-type element had developed cracks during testing. Parts of the element were still adherent to the hot side electrode. By contrast, all the P-type elements remained intact. SEM/EDS of the cross section of the interface between N-type element and metallization can be seen in Fig. 9(b) and Fig. 10 along with EDS point analysis in Table 3. The thin Cr-layer (~1 μm) is clearly visible and shows no sign of Cr diffusion into the thermoelectric material or above metal layers. Directly beneath the Cr-layer, several small cracks are visible and in addition there are areas enriched in both Ni and Pb. Formation and propagation of these cracks near the hot side electrodes was probably the main reason for the increase in R_i seen during testing. The crack formation could be caused by both vertical and horizontal stresses induced by a mismatch in thermal expansion between the thermoelectric material and the metallization and electrode materials. However, the vertical stresses should mostly be taken up by the built-in spring system under each element, while the horizontal stresses should be reduced by the soft Pb-layer between the thermoelectric material and hot side electrodes. There is no definite conclusion as to the cause of the cracking, but it is evident that the N-type material used for module #3 was too brittle to be effectively used in a module under these conditions. This is in contrast to the material that does not contain any Ge used for modules #1 and #2. Such TE legs did not show any sign of crack formation during performance testing, indicating a negative effect of Ge on the mechanical properties on the thermoelectric material. However, these modules were only tested for a single run and cracks could also eventually occur in these cases, for which more long-term testing is needed to be certain. Closer examination of the contact layers directly above the thermoelectric material and the thin Cr-layer revealed a much more mixed region with several different phases and structures. Large amounts of oxide, predominantly MgO, were found together with agglomeration of Sn and Pb rich particles. The existence of the intermetallic phase Mg_2Pb is also possible in this region. It was apparent that the oxidation and decomposition of $Mg_2(Si–Sn)$ is a serious problem even when the test is carried out in argon atmosphere with low partial pressure of oxygen (<10 ppm O_2). It is evident that the Cr-layer did not hinder either Mg or Sn from diffusing all the way through and reacting with both Pb and oxygen. Similar diffusion processes on the hot side interconnect would also exist for module #2. A schematic illustration of the different metal layers and diffusion processes taking place are found in Fig. 11.

The V_{OC} for module #3 was much lower compared to the estimated values using Eq. (1) than modules #1 and #2. Later investigations showed that the main reason for this was that the HMS used as the P-type element was not homogenous but in fact contained larger Si-grains within the structure (see Fig. 12) that could have caused a significant change in the Seebeck coefficient. This was probably the result of introducing weighing errors of the raw materials leading to a deviation from stoichiometry in the final composition. On the other hand, the HMS was very stable throughout the test and showed no interdiffusion or reaction with the metal layers or oxidation. HMS can therefore be considered a good P-type match for the N-type $Mg_2(Si–Sn)$ material used in modules #1 and #2. The spring loading method used in the module design offers effective relief of stress that would otherwise be present due to the difference in the CTE between HMS and $Mg_2(Si–Sn)$.

4. Conclusion

The performance of different silicide based thermoelectric materials has been evaluated in this study using a novel module design. One of the key aspects is the use of spring contacts on each leg to alleviate stress caused by thermal expansion mismatch between the N- and P-type elements. Another key aspect is use of diffusion bonding on the hot side which avoids the need to use soldering methods. Both of these features lend themselves to production engineering solutions and also to choice of thermoelectric materials with different CTE values, etc. Of the 3 modules tested, the best performing had an inner resistance in the region of 0.1 Ω at temperatures above 400 °C of which around 10–20% could be ascribed to the contact resistance. The maximum power achieved for these modules at a hot side temperature of 405 °C was 1.04 W and at 735 °C was 3.24 W. A simple COMSOL model shows how this equals an efficiency of around 3.7% and 5.3% respectively. However, testing above 400 °C caused significant oxidation and decomposition of the $Mg_2(Si–Sn)$ based N-type material along the hot side interconnects. The HMS P-type material was much less affected by temperature. Further work is needed to develop good diffusion barriers and possible anti-oxidation coatings that can be applied around the hot side interconnects and electrodes. Improved bonding methods are needed for the hot side in order to improve long term stability and to maintain low inner resistance of the module. Finally we advocate the use of low cost and abundant materials such as magnesium and silicon in thermoelectric applications such as waste heat recovery where power and low weight can be more important than thermoelectric efficiency.

Acknowledgements

The authors wish to acknowledge financial support from the ThermoMag Project, which was co-funded by the European Commission in the 7th Framework Program (contract NMP4-SL-2011-263207), by the European Space Agency and by the individual partner organizations.

References

[1] Amatya R, Ram RJ. J Electron Mater 2012;41(6):1011–9.
[2] LeBlanc S, Yee SK, Scullin ML, Dames C, Goodson KE. Renew Sust Energ Rev 2014;32:313–27.
[3] Zheng XF, Liu CX, Yan YY, Wang Q. Renew Sust Energ Rev 2014;32:486–503.
[4] Zaitsev VK, Fedorov MI, Gurieva EA, Eremin IS, Konstantinov PP, Samunin AY, et al. Phys Rev B 2006;74(4):045207.
[5] Bashir MBA, Mohd Said S, Sabri MFM, Shnawah DA, Elsheikh MH. Renew Sust Energ Rev 2014;37(0):569–84.
[6] Gao P, Berkun I, Schmidt R, Luzenski M, Lu X, Bordon Sarac P, Case E, Hogan T. J Electron Mater 2014;43(6):1790–803.
[7] Khan AU, Vlachos NV, Hatzikraniotis E, Polymeris GS, Lioutas CB, Stefanaki EC, et al. Acta Mater 2014;77:43–53.
[8] Bourgois J, Tobola J, Chaput L, Zwolenski P, Berthebaud D, Gascoin F, et al. Funct Mater Lett 2013;6(5):1340005.
[9] Tani J-i, Takahashi M, Kido H. J Alloys Compd 2009;488(1):346–9.
[10] Tani J, Takahashi M, Kido H. IOP Conf Ser: Mater Sci Eng 2011;18(14):142013.
[11] Fedorov MI. J Thermoelectr 2009;2:51–60.
[12] Engström I, Lönnberg B. J Appl Phys 1988;63(9):4476–84.
[13] Gelbstein Y, Tunbridge J, Dixon R, Reece M, Ning H, Gilchrist R, et al. J Electron Mater 2014;43(6):1703–11.
[14] Søndergaard M, Christensen M, Borup KA, Yin H, Iversen BB. J Electron Mater 2013;42(7):1417–21.
[15] Nemoto T, Iida T, Sato J, Sakamoto T, Nakajima T, Takanashi Y. J Electron Mater 2012;41(6):1312–6.
[16] Nemoto T, Iida T, Sato J, Sakamoto T, Hirayama N, Nakajima T, et al. J Electron Mater 2013;42(7):2192–7.
[17] Nemoto T, Iida T, Sato J, Suda H, Takanashi Y. J Electron Mater 2014;43(6):1890–5.
[18] Tollefsen, T.A., Editor^Editors. Thermoelectric materials (THELMA) workshop, Oslo; 2014.
[19] Groβ E, Riffel M, Stöhrer U. J Mater Res 1995;10(01):34–40.
[20] Riffel M, Groβ E, Stöhrer U. J Mater Sci: Mater Electron 1995;6(3):182–5.
[21] Shi X, Zamanipour Z, Krasinski J, Tree A, Vashaee D. J Electron Mater 2012;41(9):2331–7.
[22] Sakamoto T, Iida T, Honda Y, Tada M, Sekiguchi T, Nishio K, et al. J Electron Mater 2012;41(6):1805–10.
[23] Petrova LI, Dudkin LD, Khlomov VS, Fedorov MI, Zaitsev VK, Solomkin FY. Tech Phys 2000;45(5):641–3.
[24] Petrova LI, Dudkin LD, Fedorov MI, Solomkin FY, Zaitsev VK, Eremin IS. Tech Phys 2002;47(5):550–4.
[25] Petrova LI, Dudkin LD, Fedorov MI, Solomkin FY, Zaitsev VK, Eremin IS. Inorg Mater 2004;40(6):558–62.
[26] Thimont Y, Lognoné Q, Goupil C, Gascoin F, Guilmeau E. J Electron Mater 2014;43(6):2023–8.
[27] ESA. *ThermoMag homepage*; 2011 [cited 2013 15. March]; Available from: http://www.thermomag-project.eu/index.html.
[28] Fedorov MI, Zaitsev VK, Isachenko GN. Solid State Phenom 2011;170:286–92.
[29] Perumal S, Berthebaud D, Gascoin F. 12th European conference on thermoelectrics (ECT2014), Madrid, Spain; 2014.
[30] El-Genk MS, Saber HH, Caillat T, Sakamoto J. Energy Convers Manage 2006;47(2):174–200.
[31] Saber HH, El-Genk MS, Caillat T. Energy Convers Manage 2007;48(2):555–67.
[32] Mikami M, Kobayashi K, Tanaka S. Mater Trans 2011;52(8):1546–8.
[33] Guo JQ, Geng HY, Ochi T, Suzuki S, Kikuchi M, Yamaguchi Y, et al. J Electron Mater 2012;41(6):1036–42.
[34] Muto A, Yang J, Poudel B, Ren Z, Chen G. Adv Energy Mater 2013;3(2):245–51.
[35] Salvador JR, Cho JY, Ye Z, Moczygemba JE, Thompson AJ, Sharp JW, et al. Phys Chem Chem Phys 2014;16(24):12510–20.
[36] Bartholomé K, Balke B, Zuckermann D, Köhne M, Müller M, Tarantik K, et al. J Electron Mater 2014;43(6):1775–81.
[37] Fu C, Bai S, Liu Y, Tang Y, Chen L, Zhao X, et al. Nat Commun 2015;6.
[38] Kraemer D, Sui J, McEnaney K, Zhao H, Jie Q, Ren ZF, et al. Energy Environ Sci 2015;8(4):1299–308.
[39] Rowe DM, Min G. IEE Proc: Sci Meas Technol 1996;143(6):351–6.
[40] Hendricks TJ, Crane DT. In: Rowe DM, editor. Thermoelectrics and its energy harvesting – modules systems and applications in thermoelectrics. Boca Raton (Florida): CRC Press; 2012. p. 22.1–22.30.

Paper 5: Novel method for evaluating thermoelectric performance and durability of functionalized skutterudite legs

Novel method for evaluating thermoelectric performance and durability of functionalized skutterudite legs

Gunstein Skomedal[1,*], Nils R. Kristiansen[1], Reinhard Sottong[2], Hugh Middleton[1]

[1] *University of Agder, Faculty of Engineering and Science, 4879 Grimstad, Norway*

[2] *Institute of Materials Research, German Aerospace Centre (DLR), Linder Hoehe, D-51147 Koeln, Germany*

* corresponding author: gunstein.skomedal@uia.no, Telephone: +4791113267
Address: Department of Engineering Sciences, Jon Lilletuns vei 9, N-4898 Grimstad, Norway

Abstract:

Thermoelectric Generators (TEG) are a promising technology for waste heat recovery. As new materials and devices are now entering a stage of market penetration it is of interest to employ fast and efficient measurement methods for evaluating the long term stability of the thermoelectric material in combination with metallization and coating (functionalized thermoelectric legs). In this work we investigate a novel method for measuring several thermoelectric legs simultaneously. The legs are put under a common temperature gradient and the electrical characteristics are measured individually on each leg. Using this method we are able to test different types of metallization and coating concepts and look at the relative changes over time between them. In addition, thermal cycling is employed to mimic real end-user applications where rapid heating and cooling cycles are often seen, which can be challenging for the durability of thermoelectric material and metallization. Post characterization is furthermore used to investigate the effect of different temperature activated degradation processes such as oxidation and interdiffusion, and how these processes affect the performance over time. Although we only tested skutterudite material in this work, the method is fully capable of testing all kinds of materials, metallization and coating concepts.

INTRODUCTION

A thermoelectric module (TEM) is a solid state device directly converting a heat flux into electric current. Energy efficiency is high on the global agenda and thermoelectric technology is believed to hold vast potential for applications within waste heat recovery [1, 2]. A TEM consists of tens to hundreds of small dice of thermoelectric material (legs) connected electrically in series and thermally in parallel. The efficiency of a thermoelectric material is directly related to its figure of merit, $zT = (\alpha^2 \sigma T)/\kappa$, where α is the Seebeck coefficient, σ the electrical conductivity and κ the thermal conductivity.

Skutterudites one the base of $CoSb_3$ are one of the most promising candidate thermoelectric materials for medium waste heat recovery due to their high efficiencies in combination with relatively low-cost raw materials compared to other state-of-the-art materials [3, 4]. As thermoelectric modules and generators made of skutterudite are now being researched worldwide by several institutions and companies, it is of interest to be able to assess the long term thermal stability of these materials. This is an important aspect qualifying the materials for applications in e.g. automotive and industrial waste heat recovery, where often life-times of 10-20 years or more are demanded.

For skutterudite material, although a lot of work has been put into examining the change in thermoelectric properties over time, little work is published on the long term stability of the interconnects and how this affects the overall performance of the device [5, 6]. Some exception is the decade long work done by JPL/NASA on their next generation RTG's showing very promising long term stability of these systems [7, 8]. However, when taking these systems down to earth other challenges arise such as keeping complexity and price low and the effect of thermo-mechanical stresses due to thermal cycling in many applications. Oxidation is also a severe problem for skutterudite and the material needs to be protected from its surroundings during usage [9-12]. Several different solutions have been proposed such as different coating alternatives or encapsulation [13-16].

In all cases reliable methods are needed to verify both material stability together with metallization and coating over a prolonged time under conditions simulating the end use, with high temperatures and rapid heating and cooling cycles.

One way to check for stability is to test prototype unicouples or modules in thermoelectric module test set-ups. Here the unicouple or module is typically placed between a heat source on one side and a cold sink on the other side [17-21]. The total conversion efficiency of a TEM is given by the electrical power output P_{out} divided by the heat supplied Q_{in}, $\eta = P_{out}/Q_{in}$. The power is furthermore a function of the open circuit voltage, V_{OC}, and the inner series resistance (R_i). While measuring P_{out} by means of standardized equipment is straight forward, measuring Q_{in} is much harder. However, when looking at the performance of the device over time, and assuming Q_{in} can be kept fairly constant, monitoring changes in P_{out} gives a good idea of the durability of the thermoelectric device. On the other hand, this requires time to assemble the unicouples and modules, and during measurement it is also harder to distinguish between different physical effects that can explain the observed changes in the measured parameters since they are connected in series.

Therefore, in an industrial mass production perspective, it is of interest to find other methods that can yield faster and more detailed answers to evaluate both the material itself, together with metallization and coating options. This work explores a novel method of measuring several individual thermoelectric legs simultaneously, with both thermal management and on-line electrical characterization. We apply thermal cycling to different metallization and coating solutions to exemplify how the method can be used in evaluation studies. In addition, we discuss the strength of combining such on-line characterization with post characterization analysis to increase the knowledge of what kind of underlying physical degradation processes causes the observed changes in performance of the functionalized legs.

EXPERIMENTAL

Material Synthesis

Skutterudite with nominal composition $In_{0.15}Co_4Sb_{12}$ (N-type) and $In_{0.25}FeCo_3Sb_{12}$ (P-type) were obtained by gas atomizing of a melt from the elementary constituents at 1150 °C under argon atmosphere. The phase transformation into skutterudite was achieved by compacting the obtained powders with a direct current assisted sintering device (DSP 510, Dr. Fritsch) at 50 MPa and 630°C. The thermoelectric properties found in **Figure 1** were measured using an in house device to characterize the Seebeck coefficient and the electrical conductivity simultaneously as a function of temperature. Thermal diffusivity measurement was carried out by a laser flash analyzer (LFA427, Netzsch) together with density measurements by the Archimedes method. The specific thermal capacity cp was calculated using the Dulong-Petit law ($c_p = 0.23\ Jg^{-1}K^{-1}$). The sintered pellets were then metallized on both sides using a PVD facility with first a layer of Ti (1µm) and then a thicker layer of Ag (~3µm). After this the pellets were cut into cubic legs of $5x5x5mm^3$. In addition, some of the samples where coated on the un-metalized sides with a Al-based coating developed in previous work [22].

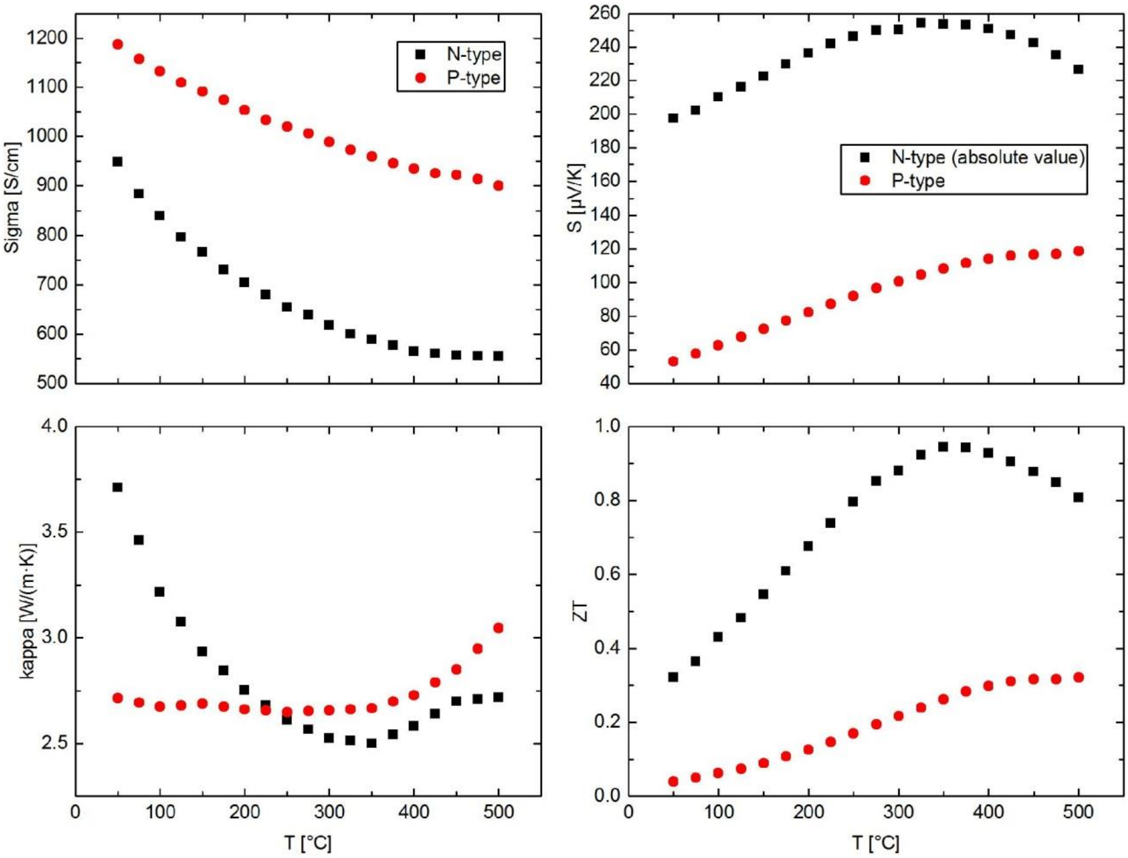

Figure 1 Thermoelectric properties of the N and P type material used in thermal cycling experiments

Thermal Cycling

Thermal cycling of the functionalized N and P type skutterudite thermoelectric legs was conducted in several runs under lab atmosphere. Four thermoelectric legs where placed between a cold side copper block and hot side electrode embedded in MACOR©. Two types of hot side electrodes were used: copper plated with silver, and nickel coated with Al-coating. An Inconel block with two heater elements was used to control the heat flow through the legs, see **Figure 2** for an overview. Thermocouples were inserted inside the Cu- and Ni-electrodes 1 mm above the thermoelectric legs. The cold side temperature was measured on the surface of the Cu block between the legs protected from radiate heating using graphite foil. Copper/nickel wires were connected to the hot side electrodes and the total voltage across each thermoelectric leg + electrode couple was recorded.

The ideal open circuit voltage for each couple was calculated from Seebeck coefficients of the thermoelectric material and Nickel (average -24µV/K between 50 and 500°C, from [23]) and Copper (4µV/K)

$$V_{OC} = \int_{T_C}^{T_H} S_{TE}(T)\, dT + S_{EL,H}(T_H - T_{RT}) + S_{EL,C}(T_C - T_{RT}) \quad \textbf{(1)}$$

where $S_{TE}(T)$ was fitted as a polynom to the measured data, $S_{TE}(T) \approx aT^3 + bT^2 + cT + d$ and S_{EL} is the Seebeck coefficient of the electrode and wire material at hot and cold side. T_H, T_C and T_{RT} are the measured hot side, cold side and room temperatures respectively. Figure 3 illustrates the temperature profile across the measurement setup. Seebeck coefficients and temperatures used in equation (1) are shown in a connection diagram. The legs were typically cycled between 150°C and 500°C on the hot side (1 hour hold at 500°C) and between 25-50°C on the cold side. An electronic load set currents for measuring the I-V curve of each leg separately at specified intervals by changing the load every second in the measurement method, where the voltage over the load and module equals

$$V = R_L I = V_{OC} - R_i I \quad \textbf{(2)}$$

where R_L is the load resistance and R_i is the inner series resistance of the thermoelectric material, electrodes and wires. The resulting I-V curve was furthermore assumed to be measured at constant temperature as the system had very little time to reach new equilibrium values due to the Peltier effect and joule heating. The total inner resistance (R_i) of each couple was estimated from the slope of the I-V curve

$$R_i = -\frac{V - V_{OC}}{I} \quad \textbf{(3)}$$

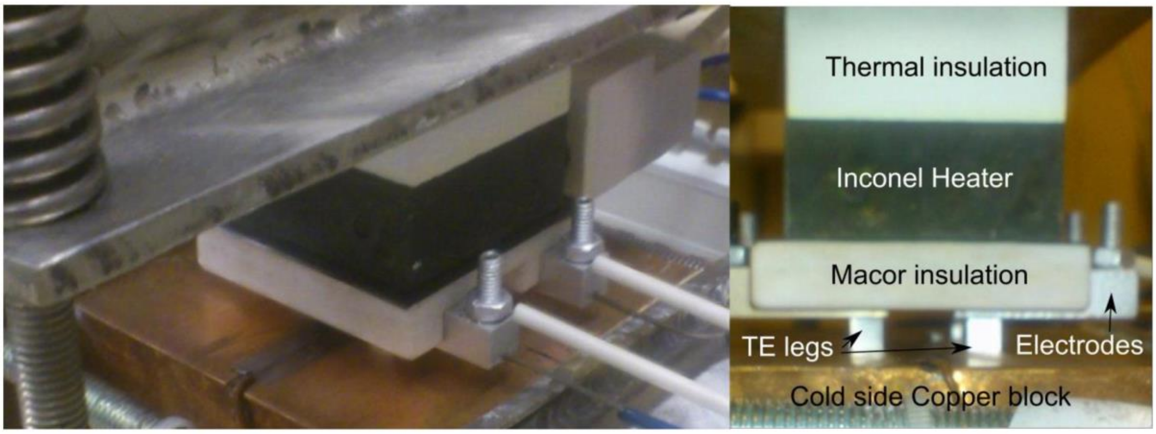

Figure 2 Pictures of the thermal cycle setup with four couples consisting of one thermoelectric leg and one hot side electrode connected for measurement.

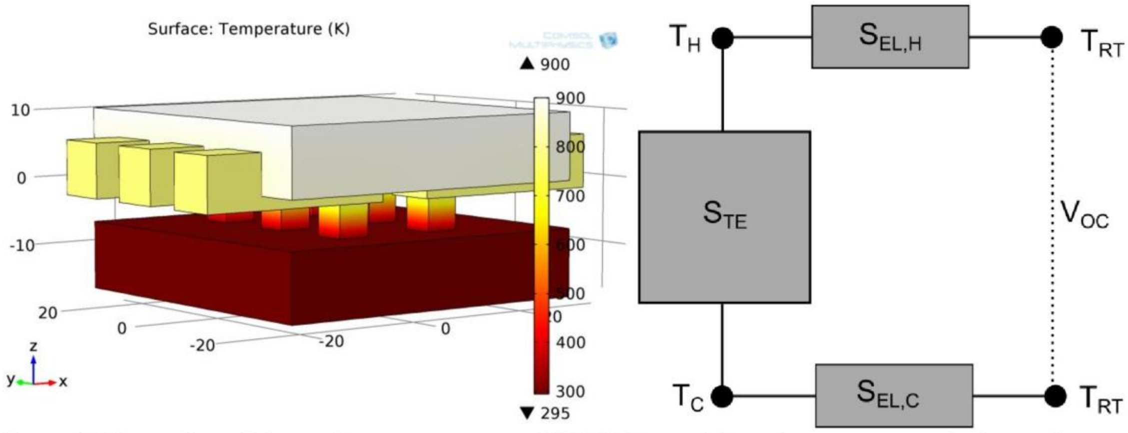

Figure 3 Illustration of the surface temperature (COMSOL model) and a temperature/voltage diagram of one unicouple (leg+electrode).

Post Characterization

To connect any observed reduction in performance with physical degradation processes, different analysis methods were employed. After the thermal cycles the thermoelectric legs were cut in half and placed in a potential seebeck micropope (PSM) measuring the spatial variation of the Seebeck coefficient over the cross section. The legs were always placed with the cold side of the legs (from thermal cycling experiment) facing the voltage and temperature sink of the PSM. A scanning electron microscope (SEM) equipped with energy-dispersive X-ray spectroscope (EDS, Zeiss Ultra 55, acc. voltage 15kV) and an electron probe micro-analyzer (EPMA, Jeol JXA-8500F) were used to study the microstructure along the cross section, especially near the hot side of the samples. Vickers Hardness (50N) was measured with a Clemex ZMT over the cross section of some samples.

RESULTS AND DISCUSSION

Thermal cycling

Several test-runs were conducted for different times and temperature. Most of these runs were done to test the setup itself and are therefore not treated further in the following discussion. Two runs will be covered in detail. An overview of the measurement conditions for these runs is found in Table 1.

Table 1 Overview over thermal cycling tests with temperature program, number of cycles and leg type (N or P) and coating.

Test	Hot side electrode	Thermal Cycle program	Cycles	Leg1	Leg3	Leg4	Leg6
2	Ag-plated Cu	25min heating, 1h 500°C, 25min cooling, 10min 150°C	112	P	N	P coated	P coated
5	Al-coated Ni	25min heating, 1h 500°C, 25min cooling, 10min 150°C	15	P coated	P	P coated	N

In all the runs V_{OC} was recorded continuously. The V_{OC} for Run 2 plotted against temperature difference for leg 4 is found in Figure 4(a), together with the ideal V_{OC} calculated from equation (1) based on the thermoelectric properties found in **Figure 1**. We clearly see how the measured V_{OC} is only 1-2% lower than the ideal V_{OC} during the first cycles. From this we can conclude that our measurement setup measures hot and cold side temperatures very close to the actual temperature on each side of the thermoelectric leg. HoweverV_{OC} decreases with continued cycling. This is even more evident if we plot the relative reduction in V_{OC} at a temperature difference of 450°C as a function of cycles as seen in Figure 4(b). We clearly observe large differences between the legs. First and foremost both leg 3 and 6 show dramatic reduction in open circuit voltage. For leg 6 this is caused by coating material penetrating into the interface between thermoelectric leg and electrode causing large disturbances to the voltage measurements. For leg 3, the N type material shows large crack formation around the edge on the hot side which also clearly will influence the produced voltage by changes thermal coupling. In addition, the silver plating of the copper electrode failed and thus oxidation of the electrode vastly influenced the results. Legs 1 and 4 both show less reduction in V_{OC} over time from 92% to 76% and 97% to 83% respectively. As changes over time are fairly similar the main difference between the two is in the offset. V_{OC} for leg 1 is much lower compared to the ideal value than for leg 4. This could be due to a difference in applied contact pressure between the two, increasing the initial thermal contact resistance of leg 1 compared to leg 4.

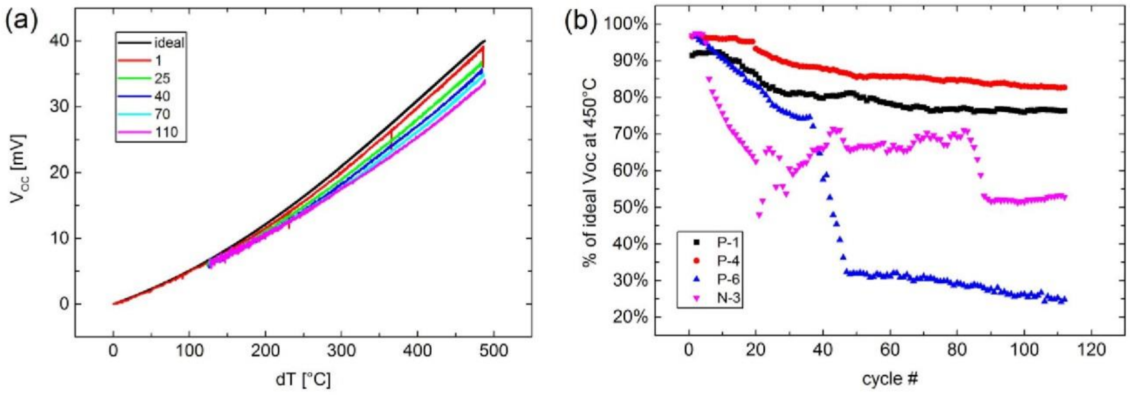

Figure 4 (a) V_{OC} as a function of temperature difference between hot and cold side of leg 4 in run 2. Ideal values are calculated from equation (1) . Different colors show numbers of cycles performed. (b) Relative reduction in V_{OC} compared to ideal values for the four different legs measured in run 2. Leg 1, 4 and 6 are P-type while leg 3 is N-type.

From the first runs it was obvious that better protection around the interface between thermoelectric leg and hot side electrode was needed. Oxygen could penetrate in from the edges during thermal cycling and oxidation from starting at the interface was observed. Also severe diffusion of copper into the thermoelectric material was seen showing that the electrodes´ Ag coating failed. This is discussed in more detail in the next section.

The following runs were all done with Nickel-electrodes and wires coated with the same Al-coating used on some of the thermoelectric legs. The metalized legs were also coated around the hot side interconnect. In addition, I-V curves for all legs were recorded for each cycle. An example of this is found in Figure 5, where the I-V curve of leg 1 is shown after different cycles. The initial total resistance of the leg, wires and electrodes (31mΩ) is an order of magnitude higher than the resistance of the thermoelectric leg itself (2-3 mΩ from Figure 1), also including metallization (7-9 mΩ measured with 4 point measurement). During cycling the resistance gradually increases as is easily observable from the I-V curves.

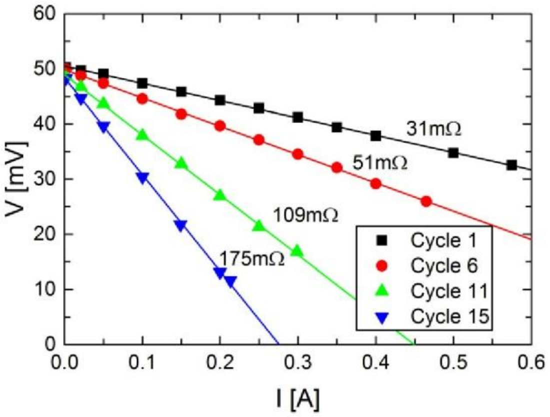

Figure 5 I-V curves of leg 1 in run 5 at 4 different cycle numbers. Indicated resistance of unicouple calculated from the slope.

In Figure 6 the V_{OC} and Ri is plotted for each leg with continued cycling. The general trend is that the open circuit voltage decreases and the inner resistance increases over time as interconnects and bulk material degrade.

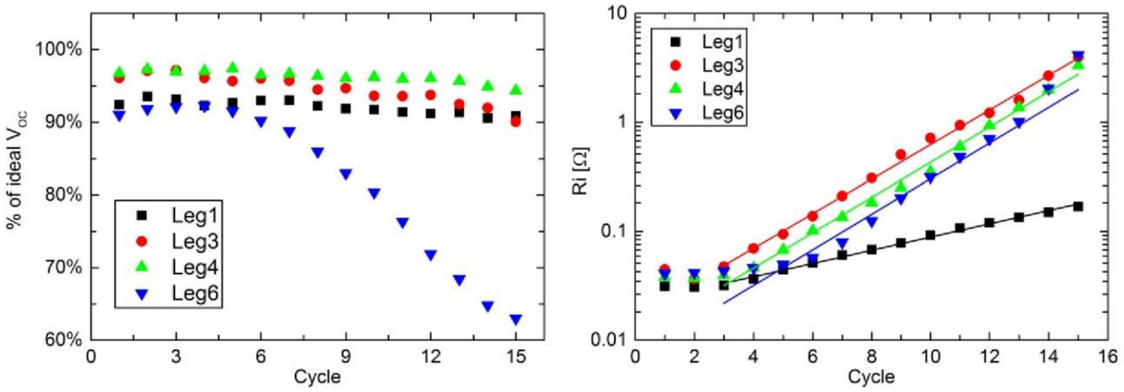

Figure 6 Change in V_{OC} (left) and R_i (right) for each cycle in Run 5. Line shows linear dependency of the logarithmic of Ri over time (cycles) indicating exponential increase.

The inner resistance of all the legs has a nearly exponential growth. This is also indicated in Figure 6(b) where the logarithm of resistance shows a linear relationship versus time. This relationship reflects the growing layer of oxide penetrating in from the sides. The contact area will reduce quickly from all sides and will in combination with the increasing thickness of the oxide dramatically increase the electrical resistance. Leg 1 is in this run an exception since the inner resistance increases much slower than for the other legs.

Both leg 1 and leg 4 were coated and can explain the much slower reduction in V_{OC} compared to the uncoated legs as should be expected. But there is a large difference when it comes to the inner resistance between leg 1 and 4. This is likely caused by a difference in oxidation rate due to a difference in the quality of the coating layers and possible cracks and leakage points in these. Another probable cause is uneven contact pressure causing crack formation in a larger degree for leg 4 than leg 1. The initial much lover V_{OC} of leg 1 (92%) in comparison to leg 4 (97%) is likely to be also a result of the lower contact pressure causing a higher thermal resistance on the interfaces between leg and electrodes.

Post Characterization

Most degradation processes we are interested in here are thermally activated. As the temperature profile is nearly linear, the rate of degradation should increase exponentially towards the hot side of the sample. There exist a number of possible thermally activated degradation processes that are relevant to our study. An overview of these processes along with how they could affect the electrical parameters we measured during testing is found in Figure 7. To find out which mechanisms are predominant and are also able to explain the observed differences in relative change between the legs, several subsequent characterization steps were conducted such as PSM, SEM/EDS, EPMA and Hardness measurements. Furthermore, this will give us valuable feedback when we want to employ thermal treatment methods for fast evaluation of thermoelectric materials at a later stage as e.g. quality control in an industrial mass production process.

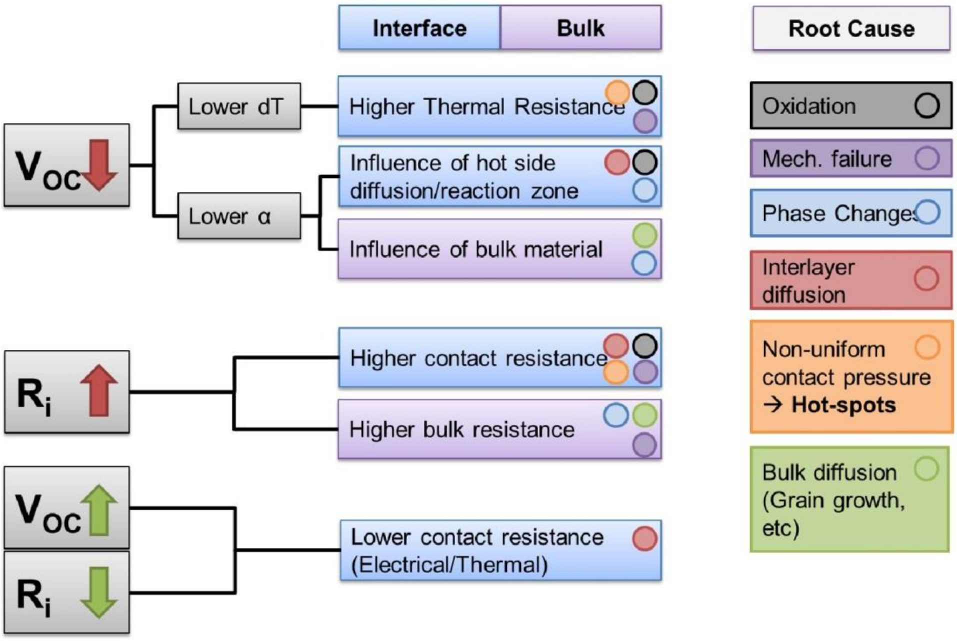

Figure 7 Possible root causes for the observed changes in V_{OC} and R_i during thermal cycling in air.

Changes in local Seebeck coefficient

A Potential-Seebeck microprobe (PSM) [Ziolkowski2013]measures the local Seebeck coefficient, which is linked to the local charge carrier density. A higher charge carrier density yields a relatively lower Seebeck coefficient [24]. In Figure 8, PSM maps of the cross section of leg 1 and leg 4 from run 2 are found. The effect of thermal cycling on the legs is clearly seen as large changes in α at the hot side (near y-axis) of the cross section. Both leg 1 and leg 4 have hot spots at one or both of the edges. Here α is drastically changed; for leg 1 it is reduced down to almost zero close to the edge indicating metallic behavior (high charge carrier density), while for leg 4 also a small region with a slightly higher α is found (lower charge carrier density). For the N-material in Figure 9 also an increase close to the edge is found. At the same time, the corners have chipped of from this leg thus the trapeze shape of the hot side.

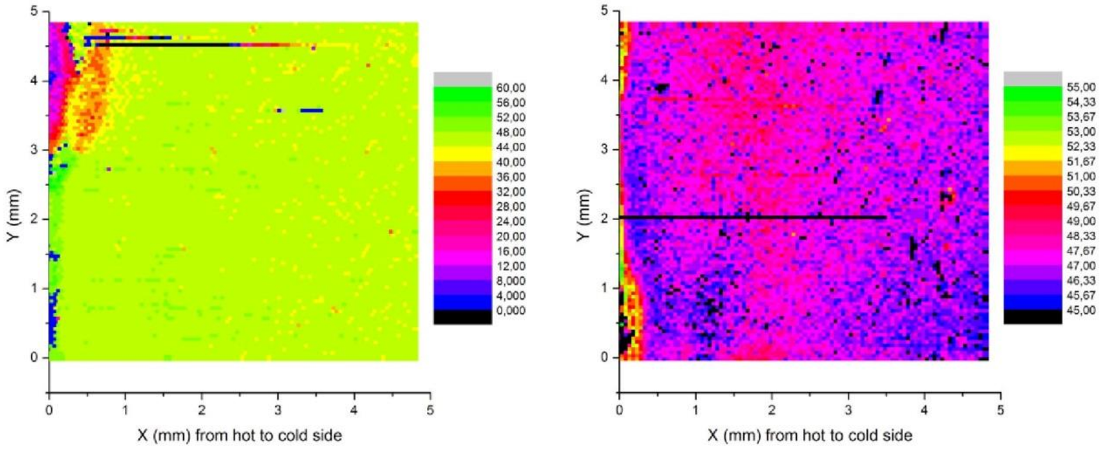

Figure 8 PSM maps of leg 1(left) and leg 4 (right) from run 2. Be aware of the difference in color-scale of Seebeck coefficient between the two

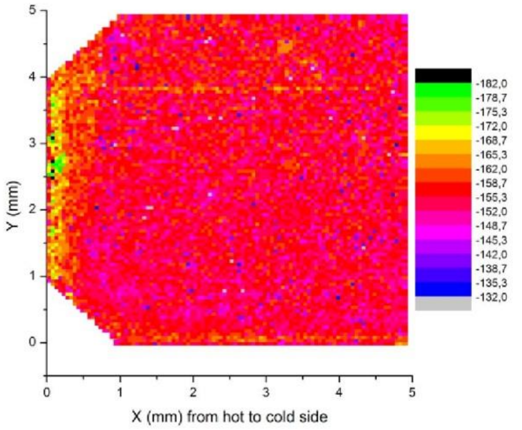

Figure 9 PSM map of leg 3 from run 2. The trapezoid shape is due to cracking at the corner during thermal cycling.

For the legs from run 5, similar effects are seen as for run 2 as shown in Figure 10. However, they are much less dominant which is expected due to much fewer cycles (15 and 112, see **Table 1**). Hot spots are found at the corners for both P and N material (leg 1 and leg 6 respectively) with slightly higher α. For the P-type material also a clear trend in decreasing α with distance from hot side is seen. In leg 6, also small inhomogenities are found in the middle of the samples, most probably remnants from the synthesis.

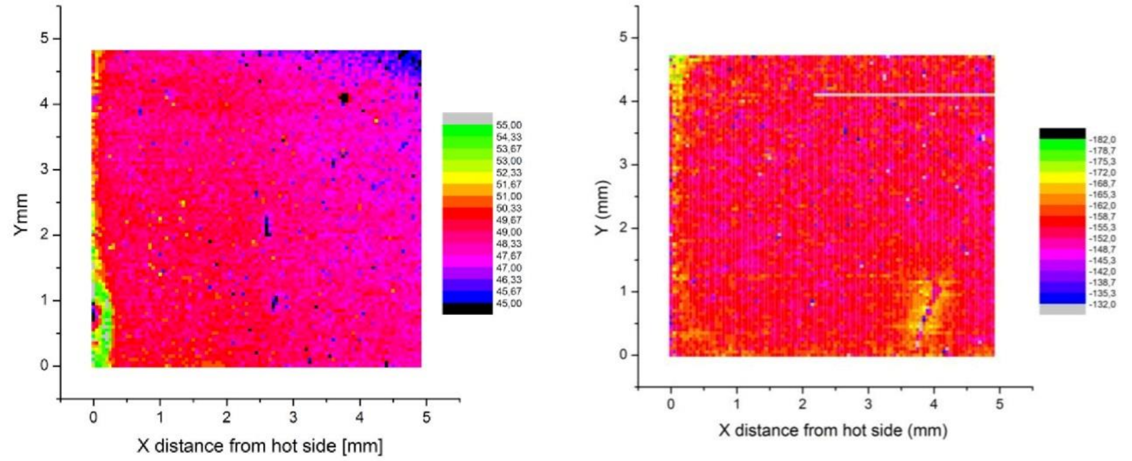

Figure 10 PSM map of leg 1 (left) and leg 6 (right) from run 5.

There also seems to be a gradual change in α over the P-type legs from hot to cold side. The average α as a function of the distance from hot side was therefore calculated for all the measured samples and the result is found in **Figure 11**. It shows a general trend of decreasing α with increasing distance from the hot side for the P-type legs. Even though the same trend is found for untreated material, this is much smaller than for the thermally cycled materials. The reason of the slight offset is probably linked to non-uniform temperature distribution during measurement as one side (right in the PSM maps) is close to the cold sink and reference electrode in the PSM. Figure 11 compares α values between several P-type legs. The α values are up to 3% higher at around 1.5-2mm from the hot side than the cold side. Substracting 1% deviation caused by equipment drift during measurement, this is still significant at 1-2% for all samples. Samples show a peak or flattening in α at around 1.5-2mm from the hot side while it is lower both towards hot and cold side. This clearly reflects large gradients in charge carrier densities not only in the immediate region of the hot side, but also much further down in the sample.

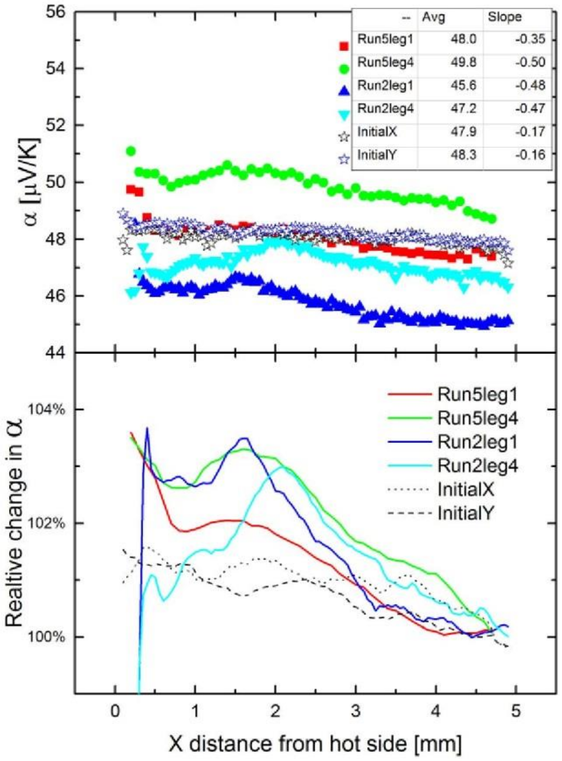

Figure 11 Upper: Average α from hot to cold side for several P-legs. For all samples the general trend is that α varies as a function of the distance from hot side (x). The star-symbols show the initial values of untreated material. Also here a small decrease in α is seen from hot to cold side. Lower: Relative change in α, moving average (±3) used to smooth curve.

Based on the PSM measurements some general points can be found in all the thermal cycling tests:

- Almost all samples had hot spots on one of the sides indicating uneven pressure and contact points during testing. These hot spots had evidently a much larger change in α than the rest of the hot side. For most legs the general trend was a small increase in α, but for run 2 also a large decrease is seen near the hot side.
- Areas with lower α indicate metallic behavior and thus diffusion and formation of intermetallic phases in these regions. In contrast, regions with slightly higher α could be a result of diffusion of one or more species in or out of the skutterudite. SEM combined with EDS and EPMA is found in the next sections which analyses this further.
- For all samples there is a slight gradient in α from hot to cold side. This could also be an effect of charge carrier redistribution closer to the hot side of the sample.
- The differences in average α between the samples are within the measurement error for absolute values of the PSM instrument which typically varies with environmental conditions, especially room temperature. Still the relative differences are highly accurate and are a valuable tool to investigate small changes in local charge carrier density that is otherwise hard to measure by other methods.

Oxidation and spallation

Thick oxide layers are found on parts of the hot side of all the legs, between the Ag/Ti metallization and SKD. This is especially evident close to the edges of the samples in contrast to the center where no oxidation is seen. This indicates oxygen transport in between the layers from the side. For run 5 this oxide layer was found for all legs, but for leg 1. The middle parts of the samples also had large regions with no oxide layer. For leg 4 these regions were much smaller. This explains why leg 1 had a much lower increase in inner resistance over time compare to all the other legs in Run 5 (see **Figure 6**).

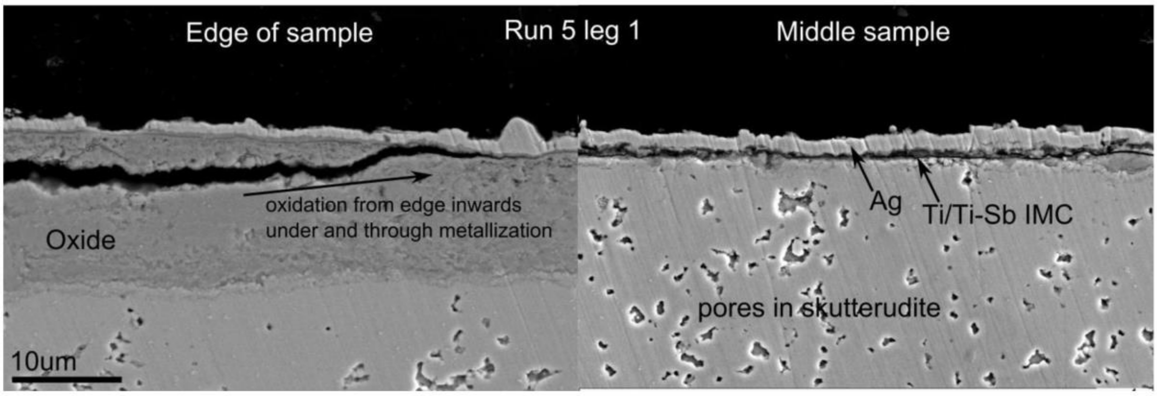

Figure 12 Example of oxidation in from edges (left) of leg 1 from run 5 and an unoxidized part in the middle of the same sample (right).

SEM images of leg 6 from run 5(N-type) found in Figure 13 shows regions near the edge of large cracks and oxygen formation within these cracks. The metallization has delaminated. In the middle of the same the metallization layer has bulged, probably caused by mismatch in thermal expansion between metallization and underlying oxide. In this case the oxygen transport over the whole hot side of the sample is possible which is seen as an oxide layer of roughly 10-15μm beneath the metallization. Again, the severe oxidation explains much of the large increase in inner resistance during thermal cycling.

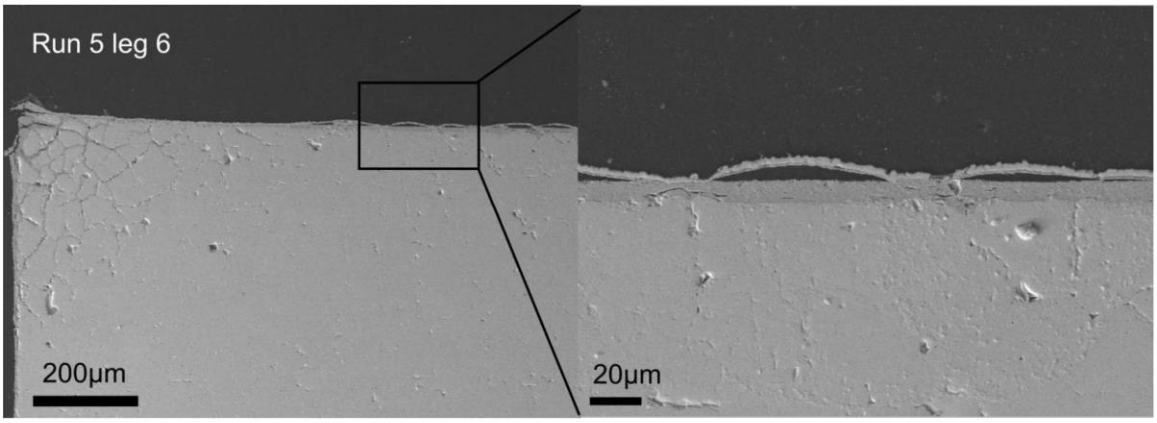

Figure 13 Oxidation and cracking at the edge of leg 6 from run 5 (left). Magnification of hot side area (right) shows bulging of metallization layer and a 15um thick oxide layer right underneath.

Cu diffusion and densification

For run 2 that lasted 112 cycles, especially two effects are found significant, in addition to oxidation. First of all Cu is found filling up pores in the thermoelectric material up to 200μm from the hot side. This shows how both Ni and Ti layers could not hinder diffusion of Cu at these temperatures. This also explains the very low Seebeck coefficient recorded in the PSM measurements. The combination of high temperature and localized pressure (hot spots) along with Cu diffusion caused densification of the originally quite porous structure of the P-type material. The sintering effect was found to a smaller degree also in samples with nickel electrodes, so diffusion of Cu seems not to be the main reason for the effect to happen.

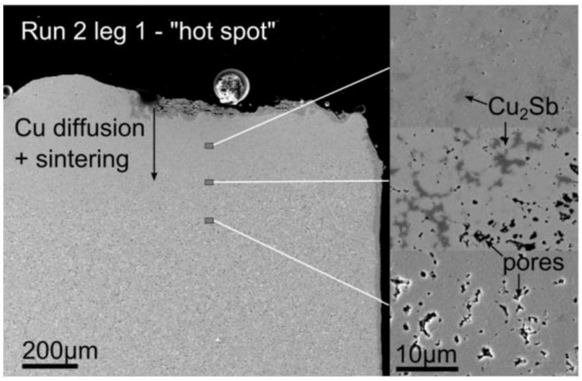

Figure 14 SEM images of hot edge of leg 1 from run 2. Cu diffusion and densification near the hot edge is clearly observed 200-300µm down from the hot side.

Diffusion at interface and in bulk

EDS area analyses across sample run 5 leg 4 were done to see if there were any significant differences in elemental distribution that could help explaining the observed change in α along the temperature gradient. Between 0.5 and 4.5mm from the hot side, the sample shows a stable nominal composition of $In_{0.24}FeCo_3Sb_{12.5}$ consistent with the original composition, although with a slight deviation from stoichiometry of the ideal Sb/(Fe+Co) ratio of 3. However, this could very well be a result of the inability of EDS to exactly determine composition.

Also EPMA point analysis of the cross section of leg 4 where done to see if any more changes could be observed that weren´t seen with EDS. EPMA yields much more precise absolute values of chemical composition compared to EDS. In Figure 15 an elemental mapping of the cross section taken from the hot side of leg 4 is found. An oxide layer of 10µm is clearly seen. Underneath this a thin layer enriched on In and Fe is found. followed by pure skutterudite. Although the first 10-20µm seem to be more homogenous with respect to Fe content, further down small areas enriched on Fe are clearly visible. Most of these enrichments seem to be located close to pores in the sample. Point analysis along the cross section of the sample from hot to cold side were also performed and can be found in Figure 16. The composition seems to be fairly constant over the sample length, although the variation between points are large due to inaccuracies in the EPMA measurement. However, it seems that both In and Fe content is significantly lower between 10 and 100µm from hot side of the sample compared to the rest. It can be speculated that diffusion of both Fe and In close to the hot side will change both the local charge carrier density and reduce the amount of pores. Formation of a thin InSb layer right underneath the oxide layer has previously been reported in literature for samples with the same composition [25] and is also found here. This layer greatly reduced the oxidation rate by acting as a kind of diffusion barrier. Also some diffusion of Sb is probable, although it cannot be detected with EDS or EPMA. PSM on the other hand is very sensitive to small changes in the charge carrier density as already discussed. The slight trend we see in the PSM measurements could therefore reflect diffusion and phase changes hardly detectable by other methods. A last point is that if we normalize the In and Fe content to the nominal composition of the material $In_yFe_xCo_{1-x}Sb_{12}$ we find that they correlate well and give a near constant In/Fe ratio which is expected and shows that the EPMA measurements are consistent.

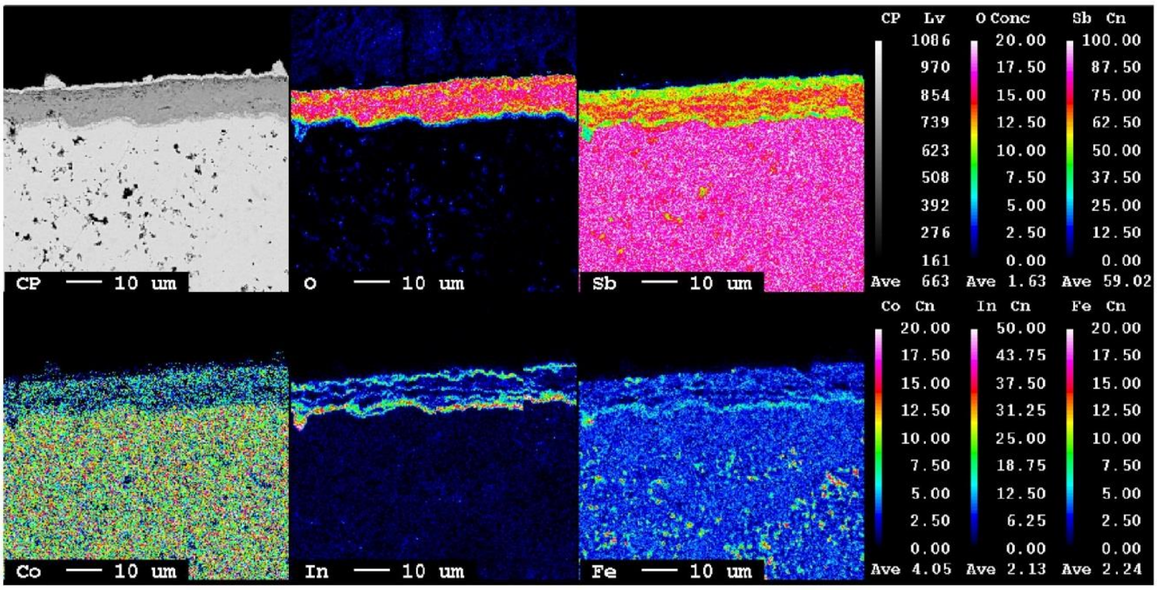

Figure 15 EPMA mapping of the hot side cross section of sample 54.

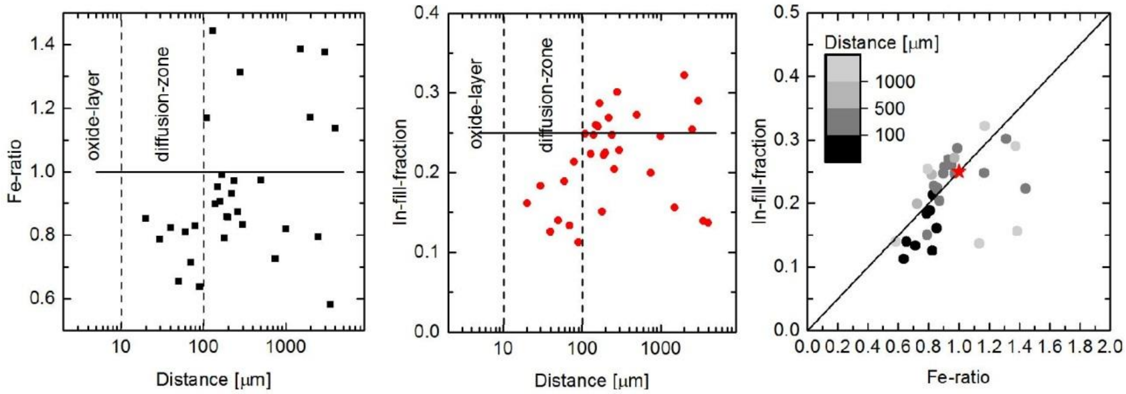

Figure 16 Fe-ratio (a) and In fill fraction (b) calculated from EPMA measurements as a function of distance from hot side of leg 4 from run 5. Straight lines indicate nominal (average) composition. In (c) the Fe-ratio is plotted against the In fill fraction. It is clearly seen how higher Fe ratio correlates with higher In filling as expected. Relatively large variations are seen across the whole sample, although the first 100μm seem to have a lower average Fe and In content than the rest of the sample.

Underneath two examples of the crystallite sizes are found for areas at a distance 30 and 300μm from the hot side of leg 1 from run 5. ImageJ with a morphological filter [REF] was used to calculate the average crystallite sizes between the two areas. The software fits an ellipsoid with the same area to each grain and calculates the long and short axis length. The average of these values is then used as an estimate of the crystallite size. A histogram of the values for each crystallite is found in Figure 18. The "hot side" area shows slightly lower average values of 214 nm versus 261 nm. Hardness measurement (HV50) of the same area closest to the hot side gave values of 690, compared to 540+-40 over the remainder of the cross section. This furthermore indicates a grain refining near the hot side leading to an increase in hardness due to grain boundary strengthening (Hall-Petch effect [REF]). Longer cycling or annealing times along with more dense samples is needed to investigate this effect further. This was only observed for the P-type material, and not the N-type. The effect of Fe-addition in skutterudites on grain redistribution is therefore something to investigate in further work.

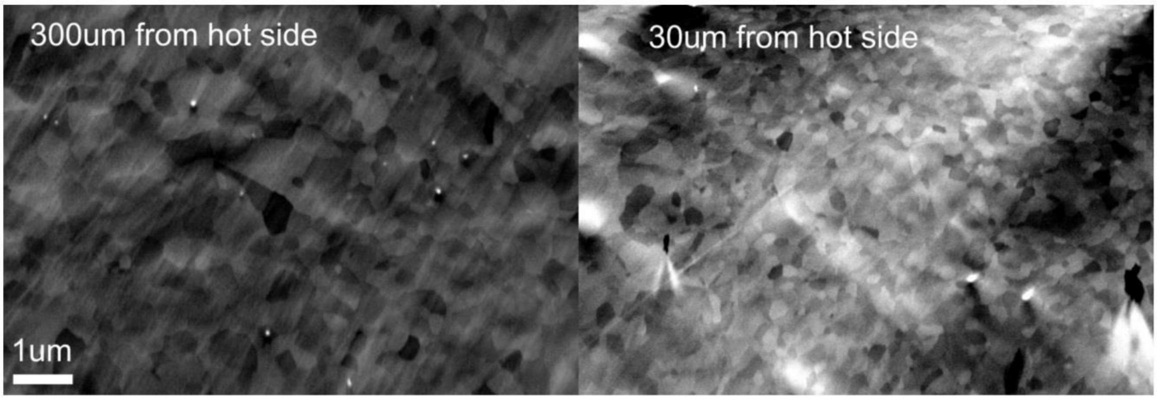

Figure 17 Forward scattered electron image of densfied area/hot spot approxomatly ~30µm (a) and ~300µm (b) from the edge of leg 1 from run 5. Crystallites of average diameter between 100-500nm are clearly seen.

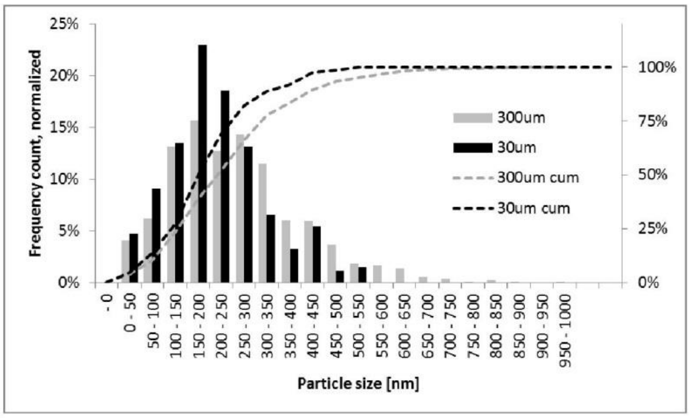

Figure 18 Crystallite size distribution of crystallites seen in Figure 17.

CONCLUSION

Sintered and functionalized Skutterudite legs made from gas atomized powders with metallization of Ti/Ag and protective coatings of Alwere tested under thermal cycles in air atmosphere between 150 and 500°C. We applied a new method of measuring individual legs simultaneously, recording I-V curves to find how V_{OC} and R_i changed during thermal cycling. A subsequent characterization of the legs was done to investigate the root cause of the observed changes in electrical properties.

- The measurement setup shows high accuracy in measurement of temperature and electric characterization. The relative changes between legs are also very apparent which shows how this tool could be valuable when evaluating several different coating and metallization concepts and their long term stability.
- In Run 2, Cu plated with Ag was used as the hot side electrode material. The Ti/Ag layer did not hinder diffusion of Cu into the SKD which caused a drastic reduction in the Seebeck coefficient close to the hot side. This fits well with the observed reduction in V_{OC} during testing. Also an increased thermal resistance at the hot side could cause lower dT over the active thermoelectric material further reducing the V_{OC}.
- In subsequent runs the electrodes were replaced with Ni to hinder diffusion into SKD. The V_{OC} is much more stable for most samples in this case due to no interdiffusion of Ni into SKD. From the PSM measurements the Seebeck coefficient instead increases closer to the hot side

for some samples. The R_i on the other hand increases steadily for all samples, although coated samples generally show a slower increase. Oxidation and crack-formation is the main reason for the increased R_i for all the samples.

- The increase in Seebeck coefficient close to the hot side for the P-type material could be ascribed to a combined diffusion and sintering effect. This sinter-effect is especially clear from the microscopy pictures and hardness measurement of the P-type material which shows a 20% increase in hardness close to the hot side compared to the rest of the samples. It is unclear what exact mechanisms causes the region with high α, but a reduction of charge carriers due to diffusion and oxidation/sublimation of for example In, Sb and Fe out of the hot zone could yield a higher α.
- The gradual increase in α from the middle of samples towards the hot side could be a combination of several temperature activated processes. At a region 100μm below the hot side diffusion of In and Fe is seen also in EPMA. Grain refinement is also a possible path, although the evidence for this is not conclusive. For the rest of the cross section of the sample, no phase separation is seen, and no significant difference in crystallite size is found. However, since the changes in α are so small (1-2%) it could still be a slight effect of decomposition and diffusion of In, Sb or Fe even if this is not observable in EDS/EPMA.
- There is a large difference between N and P-type material, not only in thermoelectric properties, but also mechanically. First of all, the P-type material is much more porous than the N-type material. It is evidently not sintered well enough and a sinter effect during thermal cycling is seen close to the hot side for all P-samples (>400-450°C). The N-type material was harder but also more brittle. This is especially seen on the edges/corners of the legs which had cracked and chipped off. The only exception is the legs coated on the side, indicating an accelerated embrittlement due to oxidation. This shows the importance of adequate coating solutions that hinder penetration of oxygen in to the contact layers and hot side of the thermoelectric legs.

REFERENCES

1. Rowe, D.M., *Thermoelectric Waste Heat Recovery as a Renewable Energy Source.* International Journal of Innovations in Energy Systems and Power, 2006. **1**(1).
2. EERE, *ITP Materials: Engineering Scoping Study of Thermoelectric Generator Systems for Industrial Waste Heat Recovery*, 2013.
3. Uher, C., *Skutterudite-Based Thermoelectrics*, in *Thermoelectrics Handbook, Macro to Nano*, D.M. Rowe, Editor. 2006, CRC Press: Boca Raton, Florida, p. 34.1-34.17.
4. LeBlanc, S., et al., *Material and manufacturing cost considerations for thermoelectrics.* Renewable and Sustainable Energy Reviews, 2014. **32**(0): p. 313-327.
5. Liu, W., et al., *Current progress and future challenges in thermoelectric power generation: From materials to devices.* Acta Materialia, 2015. **87**: p. 357-376.
6. Rull-Bravo, M., et al., *Skutterudites as thermoelectric materials: revisited.* RSC Advances, 2015. **5**(52): p. 41653-41667.
7. Thierry, C., et al., *Development of High Efficiency Segmented Thermoelectric Couples*, in *11th International Energy Conversion Engineering Conference*. 2013, American Institute of Aeronautics and Astronautics.
8. Yang, J. and T. Caillat, *Thermoelectric Materials for Space and Automotive Power Generation.* MRS Bulletin, 2006. **31**(03): p. 224-229.
9. Hara, R., et al., *Aging effects of large-size n-type CoSb3 prepared by spark plasma sintering.* Journal of Alloys and Compounds, 2003. **349**(1–2): p. 297-301.

10. Godlewska, E., et al., *Degradation of CoSb3 in Air at Elevated Temperatures.* Oxidation of Metals, 2010. **74**(3-4): p. 113-124.
11. Zhao, D., et al., *High temperature oxidation behavior of cobalt triantimonide thermoelectric material.* Journal of Alloys and Compounds, 2010. **504**(2): p. 552-558.
12. Leszczynski, J., K. Wojciechowski, and A. Malecki, *Studies on thermal decomposition and oxidation of CoSb3.* Journal of Thermal Analysis and Calorimetry, 2011. **105**(1): p. 211-222.
13. Saber, H.H. and M.S. El-Genk, *Effects of metallic coatings on the performance of skutterudite-based segmented unicouples.* Energy Conversion and Management, 2007. **48**(4): p. 1383-1400.
14. Godlewska, E., et al., *Protective Coating to Suppress Degradation of CoSb3 Thermoelectric at Elevated Temperatures.* Ceramic Materials, 2010. **62**(4): p. 490-495.
15. Dong, H., et al., *Improved oxidation resistance of thermoelectric skutterudites coated with composite glass.* Ceramics International, 2012(0).
16. Dong, H., et al., *Fabrication and thermal aging behavior of skutterudites with silica-based composite protective coatings.* Journal of Alloys and Compounds, 2012. **527**(0): p. 247-251.
17. Saber, H.H., M.S. El-Genk, and T. Caillat, *Tests results of skutterudite based thermoelectric unicouples.* Energy Conversion and Management, 2007. **48**(2): p. 555-567.
18. Nemoto, T., et al., *Improvement in the Durability and Heat Conduction of uni-leg Thermoelectric Modules Using n-type Mg2Si Legs.* Journal of Electronic Materials, 2014. **43**(6): p. 1890-1895.
19. Wang, H., et al., *Determination of Thermoelectric Module Efficiency: A Survey.* Journal of Electronic Materials, 2014. **43**(6): p. 2274-2286.
20. Muto, A., et al., *Skutterudite Unicouple Characterization for Energy Harvesting Applications.* Advanced Energy Materials, 2013. **3**(2): p. 245-251.
21. Salvador, J.R., et al., *Conversion efficiency of skutterudite-based thermoelectric modules.* Physical Chemistry Chemical Physics, 2014. **16**(24): p. 12510-12520.
22. Skomedal, G., et al., *Methods for Enhancing the Thermal Durability of High-Temperature Thermoelectric Materials.* Journal of Electronic Materials, 2013. **43**(6): p. 1946-1951.
23. Schröder, K. and A. Giannuzzi, *Thermoelectric Power and Resistivity of Nickel, Cobalt, and Iron near the Curie Temperature.* physica status solidi (b), 1969. **34**(2): p. K133-K137.
24. Goldsmid, H.J., *Introduction to Thermoelectricity*. Springer Series in Material Science. 2009: Springer.
25. Park, K.-H., et al., *High-Temperature Stability of Thermoelectric Skutterudite In0.25Co3FeSb12.* Journal of Electronic Materials, 2012. **41**(6): p. 1051-1056.

Appendix II. Thermal cycling experiments

This appendix show the experimental setup used in Paper 5 in more detail, along with extra test-results not published. The setup is made on an existing rig for testing thermoelectric modules design and constructed by Nils Randulf Kristiansen.

Experimental Setup

A sketch of the experimental setup is shown in Figure II.1. Four to six thermoelectric legs are placed directly on a cold side copper block. Above this, four to six separate hot side electrodes embedded in insulating MACOR© are pressed down on the thermoelectric legs. Electrode material can easily be changed since only press-contact is used between the parts. The cold side temperature is measured at the surface of the copper block, while the hot side is measured 1 mm above the thermoelectric materials in a hole coming in from the side of the electrode as seen in the pictures in Figure II.2. From this the temperature gradient, dT, over the legs are calculated.

From each electrode a wire is fastened with a screw as seen in Figure II.3, which measures the total open circuit voltage (dV in Figure II.1) resulting from the Seebeck voltage over thermoelectric leg, electrode and wire material under a temperature gradient. The temperature and voltage signals are continuously monitored with a Labview program. The same program is also used for controlling the power supplies (PS) giving power to the heater elements mounted in the heater block, in addition to an active load used for measuring I-V curves. A PID control is used to adjust the setpoint of the PS to achieve the wanted hot side temperatures. On the cold side, a continuous flow of water is running through the cold block made of copper. The water loop is a closed system, where heat dissipation is achieved through a radiator with a fan blowing fresh laboratory air through it. This ensures that the temperature of the cooling water never exceeds a few degrees more than the room temperatures (20-25°C). The cold side temperature is measured in a shallow groove on the surface of the cold block, in the middle between all thermoelectric legs as indicated in Figure II.1. The temperatures varies between 20°C and up to 30°C under maximum power of the heaters (200 W), which equals a hot side temperature of between 600 and 800°C depending on the total area and length of TE-legs tested.

The whole setup; cold block, TE-legs, electrodes, insulating block, heater block and top insulation, is pressed together with four manually adjustable springs as seen in

Figure II.3. Uniform contact pressure is achieved by carefully tightening the nuts so that the springs are compressed the same distance.

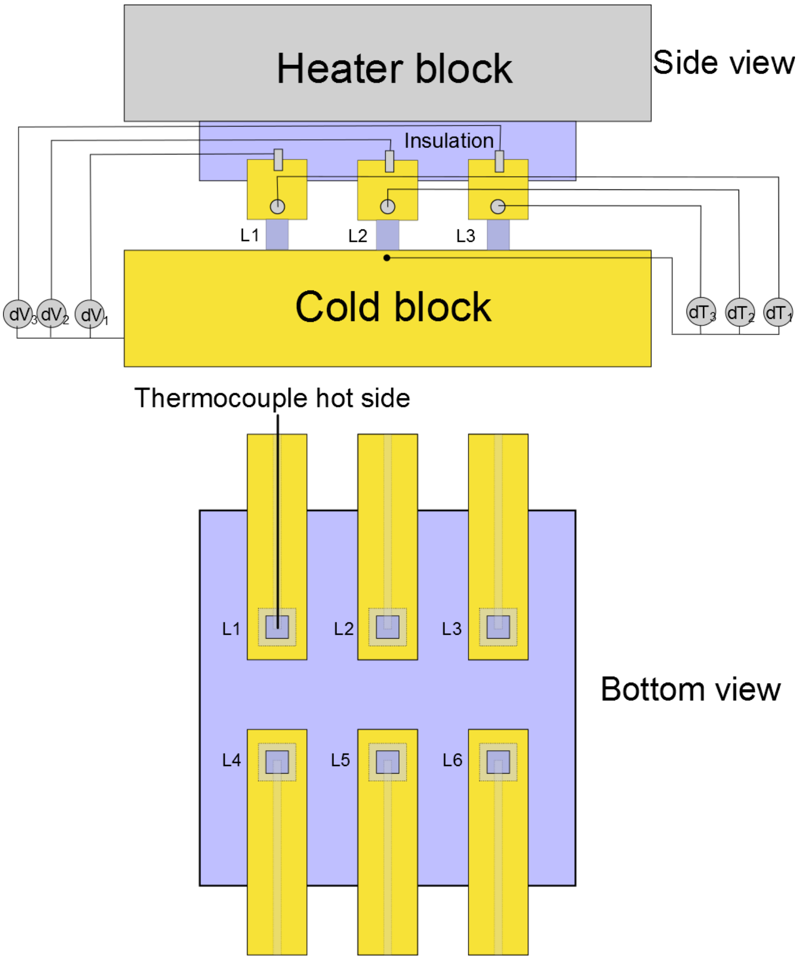

Figure II.1 Schematic overview over experimental setup. L1-L6 indicates thermoelectric legs of size 2-8 mm.

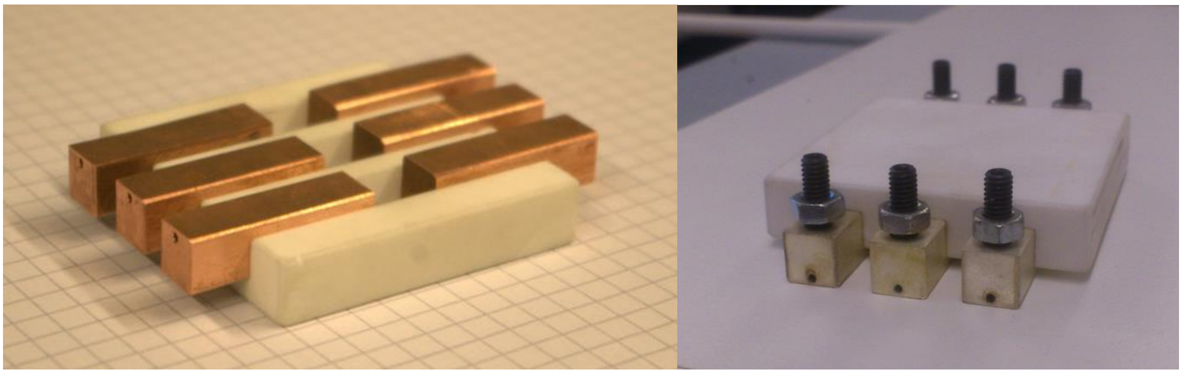

Figure II.2 Pictures of hot side copper electrodes (left) and Ag-plated (right) embedded in Macor © insulation. The hot side temperature is measured with K-type thermocouples (Ø=1mm) inserted into the side holes of the electrodes. Wire for electrical characterization are pressed down on the electrode with a nut achieving good electrical contact.

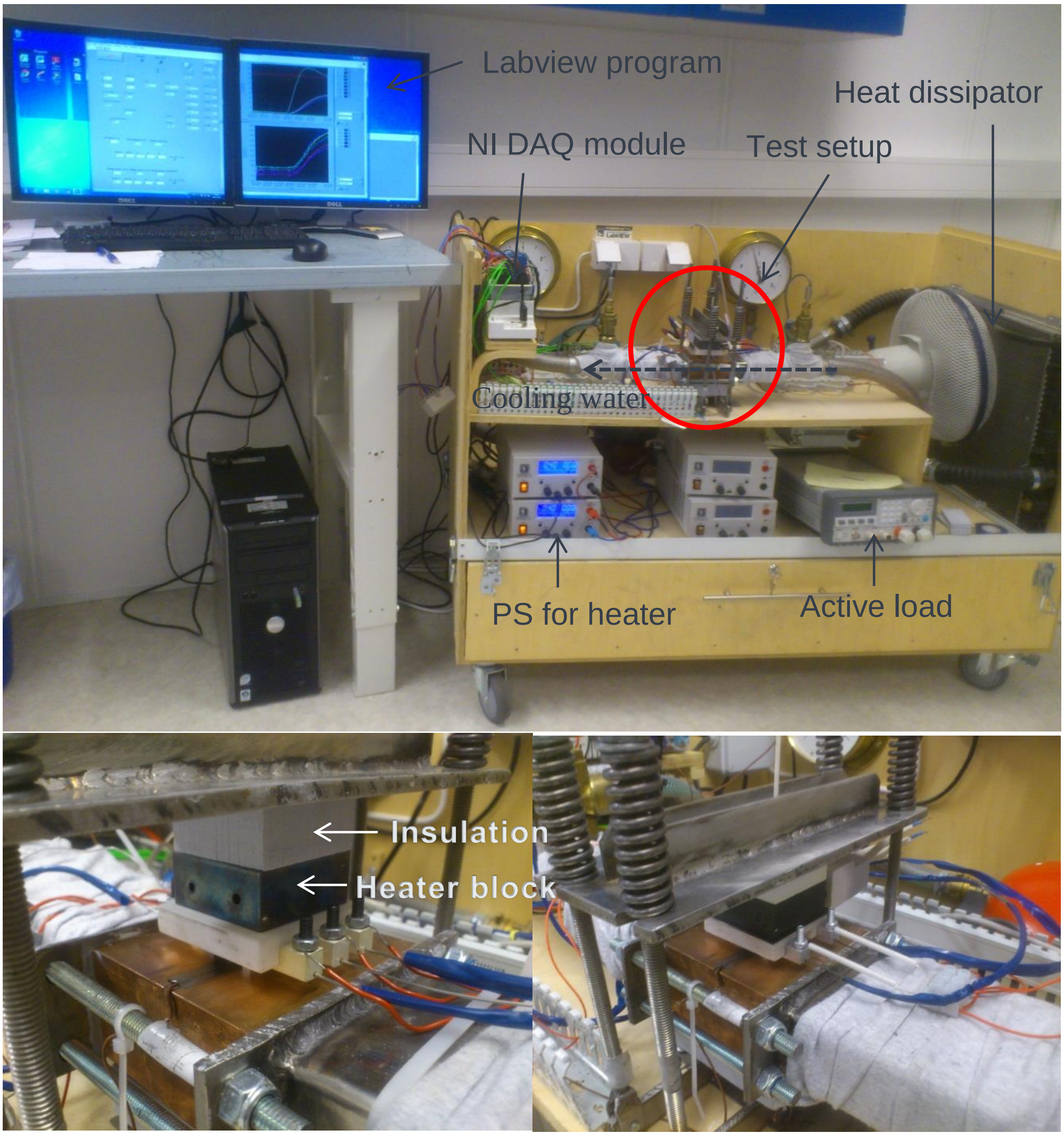

Figure II.3 Pictures of the experimental rig used for thermal cycling experiments.

Test results

Seven test-runs have been performed to assess both the instrument and also some functionalized thermoelectric legs made of skutterudite with different type of metallization and coatings. An overview over all these runs (except the first run) are found in Table II.1. Here the metallization type, electrode type, coating and cycling program are given, in addition to results from the testing. Furthermore, evolution in temperatures, open circuit voltage (all runs) and inner resistance (run 4 to 7) are found in figures II.4 to II.8, in addition to Figure 4.26 in chapter 4.

Table II.1 Overview over all thermal cycling test done with the setup, both those made for testing the method itself in addition to real testing of functionalized skutterudite legs. Two TE-materials, one n-type (N-ref) and p-type (P-ref) were used which properties are found in Paper 5.

Test nr	Cycling program	Leg nr	TE-material	Metallizaion	Coating	Hot side electrodes	Summary performance	Comments
2	150-500°C @1h for 112 cycles	1	P-ref	Ti + Ag	-	Cu-block with Ag + Al	Gradual reduction of Voc of 16%	
		3	N-ref	Ti + Ag	-	Cu-block with Ag only	Rapid reduction already after 5 cycles, down 50%	
		4	P-ref	Ti + Ag	Al	Cu-block with Ag + Al	Gradual reduction of Voc of 14%	
		6	P-ref	Ti + Ag	Al	Cu-block with Ag + Al	Fast reduction from beginning, more rapid after 37 cycles, down 75%	Some Al-coating on interface between TE-leg and electrode contributing to increase in Ri.
3	150-500°C @1h for 12 cycles	1	P-ref	Ag+Ti	Al	Ni-block with Ni-wire	Quite stable Voc, almost no change	
		3	N-ref	Ag+Ti	-	Ni-block with Ni-wire	Decrease from -0.95 to -0.67	
		4	N-ref	Ag+Ti	Al	Ni-block with Ni-wire	Decrease from -0.97 to -0.73	
		6	P-ref	Ag+Ti	-	Ni-block with Ni-wire	Decrease from 0.58 to 0.5V	
4	150-270/370°C @0.5h for 200cycles	1	P-ref	Ti + Ag	-	Ni-block with Ni-wire	Got ruined after one heater did not turn of after cycle 67. Voc decrease	
		3	P-ref	Ti + Ag	-	Ni-block with Ni-wire	Got ruined after one heater did not turn of after cycle 67. Voc stable	
		4	N-Ref	Ti + Ag	-	Ni-block with Ni-wire	Gradual increase in Ri. Voc stable	
		6	N-Ref	Ti + Ag	-	Ni-block with Ni-wire	Gradual increase in Ri. Voc stable	
5	300°C 4 cycles @1h + 500°C 14cycles @1h	1	P-ref	Ti + Ag	Al	Ni-block with Ni-wire + Al-coating	Gradual incraese in Ri from 0.022 to 0.110. Voc stable	
		3	P-ref	Ti + Ag	-	Ni-block with Ni-wire + Al-coating	Rapid increase in Ri from start. Some decrease in Voc	Some Al-coating on interface between TE-leg and electrode contributing to increase in Ri.
		4	P-ref	Ti + Ag	Al	Ni-block with Ni-wire + Al-coating	Rapid increase in Ri after cycle 10. Some decrease in Voc	
		6	N-Ref	Ti + Ag	-	Ni-block with Ni-wire + Al-coating	Rapid increase in Ri after cycle 13. Voc decreases fast	
6	250°C 4cycles @1h + 400-450°C 48cycles @1h	1	P-ref	Ti/TiN/ Ag	-	Ni-block with Ni-wire	Rapid increase of Ri after cycle 17. Voc decreased a lot.	
		3	P-ref	Ti/TiN/ Ag	Al	Ni-block with Ni-wire	Ri very fast reached high values because of the paint. Voc stable	Some Al-coating on interface between TE-leg and electrode contributing to increase in Ri.
		4	N-Ref	Ti/TiN/ Ti/TiN/ Ag	-	Ni-block with Ni-wire	High initial Ri, gradual increase from 0.040 to 1. Voc decreased a lot.	Not good enough contact, can cause high Ri during run
		6	N-Ref	Ti/TiN/ Ti/TiN/ Ag	Al	Ni-block with Ni-wire	Gradual increase of Ri from 0.02 to 0.130. Voc stable	
7	Gradual increase from 350 to 460°C for 6-10cycles each @ 1h	1	P-ref	Ti/TiN/ Ni	-	Ni-block with Ni-wire	Ri stable until 440°C when it suddenly decreased (diff bonding). Then increase again at 460°C. Voc stable	Very high initial Ri due to partly delaminated Ni-layer
		3	P-ref	Ti/TiN/ Ni	Al	Ni-block with Ni-wire	Ri ran in roof fast. Voc also a bit later.	Very high initial Ri due to partly delaminated Ni-layer. Al between leg and electrode.
		4	N-Ref	Ti/TiN/ Ti/TiN/ Ag	-	Ni-block with Ni-wire	Gradual increase of Ri from 0.021 to 0.365. **Voc deacreses at 460C.**	
		6	N-Ref	Ti/TiN/ Ti/TiN/ Ag	Al	Ni-block with Ni-wire	Gradual increase of Ri from 0.018 to 0.108. Voc stable	

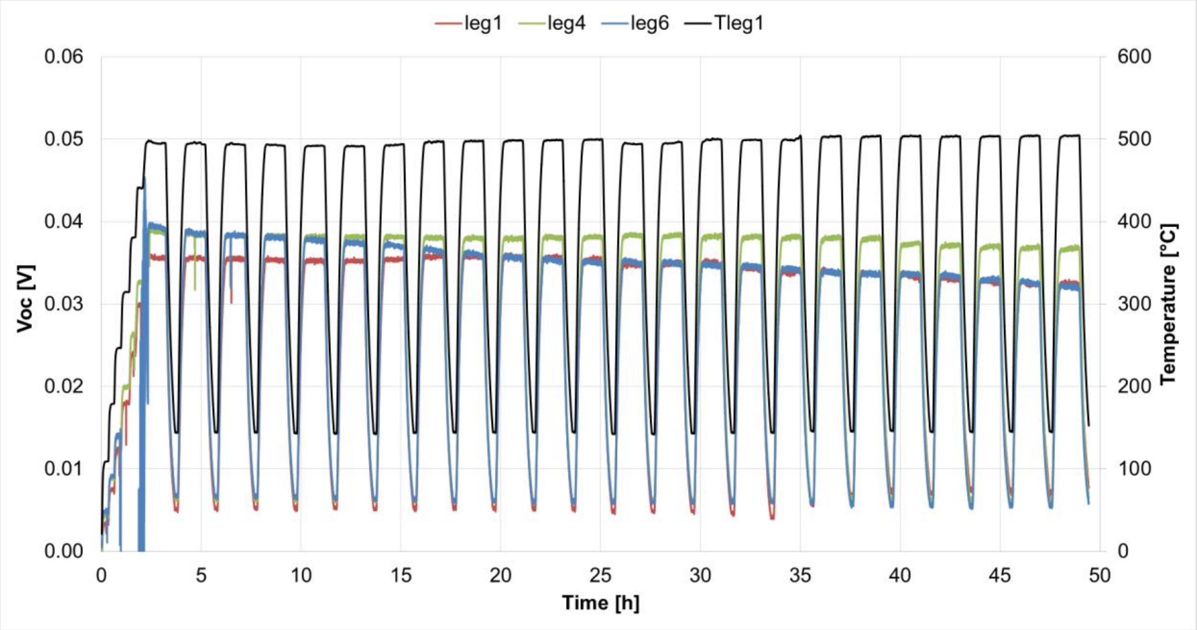

Figure II.4 Data from run 2, showing open circuit voltage (V_{OC}) of legs 1, 3 and 6 (p-type) and hot side temperature of leg 1 of the 24 first cycles (of total 113). The V_{OC} is seen to gradually reduce, especially for leg 6, while the temperature is fairly stable, although with a slight increase due to higher thermal interface resistance between leg and electrode. For a total overview over all cycles see Paper 5.

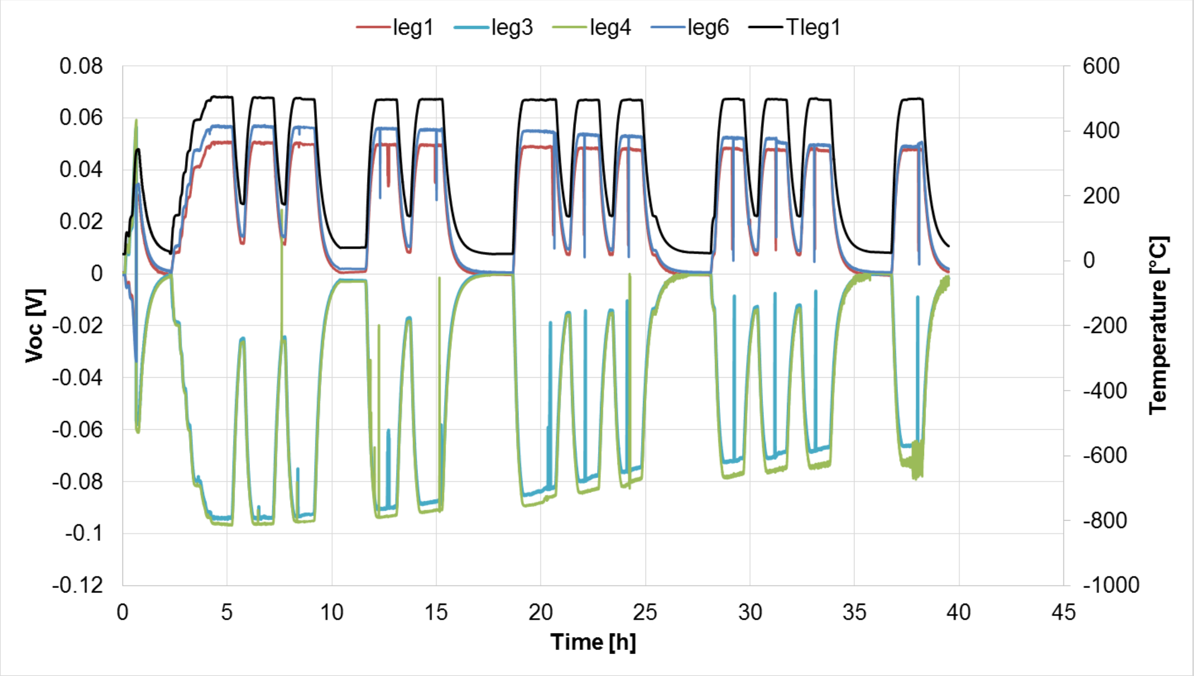

Figure II.5 Data from run 3, showing V_{OC} of all legs and hot side temperature of leg 1. Leg 1 and 3 are p-type while leg 4 and 6 are n-type. All legs except leg 1 (coated) shows significant reduction in V_{OC} due to oxidation an increase in hot side interface thermal resistance.

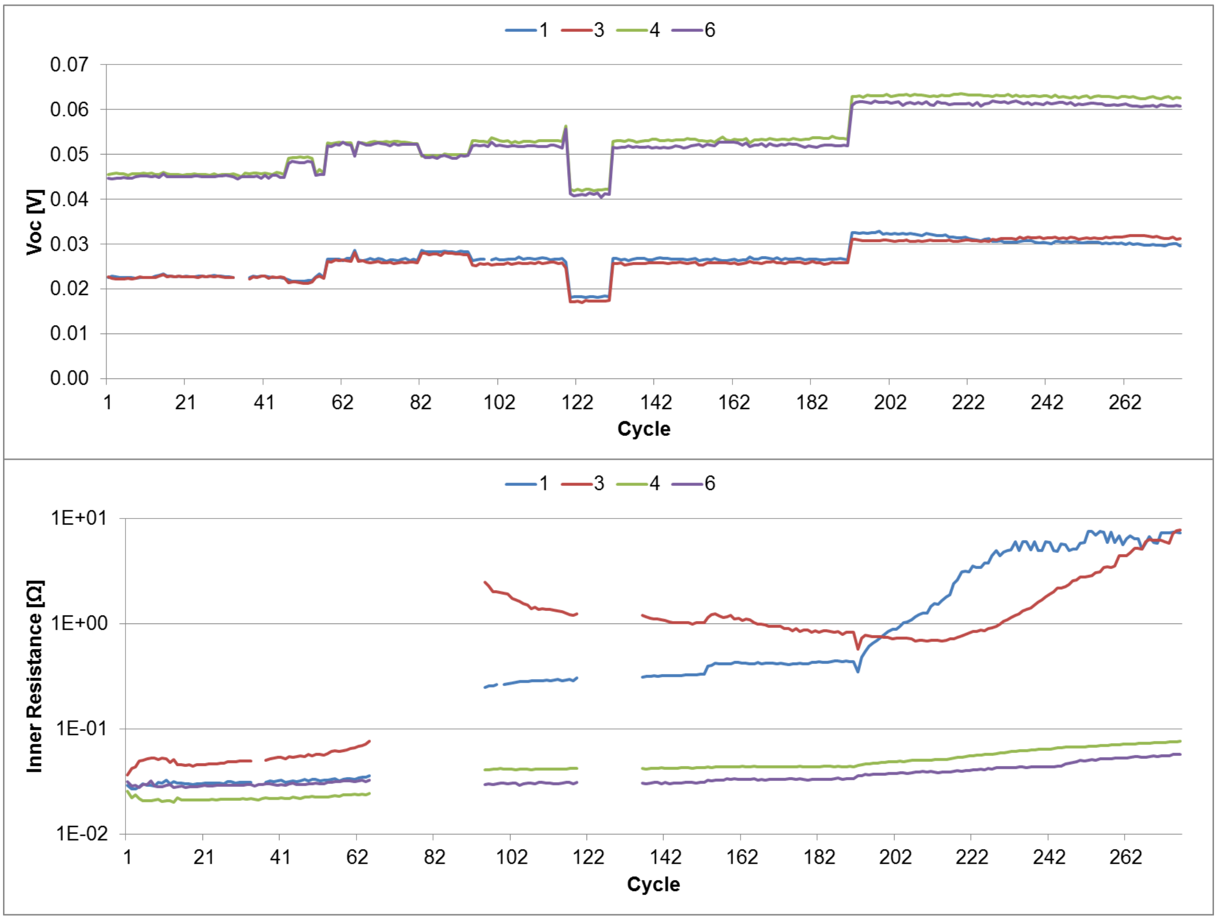

Figure II.6 Data from run 4, with V_{OC} (upper) and R_i (lower) for each leg as a function of cycle number. V_{OC} increases due to gradual increase of hot side temperature, while Ri increases due to different degradation processes. Especially leg 1 and 3 are severely damaged after cycle 90 due to heaters above these legs running on max power for a limited time.

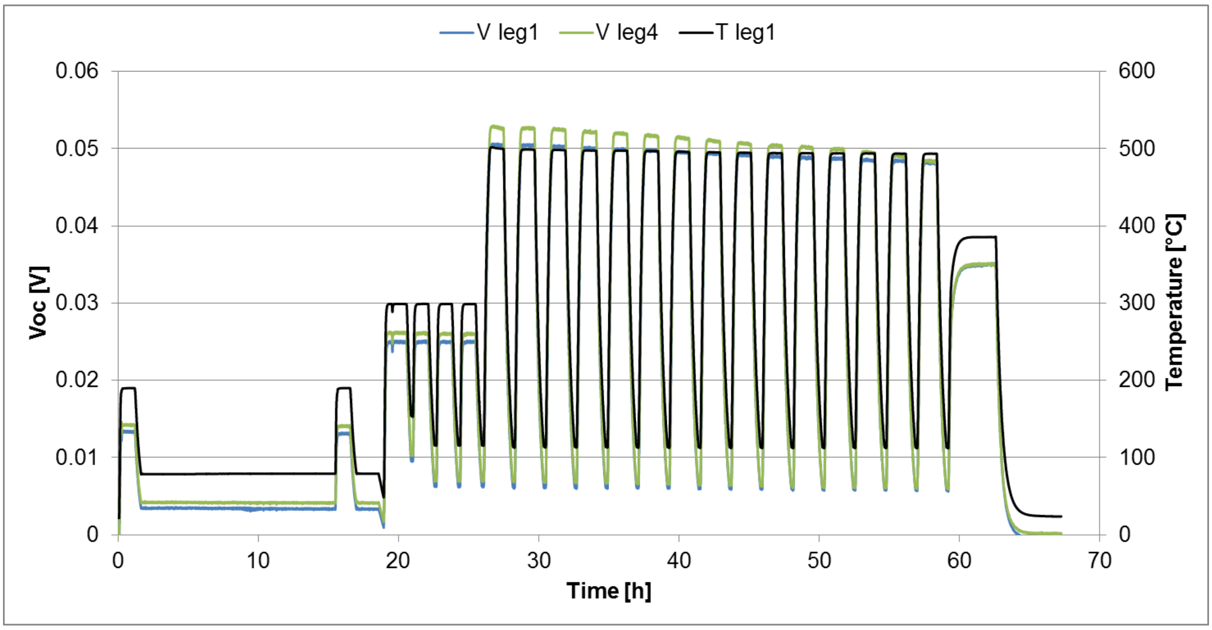

Figure II.7 Data from run 5, showing V_{OC} of leg 1 and 4, and hot side temperature of leg 1. In total 15 cycles were performed at 500°C. Corresponding I-V data found in Paper 5.

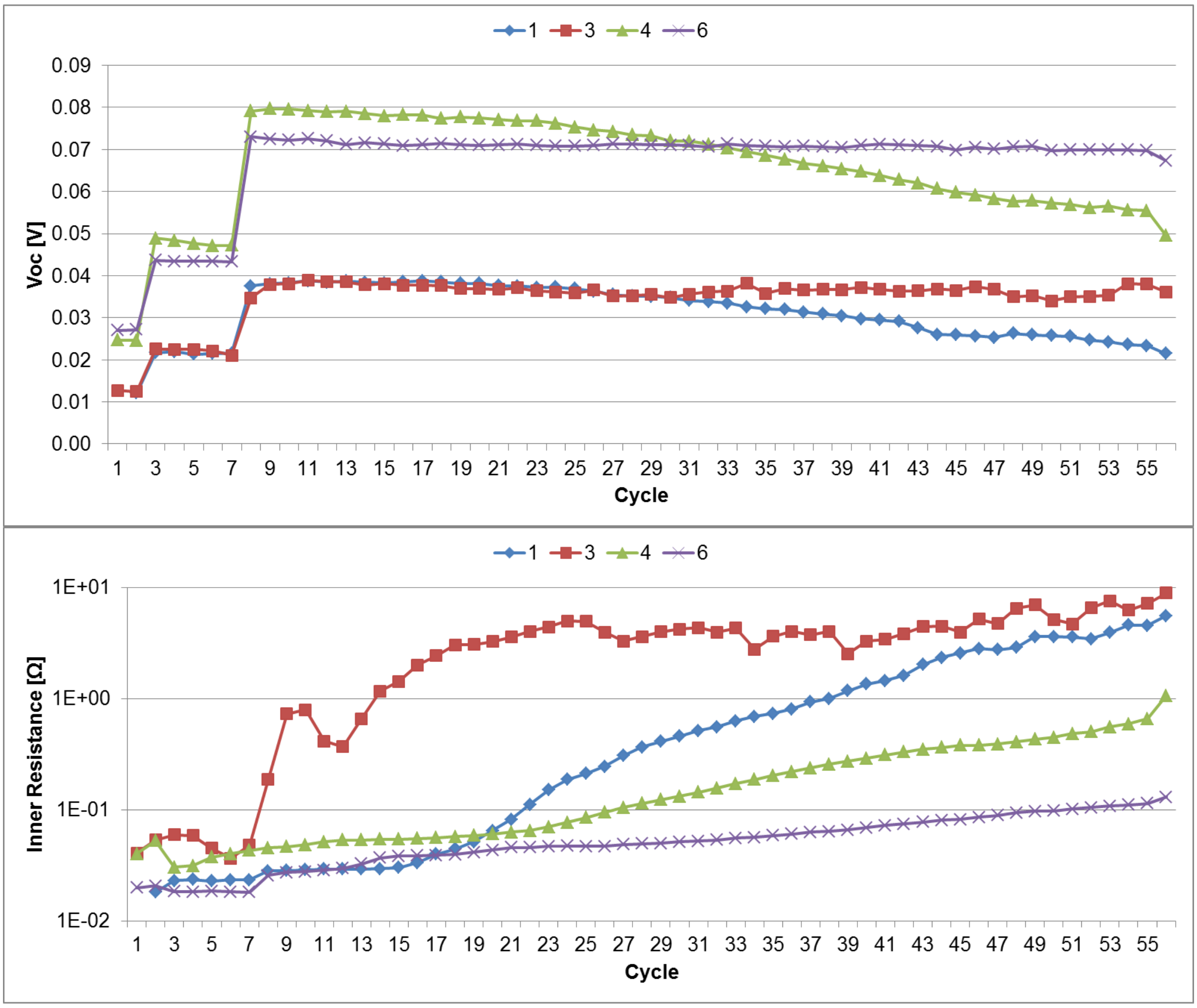

Figure II.8 Data from run 6, with V_{OC} (upper) and R_i (lower) for each leg as a function of cycle number. V_{OC} of leg 1 and 6 decrease steadily during testing. R_i increases rapidly for leg 3 and more slowly for the others, especially leg 6 due to coating hindering severe oxidation.